Springer Proceedings in Physics 233

Amalia Martínez-García
Indrani Bhattacharya
Yukitoshi Otani
Rainer Tutsch *Editors*

Progress in Optomechatronic Technologies

Proceedings of International Symposium on Optomechatronic (2018)

Springer

Springer Proceedings in Physics

Volume 233

Indexed by Scopus

The series Springer Proceedings in Physics, founded in 1984, is devoted to timely reports of state-of-the-art developments in physics and related sciences. Typically based on material presented at conferences, workshops and similar scientific meetings, volumes published in this series will constitute a comprehensive up-to-date source of reference on a field or subfield of relevance in contemporary physics. Proposals must include the following:

- name, place and date of the scientific meeting
- a link to the committees (local organization, international advisors etc.)
- scientific description of the meeting
- list of invited/plenary speakers
- an estimate of the planned proceedings book parameters (number of pages/articles, requested number of bulk copies, submission deadline).

More information about this series at http://www.springer.com/series/361

Amalia Martínez-García · Indrani Bhattacharya ·
Yukitoshi Otani · Rainer Tutsch
Editors

Progress in Optomechatronic Technologies

Proceedings of International Symposium on Optomechatronic (2018)

Springer

Editors
Amalia Martínez-García
Centro de Investigaciones en Óptica
León, Guanajuato, México

Indrani Bhattacharya
University of Calcutta
Kolkata, West Bengal, India

Yukitoshi Otani
Center for Optical Research and Education
Utsunomiya University
Utsunomiya, Tochigi, Japan

Rainer Tutsch
Institute of Production Technology
Braunschweig University
Braunschweig, Niedersachsen, Germany

ISSN 0930-8989 ISSN 1867-4941 (electronic)
Springer Proceedings in Physics
ISBN 978-981-32-9631-2 ISBN 978-981-32-9632-9 (eBook)
https://doi.org/10.1007/978-981-32-9632-9

This Springer imprint is published by the registered company Springer Nature Singapore Pte Ltd.
The registered company address is: 152 Beach Road, #21-01/04 Gateway East, Singapore 189721, Singapore

Preface

This volume contains a series of technical papers presented at 19th International Symposium on Optomechatronic Technology (ISOT 2018) organized by the International Society for Optomechatronics (ISOM) and Centro de Investigaciones en Óptica (CIO) and held in Cancún, Quintana Roo, México, during November 5–8, 2018.

Symposium had topics relating to optical metrology, optical imaging/interferometry, optical fiber sensors, polarization sensing and imaging, laser-based sensors, optical sensors on robotics autonomous vehicles and other applications, optofluidics, optomechatronics for sensing and imaging, micro-optoelectro-mechanical systems, optical inspection for industry, adaptive optics, visual motion tracking and control, biomedical applications, vision-based monitoring and control, optical manipulation and tweezers and their applications, material laser processing, actuators based on optics and optomechatronics, 3D processing, 3D fabrication and 3D printer, thin film technology, solar cell and two special sessions of polarization technology and sensors based on the use of lasers and fiber optics.

This collection of twenty-two chapters presents experimental and computational investigations on important areas of optomechatronics. Symposium was intended to be interdisciplinary forums for engineers, technicians, researchers and managers involved in all fields of optics, optomechatronics, mechanics and mechanical engineering.

We very sincerely thank the authors who have contributed to this volume, presenters, reviewers and session chairs for their participation, support and contribution to this symposium.

Amalia Martínez-García
Laboratory of Optical and
Mechanical Testing
Centro de Investigaciones en Óptica, A. C.
León, México

Indrani Bhattacharya
University of Calcutta
Kolkata, India

Yukitoshi Otani
Utsunomiya University
Utsunomiya, Utsunomiya

Rainer Tutsch
Braunschweig University
Braunschweig, Germany

Brief Description of the Book

The objective of this book is to show the development of technology integrated with optics, mechanics, electronics as well as computation which is known as optomechanics. Optomechatronics is an interdisciplinary field of engineering that works on systems that consist of synergistically integrated mechanical, electrical and optical components based on the exchange of energy and information. Many optomechatronic systems incorporate control circuits, resulting in robustness against external interference and partially autonomous operation. Optomechatronic systems can be found in many areas of applications, such as industrial production, automotive technology, space and air technology, medical mechanisms and input goods. Examples of optomechanical systems are: guided vision robots, laser machining systems, autonomous vehicles, optical storage mechanisms (CDs, DVDs), laser printers, digital cameras with active optics (auto-iris, autofocus, zoom lens), scanning microscopes, endoscopic mechanisms, adaptive optics in astronomy, etc.

In contrast to the immense impact of optomechatronics on technology and economics, it is hardly noticed by the general public. Improving the public visibility of optomechatronics would make it more attractive to young scientists and engineers. The development of optomechatronic devices and systems and their implementation in solving problems and applications requires deep knowledge in the fields of mechanics, electronics, optics and information technology, as well as experience in systems engineering.

This book is presenting twenty-two chapters that feature optical metrology, fiber optics, photonic crystal waveguides, nano-antennas excitation, acousto-optic systems, 3D fabrication and 3D printer, solar irradiance data and solar sensor, machine vision, robotics and other applications.

We hope that the presented material in this book is a reference for researchers and professionals on mechanical, materials, optical metrology and optomechatronics engineering. Finally, it is used by a large number of universities and research institutes around the world.

Contents

Editors and Contributors

About the Editors

Amalia Martínez-García is a full-time researcher at the Centro de Investigaciones en Óptica, CIO, Mexico. She received her Ph. D. in Optics at CIO and has been a Visiting Professor at the Universidad de Santiago de Chile, Utsunomiya University, and University of the Basilicata. She is a member of Mexico's National System of Researchers and the Mexican Academy of Optics (AMO), Optical Society (OSA), Society of Photo-Optical Instrumentation Engin eers (SPIE) and International Society of Optomechatronics (ISOM). She was President of the AMO in 2015–2016. Her research interests focus on the field of optical metrology. She has participated in conferences organization, being co-organizer and initiator of the Meeting Participation of the Woman in Science, annual event at Mexico since 2004 to date. She was chair of Fifth International Symposium on Experimental Mechanics & Ninth Symposium on Optics in Industry, 2015, and of International Symposium on Optomechatronic Technology, 2018. She is author of eighty papers in journals indexed in the Journal Citation Reports.

Dr. Indrani Bhattacharya is a Postdoctoral researcher associated with Prof. Ayan Banerjee of Light–Matter Interaction Lab, Indian Institute of Science Education and Research, IISER, Kolkata and Prof. Vasudevan Lakshminarayanan of School of Optometry, University of Waterloo, Canada. She has completed her B.Sc. with Hons. in Physics and M.Sc.(Tech.) in Applied Physics with specialization in Optics and Opto-electronics from University of Calcutta. She has just completed her Ph.D. in Technology from the Department of Applied Optics and Photonics, University of Calcutta. She is having 20 years industry and 9 years academic experience. Her research areas include Diffractive Optics, Biomimetics, Optical Tweezers, Point Spread Function Engineering, In-Vivo and In-Vitro Biomedical Applications, Optical Fibre Sensors. She is a member of Optical Society of India, International Society of Optics and Photonics, International Society of Optomechatronics. She has published 12 research articles which include Conference, Journal, Book and Book Chapter publications during her 9 years academic and research career.

Prof. Yukitoshi Otani is Professor in the Department of Optical Engineering, Utsunomiya University. He has completed his B.S. and M.S. from Tokyo University of Agriculture and Technology; Ph.D. from the Department of Precision Engineering, University of Tokyo. He has more than 25 years of academic and research experience. His fields of specialization are polarization science and engineering, optical measurement for surface topography and optomechatronics. He was selected as Fellow in 2010 by the International Society for Optics and Photonics.

Prof. Dr. Rainer Tutsch is Professor in TU Braunschweig, Institut für Produktionsmesstechnik, Braunschweig. His main field of research is optical techniques for 3D measurement of shape and deformation, with applications in quality assurance, material research, reverse engineering, etc; development and application of multisensor coordinate measuring machines and techniques of sensor and data fusion; micro-metrology with techniques like microscopy, white-light interferometry, laser-interferometry and scanning electron microscopy; Acoustic holography and industrial applications of spectroscopic techniques. He has published many papers in these areas. He is an active member of two workgroups for standardization: Fundamentals of Metrology and Optical 3D Metrology. He is editorial board member of several international conferences. He is also board member of the *International Journal of Optomechatronics* and official reviewer of Measurement.

Contributors

Yasuhiko Arai Kansai University, Suita, Osaka, Japan

Akbar Assa University of Toronto, Toronto, Canada

Mahrokh Avazpour Facultad de Ciencias Físico Matemáticas, Benemérita Universidad Autónoma de Puebla, Ciudad Universitaria, Puebla, Mexico

Josué I. Basulto Centro de Investigaciones en Óptica A. C., León, Guanajuato, Mexico

Indrani Bhattacharya Department of Applied Optics and Photonics, University of Calcutta, Kolkata, India

Beethoven Bravo-Medina Centro de Investigaciones en Óptica A. C., León, Mexico

Samantha A. Cajero Roodriguez CONACYT—Centro de Investigaciones en Óptica, A. C., Unidad Aguascalientes, Aguascalientes, Mexico

Juan M. Callejas-Cornejo PICYT—Centro de Investigaciones en Optica A. C., Unidad Aguascalientes, Aguascalientes, Mexico

V. Castillo-Gallardo Facultad de Ciencias Físico-Matemáticas, UMSNH. Avenida Francisco J. Múgica S/N, Morelia, Michoacán, Mexico

Luis V. Coronado CONACYT—Centro de Investigaciones en Óptica, A. C., Unidad Aguascalientes, Aguascalientes, Mexico

F. J. Cuevas Optical Metrology, Centro de Investigaciones en Óptica A. C., León, Mexico

Moisés Cywiak Centro de Investigaciones en Óptica A. C., León, Guanajuato, Mexico

M. de Coss-Maritza Universidad Autónoma de Yucatán, Mérida, Yucatán, Mexico

Jonny Paul Zavala de Paz Universidad Politécnica de Querétaro, Querétaro, Mexico

Carmen E. Domínguez-Flores Centro de Investigaciones en Óptica A. C., León, Guanajuato, Mexico

Jorge Mauricio Flores Moreno Centro de Investigaciones en Óptica A. C., León, Guanajuato, Mexico

Ruben Garrido Departamento de Control Automático, CINVESTAV-IPN, Mexico City, Mexico

Mohammad Ghahramani Ryerson University, Toronto, ON, Canada

Francisco Javier González Universidad Autónoma de San Luis Potosi, San Luis Potosi, Mexico

Jose A. González Laboratorio de Inteligencia Artificial y Supercomputo, Instituto de Física y Matemáticas, Universidad Michoacana de San Nicolás de Hidalgo, Morelia, Mexico

Ruediger Grunwald Max-Born-Institute for Nonlinear Optics and Short Pulse Spectroscopy, Berlin, Germany

Manabu Hashimoto Chukyo University, Nagoya-shi, Aichi, Japan

Lakshminarayan Hazra Department of Applied Optics and Photonics, University of Calcutta, Kolkata, India

Erick Ipus Centro de Investigaciones en Óptica A. C., León, Mexico

Cesar Isaza Universidad Politécnica de Querétaro, Querétaro, Mexico

Farrokh Janabi-Sharifi Department of Mechanical and Industrial Engineering, Ryerson University, Toronto, ON, Canada

S. Juan Manuel Franco Centro de Investigaciones en Óptica A. C., León, Guanajuato, Mexico

Danish Khan School of Electronics Engineering, IT College, Kyungpook National University, Daegu, Korea

Min Young Kim School of Electronics Engineering, Research Center for Neurosurgical Robotic System, IT College, Kyungpook National University, Daegu, Korea

Evgeny Kuzin INAOE, Puebla, Mexico

Florian Lemke Department of Microsystems Engineering – IMTEK, Laboratory for Microactuators, University of Freiburg, Freiburg, Germany

Daniel López-Cortés Centro de Investigaciones en Óptica A. C., León, Guanajuato, Mexico

A. López-Martínez Optical Metrology, Centro de Investigaciones en Óptica A. C., León, Mexico

E. Lozano-Trejo Facultad de Ciencias Físico-Matemáticas, UMSNH. Avenida Francisco J. Múgica S/N, Morelia, Michoacán, Mexico

J. Lugo-Jiménez Universidad Autónoma de Yucatán, Mérida, Yucatán, Mexico

Daniel Luis Noriega Centro de Investigaciones en Óptica A. C., León, Guanajuato, Mexico

Fernando Martell CONACYT—Centro de Investigaciones en Óptica, A. C., Unidad Aguascalientes, Aguascalientes, Mexico

Mehran Mehrandezh Faculty of Engineering and Applied Science, University of Regina, Regina, Canada

H. Méndez-Dzul Instituto Nacional de Astrofísica, Óptica y Electrónica, Tonantzintla, Puebla, Mexico

Javier Méndez-Lozoya Universidad Autónoma de San Luis Potosi, San Luis Potosi, Mexico

Fernando Mendoza Santoyo Centro de Investigaciones en Óptica A. C., León, Guanajuato, Mexico

A. Mendoza-Suárez Facultad de Ciencias Físico-Matemáticas, UMSNH. Avenida Francisco J. Múgica S/N, Morelia, Michoacán, Mexico

David Monzón-Hernández Centro de Investigaciones en Óptica A. C., León, Guanajuato, Mexico

Julio Mosquera Universidad del Quindío. Armenia, Quindío, Colombia

Noriko Nagata Kwansei Gakuin University, Sanda-shi, Hyogo, Japan

Mauricio Ortiz Facultad de Ciencias Físico-Matemáticas, Universidad Michoacana de San Nicolás de Hidalgo, Morelia, Mexico

M. Ortíz-Gutiérrez Facultad de Ciencias Físico Matemáticas, Universidad Michoacana de San Nicolás de Hidalgo, Morelia, Michoacán, Mexico

Binal P. Bruno Laboratory for Microactuators, Department of Microsystems Engineering, University of Freiburg, Freiburg, Germany

Manuel I. Peña-Cruz CONACYT—Centro de Investigaciones en Óptica, A. C., Unidad Aguascalientes, Aguascalientes, Mexico

Georgina Beltrán Pérez Facultad de Ciencias Físico Matemáticas, Benemérita Universidad Autónoma de Puebla, Ciudad Universitaria, Puebla, Mexico

Yves J. Pérez D. Departamento de Control Automático, CINVESTAV-IPN, San Pedro Zacatenco, México City, Mexico

H. Pérez-Aguilar Facultad de Ciencias Físico-Matemáticas, UMSNH. Avenida Francisco J. Múgica S/N, Morelia, Michoacán, Mexico

M. Pérez-Cortés Universidad Autónoma de Yucatán, Mérida, Yucatán, Mexico

Arturo Díaz Ponce CONACYT—Centro de Investigaciones en Óptica, A. C., Unidad Aguascalientes, Aguascalientes, Mexico

L. Puente-Díaz Facultad de Ciencias Físico-Matemáticas, UMSNH. Avenida Francisco J. Múgica S/N, Morelia, Michoacán, Mexico

Ely Karina Anaya Rivera Universidad Politécnica de Querétaro, Querétaro, Mexico

Sina Sajjadi Faculty of Engineering and Applied Science, University of Regina, Regina, Canada

Jose Amilcar Rizzo Sierra Universidad Politécnica de Querétaro, Querétaro, Mexico

J. V. Sosa-Balderas Optical Metrology, Centro de Investigaciones en Óptica A. C., León, Mexico

Marija Strojnik Centro de Investigaciones en Óptica A. C., León, Mexico

Koichi Taguchi Chukyo University, Nagoya-shi, Aichi, Japan

Kensuke Tobitani Kwansei Gakuin University, Sanda-shi, Hyogo, Japan

Iván Salgado Transito CONACYT—Centro de Investigaciones en Óptica, A. C., Unidad Aguascalientes, Aguascalientes, Mexico

Aleksandar Vakanski University of Idaho, Idaho Falls, ID, USA

Luis M. Valentín-Coronado CONACYT—Centro de Investigaciones en Óptica, A. C., Unidad Aguascalientes, Aguascalientes, Ags, Mexico

Gonzalo Vargas Laboratorio de Inteligencia Artificial y Supercomputo, Instituto de Física y Matemáticas, Universidad Michoacana de San Nicolás de Hidalgo, Morelia, Mexico

C. Vinajera Universidad Autónoma de Yucatán, Mérida, Yucatán, Mexico

Ulrike Wallrabe Laboratory for Microactuators, Department of Microsystems Engineering – IMTEK, University of Freiburg, Freiburg, Germany

Matthias C. Wapler Department of Microsystems Engineering – IMTEK, Laboratory for Microactuators, University of Freiburg, Freiburg, Germany

Pascal M. Weber Department of Microsystems Engineering – IMTEK, Laboratory for Microactuators, University of Freiburg, Freiburg, Germany

Etna Yáñez Centro de Investigaciones en Óptica A. C., León, Guanajuato, Mexico

Three-Dimensional Shape Measurement Beyond Diffraction Limit for Measurement of Dynamic Events

Yasuhiko Arai

Abstract Speckle interferometry is one of the important measurement methods of deformation on an object with rough surfaces. In this paper, a method which can be applied to a three-dimensional (3-D) shape measurement for dynamic events is proposed. In the method, the differential coefficient distribution of the shape of such an object is detected by giving a known lateral shift in the computer memory in order to analyze using one-shot speckle pattern. The 3-D shape can be reconstructed by integrating the differential coefficient distribution. The method is also applied to the 3-D shape measurement of superfine structure beyond the diffraction limit. Furthermore, the influence of magnitude of lateral shift on shape is discussed.

1 Introduction

The imaging of fine structures beyond the diffraction limit using a lens system under interferometry is generally difficult by the diffraction phenomena. Many papers [1–7] concerning the imaging of objects beyond the diffraction limit have been reported; for example, on the Abbe diffraction principle. With Abbe's idea, it is thought that the image of an object, which is a finer structure than the diffraction limit, cannot be acquired without imaging all of the refraction lights which pass through a lens system. If the signal of the shape of an object can be detected without the focusing of these beams, a 3-D shape of the measured objects can be measured without the effects of diffraction.

The shape measurement of a 3-D object, which is based on the measurement principle of speckle interferometry [8–24], was proposed using the lateral shift of the measured object in order to effectively apply speckle interferometry [25].

In this paper, the shape measurement of a 3-D object is improved to the method for dynamic events. Furthermore, the influence of magnitude of lateral shift on shape is discussed.

Y. Arai (✉)
Kansai University, 3-3-35, Yamate-cho, Suita, Osaka, Japan
e-mail: arai@kansai-u.ac.jp

A. Martínez-García et al. (eds.), *Progress in Optomechatronic Technologies*,
Springer Proceedings in Physics 233, https://doi.org/10.1007/978-981-32-9632-9_1

The experiments using some kinds of diffraction gratings are performed. It is confirmed that the shape of a superfine structure can be measured by the proposed method. Furthermore, the measured results are compared with those obtained using atomic force microscopy (AFM). It can be confirmed that the 3-D shape beyond the diffraction limit can be measured at high resolution using speckle interferometry.

2 Speckle Interferometer

When coherent light, such as a laser beam, strikes a rough surface, the light rays are scattered from the surface and interfere with each other in a complex manner. Such interference generates the image of a speckle pattern. The phase information concerning the deformation is recorded as the intensity distribution of the lights which are scattered from the surface of the measured object in the speckle pattern [8–10].

When the speckle interferometer, as shown in Fig. 1a, is set up, a high-resolution deformation can be detected by the optical system using only two sheets of speckle patterns before and after the deformation of the object [12–18]. The system uses a plane wave as the reference beam of the optical system. Then, the speckle pattern in the frequency domain can be obtained, as shown in Fig. 1b. The deformation distribution can be measured by using only two speckle patterns before and after the deformation can be performed by extracting only signal components, as shown in Fig. 1c, from speckle patterns in the frequency domain [13–15]. Furthermore, the new optical system, as shown in Fig. 2, is set up in this paper. A piezo stage, which can provide a lateral shift (dx) to the measured object, is placed in the optical system. The lateral shift is provided in the horizontal direction by using the stage in order to perform 3-D shape measurements.

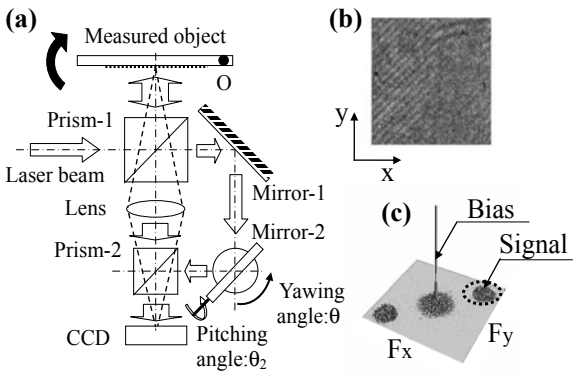

Fig. 1 Speckle interferometry using only two speckle patterns: **a** optical system, **b** speckle pattern, **c** signal of speckle pattern in frequency domain

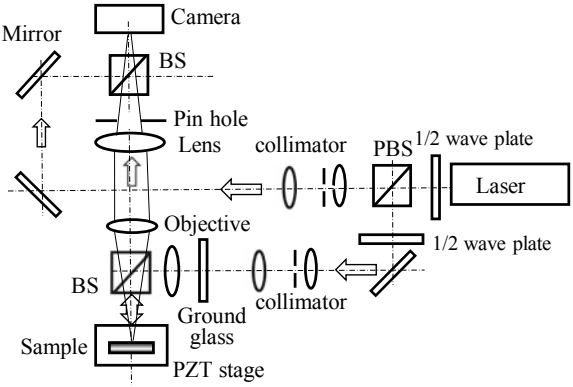

Fig. 2 Optical system

3 Principle of Three-Dimensional Shape Measurement

In this case, the cross-sectional shape before a shift is defined as f(x). When the lateral shift of the measured object is given by dx, the cross-sectional shape of the measured object in the x-direction after the shift becomes f(x + dx). When the two speckle patterns before and after the lateral shift are extracted and analyzed with high resolution, the deformation value at the measured point becomes ϕ(x).

$$\phi(x) = f(x) - f(x + dx) \tag{1}$$

In addition, the analyzed deformation, ϕ(x), is divided by the lateral shift (dx). The value can be assumed to be equivalent to an approximate-differential coefficient in the x-direction.

$$\phi(x)/\delta x = (f(x) - f(x + dx))/dx \tag{2}$$

Furthermore, when this differential coefficient is integrated over the x-direction, the 3-D shape f(x) in the x-direction can be obtained.

$$f(x) \cong \int [\phi(x)/dx]\, dx \tag{3}$$

Because the differential coefficient is a finite difference value based on the limited small finite value dx in the actual calculation, the calculated 3-D shape f(x) is a pseudo-integrated value in the integration calculation. The validity of the proposed method as a 3-D shape measurement method was discussed in the previous paper [25].

4 One-Shot Speckle Pattern 3-D Shape Measurement Method

4.1 Production of Artificial Speckle Pattern Without Physical Shift

Because the measured object must be shifted in practice to analyze 3-D shapes in the method proposed in the previous paper [25], a time interval between measurements for physically moving the object is required in the measurement. Therefore, dynamic events cannot be measured by that method.

In this study, a one-shot analysis method is proposed for measuring a dynamic event. The key point in the conventional method is to get the derivative distribution of the phase of the speckle pattern at each point. The information of the derivative distribution was taken by the movement (lateral shift) of the object in this method. If the derivative distribution of phase can be detected without any physical movement, the measurement for a dynamic event by one-shot speckle interferometry would be able to be performed under the measurement method proposed in the previous paper [25].

In this study, the speckle pattern obtained in one-shot was shifted as a virtual displacement in computer memory. The second speckle pattern was produced artificially in the computer by using spatial information of speckle patterns. By using both real and artificial speckle patterns, the 3-D shape measurement is realized.

Concretely, the speckle pattern in the memory of a computer is arranged two dimensionally, as shown in Fig. 3a. The speckle pattern is shifted by k in the memory, as shown in Fig. 3b. This operation can create the second-shifted speckle pattern, instead of a real lateral shift using the piezo stage. In the new operation, fringe analysis can be performed without the influence of any mechanical vibration or air

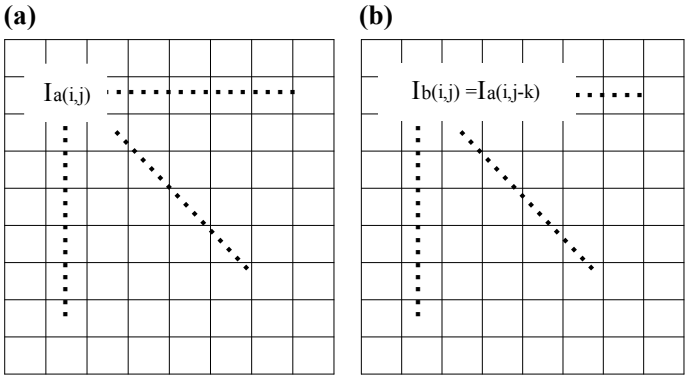

Fig. 3 Principle of production artificial lateral shifted image: **a** original speckle pattern, **b** speckle pattern with artificial lateral shift

fluctuations that might take place during a physical lateral shift. As a result, not only can dynamic events be analyzed but measurements can also be performed stably and at high resolution.

4.2 Confirmation of the Validity of Measurement Principle

The measurement principle of the proposed method using only a one-shot speckle pattern image was tested by using a diffraction grating with relatively large pitch (1.67 μm), as shown in Fig. 4a. Because this long-pitch grating is produced by mechanical technology, the cross-section of the grating is a saw shape. The speckle patterns before and after a real lateral shift (60 nm) are shown in Fig. 4b, c. The principle of the method is discussed using a grating where the 3-D shape is a unique shape (saw shape).

First, the 3-D shape was analyzed by two real speckle patterns using the conventional method. The results are shown in Fig. 5a and b as the slope and shape distributions, respectively. Second, 3-D shape analysis using the real speckle pattern shown in Fig. 4a and the artificial speckle pattern produced by using the proposed method was performed. In this case, the artificial speckle pattern was produced by shifting five pixels on the camera element in order to fulfill the same lateral shift as the real physical lateral shift.

By considering lens magnification (; 200 times) and so on, the width of one pixel was set as corresponding to 12 nm in preparation of the measurement experiment. The results are shown in Fig. 5c, d. It can be confirmed that the results in Fig. 5a, b using the physical lateral shift agree well with the results in Fig. 5c, d. These results confirm the validity of the principle of the method using the virtual shift.

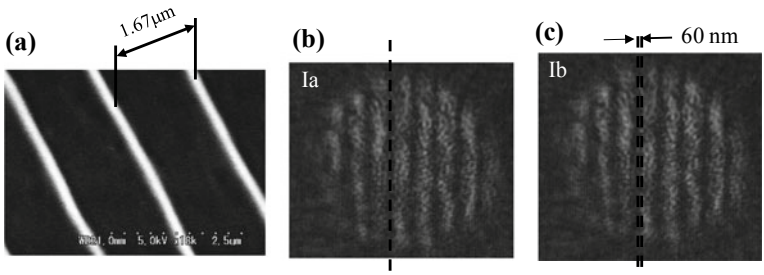

Fig. 4 Diffraction grating using experiment of confirming principle and speckle patterns before and after lateral shift by PZT stage: **a** SEM image of grating, **b** original position, **c** speckle pattern after lateral shifted (60 nm)

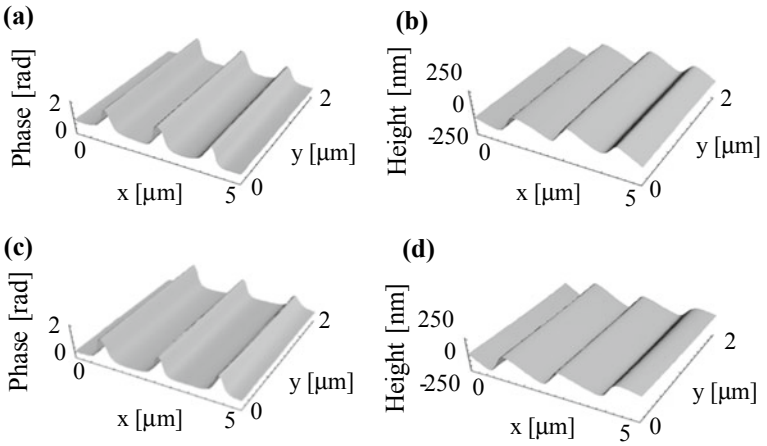

Fig. 5 Slope and 3-D shape distribution in experiment for confirming principle: **a** slope distribution using real speckle patterns, **b** shape distribution using real speckle patterns, **c** slope distribution using artificial speckle patterns, **d** shape distribution using artificial speckle patterns

4.3 Influence of the Magnitude of Lateral Shift

This analysis is based on the derivative operation. Then, the pseudo-derivative is employed in the practical analysis. Because the lateral shift is finite, it can be thought that the magnitude of the lateral shift would influence the analyzed result. In cases such as these, it should be understood that there is generally an optimal condition concerning the magnitude of the lateral shift.

In what follows, the influence of the magnitude of the lateral shift on the result from the new technique using artificial lateral shift is discussed. In this experiment, a diffraction grating with a pitch 833 nm, as shown in Fig. 6a, was used. Because this grating was also produced by mechanical technology, it had a saw-shaped cross-

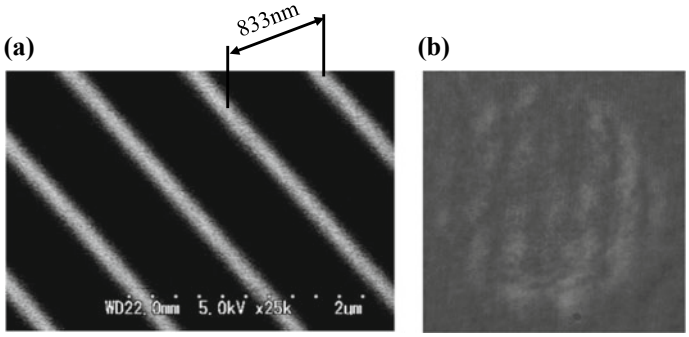

Fig. 6 Diffraction grating using experiment of checking effect by change of lateral shift quantity: **a** SEM image of grating, **b** real speckle pattern

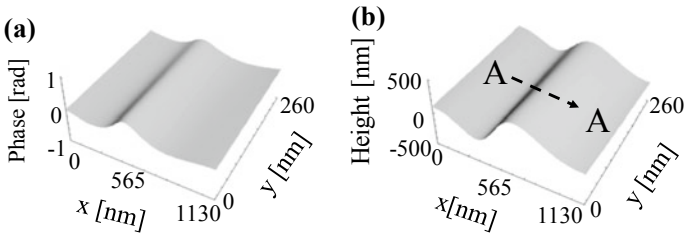

Fig. 7 Slope and 3-D shape distribution in experiment for confirming principle: **a** slope distribution using artificial speckle patterns, **b** shape distribution using artificial speckle patterns

Fig. 8 Effect of change of lateral shift in 3D shape measurement

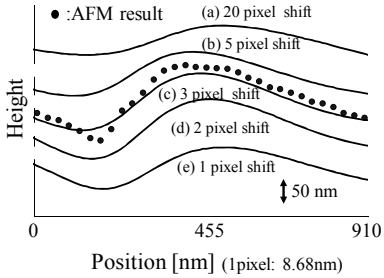

section. The lens magnification and numerical aperture (NA) were 200 and 0.62, respectively. The width of one pixel was set as corresponding to 8.7 nm in this experiment. By shifting the image shown in Fig. 6b artificially, the slope of phase and shape of the object surface could be detected, as shown in Fig. 7a and b, respectively. The height distribution in section A–A of Fig. 7b is shown in Fig. 8c.

In this case, the magnitude of the lateral shift was three pixels. After increasing or decreasing the magnitude of lateral shift, it was confirmed that the cross-section of the shape changed, as shown in Fig. 8. The dotted line in Fig. 8 is the measured result by AFM. It was confirmed that the optimum shift magnitude was about 3 pixels (≅26.0 nm) in this case. It was confirmed that there is the optimal lateral shift.

4.4 Measurement Beyond the Diffraction Limit of a Lens

The proposed one-shot speckle pattern method was applied to the measurement of feature sizes beyond the diffraction limit of a lens. In the experiment, a grating with 278 nm pitch, as shown in Fig. 9a, was measured using a 532 nm wavelength laser. The cross-section of the 3-D object in this case was a sinusoidal wave because the grating was produced by holography.

The grabbed speckle pattern is shown in Fig. 9b. An objective with NA and magnification 0.62 and 200, respectively, was used. The diffraction limit of the lens was 523.4 nm.

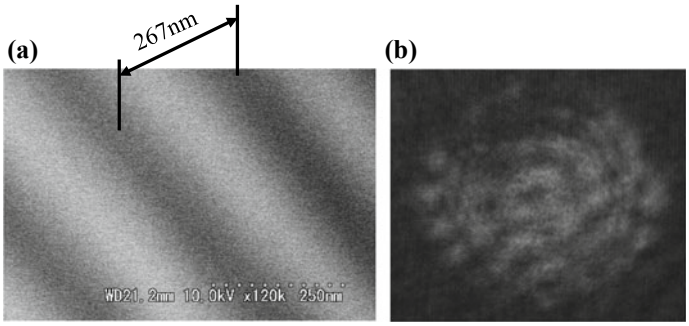

Fig. 9 Measurement in the case of grating beyond the limit of diffraction: **a** SEM image of grating, **b** real speckle pattern

The slope and shape distributions are shown in Fig. 10a, b. The shape of the section B–B from Fig. 10b is shown in Fig. 11. The dotted line in Fig. 11 is the result from AFM. It was confirmed that the result using new one-shot speckle interferometry agreed with the result by AFM well. It was confirmed that the grating feature sizes beyond the diffraction limit of the lens can be observed by the new method.

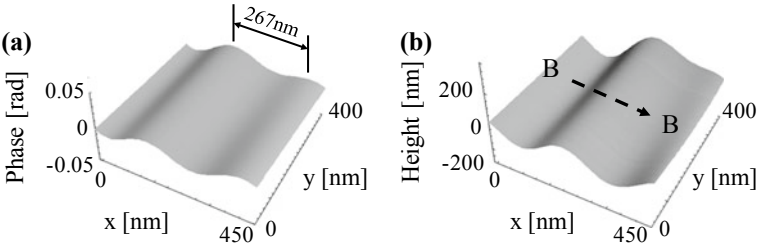

Fig. 10 Measurement result in the case of grating beyond the limit of diffraction: **a** slope distribution using artificial speckle patterns, **b** shape distribution using artificial speckle patterns

Fig. 11 Measurement result of section B–B

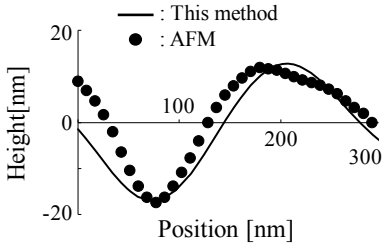

5 Conclusion

In this paper, a basic method for measuring dynamic events using only a one-shot speckle pattern was proposed. The validity of the proposed method was investigated with diffraction gratings and was confirmed from experimental results. Furthermore, the magnitude of lateral shift was also discussed. Next, it was confirmed that there was an optimal lateral shift. It was also confirmed that the new method could be used for feature sizes beyond the diffraction limit of the lens.

References

1. Y. Garini, B.J. Vermolen, I.T. Young, From micro to nano: recent advances in high-resolution microscopy. Curr. Opin. Chem. Biol. **16**, 3–12 (2005)
2. R. Heintzman, G. Ficz, Beaking the resolution limit in light microscopy. Brief. Funct. Genomics Proteomics **5**, 289–301 (2006)
3. B. Huang, Super-resolution optical microscopy: multiple choices. Curr. Opin. Chem. Biol. **14**, 10–14 (2010)
4. S.W. Hell, J. Wichmann, Breaking the diffraction resolution limit by stimulated-emission—stimulated-emission-depletion fluorescence microscopy. Opt. Lett. **19**, 780–782 (1994)
5. E. Betzig, G.H. Patterson, R. Sougrat, O.W. Lindwasser, S. Olenych, J.S. Bonifacino, M.W. Davidson, J. Lippincott-Schwartz, H.F. Hess, Imaging intracellular fluorescent proteins at nanometer resolution. Science **313**, 1642–1645 (2006)
6. M.G.L. Gustafsson, Surpassing the lateral resolution limit by a factor of two using structured illumination microscopy. J. Microsc. Oxf. **198**, 82–87 (2000)
7. H. Florian, G. Alexander, A. Sergiu, N. Wiwat, K. Fritz, H. Rainer, Nano-FTIR absorption spectroscopy of molecular fingerprints at 20 nm spatial resolution. Nano Lett. **12**, 3973–3978 (2012)
8. G. Cloud, *Optical Methods of Engineering Analysis* (Cambridge University Press, New York, 1995), pp. 395–476
9. D. Malacara, *Optical Shop Testing* (Wiley, New York, 1992), pp. 501–652
10. R.S. Sirohi, *Speckle Metrology* (Marcel Dekker, New York, 1993), pp. 99–234
11. B.J. Thompson, *Selected papers on Electronic Speckle Pattern Interferometry Principles and Practice* (SPIE Optical Engineering Press, Bellingham, Washington, 1996), pp. 1–518
12. Y. Arai, S. Yokozeki, In-plane displacement measurement using electronic speckle pattern interferometry based on spatial fringe analysis method. Opt. Eng. **43**, 2168–2174 (2004)
13. Y. Arai, Electronic Speckle Pattern Interferometry based on spatial information using only two sheets of speckle patterns. J. Mod. Opt. **61**, 297–306 (2014)
14. Y. Arai, Improvement of measuring accuracy of spatial fringe analysis method using only two speckle patterns in electronic speckle pattern interferometry. Opt. Eng. (2014). https://doi.org/10.1117/1.oe.53.3.034107
15. Y. Arai, Development of in-plane and out-of-plane deformation simultaneous measurement method for the analysis of buckling. Opt. Eng. **54** (2015). https://doi.org/10.1117/1.oe.54.2.024102
16. Y. Arai, Simultaneous in-plane and out-of-plane deformation measurement by speckle multi-recording method. Measurement **91**, 582–589 (2016)
17. Y. Arai, Influence of error sources in speckle interferometry using only two speckle patterns. Opt. Eng. **55** (2016). https://doi.org/10.1117/1.oe.55.12.124101
18. Y. Arai, Measurement of buckling deformation using speckle interferometry with same sensitivity in three-dimensions. Opt. Eng. **56** (2017). https://doi.org/10.1117/1.oe.56.4.044102

19. E.B. Flynn et al., Three-wavelength electronic speckle pattern interferometry with the Fourier-transform method for simultaneous measurement of microstructure-scale deformations in three dimensions. Appl. Opt. **45**, 3218–3225 (2006)
20. S. Schedin et al., Simultaneous three-dimensional dynamic deformation measurements with pulsed digital holography. Appl. Opt. **38**, 7056–7062 (1999)
21. T. Takatsuji et al., Simultaneous measurement of three orthogonal components of displacement by electronic speckle-pattern interferometry and the Fourier transform method. Appl. Opt. **36**, 1438–1445 (1997)
22. A. Martinez et al., Three-dimensional deformation measurement from the combination of in-plane and out-of-plane electronic speckle pattern interferometers. Appl. Opt. **24**, 4652–4658 (2004)
23. C. Joenathan et al., Large in-plane displacement measurement in dual-beam speckle interferometry using temporal phase measurement. J. Mod. Opt. **45**, 1975–1984 (1998)
24. C. Joenathan et al., Speckle interferometry with temporal phase evaluation for measuring large-object deformation. Appl. Opt. **37**, 2608–2614 (1998)
25. Y. Arai, Three-dimensional shape measurement beyond the diffraction limit of lens using speckle interferometry. Mod. Opt. (2018). https://doi.org/10.1080/09500340.2018.147026

Azimuthal Walsh Filters: An Interesting Tool to Produce 2D and 3D Light Structures

Indrani Bhattacharya and Lakshminarayan Hazra

Abstract Azimuthal Walsh filters, derived from radially invariant azimuthal Walsh functions, can be used as an effective tool for producing 2D and 3D light structures near the focal plane of a rotationally symmetric imaging system by manipulating the far-field diffraction characteristics when used as pupil filters. Starting with the definition of azimuthal Walsh functions and using the scalar diffraction theory, this research work reports the possibility of modifying the beam structure around the far-field plane by diffraction characteristics of azimuthal Walsh filters placed on the exit pupil plane when computed analytically. The asymmetrical beam produced due to the inherent phase asymmetries introduced by azimuthal Walsh filters may find many important applications in micro- and nano-photonics.

Keywords Diffractive optics · Diffraction · Apertures · Phase-only filters · Optical micro- and nano-manipulations · Optical tweezers

1 Introduction

The possibility of using azimuthal Walsh filters, derived from the orthogonal set of azimuthal Walsh functions, has been proposed to manipulate the far-field diffraction patterns of a rotationally symmetric imaging system. Starting with the definition of Walsh functions, this research work reports the diffraction characteristics of azimuthal Walsh filters placed on the exit pupil plane when computed analytically at the far-field plane. The transverse intensity distributions along the far-field plane show asymmetrical patterns due to the phase asymmetries introduced by these filters. Azimuthal Walsh filters may be used as unique pupil plane filters for tailoring 2D and 3D transverse intensity distributions near the focal plane of the imaging system.

I. Bhattacharya (✉) · L. Hazra
Department of Applied Optics and Photonics, University of Calcutta, JD-2, Sector-III, Kolkata 700106, India
e-mail: bindrani03@gmail.com

A. Martínez-García et al. (eds.), *Progress in Optomechatronic Technologies*,
Springer Proceedings in Physics 233, https://doi.org/10.1007/978-981-32-9632-9_2

2 Walsh Functions

Walsh functions [1] form a complete set of normal orthogonal functions [2] over a given finite interval (0,1) and take the values of either $+1$ or -1 within the pre-specified domain, except at finite points of discontinuity where the value of the function is zero. The order of the Walsh function is equal to the number of zero crossings or phase transitions within the specified domain. Walsh functions have the interesting property that an approximation of a continuous function over a finite interval by a finite number of base functions of this set leads to a piecewise constant approximation to the function [3]. Walsh filters of various orders may be obtained from the corresponding Walsh functions by realizing values of $+1$ or -1 with 0 or π phase respectively.

2.1 Azimuthal Walsh Functions

Azimuthal Walsh function $W_\nu(\theta)$ of index $\nu \geq 0$ and argument θ within a domain $(0, 2\pi)$, over a sector bounded by 0 and 1 as inner and outer radii, respectively, is defined as [4]:

$$W_\nu(\theta) = \prod_{m=0}^{\gamma-1} \text{sgn}\left[\cos\left(\nu_m 2^m \frac{\theta}{2}\right)\right] \tag{1}$$

where the integer ν can be expressed in the form:

$$\nu = \sum_{m=0}^{\gamma-1} \nu_m 2^m \tag{2}$$

ν_m are the bits, 0 or 1 of the binary numeral for ν and 2^γ is the largest power of 2 that just exceeds ν.

The orthogonality condition implies:

$$\int_0^{2\pi} W_\nu(\theta) W_\ell(\theta) d\theta = \frac{1}{2}\delta_{\nu\ell} \tag{3}$$

where $\delta_{\nu\ell}$ is the Krönecker delta defined as:

$$\begin{aligned} \delta_{\nu\ell} &= |\, 0, \nu \neq \ell \\ &\quad\ |1, \nu = \ell \end{aligned} \tag{4}$$

Manipulating the values of ν_m, the azimuthal Walsh functions of different orders, namely zero and above, can be generated [5].

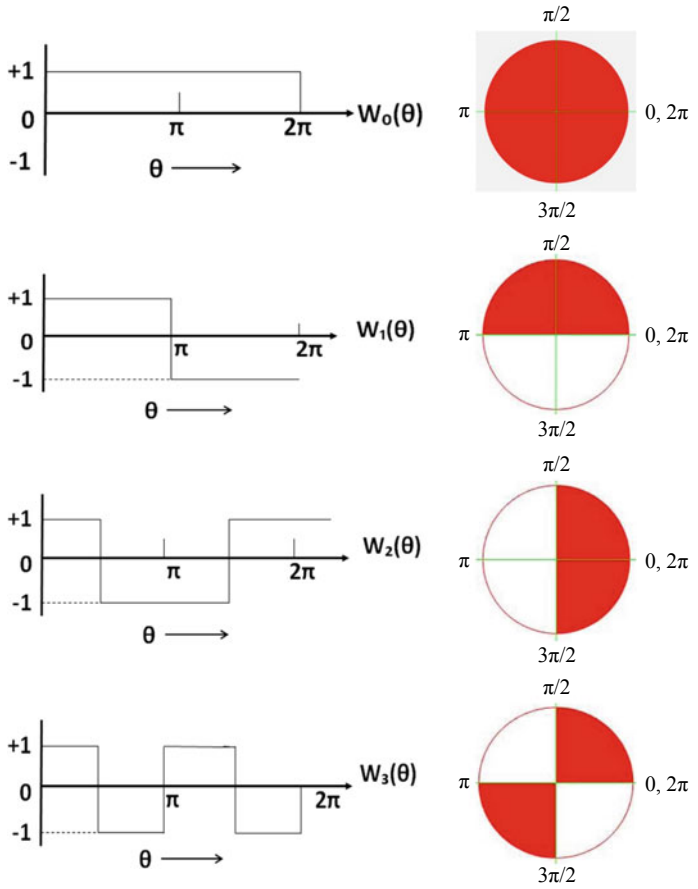

Fig. 1 Polar plot of azimuthal Walsh functions, $W_\nu(\theta)$, for $\nu = 0$, 1, 2 and 3

Figure 1 shows the polar plots of azimuthal Walsh functions for orders $\nu = 0$, 1, 2 and 3. The darker region of the circle is having transmittance $+1$ and the lighter region is having transmittance -1.

2.2 Azimuthal Walsh Filters Derived from Azimuthal Walsh Functions

Azimuthal Walsh filters derived from azimuthal Walsh functions also form a set of orthogonal phase filters that takes on the values $+1$ or -1 corresponding to the phase values of 0 or π. Order of these filters is given by the number of phase transitions within the angular domain of $(0, 2\pi)$. Azimuthal Walsh filter can be represented

by sector-shaped aperture bounded by constant inner and outer radii with varying angles θ_1 and θ_2 within the domain $(0, 2\pi)$. The values of inner and outer radii are taken as $R_1 = 0$ and $R_2 = 1$. In general, azimuthal Walsh filters can be considered as combination of binary phase filters or azimuthally varying zone plates which are having unique properties of introducing phase factors to the interacting light beam.

3 Analytical Formulation of 2D Intensity Distributions at Far-Field Plane Due to Azimuthal Walsh Filters Placed on the Exit Pupil Plane

The schematic diagram of a rotationally symmetric imaging system with azimuthal Walsh filter placed on the exit pupil plane is shown in Fig. 2a.

The normalized coordinates for a point, P on the pupil is (r, θ), where r = ρ/R, ρ is the radial distance of P from the centre of the exit pupil, and R is the radius of the pupil as depicted in Fig. 2b. The numerical aperture of the pupil plane can be expressed as:

$$p = \frac{2\pi}{\lambda}(n \sin \alpha)\xi \tag{5}$$

where α is the angle subtended by the pupil plane at the centre of the far-field plane and $(n \sin \alpha)$ is the image space numerical aperture, n is the refractive index of the image space and λ is the operating wavelength.

Each azimuthal Walsh function, $W_\nu(\theta)$ for $\nu = 0, 1, 2, 3, \ldots$ can be considered to be consisting of 2^N no. of sectors where the value of N depends on the order of ν. For zero-order azimuthal Walsh filter, $W_0(\theta)$, the no. of sector is 1. For first-order azimuthal Walsh filter, $W_1(\theta)$, the no. of sectors is 2. For second-order azimuthal Walsh filter, $W_2(\theta)$, the no. of sectors is 3. For third-order azimuthal Walsh filter,

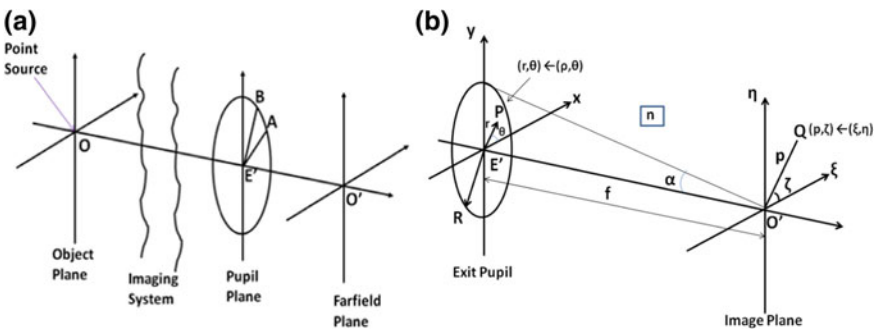

Fig. 2 **a** Schematic diagram of a rotationally symmetric imaging system; **b** A point P on the exit pupil plane and a point Q on a transverse far-field imaging plane

$W_3(\theta)$, the no. of sectors is 4, and so on. The value of transmission T in each of these sectors is either $+1$ or -1, depending upon the phase factor 0 or π.

Far-field amplitude distribution for azimuthal Walsh function, $W_\nu(\theta)$, can be calculated as [6–8]:

$$A(p,\zeta) = \sum_{s=0}^{N} T_s\left[C_s(p,\zeta;\theta) - iS_S(p,\zeta;\theta)\right] \tag{6}$$

where $C_S(p,\zeta;\theta)$ and $S_S(p,\zeta;\theta)$ are the real and imaginary parts of $A(p,\zeta)$ [5] at the far-field plane and T_s is the transmission factor of the pupil function given by:

$$T_s = \sum_{s=0}^{N} e^{ik\psi_s} \tag{7}$$

Over the sth sector of $W_\nu(\theta)$, the value of $k\psi_s$ is 0 or π, if $W_\nu(\theta) = +1$ or -1, respectively.

The corresponding intensity distribution, $I(p,\zeta)$, can be calculated as:

$$I(p,\zeta) = \left[\sum_{s=0}^{N} T_s\left[C_s(p,\zeta;\theta)\right]\right]^2 + \left[\sum_{s=0}^{N} T_s\left[S_s(p,\zeta;\theta)\right]\right]^2 \tag{8}$$

The normalized intensity point spread function at the far-field plane $I_N(p,\zeta)$ is given by:

$$I_N(p,\zeta) = I(p,\zeta)\big/ I(0,0) \tag{9}$$

where $I(0,0)$ is the intensity distribution at the origin of the far-field plane, where $p = 0, \zeta = 0$.

4 Results and Discussions

The azimuthal Walsh filter $W_\nu(\theta)$ of order $\nu = 0, 1, 2, 3, \ldots$ is placed on the exit pupil of a rotationally symmetric imaging system (Fig. 1), and the complex amplitude distributions on a transverse far-field plane are computed from (6). The inherent phase asymmetry imposed by azimuthal Walsh filters placed on the exit pupil plane leads to asymmetrical amplitude point spread function in the far-field plane [9].

Normalized transverse intensity distribution along the far-field plane, $I_N(p,\zeta)$ with the variation of reduced transverse distance, p along azimuthal variation of ζ has been shown for azimuthal Walsh filters from 0 to 9. The 2D normalized intensity variations along with contour plots are shown for each individual order of azimuthal Walsh filter. Except for zero order, the normalized intensity distribution

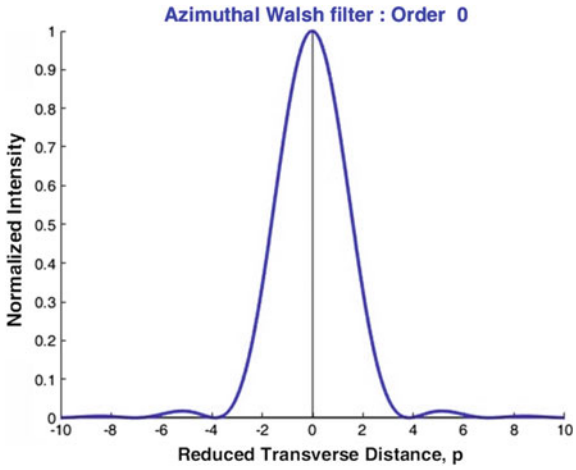

Fig. 3 The normalized intensity distribution at far-field plane due to zero-order azimuthal Walsh filter on the exit pupil

against reduced transverse distance shows asymmetrical variation along different azimuths.

Figure 3 shows the normalized transverse intensity distribution along the far-field plane for zero-order azimuthal Walsh filter on the exit pupil, which is the Airy pattern with no azimuthal dependence. The normalized intensity distribution with the central maxima at the origin of the far-field plane with magnitude one is illustrated in Fig. 3.

Tables 1 and 2 enlist azimuthal Walsh filters $W_\nu(\theta)$, for orders $\nu = 0, 1, 2, 3, \ldots, 9$ along with their respective 2D intensity distributions at the far-field plane with the corresponding contour plots. The contour plots corresponding to intensity distribution have been colored, to highlight the position of the peak or maximum value compared to other values of intensity. The yellow color represents the location of peak values or maxima of the intensity distribution patterns obtained for any particular order ν. It is apparent from 2D IPSF that the central dark region of the intensity distribution spreads out as order ν increases.

The 3D view of intensity distribution of the diffracted beam of light can be generated from the 2D pattern, as presented for zero-order azimuthal Walsh filter, $W_0(\theta)$ in Table 3. The intensity distribution is showing central maxima with alternate dark and bright concentric rings of diminishing amplitude arranged in a symmetric fashion about the centre and is independent of azimuthal variation along the far-field plane. The central yellow patch in the contour plot corresponds to the location of peak value or the maxima of the intensity distribution.

The 3D intensity distribution of the diffracted beam of light generated from 2D pattern for first-order azimuthal Walsh filter, $W_1(\theta)$, is presented in Table 4. The intensity distribution is asymmetric showing dependence on azimuthal variation along the far-field plane with central minima. The yellow patches in the contour pattern show the locations of peak values or the maxima of the intensity distribution. It is seen that the peak values are located at both sides of the origin.

Table 1 Azimuthal Walsh filters $W_\nu(\theta)$ for orders $\nu = 0, 1, 2, 3$ and 4 and their 2D transverse intensity distributions on far-field plane

Order	Corresponding azimuthal Walsh filters	2D IPSF	Contour IPSF	Scale
0			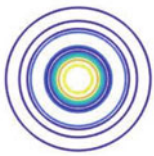	
1		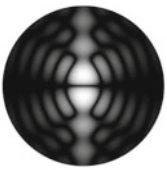		
2		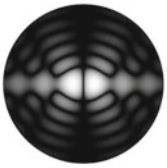	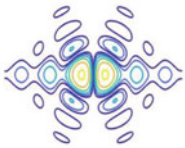	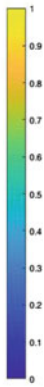
3			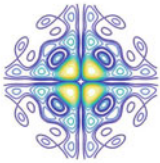	
4			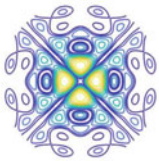	

5 Discussions and Further Scope of the Study

We have used MATLAB 2017a platform for the advance level computation to generate high-quality images for the far-field diffraction pattern due to different orders of azimuthal Walsh filters. Practical implementation of these filters may be achieved by using high-speed spatial light modulators [10], where the in situ generation of different orders of azimuthal Walsh filters is possible and combinations of lower order filters to achieve higher orders may be explored. Further scope of research

Table 2 Azimuthal Walsh filters $W_v(\theta)$ for orders $v = 5, 6, 7, 8$ and 9 and their 2D transverse intensity distributions on far-field plane

Order	Corresponding azimuthal Walsh filters	2D IPSF	Contour IPSF	Scale
5				
6				
7				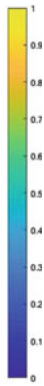
8				
9			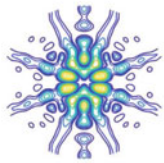	

includes efficient use of azimuthal Walsh filters near the focus of an imaging system to cater the needs of complex imaging required for advanced microscopy, 3D imaging, lithography, optical superresolution, optical tomography, to name a few.

A very promising application of azimuthal Walsh filters may be in the field of optical micro- and nano-manipulations, where a tightly focused 2D or 3D light distributions of fundamental or higher order modes are required for investigating the spin orbital interaction (SOI) of light [11, 12] in optical tweezers (OT) within the refractive index stratified media [13, 14]. This can be used to produce a gradient

Table 3 Azimuthal Walsh filter $W_0(\theta)$ for order $\nu = 0$ and its 3D view of 2D transverse intensity distribution at the far-field plane

Order	Corresponding azimuthal Walsh filters	Contour IPSF	3D view of IPSF generated from 2D
0			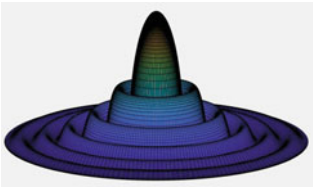

Table 4 Azimuthal Walsh filter $W_1(\theta)$ for order $\nu = 1$ and a snapshot of the 3D transverse intensity distribution at the far-field plane

Order	Corresponding azimuthal Walsh filters	2D IPSF	Contour IPSF
1		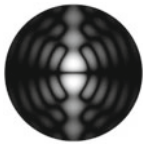	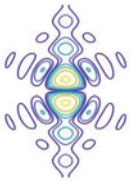

3D view of IPSF generated from 2D

force trap [15] for manipulating particles of sizes comparable to a single atom up to 100 μm without any mechanical contact.

Acknowledgments The author acknowledges the support of Department of Applied Optics and Photonics, University of Calcutta, India for this research work.
Special acknowledgment to Prof. Dr. Ayan Banerjee, Group Leader of Light–Matter Interactions Lab under the Department of Physical Sciences, Indian Institute of Science Education and Research (IISER), Kolkata, India for supporting further extension of the research work in the field of optical micro-manipulation.
The author would like to thank Science and Engineering Research Board, SERB of Department of Science and Technology, DST, Govt. of India to support the travel grant to Cancun, Mexico.

References

1. J.L. Walsh, A closed set of normal orthogonal functions. Am. J. Math. **45**(1), 5–24 (1923)
2. H.F. Harmuth, *Transmission of Information by Orthogonal Functions* (Springer, Berlin, 1972), p. 31
3. L.N. Hazra, Walsh filters in tailoring of resolution in microscopic imaging. Micron **38**(2), 129–135 (2007)
4. I. Bhattacharya, L.N. Hazra, Study of imaging characteristics of azimuthal Walsh filters. Am. J. Electron. Commun. (AJECT) **1**(2), 50–54 (2014)
5. I. Chattopadhyay, Far-field diffraction characteristics of azimuthal Walsh filters: a veritable potpourri of 2D and 3D light structures, Ph.D. Thesis, 8 June, 2018
6. A.I. Mahan, C.V. Bitterli, S.M. Cannon, Far-field diffraction patterns of single and multiple apertures bounded by arcs and radii of concentric circles. J. Opt. Soc. Am. A **54**(6), 721–732 (1964)
7. R.A. Lessard, S.C. Som, Imaging properties of sector-shaped apertures. App. Opt. **II**(4), 811–817 (1972)
8. T. Vierke, J. Jahns, Diffraction theory for azimuthally structured Fresnel zone plate. J. Opt. Soc. Am. A **31**(2), 363–372 (2014)
9. I. Bhattacharya, A. Saha, L.N. Hazra, Asymmetrical PSF by Azimuthal Walsh filters, in *Advances in Optical Science and Engineering Silicon Photonics II: Proceedings of 2015 Second International Conference on Opto-Electronics and Applied Optics*, ed. by V. Lakshminarayanan, I. Bhattacharya (IEEE Xplore Digital Library, at University of British Columbia, Vancouver, Canada, 2015)
10. S. Mukhopadhyay, S. Sarkar, K. Bhattacharya, L.N. Hazra, Polarisation phase shifting interferometric technique for phase calibration of a reflective phase spatial light modulator. Opt. Eng. **52**(3), 035602-1–035602-6 (2013)
11. K.Y. Bliokh, A.Y. Bekshaev, F. Nori, Extraordinary momentum and spin in evanescent waves. Nature Commun. **5**, 330 (2014)
12. D. Pal, I. Bhattacharya, A. Banerjee et al., Spin momentum locking in a tightly focused Gaussian beam, in *OSI-ICO International Symposium on Optics (OSI-ICO)*, 18–22 Sept 2019 (IIT Kanpur, India, 2018)
13. B. Roy et al., Control transportation of mesoscopic particles by enhanced spin-orbit interaction of light in an optical trap. Phys. Rev. A **87**, 043823 (2013)
14. S.D. Gupta, N. Ghosh, A. Banerjee, *Wave Optics: Basic Concepts and Contemporary Trends* (CRC Press, 2015)
15. A. Ashkin, Acceleration and trapping of particles by radiation pressure. Phy. Rev. Lett. **24**(4), 156–159 (1970)

Self-adaptive Speckle Pattern Based 3D Measurement System

Danish Khan and Min Young Kim

Abstract Speckle size plays an important role in speckle-based 3D measurement systems. In real-time systems, frequent speckle size variation may be required as the object goes out of the specified range or the camera aperture has to be adjusted to observe the optimal speckle size on the image plane. In this paper, we present a system that adapts itself to achieve the desired speckle size when the measuring distance is changed. The system uses a motorized stage to vary the distance of the diffuser and the observation plane to change the speckle size which is calculated in real time. The performance of the proposed system is compared with the conventional speckle pattern and the result indicates that the proposed speckle method substantially improves the optimal range of the measurement system.

1 Introduction

The use of speckle pattern for three-dimensional (3D) shape acquisition is justified and well proven. A number of commercial 3D sensors such as Microsoft Kinect, Prime Sense, and Intel Real Sense exploit some kind of speckle pattern to retrieve the geometrical 3D information. Among different types of speckle patterns, the speckles generated by a coherent laser light are widely adopted in stereo photogrammetric systems [1–3]. The laser light reflected from a surface with variation in thickness (rough surface) produces a grainy pattern due to the interference of the scattered waves. This pattern is known as laser speckle pattern and assists in establishing the correspondence between the stereo pairs. Speckle size is an important factor to change the appearance of the pattern and determines the range and resolution of the 3D measurement systems [3–5]. Depending on the employed algorithm, an optimal

D. Khan · M. Y. Kim (✉)
School of Electronics Engineering, IT College, Kyungpook National University, 1370 Sankyuk-dong, Buk-gu, Daegu 702-701, Korea
e-mail: mykim@ee.knu.ac.kr

M. Y. Kim
Research Center for Neurosurgical Robotic System, Kyungpook National University, 1370 Sankyuk-dong, Buk-gu, Daegu 702-701, Korea

A. Martínez-García et al. (eds.), *Progress in Optomechatronic Technologies*,
Springer Proceedings in Physics 233, https://doi.org/10.1007/978-981-32-9632-9_3

speckle size is required for the accurate and dense 3D reconstructions. A number of factors depend on the speckle size, such as the radius of the focused laser spot, the roughness of the diffuser, aperture, and focal length of the imaging system. These conditions can be optimized to achieve the required speckle size at a certain distance. Nevertheless, the speckle size also depends on the distance at which it is imaged by a camera. When the object goes out of a specified range, the spatial resolution has to be compromised or else manually changing the speckle size is required. Furthermore, the objects with different reflectance property exhibit different results on the speckle size estimation. Even at the same distance, the adjustment of speckle size is required when different objects are measured. A typical approach to change the speckle size is to change the distance between the rough surface and the observation plane. In real-time systems when the objects are dynamic or continuously moving, maintaining the speckle size is a strenuous task and often disturbs the hardware setup prompting to the recalibration of the system.

To cope with the aforementioned issue in speckle-based 3D acquisition systems, we present the concept of self-adaptive speckle pattern (SASP). The pattern maintains the optimal speckle size (defined by the user) during the measurements when the size changes due to any reason.

2 Proposed System for SASP

Figure 1 depicts the optical configuration of the proposed SASP in conjunction with a stereo vision system. The laser beam is focused on a ground glass diffuser using a lens to generate the speckle pattern on the measuring object. The speckles observed on the measuring object can be mathematically described as

$$\sigma_o = \frac{\lambda Z}{D} \tag{1}$$

where Z is the distance from the diffuser to observation plane, D is the diameter of the illuminating area, and λ is the wavelength of the laser.

The speckle size can be adjusted by altering the Z distance in Fig. 1. For tuning the speckle size on the go, the diffuser is fixed on a mini motorized precision linear stage (PI-M-111) connected to a DC motor controller. The stage can be moved in the backward and forward direction within the range of 25 mm. Any one image from the stereo pair can be used to calculate the speckle size. On the basis of the calculated speckle size, the stage can be moved to the position where the optimal speckle size can be achieved. After achieving the optimal speckle size, the 3D coordinates of the object can be extracted by the stereo camera system. This paper only deals with adjusting the speckle size for 3D measurement. The 3D measurement process is not the scope of this paper.

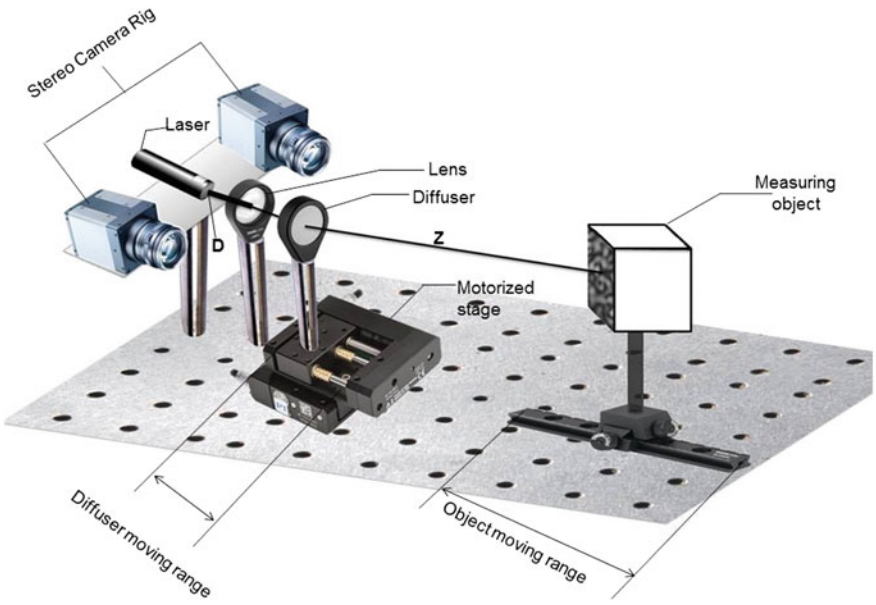

Fig. 1 Hardware setup for the proposed system

3 Real-Time Speckle Size Calculation

The average speckle size can be estimated by calculating the autocovariance function of the digitized intensity speckle pattern [6]. The full width at half maximum (FHWM) of the Gaussian fit to the sum of the normalized autocorrelation function provides the average size of a speckle. This method works best when the entire image is full of speckles with no dark background. If the large part of the image is without the speckles, it will have a high peak in the center with little fluctuation elsewhere. The average speckle size cannot be estimated in such a case. The raw images acquired from the cameras in laser speckle-based systems contain a substantial amount of dark long-range background as the object containing the speckles covers only some part of the image. Dekiff et al. calculated speckle size at the exact center patch of 512 × 512 pixels of the speckle image [5]. In real-time systems where objects are moving or constantly changing, the measuring object may not be in the middle of the image. They can be located at any position, and to calculate the speckle size in real time, the part of the image containing only the speckle pattern is desired. For this purpose, a framework is developed which comprises the following steps:

1. Binarize the grayscale image using the following condition:

$$I_B(i,j) = \begin{cases} 1 & \text{for } I(i,j) \geq t \\ 0 & \text{for } I(i,j) < t \end{cases} \tag{2}$$

where $I_B(i, j)$ is the pixel value at the (i, j) position after binarization, $I(i, j)$ is the pixel value at the (i, j) position before binarization and t is the threshold.

2. Extract the largest blob in the binarized image using the connected components.
3. Calculate the centroid of the largest blob.
4. By using the centroid location of the binarized image, extract the 200 × 200 or 300 × 300 patch from the original grayscale image around the centroid.

Figure 2 shows the example of extracting the image patch to calculate the speckle size containing only a speckle pattern. The image of the measuring object shown in the figure is acquired with the projected speckle pattern. It can be seen that the large part of the raw image is black and it is not suitable to calculate the speckle size. There is an abrupt change in the intensities of the background and the object. The intensity of pixels representing the object is greater due to the speckles and the intensity of the background pixels is always less than 10 as the images are captured without the ambient light in the dark environment. Hence the binarization of the image with the threshold of 5–10 in (2) easily segment out the object with some noise. Extracting the largest blob yields only the object without the background noise. Once the object is clearly segmented from the background, the centroid of the object can be estimated using the center of mass. A window of 300 × 300 pixels is extracted around the centroid which yields the speckle image to estimate a fair speckle size.

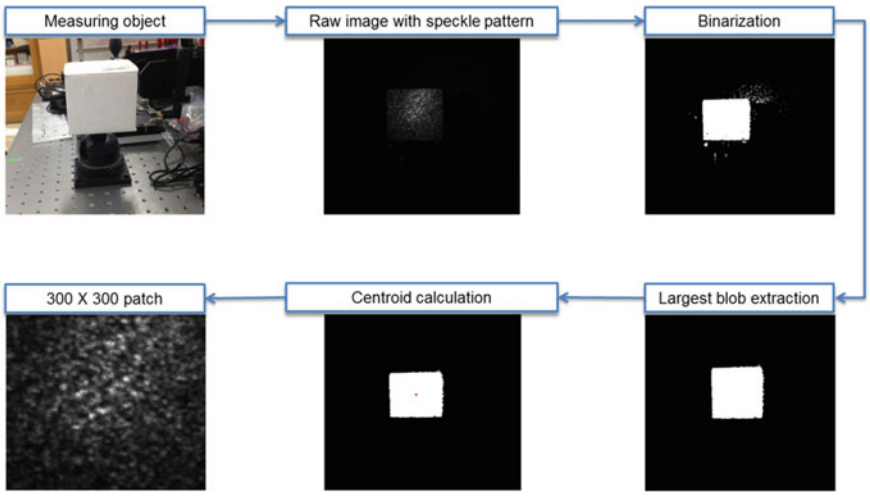

Fig. 2 Real-time speckle size calculation

4 Experiments and Results

To verify the workability of the SASP, first, the speckle size is calculated at five different distances (30, 50, 70, 90, and 110) cm with the fixed diffuser. As can be seen in Fig. 3a, there is an instant decrease in the speckle size as the target moves from 30 to 50 cm. The speckle size is decreasing as the distance is increasing. This is due to the fact that the speckles have low brightness and contrast with the increasing distance. To maintain the brightness of the speckle at different distances, the camera aperture has to be adjusted. After calculating the speckle size with the fixed diffuser, the SASP is tested and the speckle size is measured at the same distances as the fixed pattern. In contrast to the fixed pattern, the variation trend of speckle size by the SASP is stable and it maintains the optimal speckle size which was defined to be 7–9 pixels in this case.

To realize the effect of SASP on 3D measurements, the 3D point clouds of the same object are extracted at the above stated five distances using the stereo pairs. A method is used which requires only one stereo pair to extract the 3D point cloud [3]. The number of 3D points acquired by both SASP and the fixed pattern is compared and shown in Fig. 3b. The plot of 3D points with respect to distance suggests that the optimal range for the fixed speckle pattern is 50–90 cm. The number of 3D points is very less at the distance of 30 cm and it starts to decrease again after the target moves away from the 90 cm. By the same plot of the SASP, we can assume that the SASP improves the performance of the 3D measurement system considerably. The numbers are in between 10,500 and 9000 at the range of 50–110 cm. At the distance of 30 cm, the numbers are slightly reduced but better than the fixed pattern.

Figure 4 shows the 3D shape of the object acquired at 110 cm by both systems. The density of the object is clearly better when acquired by the SASP. It can be said that the SASP increased the range of the measurement system by allowing optimal 3D acquisitions at different distances.

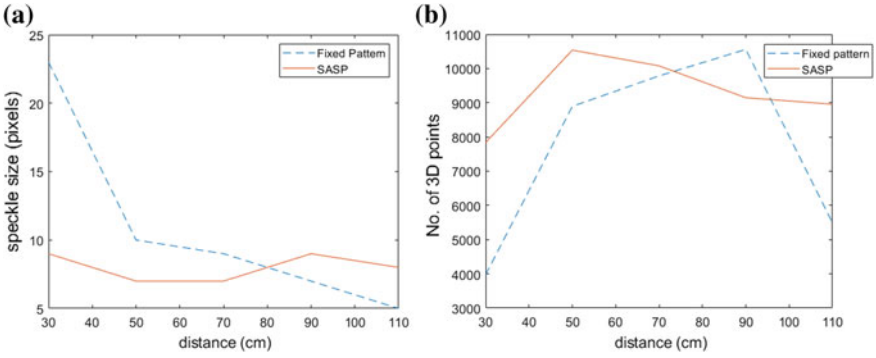

Fig. 3 Comparison of fixed pattern versus SASP, **a** speckle size at different distances, **b** no. of 3D points at different distances

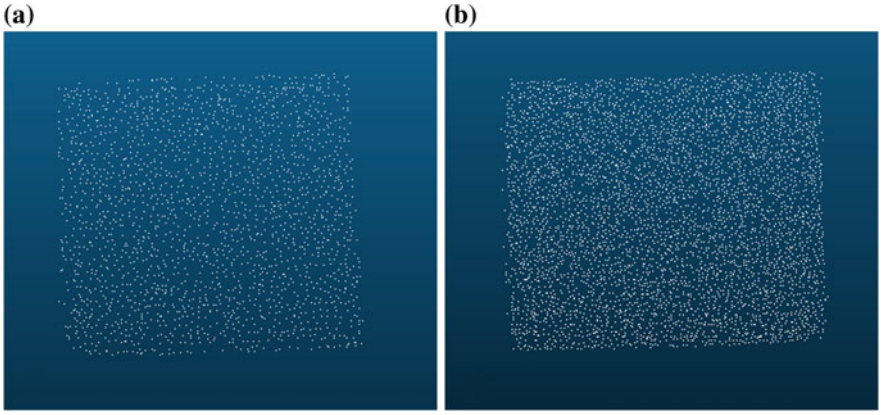

Fig. 4 3D shape acquisition at 110 cm, **a** fixed pattern, **b** SASP

5 Conclusion

Like an autofocus system in modern digital cameras adjusts the camera lens to obtain the focus on the subject, the proposed system adjusts the speckle size to get the optimal 3D reconstructions of the measuring object. The result demonstrates that the optimal measurement range of the 3D measurement system can be extended by employing SASP. This can improve the density of the 3D models and robustness to object change in any laser speckle-based 3D measurement system. As the method uses only one image to calculate the speckle size, the proposed SASP can also be used in single camera systems.

Acknowledgements This work was supported by the DGIST R&D Program of the Ministry of Science, ICT and Future Planning (17-ST-01).

References

1. M. Schaffer, M. Grosse, R. Kowarschik, High-speed pattern projection for three-dimensional shape measurement using laser speckles. Appl. Opt. **49**(18), 3622–3629 (2010)
2. S. Heist, P. Lutzke, P. Dietrich, P. Kühmstedt, G. Notni, Experimental comparison of laser speckle projection and array projection for high-speed 3D measurements, in *Optical Measurement Systems for Industrial Inspection IX, 2015. International Society for Optics and Photonics*, p. 952515
3. D. Khan, M.A. Shirazi, M.Y. Kim, Single shot laser speckle based 3D acquisition system for medical applications. Opt. Lasers Eng. **105**, 43–53 (2018). https://doi.org/10.1016/j.optlaseng.2018.01.001
4. G. Crammond, S. Boyd, J. Dulieu-Barton, Speckle pattern quality assessment for digital image correlation. Opt. Lasers Eng. **51**(12), 1368–1378 (2013)

5. M. Dekiff, P. Berssenbrügge, B. Kemper, C. Denz, D. Dirksen, Simultaneous acquisition of 3D shape and deformation by combination of interferometric and correlation-based laser speckle metrology. Biomed. Opt. Express **6**(12), 4825–4840 (2015)
6. H. Lin, *Speckle Mechanism in Holographic Optical Coherence Imaging* (University of Missouri–Columbia, 2009)

Fabrication of an Adaptive Micro Fresnel Mirror Array

Binal P. Bruno, Ruediger Grunwald and Ulrike Wallrabe

Abstract We present in this paper the design and fabrication of a miniaturized array of piezoelectrically tunable Fresnel mirrors, which can be used to generate propagation invariant and self-healing interference pattern. The mirrors are actuated using a circular piezoelectric actuator, and the resulting change in the tilting angles of the mirrors changes the widths of the interference patterns generated. The array consists of four Fresnel mirrors arranged in 2×2 configuration with each mirror having an area of 2×2 mm^2. The achievable mirror angle ranges from -10 to $+10$ mrad.

1 Introduction

A Fresnel mirror consists of two mirror segments, inclined at a small angle to each other. The tilt of the mirrors results in the generation of an interference pattern when illuminated with a coherent light source. The two mirrors split the collimated laser beam into two coherent overlapping light sheets, resulting in the generation of an interference pattern propagating along the optical axis [1]. The resulting pattern, which can also be regarded as a 2D Bessel beam, is propagation invariant and self-healing and the size of the patterns depends on the tilting angle between the mirrors and the wavelength of the illuminating light source. Adaptive Fresnel mirrors were applied to adaptive pulse autocorrelation [2] and to generate laser-induced periodic surface structures [3].

In this paper, we present further development of the first tunable Fresnel mirror designed by Brunne et al. [4] by reducing the size of the mirror from 5 to 2 mm and

B. P. Bruno (✉) · U. Wallrabe
Laboratory for Microactuators, Department of Microsystems Engineering, University of Freiburg, Freiburg, Germany
e-mail: binal.bruno@imtek.uni-freiburg.de

U. Wallrabe
e-mail: wallrabe@imtek.uni-freiburg.de

R. Grunwald
Max-Born-Institute for Nonlinear Optics and Short Pulse Spectroscopy, Berlin, Germany

A. Martínez-García et al. (eds.), *Progress in Optomechatronic Technologies*,
Springer Proceedings in Physics 233, https://doi.org/10.1007/978-981-32-9632-9_4

fabricating a 2 × 2 array of them. In Sect. 2, we describe the working principle and the results from the mechanical design and simulation of the device. The fabrication process discussed in Sect. 3 is followed by the mechanical characterization of the mirror array in Sect. 4. The results are summarized and further improvements are discussed in Sect. 5.

2 Design and Simulation

A tunable Fresnel mirror consists of two movable mirror segments that meet at the center line of the device. Upon actuation, the deflection of the mirrors is changed which alters the mirror angle. The two mirrors, made from a silicon wafer coated with aluminum, are fixed on a soft silicone (PDMS) layer and are actuated by a piezoelectric bimorph bending disk attached to the PDMS layer (Fig. 1a, b). When an electric field is applied to the piezo disks, they undergo a sperical deflection, which acts as a pressure load on the PDMS layer. As a result, the two mirrors are pulled downwards as shown in Fig. 1c, and as the mirrors themselves are stiff, they maintain their planar surface thereby. The maximum achievable mirror angle depends on the thickness of the silicon wafer, the piezoelectric material used, the geometry of the hinge, the thickness of the PDMS base layer, and Young's moduli of the PDMS at the hinges and base.

The array of Fresnel mirrors presented here consists of four Fresnel mirrors, each with a mirror area of 2 × 2 mm^2, arranged in 2 × 2 configuration as can be seen in Fig. 1a. The individual mirrors are made from a silicon wafer with a thickness of 200 μm and feature an area of 1 × 2 mm^2 each. To facilitate the tilting movement of the mirrors, the hinge geometry was designed to be trapezoidal with a hinge width as narrow as possible on the mirror side. The mirrors are actuated using four circular piezo bimorphs, each with a thickness of 240 μm. For simplicity, a single Fresnel mirror was simulated in COMSOL Multiphysics with quarter symmetry. The diameter of the individual actuators was chosen using a parametric sweep with a trade-off between the achievable mirror angle and the pitch of the array. The Young's

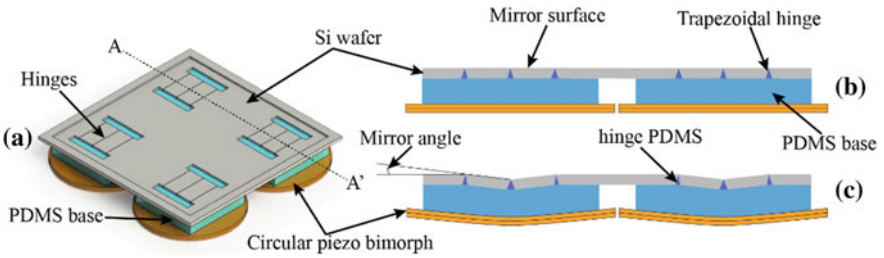

Fig. 1 **a** 3D model of the 2 × 2 array of Fresnel mirrors, each having an area of 2 × 2 mm^2. The actuation principle of the Fresnel mirror at cross section (A–A′) of the mirrors is sketched in **b** at 0 V and **c** at 200 V

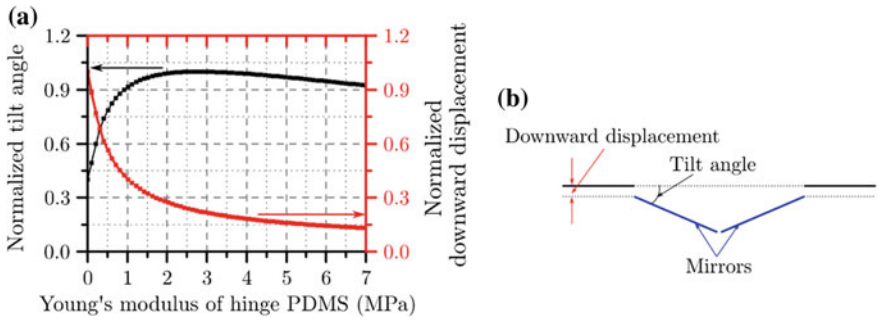

Fig. 2 **a** Plot showing the change in the mirror tilt and displacement as a function of Young's modulus of the PDMS filled in the mirror hinges, normalized to the respective maximum values. **b** Downward displacement and tilting of the mirrors upon actuation

modulus and the Poisson ratio of the silicone are taken from the materials library of COMSOL. A simple linear model is sufficient for simulation since the expected strain levels are small, in the range of <10% [5].

The thickness and stiffness of the PDMS base layer largely affect the achievable mirror angle. By doing a parametric sweep, a thickness of around 300 μm at Young's modulus in the range of 500–700 kPa was found to provide optimal performance. In the case of the mirror hinges, the main parameters to consider are Young's modulus of the PDMS filled in the hinges and the geometry of the hinge. The fabrication process (KOH etching) limits the geometry of the hinge to the dimensions of 280 μm on the backside and 7 μm on the mirror side. Moreover, two possible situations could occur according to the stiffness of the hinges. If the stiffness of the hinge is too large, the rotation about the hinge is suppressed resulting in low tilting angle, and if the stiffness is too low, the out of plane translational displacement dominates the rotation of the hinge. The variation in the tilting angle and the downward deflection normalized to their respective maximum values with regard to Young's modulus of the hinge PDMS is shown in Fig. 2a. The maximum mirror angle is achieved when the hinge has a stiffness of 2.7 MPa. A PDMS with Young's modulus of 1.5 MPa was chosen for fabrication because of the availability of the material. With this configuration, the maximum achievable mirror angle was simulated to be in the range of ±12 mrad, which is 98% of the value at the maximum, and the downward displacement of the mirrors amounts to 4 μm.

3 Fabrication

The fabrication process starts with the manufacturing of the mirror hinges. A 400 nm layer of SiO and 110 nm of SiN is deposited on a 200 μm thick silicon wafer using thermal oxidation and LPCVD process, respectively. The SiN and SiO layers act as the etch mask for the KOH etching process. The oxide and nitride layers at the hinge

openings on the backside are removed by reactive ion etching with a layer of *AZ1518* photoresist acting as an etch mask. The wafer is then etched using KOH to achieve a trapezoidal hinge geometry. Afterward, a 300 nm thick aluminum layer is deposited on the front side of the wafer to get a reflective optical surface. The aluminum layer is covered with a layer of UV curable tape to protect the mirror surface during the subsequent processing (Fig. 3).

The piezo actuator is fabricated from two 120 μm thick sheets of PZT from *Ekulit GmbH*. The upper and lower piezo sheets are cut into a circular shape with a radius of 16 mm and four circular contact notches are cut into the lower sheet using UV laser (*Trumark 6330* from *Trumpf Laser GmbH*) (Fig. 4a). The two sheets are glued together using high-temperature epoxy (*HTG-240*), and the electrodes for each mirror in the array are separated by hatching as shown in Fig. 4b. The PDMS base layer made of *RTV23* by *Neukasil*, with Young's modulus of 600 kPa, is fabricated directly on the bimorphs using a negative mold (Fig. 4c).

Individual 2 × 2 Fresnel mirror arrays are separated from the Si wafer by using UV laser. The mirror arrays are cleaned in an ultrasonic bath in deionized water, the backside of the hinges are treated with an adhesion promoter (*Dow Corning 92-023*), and the hinges are filled with PDMS (*RTV615* from *Momentive Performance Materials*) with Young's modulus of 1.5 MPa. The SiN and SiO underneath the aluminum layer prevent creeping of the PDMS to the front side of the mirror. The piezo bimorph actuator with the silicone base layer is aligned and attached to the backside of the mirror while PDMS is being cured (Fig. 4d). After curing, the piezo bimorph is laser structured from the backside to separate and decouple the individual actuators for each mirror, and the mirrors are made free to move around the hinges

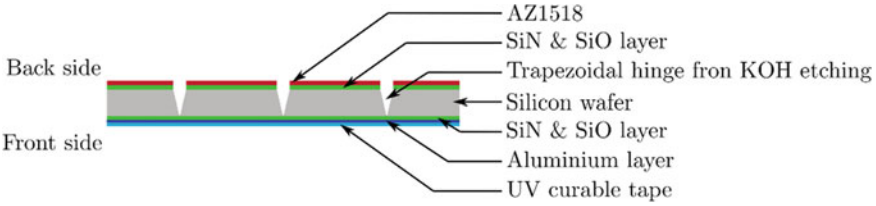

Fig. 3 Cross section of a mirror hinge after cleanroom fabrication

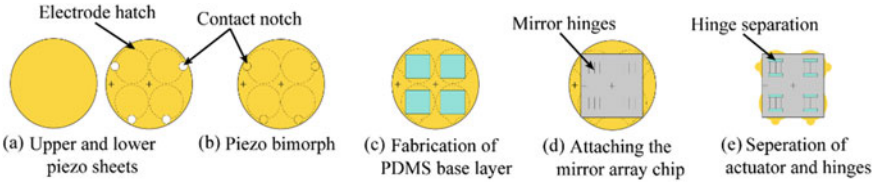

Fig. 4 Process steps in the fabrication of Fresnel mirror array. The laser structured piezo sheets (**a**) which are glued to form a bimorph (**b**). Fabrication of PDMS base layer on the bimorph (**c**). Attaching the mirror chip (**d**) and separating the hinges and the individual bimorph actuators (**e**)

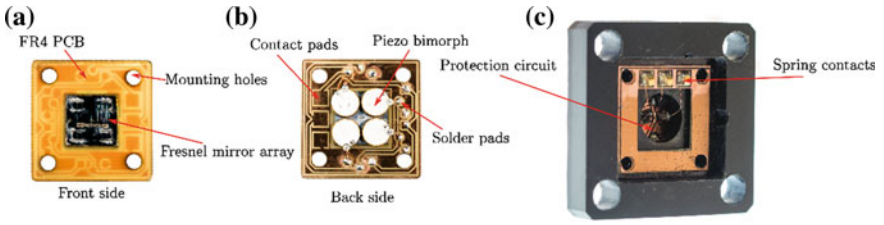

Fig. 5 Mirror holder (**a** and **b**) and the mirror mount with the protection circuit (**c**) for the Fresnel mirror array

by separating those from the front side (Fig. 4e). Now that the mirrors are free to move, the UV tape on the front side is exposed to UV light and peeled off to reveal the mirror surface. The finished mirror array is carefully aligned and glued to a laser structured FR4 PCB substrate (Fig. 5a) for easier handling and providing electrical connections.

4 Mechanical Characterization

The device is mounted on a custom mount (Fig. 5c), which also contains an electrical protection circuit that prevents the depolarization of the piezo sheets. The circuit limits the voltage against the direction of polarization to 33% of the coercive field strength where it is safe to operate [6]. The deflection of the mirrors is measured for electric fields in the range of ±2 kV/mm using a profilometer equipped with a confocal distance sensor while actuating at 1 Hz sinusoidal signal. The angle between the device plane and the mirror plane is evaluated for each applied electric field from the measured surface.

The tilt angle as a function of the electric field is shown in Fig. 6a. A negative tilt angle denotes the mirrors deflecting downwards. The deflection range reaches 22

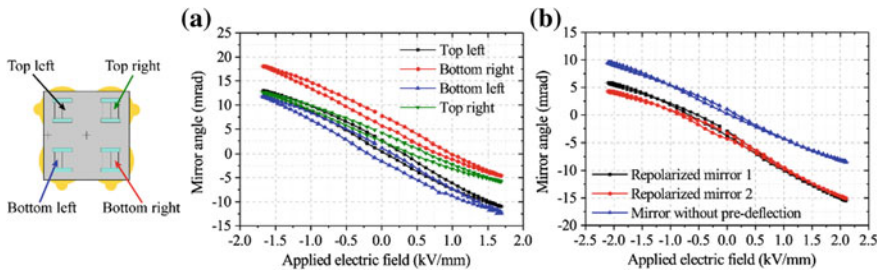

Fig. 6 **a** The mirror angle as a function of the applied electric field for all mirrors in the array. **b** The defined pre-deflection in the mirror angle generated by depolarization and repolarization of the piezo bimorph actuator

mrad, which is close to simulated results. However, each mirror shows a different, undesired pre-deflection. Typically, only negative angles are required for application, which reduces the deflection range in the symmetric case by 50%. To overcome this problem, a pre-deflection can be defined by depolarizing the piezo sheets before gluing and finally repolarizing the piezo by applying an electric field higher than the coercive field strength. The effect of this remanent strain in the piezo bimorphs is shown in Fig. 6b. Using this method, we were able to increase the range of usable angles from 10 to 15 mrad.

5 Summary and Outlook

In this paper, we presented the design and fabrication of an array of Fresnel mirrors. The device was optimized using FEM simulations, which showed a maximum achievable mirror deflection of ± 12 mrad, and a fabrication process that relies on KOH etching, PDMS processing, and laser cutting was established. The mechanical characterization of the fabricated device yielded a similar range of tilt angle. However, the mirrors showed different pre-deflections among the mirrors of the same array, which is undesired as the mirrors need to be actuated synchronously. Hence, each mirror needs to be addressed according to its own voltage dependence. Furthermore, the deflection range is reduced by 50% in the symmetric case as only negative angles are required for applications. One possible solution to this problem is to introduce a defined pre-deflection by depolarizing and repolarizing the piezo actuators. The maximum deflection range can also be increased further by increasing the electric field against the polarization from 33 to 85% [7].

Acknowledgements This work was supported by Deutsche Forschungsgemeinschaft (DFG) within grant no. WA1657/3-2.

References

1. A. Fresnel, *Théorie de la lumière, Ouevres complètes d'Augustin Fresnel, Tome II* (Imperial, Paris, 1868), p. 55
2. A. Treffer, J. Brunne, M. Bock, S. König, U. Wallrabe, R. Grunwald, Adaptive non-collinear autocorrelation of few-cycle pulses with an angular tunable bi-mirror. Appl. Phys. Lett. **108**, 051103 (2016)
3. J. Brunne, A. Treffer, M. Block, R. Grunwald, U. Wallrabe, Fast optical line shaper for ultrashort-pulse laser nanomachining, in *Proceedings of the IEEE Optical MEMS and Nanophotonics* (Istanbul, 2011)
4. J. Brunne, M.C. Wapler, R. Grunwald, U. Wallrabe, A tunable piezoelectric Fresnel mirror for high-speed lineshaping. J. Micromech. Microeng. **23**, 115002 (2013)
5. F. Schneider, T. Fellner, J. Wilde, U. Wallrabe, Mechanical properties of silicones for MEMS. J. Micromech. Microeng. **18**, 065008 (2016)

6. K. Ruschmeyer, *Piezokeramik. Grundlagen, Werkstoffe, Applikationen* (Expert-Verlag, Renningen-Malmsheim, 1995), p. 155
7. B.P. Bruno, A.R. Fahmy, M. Stürmer, U. Wallrabe, M.C. Wapler, Properties of piezoceramic materials in high electric field actuator applications. Smart Mater. Struct. **28**, 015029 (2019)

Effects of the Roughness in the Optical Response of a 2DPC That Have Dielectric or Dispersive LHM Cylindrical Inclusions: The Triangular Lattice

V. Castillo-Gallardo, L. Puente-Díaz, E. Lozano-Trejo, H. Pérez-Aguilar and A. Mendoza-Suárez

Abstract In this work, a numerical technique known as integral equation method (IEM) was used to model the optical response of two-dimensional photonic structures of hexagonal lattice with rods that have smooth and rough surfaces, under TM polarization. Photonic structures were modeled by different materials. One of them was formed with dielectric–dielectric media and the other with dielectric–dispersive LHM media. We found that the optical response was modulated by the roughness of the surface of the inclusions. We also observed that the scattering patterns depend on the type of photonic structure and the incidence angle. Additionally, when we consider the two-dimensional photonic structure with rough surfaces, we approach a real physical system and this causes changes in the reflective optical properties. This property is very useful and has multiple applications in waveguides, filters, omnidirectional mirrors, beam splitters, and so on.

1 Introduction

Photonic crystals (PCs) are periodic arrays of different materials in one (1DPC), two (2DPC), and three dimensions (3DPC) with unit cells, whose magnitude is on the order of the wavelength of the light [1]. The properties of PCs have been the subject of much research in the last few years because of its potential to develop completely optical integrated circuits [2], or optical sensors [3]. In 2DPCs periodicity occurs in two directions, while in the other it is invariant. One of the purposes of this type of material is to control the reflection and/or transmission of light through its structure by the diffraction phenomenon. The reflective optical properties of the 2DPC depend on the type of periodicity, geometry of the inclusions, the refractive index contrast, and the filling fraction of the photonic structure [4].

V. Castillo-Gallardo · L. Puente-Díaz · E. Lozano-Trejo · H. Pérez-Aguilar (✉) · A. Mendoza-Suárez
Facultad de Ciencias Físico-Matemáticas, UMSNH. Avenida Francisco J. Múgica S/N, C.P. 58030 Morelia, Michoacán, Mexico
e-mail: hiperezag@yahoo.com

A. Martínez-García et al. (eds.), *Progress in Optomechatronic Technologies*,
Springer Proceedings in Physics 233, https://doi.org/10.1007/978-981-32-9632-9_5

When proposing a PC, it is necessary to study the optical response of the system. This has been done by numerical simulation calculations using the integral equation method (IEM) [5]. The IEM is based on the Green's second integral theorem applied to the Helmholtz's equation, in which a set of coupled integral equations is obtained as functions of the field and its normal derivative evaluated in the contours that separate the regions of the system. In order to have a finite sampling of points, the contours are divided into small regions, Δs. So the coupled equations are approximated by sums that result in an inhomogeneous matrix system, whose solution determines the source functions. With these source functions, the optical response is obtained.

In the last decade, several physical systems have been studied in which the roughness of surfaces is analyzed, such as scattering of light by rough surfaces [6–10], optical dispersion loss in waveguides [11], coherence effects in propagation through 1DPC [12], corrections to electromagnetic Casimir energies [13], among others. However, there is no evidence of a numerical study of the surface roughness in a 2DPC, despite the fabrication of photonic crystal structures that present certain irregularities in the structure [14–16]. All numerical calculations of photonic bands of metal/dielectric 2DPC have been considered with smooth surfaces [17]. For this reason, we are interested in exploring the consequences of having roughness on the walls of inclusions of a 2DPC. In this work, the IEM is used to calculate the optical response of 2DPCs of the hexagonal periodicity with cylindrical inclusions with smooth and rough surfaces, under TM polarization. The results show that the roughness of the surfaces modulates the optical response, and the scattering patterns depend on the type of photonic structure, the wavelength of the beam of illumination, and the incidence angle.

The structure of the paper is organized as follows: In the next section we give a brief explanation of the IEM applied to a finite 2DPC. Section 3 summarizes the results for a finite 2DPC of hexagonal lattice formed by cylindrical inclusions with smooth and rough surfaces, under TM polarization. Finally, in Sect. 4, we state the conclusions of this work.

2 Theoretical Approach

In previous works, the IEM has been developed to calculate band structures associated with infinite 2DPC [18, 19]. However, in practice, a 2DPC has a finite length. The IEM is also suitable to calculate the distribution of the electromagnetic field in the near and far region for a 2DPC truncated. Let us consider the problem of calculating the reflectance of a 2DPC with finite length that is illuminated with an incident field $\Psi_{inc}(\mathbf{r}, t) = \Psi_{inc}(\mathbf{r})e^{-i\omega t}$. Figure 1 shows the diagram of a finite 2DPC of hexagonal lattice composed by cylindrical inclusions with rough surfaces. Regions 1 and q are characterized by a (real) refractive index $n_{1,q} = \sqrt{\varepsilon_{1,q}(\omega)}$, and regions 2 to $q-1$ are characterized by the corresponding refractive indices $n_j = \pm\sqrt{\varepsilon_j(\omega)\mu_j(\omega)}$, which involve the material's properties and are given in terms of magnetic permeability μ_j

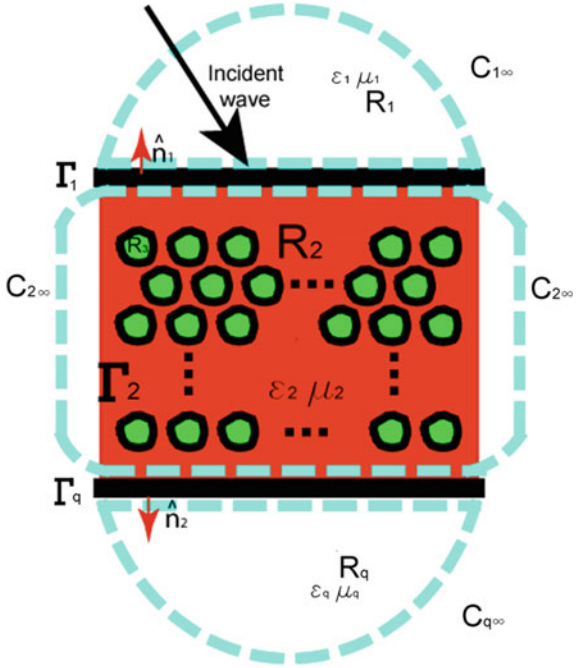

Fig. 1 Scheme of a finite 2DPC to apply the IEM through the integration contours are indicated by the dashed curves. R_1 and R_q represent the regions enclosing the incident and transmission media, respectively

and electric permittivity ε_j, where both of these functions depend on the frequency ω. The sign appearing in the refractive index equation must be taken as negative when considering an LHM and positive when the medium is a dielectric material. We now provide a brief description of the method for calculating the scattered fields. Details that complement the presentation can be found in [5, 7].

Applying Green's integral theorem, the field in region 1 can be expressed as:

$$\Psi^{(1)}(\mathbf{r}) = \Psi_{inc}(\mathbf{r}) + \frac{1}{4\pi}\sum_{j=1}^{M}\int_{\Gamma_j}\left[\frac{\partial G_1(\mathbf{r},\mathbf{r}')}{\partial n_j}\Psi^{(1)}(\mathbf{r}) - G_1(\mathbf{r},\mathbf{r}')\,\Phi^{(1)}(\mathbf{r})\right]ds', \quad (1)$$

where $\Psi_{inc}(\mathbf{r})$ represents the incident field, and the sum of the integrals represents the scattered field. $\partial/\partial n_j$ is the normal derivate operator, $G_1(\mathbf{r},\mathbf{r}')$ is a suitable Green function in the region R_1. The source functions $\Psi^{(1)}(\mathbf{r})$ and $\Phi^{(1)}(\mathbf{r})$ represent the values of the field and its normal derivative evaluated on the surface, respectively.

Following the same steps for region j, the field $\Psi^{(j)}(\mathbf{r})$ can be expressed as:

$$\Theta_j(\mathbf{r})\Psi^{(j)}(\mathbf{r}) = \frac{1}{4\pi}\sum_{j=1}^{M}\int_{\Gamma_j}\left[\frac{\partial G_j(\mathbf{r},\mathbf{r}')}{\partial n_j}\Psi^{(j)}(\mathbf{r}) - G_j(\mathbf{r},\mathbf{r}')\,\Phi^{(j)}(\mathbf{r})\right]ds', \quad (2)$$

where $\Phi_j(\mathbf{r})$ is unity for points inside medium j, and zero otherwise; $G_j(\mathbf{r}, \mathbf{r}')$ is the Green function for medium j.

Mendoza-Suárez et al. calculated the discrete approximations of the two different integral terms appearing in (1) and (2) [18]. Moreover, considering the conditions of continuity of the field and its normal derivative along the different contours Γ_q, the system of equations for a 2DPC of finite length can be expressed as:

$$\sum_{n=1}^{Na}\left(\delta_{mn(1)} - N^{(1)}_{mn(1)}\right)\Psi_{n(1)} + \frac{f_1}{f_2}\sum_{n=1}^{Na} L^{(1)}_{mn(1)}\Phi_{n(1)} = \Psi^{inc}_m, \tag{3}$$

$$\begin{aligned} &-\sum_{n=1}^{Na} N^{(2)}_{mn(1)}\Psi_{n(1)} + \sum_{n=1}^{Na} L^{(2)}_{mn(1)}\Phi_{n(1)} - \sum_{n=1}^{Nb} N^{(2)}_{mn(1)}\Psi_{n(1)} \\ &+\sum_{n=1}^{Nb} L^{(2)}_{mn(1)}\Phi_{n(1)} + \cdots - \sum_{n=1}^{Nq} N^{(2)}_{mn(1)}\Psi_{n(1)} + \sum_{n=1}^{Nq} L^{(2)}_{mn(1)}\Phi_{n(1)} = 0 \end{aligned}, \tag{4}$$

$$\sum_{n=1}^{Nb}\left(\delta_{mn(2)} - N^{(3)}_{mn(2)}\right)\Psi_{n(2)} + \frac{f_3}{f_2}\sum_{n=1}^{Nb} L^{(3)}_{mn(2)}\Phi_{n(2)} = 0, \tag{5}$$

$$\sum_{n=1}^{Nc}\left(\delta_{mn(3)} - N^{(3)}_{mn(3)}\right)\Psi_{n(3)} + \frac{f_3}{f_2}\sum_{n=1}^{Nb} L^{(3)}_{mn(3)}\Phi_{n(3)} = 0, \tag{6}$$

$$\ldots,$$

$$\sum_{n=1}^{Nq-1}\left(\delta_{mn(q-1)} - N^{(3)}_{mn(q-1)}\right)\Psi_{n(q-1)} + \frac{f_3}{f_2}\sum_{n=1}^{Nq-1} L^{(3)}_{mn(q-1)}\Phi_{n(2n-1)} = 0 \tag{7}$$

and

$$\sum_{n=1}^{Nq}\left(\delta_{mn(q)} - N^{(4)}_{mn(q)}\right)\Psi_{n(q)} + \frac{f_q}{f_2}\sum_{n=1}^{Nq} L^{(4)}_{mn(q)}\Phi_{n(q)} = 0, \tag{8}$$

where $n(j)$, $j = a, b, \ldots, q$ is used to denote the different integration paths Γ_a, Γ_b, …, Γ_q, and $n = 1, 2, \ldots, N_q$ denotes their corresponding points resulting from a given partition. m indicates the mth point [observer's coordinates $\mathbf{r} = (x_m, y_m)$] along the contour Γ_q. We called N_q the number of points taken along the corresponding contour Γ_q. The matrix elements $N^{(p)}_{mn(q)}$ and $L^{(p)}_{mn(q)}$ are given in [18]. Additionally, quantity f_j is given by:

$$f_j = \begin{cases} \mu_j & \text{for E polarization,} \\ \varepsilon_j & \text{for H polarization.} \end{cases} \tag{9}$$

Thus, (3)–(8) constitute an inhomogeneous system of $2\sum_{p=1}^{q} N_p$ linear equations, which can be solved numerically to determine the source functions (the field and its

normal derivative) along Γ_q contours. With these functions it is possible to obtain the scattered field.

The far-field amplitude is given by:

$$A(\theta_S, \omega) = \int_{\Gamma_q} \left[-i\frac{\omega}{c}\left(\hat{n}_q' \cdot \hat{\mathbf{r}}\right)\Psi_q(\mathbf{r}') - \frac{\partial \Psi_q(\mathbf{r}')}{\partial \hat{n}_q'} \right] \times \exp\left(-i\frac{\omega}{c} r' \cdot \hat{r}\right) ds', \quad (10)$$

with $\hat{\mathbf{r}} = (-\cos\theta_s, \sin\theta_s)$. Then the differential reflectance coefficient can be obtained by:

$$\frac{\partial R}{\partial \theta_s} = h|A(\theta_s, \omega)|^2, \quad (11)$$

where h is a normalization factor that depends on the incident wave. In the case of an incident Gaussian wave, this factor is $h = \left(2(2\pi)^{3/2} gk\cos\theta_0\right)^{-1}$, g being the $1/e$ half-width of the modulus projected on the plane $x = 0$, and k represents the wave number. The reflectance as a function of the frequency is obtained by one's integrating over all the scattering angles in the incident region. That is,

$$R(\omega) = \int_{-\pi/2}^{\pi/2} \frac{\partial R}{\partial \theta_s} d\theta_s. \quad (12)$$

In a similar way, it is possible to apply an analogous procedure to determine the far-field amplitude in the transmission zone to calculate the transmittance.

3 Optical Response of a Finite 2DPC

The optical response of a two-dimensional photonic structure consisting of a periodic array of parallel dielectric cylindrical inclusions embedded in background dielectric material (in both cases, vacuum), whose intersections with a perpendicular plane form a hexagonal lattice, is presented in this section. The rough surface profile on the inclusion wall of circular cross-section is obtained by means of a realization of a Gaussian-correlated random process that obeys a negative exponential probability density function (PDF).

Optical properties of dispersive LHM are given by the dielectric function:

$$\varepsilon(\omega) = 1 - \frac{\omega_p^2}{\omega^2} \quad (13)$$

and the magnetic permeability

$$\mu(\omega) = 1 - \frac{F\omega^2}{\omega^2 - \omega_0^2}, \tag{14}$$

where the plasma frequency is ω_p= 10 c/D, the resonance frequency is ω_0= 4 c/D, and the LHM filling fraction is $F = 0.56$ [20]. Here the speed of light in vacuum is c, and lattice parameter is D. The region where the LHM presents a negative refraction index is within the frequency range $\omega_p < \omega < \omega_{LH}$ with $\omega_{LH} = \omega_0/\sqrt{(1-F)}$. In our analysis, $D = 1\,\mu$m was considered. With this, the plasma and resonance frequencies (in reduced units) are $\omega_p = 1.592$ ($\lambda = 628$ nm) and $\omega_0 = 0.637$($\lambda = 1.569\,\mu$m), respectively [18].

Reflectance and transmittance with scattering patterns for a photonic structure with 500 (5 × 100) dielectric circular cylinders are shown in Fig. 2a–c. Similarly, a photonic structure with 720 (6 × 120) dispersive LHM circular cylinders is given in Fig. 2d–f.

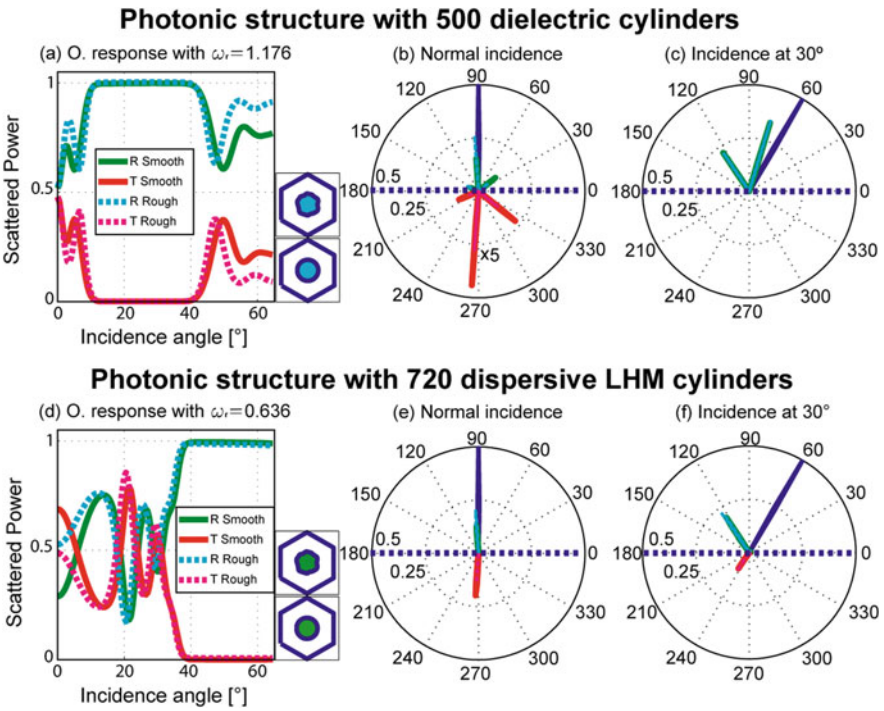

Fig. 2 Reflectance (R) and transmittance (T) as a function of the incidence angle of a photonic structure with **a** 500 dielectric cylinders and **d** 720 dispersive LHM cylinders, under TM polarization. Photonic structures were illuminated with reduced frequency beams $\omega_r = 1.176$ ($\lambda = 850$ nm) and $\omega_r = 0.636$ ($\lambda = 1.57\,\mu$m), respectively. Scattering patterns of each photonic structure for **b** and **e** normal incidence, and **c** and **f** incidence at 30°. The solid curves correspond to smooth inclusions surfaces and the dashed lines represent rough inclusions surfaces

In Fig. 2a, d, the optical response of the 2D photonic structure with smooth and rough surfaces has been compared. The dashed curves correspond to system with rough surfaces and the solid curves for smooth surfaces. In this case, the roughness was modeled with parameters of the correlation length $l_c = 0.05\lambda$ and the standard deviation of heights $\sigma = 0.01\lambda$. In both cases, the filling fraction $f = 0.10$ was used. Photonic structures were illuminated with a Gaussian beam. The $1/e$ half-width of the modulus of the incident Gaussian beam projected onto the center of the structures was $g = 12$ μm with TM polarization. For these cases, the optical reflectance and transmittance are modulated due to the roughness of the surface of the inclusions. However, the scattering patterns remain unchanged, as shown in Fig. 2b, c, e, f. Thus, scattering patterns depend on the type of photonic structure and the incidence angle.

4 Conclusions

Using the integral method, it was possible to study the propagation of electromagnetic waves through truncated periodic photonic structures. This provided the opportunity to model the reflectance and transmittance with the scattering patterns of a couple of two-dimensional photonic structure consisting of a periodic array of parallel dielectric rods of circular cross-section embedded in the background dielectric material. We found that the optical response was modulated by the roughness of the surface of the inclusions. We also observed that the scattering patterns depend on the type of photonic structure and the incidence angle. This property is very useful and has multiple applications in waveguides, filters, omnidirectional mirrors, beam splitters, and so on.

Acknowledgments This research was supported by Consejo Nacional de Ciencia y Tecnología through a scholarship for Castillo-Gallardo, Puente-Díaz and Lozano-Trejo. Also, Pérez-Aguilar and Mendoza-Suárez express their gratitude to the Coordinación de la Investigación Científica of the Universidad Michoacana de San Nicolás de Hidalgo for the financial support granted for the development of this research project.

References

1. J.D. Joannopoulos, S.G. Johnson, J.N. Winn, R.D. Meade, *Photonic Crystals: Molding the Flow of Light* (Princeton University Press, 2008), Chaps. 4–6
2. A. Mukherjee, A.D. Ariza-Flores, R.F. Balderas-Valadez, V. Agarwal, Controlling the optical properties of composite multilayered photonic structures: effect of superposition. Opt. Express **21**, 17324–17339 (2013). https://doi.org/10.1364/OE.21.017324
3. T.V.K. Karthik, L. Martinez, V. Agarwal, Porous silicon ZnO/SnO2 structures for CO2 detection. J. Alloy. Compd. **731**, 853–863 (2017). https://doi.org/10.1016/j.jallcom.2017.10.070
4. T.F. Krauss, R.M. De La Rue, Photonic crystals in the optical regime: past, present and future. Prog. Quant. Electron. **23**, 51–96 (1999). https://doi.org/10.1016/S0079-6727(99)00004-X

5. A. Mendoza-Suárez, F. Villa-Villa, Numerical method based on the solution of integral equations for the calculation of the band structure and reflectance of one- and two-dimensional photonic crystals. J. Opt. Soc. Am. B **23**, 2249–2256 (2006). https://doi.org/10.1364/JOSAB.23.002249
6. A.A. Maradudin, T. Michel, A.R. McGurn, E.R. Méndez, Enhanced backscattering of light from a random grating. Annals Phys. **203**(2), 255–307 (1990). https://doi.org/10.1016/0003-4916(90)90172-K
7. H.I. Pérez, C.I. Valencia, E.R. Méndez, J.A. Sánchez-Gil, On the transmission of diffuse light through thick slits. J. Opt. Soc. Am. A **26**(4), 909–918 (2009). https://doi.org/10.1364/JOSAA.26.000909
8. H. Perez-Aguilar, A. Mendoza-Suárez, E.S. Tututi, I.F. Herrera-González, Disordered field patterns in a waveguide with periodic surfaces. Prog. Electromagn. Res. **48**, 329–346 (2013). https://doi.org/10.2528/PIERB12120509
9. T. Nordam, P.A. Letnes, I. Simonsen, A.A. Maradudin, Numerical solutions of the Rayleigh equations for the scattering of light from a two-dimensional randomly rough perfectly conducting surface. J. Opt. Soc. Am. A **31**, 1126–1134 (2014). https://doi.org/10.1364/JOSAA.31.001126
10. A. González-Alcalde, J.P. Banon, O.S. Hetland, A.A. Maradudin, E.R. Méndez, T. Nordam, I. Simonsen, Experimental and numerical studies of the scattering of light from a two-dimensional randomly rough interface in the presence of total internal reflection: optical Yoneda peaks. Opt. Express **24**, 25995–26005 (2016). https://doi.org/10.1364/OE.24.025995
11. S. Hughes, S. Ramunno, J.F. Young, J.E. Sipe, Optical scattering loss due to disorder and fabrication roughness in semiconductor photonic crystal slab waveguides, in *International Quantum Electronics Conference IThL5* (2004). https://doi.org/10.1364/IQEC.2004.IThL5
12. A. Mandatori, M. Bertolotti, C. Sibilia, B.J. Hoenders, M. Scalora, Coherence effects in propagation through one-dimensional photonic bandgap structures with a rough glass interface. J. Opt. Soc. Am. B **24**, 2921–2929 (2007). https://doi.org/10.1364/JOSAB.24.002921
13. H.Y. Wu, M. Schaden, Perturbative roughness corrections to electromagnetic Casimir energies. Phys. Rev. D **89**, 105003 (2014). https://doi.org/10.1103/PhysRevD.89.105003
14. L. Ondič, M. Varga, I. Pelant, J. Valenta, A. Kromka, R.G. Elliman, Silicon nanocrystal-based photonic crystal slabs with broadband and efficient directional light emission. Scientific Reports **7**, 5763 (2017). https://doi.org/10.1038/s41598-017-05973-y
15. R.F. Balderas-Valadez, V. Agarwal, C. Pacholski, Fabrication of porous silicon-based optical sensors using metal-assisted chemical etching. RSC Adv. **6**(26), 21430–21434 (2016). https://doi.org/10.1039/C5RA26816H
16. J.E. Baker, R. Sriram, B.J. Miller, Two-dimensional photonic crystals for sensitive microscale chemical and biochemical sensing. Lab Chip **15**, 971–990 (2015). https://doi.org/10.1039/C4LC01208A
17. Y.X. Zong, J.B. Xia, Photonic band structure of two-dimensional metal/dielectric photonic crystals. J. Phys. D: Appl. Phys. **48**(35), 355103 (2015). http://iopscience.iop.org/article/10.1088/0022-3727/48/35/355103/meta
18. A. Mendoza-Suárez, F. Villa-Villa, J.A. Gaspar-Armenta, Band structure of two-dimensional photonic crystals that include dispersive left handed materials and dielectrics in the unit cell. J. Opt. Soc. Am. B **24**, 3091–3098 (2007). https://doi.org/10.1364/JOSAB.24.003091
19. V. Castillo-Gallardo, L.E. Puente-Díaz, H. Pérez-Aguilar, A. Mendoza-Suárez, F. Villa-Villa, Band structure of two-dimensional photonic crystals that include dispersive left-handed materials with rough surfaces in their lattice. Unpublished
20. D. Bria, B. Djafari-Rouhani, A. Akjouj, L. Dobrzynski, J.P. Vigneron, E.H. El Boudouti, A. Nougaoui, Band structure and omnidirectional photonic band gap in lamellar structures with left-handed materials. Phys. Rev. E **69**, 066613 (2004). https://doi.org/10.1103/PhysRevE.69.066613

Nano-antennas Excitation with Visible Light and Their Observed Response with a Confocal Microscope in the THz Range

Daniel Luis Noriega, Fernando Mendoza Santoyo, Jorge Mauricio Flores Moreno, Javier Méndez-Lozoya and Francisco Javier González

Abstract A confocal microscope was used to observe the electromagnetic field produced from a cluster of nano-antennas excited with visible light. The experimental results show the dynamic behavior of the iron oxide nanoparticles deposited over the nano-antennas cluster.

1 Introduction

Antennas have been used for over a century to control the emission and reception of many types of electromagnetic radiation. The re-escalation of said antennas to smaller sizes gave birth to devices, like the optic nano-antennas, that can focus farther than the diffraction limit; this allows seeking and highlighting for better optic processes, like high harmonic generation [1], fluorescence [2, 3], Raman scattering [4, 5] and infrared absorption [6, 7].

It is well known that the metallic particles maintain resonance plasmonic modes in visible wavelengths, making them natural optic antennas [1, 8]. The objective of this research work is to characterize qualitatively the dynamic behavior of superparamagnetic nanoparticles by exposing them to an electromagnetic field generated by excited nano-antennas of the bowtie type. Particles which are reduced to smaller sizes than their magnetic domain (or close to it) manifest a property called superparamagnetism. The said particles are highly susceptible to magnetic fields. They do not precipitate once they are monodispersed in a fluid, and if the exterior magnetic field is removed, they demagnetize; also, they have a native strength to not agglomerate by themselves [9].

D. Luis Noriega (✉) · F. Mendoza Santoyo · J. M. Flores Moreno
Centro de Investigaciones en Óptica A.C., Lomas del Bosque 115, Col, Lomas del Campestre, 37150 León, Guanajuato, Mexico
e-mail: dluis@cio.mx

J. Méndez-Lozoya · F. J. González
Universidad Autónoma de San Luis Potosi, Alvaro Obregon 64, Centro, 78000 San Luis Potosi, SLP, Mexico

A. Martínez-García et al. (eds.), *Progress in Optomechatronic Technologies*,
Springer Proceedings in Physics 233, https://doi.org/10.1007/978-981-32-9632-9_6

The confocal microscopy is a technique which increases the optic resolution and contrast of an image by using a pinhole that obstructs the light that is out of the focal plane. This results in a system that not only discriminates field of view over the focal plane but it also permits depth selection inside of the specimen under observation. To form the image, the confocal microscope relies on a scanning system in which a laser illuminates a small section of the specimen and a sensor retrieves the information; then the laser moves to the next section of the sample over the same focal plane (typically, with mirrors mounted on a piezoelectric transducer) and the sensor retrieves the information of the new section. The process repeats until all the desired part of the image is reconstructed (within the required field of view). Through digital image processing the information of each section of the sample is stitched together and a digital image of the specimen under study is acquired [10].

2 Methodology

We used iron oxide Fe_3O_4 nanoparticles (Np) with a size of 50–100 nm scattered in an immersion fluid (no polar) by means of an ultrasonic bath. Then, 20 μl of the immersion fluid with the dispersed Np was deposited over the substratum of the THz nano-antennas (Na). The Np were forced to get close to the substratum with two neodymium magnets, with the aim to increase the density of Np in the Na vicinity, given that the electromagnetic field produced by the Na affects only the Np that are located a few micrometers from the said Na. After the magnets were removed, the substratum was irradiated with two wavelengths, one for observation ($\lambda_o = 543$ nm) and one for excitation ($\lambda_e = 1$ μm). Images of the process were captured with the help of a confocal microscope.

3 Results

Figure 1 presents a series of images with a field of view of 21 × 23 μm where the concentration of Np was 0.42 g/l. The images were taken along an interval of 20 min. Figure 2 shows the same area over the substratum, with the same Np, but now we turn off the λ_e, so the Np enter a period of relaxation of ~20 min, with the aim to check if the behavior observed in the Fig. 1 is triggered solely by the λ_e and not by the λ_o. As can be seen in Fig. 2, there is no observable phenomenon, other than the slight fading of circles.

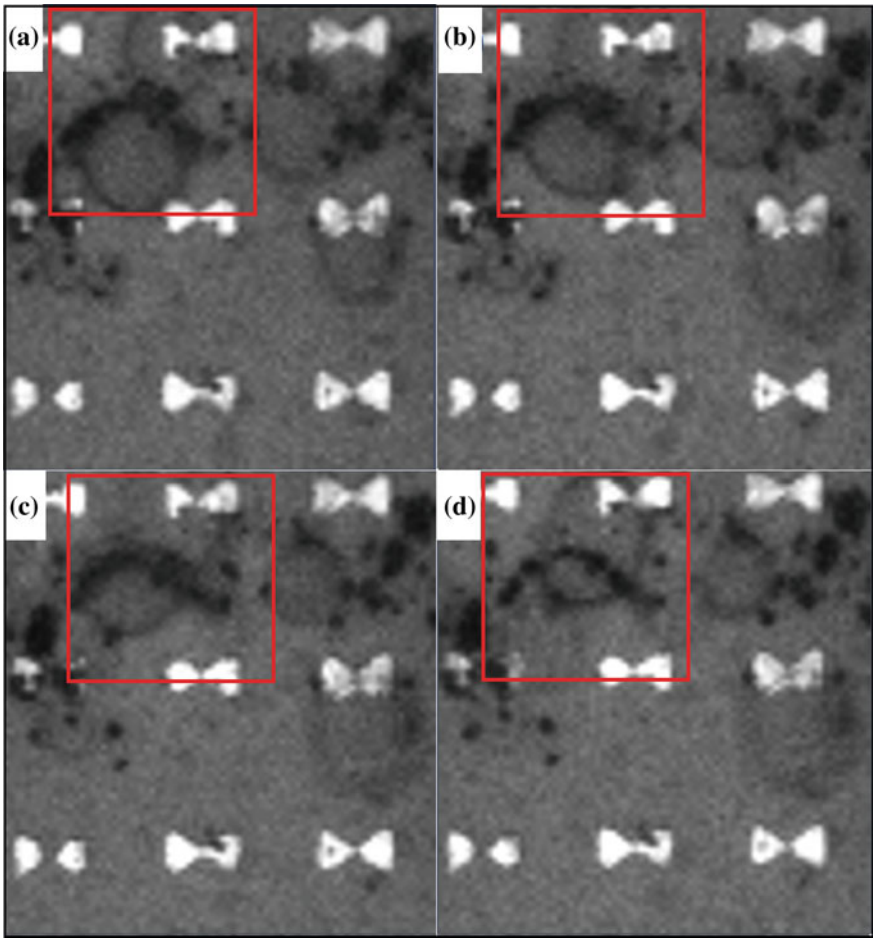

Fig. 1 Images of substratum being irradiated by both λ_e and λ_o in a time of: **a** $t \approx 0$ min. **b** $t \approx 7$ min. **c** $t \approx 14$ min. **d** $t \approx 20$ min. Inside the *red square* we can observe the formation and dispersion of *circles*

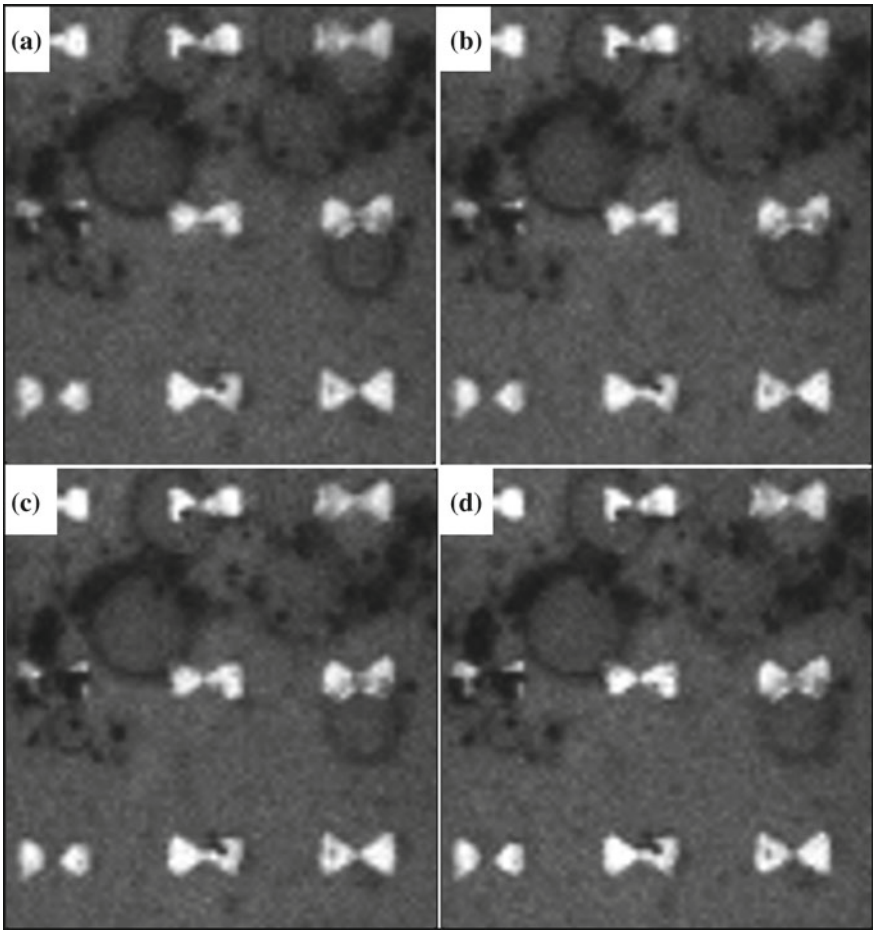

Fig. 2 Substratum without λ_e at a time: **a** $t \approx 0$ min. **b** $t \approx 7$ min. **c** $t \approx 14$ min. **d** $t \approx 20$ min

4 Conclusions

In this preliminary research set, as a proof of principle, we observed a rearrangement of the Np when the substratum was irradiated with the λ_e, but the same phenomenon did not repeat when the λ_e was absent, which make us think that the λ_o by itself is not enough to excite the Na. The observed response of the Np to the electromagnetic field produced by the Na is slow and not always the same (as the one presented here). As future work, we intend to improve the experimental methodology until the dynamic clustering of the Np due to the electromagnetic field generated by the Na is repeatable. We will also characterize the dynamics of the Np as a result of the electromagnetic field from the excited Na.

Acknowledgments F. J. González would like to acknowledge the support from Project 32 of "Centro Mexicano de Innovación en Energía Solar" and by the National Laboratory Program from CONACYT through the Terahertz Science and Technology National Lab (LANCYTT).

References

1. T.H. Taminiau, F.D. Stefani, F.B. Segerink, N.F. van Hulst, Optical antennas direct single-molecule emission. Nat. Photonics **2**(4), 234–237 (2008)
2. S. Kim, J. Jin, Y.-J. Kim, I.-Y. Park, Y. Kim, S.-W. Kim, High-harmonic generation by resonant Plasmon field enhancement. Nature **453**(7196), 757–760 (2008)
3. R.M. Bakker, V.P. Drachev, Z. Liu, H.-K. Yuan, R.H. Pedersen, A. Boltasseva, J. Chen, J. Irudayaraj, A.V. Kildishev, V.M. Shalaev, Nanoantenna array-induced fluorescence enhancement and reduced lifetimes. New J. Phys. **10**(12), 125022 (2008)
4. P. Anger, P. Bharadwaj, L. Novotny, Enhancement and quenching of single-molecule fluorescence. Phys. Rev. Lett. **96**(11), 113002 (2006)
5. K. Kneipp, Y. Wang, H. Kneipp, L.T. Perelman, I. Itzkan, R.R. Dasari, M.S. Feld, Single molecule detection using surface-enhanced Raman scattering (SERS). Phys. Rev. Lett. **78**(9), 1667–1670 (1997)
6. G. Das, F. Mecarini, F. Gentile, F. De Angelis, H. Mohan Kumar, P. Candeloro, C. Liberale, G. Cuda, E. Di Fabrizio, Nano-patterned SERS substrate: application for protein analysis vs. temperature. Biosens. Bioelectron. **24**(6), 1693–1699 (2009)
7. F. Neubrech, A. Pucci, T.W. Cornelius, S. Karim, A. García-Etxarri, J. Aizpurua, Resonant plasmonic and vibrational coupling in a tailored nanoantenna for infrared detection. Phys. Rev. Lett. **101**(15), 157403 (2008)
8. E.R. Encina, E.A. Coronado, Plasmonic nanoantennas: angular scattering properties of multipole resonances in noble metal nanorods. J. Phys. Chem. C **112**(26), 9586–9594 (2008)
9. L.H. Reddy, J.L. Arias, J. Nicolas, P. Couvreur, Magnetic nanoparticles: design and characterization, toxicity and biocompatibility, pharmaceutical and biomedical applications. Chem. Rev. **112**(11), 5829–5830 (2012). https://doi.org/10.1021/cr300068p
10. B.R. Masters, *Confocal Microscopy and Multiphoton Excitation Microscopy: The Genesis of Live Cell Imaging* (SPIE Press, 2006, ISBN 0-8194-6118-0)

Acousto-Optic Dispersion Applicability to Plastic Auto-Part Color Characterization

Jose Amilcar Rizzo Sierra, Cesar Isaza, Ely Karina Anaya Rivera, Jonny Paul Zavala de Paz and Julio Mosquera

Abstract Acousto-optic dispersion occurs when light interacts with a translucent material in which a sound-induced spatial distribution of its refractive index is present. That diffracted light can then be analyzed for different properties of the source. The experimental and theoretical basis of the phenomena were proposed in early twentieth century, mainly by Brillouin and Raman, respectively. Over time, acousto-optics has transited towards applied technology such as image processing in military applications. In this paper, we propose an acousto-optic image acquiring system to study plastic auto-parts color characterization via hyperspectral imaging. Current methodologies regarding the same subject use mainly colorimeters, which by default cannot provide the same amount of spectral information than an acousto-optic system could gather. Therefore, a distinctive potential of acousto-optic technology lies within the subject of plastic auto-parts cosmetic corrosion (PACC) characterization, term which would refer to the study of undesirable changes in color (in plastic auto-parts) due to time and exposure.

1 Introduction

Auto-parts industry is one of the most important industrial sectors in Mexico. In 2016 figures it represented 2.8% of its gross domestic product and 16.9% of its total manufacture activity, and the country consolidated itself as the 7th world's largest auto-parts producer in 2017. The industry has shown an overall growth of more than 40% from 2008 to 2016. That represented an approximate growth from 9.5 to 16.9% of the manufacture sector GDP in that time frame [1, 2]. That dynamic has

This research was partially supported by a grant from CONACYT-México. *Problemas Nacionales* program: PN3967-2016.

J. A. Rizzo Sierra (✉) · C. Isaza · E. K. Anaya Rivera · J. P. Zavala de Paz
Universidad Politécnica de Querétaro. El Marqués, Querétaro, Mexico
e-mail: amilcar.rizzo@gmail.com

J. Mosquera
Universidad del Quindío. Armenia, Quindío, Colombia

A. Martínez-García et al. (eds.), *Progress in Optomechatronic Technologies*,
Springer Proceedings in Physics 233, https://doi.org/10.1007/978-981-32-9632-9_7

brought intense research and development activity in Mexico related to the sector as well, both in private and public institutions, in a much needed and developing a supporting role to the industry. One of the current concerns that more technology and economy-savvy customers have been expressing to automotive industry relates to undesirable cosmetic or aesthetic changes due to time and exposure on all kinds of plastic auto-parts used for both interior and exterior application in motor vehicles. It is understood that this represents one of the most important factors upon which buying decisions are made by actual customers, complementing usual factors such as vehicle performance, security, communication capabilities, and technology integration features, along with a numerous list of others. Facing that, the automotive industry has had to develop standards and protocols to ensure its processes can come up with products with sufficient quality to meet these and other consumers' criteria. For example: research, development, and testing of plastic materials which retain their cosmetic properties in terms of color for at least a period of time equivalent to the engine/chassis warranty is one of the goals within this subject. Besides being one of the customer's main concerns regarding automotive aesthetics perceptions and requirements, the subject has itself importance as well, since industrial treatments to plastic materials which happen to prove themselves to fulfill cosmetic requirements could affect other material properties as well, such as mechanical ones. Additionally, currently typically used standards to validate a new material before incorporating it to production lines lack of proper technical measurement for the optical aspects defining key properties in the context of plastic auto-parts cosmetics, such as color. One important aspect to consider is that current tests employed in the industry are, in one stage or another, based on human naked eye observations, prone to different types of methodological subjectivity, as investigated in [3, 4]. Thus, we propose in this paper a new methodology to study changes in automotive plastic components using acousto-optic filtering of the light coming from them. The technology has the ability to work with a wide range of the light spectrum; from the near infrared to the ultraviolet [5–16]. Images are acquired at a reflectance versus wavelength resolution that gives hyperspectral and polarization information about a particular material, the last aspect complementing the information that can be gathered by means of solid state integrated sensor based spectroscopy technologies such as those used in ecology/botany [17–21], and recently proposed proof of concept new technologies [14, 22–24]. Some of these non acousto-optics tunable filter (AOTF) based technologies are specifically referred or used as Colorimeters [25, 26], representing the main data gathering devices currently supporting the automotive industry on the subject of this paper.

2 Related Works

2.1 Plastic Auto-Parts Studies and Standards

With the development of automotive industry, measurement standards and methodologies for auto-parts quality control monitoring have been evolving as well. Specifically related to this paper are the methodologies used to assert and evaluate cosmetic corrosion of auto-parts. While there's ample literature on the subject of cosmetic corrosion in metallic auto-parts (with or without coatings), that's not so much the case for plastic auto-parts. Cosmetic corrosion in this context widely means undesired changes in appearance, color, and finish in auto-parts, such as exterior and interior painting and plastic applications. Different methodologies used to study the subject as been proposed and used in [27–29]. As methodologies, these can be roughly categorized as follows: (a) open environment non-accelerated or accelerated exposure tests, and (b) open environment laboratory simulated non-accelerated or accelerated exposure tests. Among the studied components are steel auto-parts, with or without utility coatings [30–33]. However, the main objectives of those tests are related to security requirements compliance rather than quality or long term cosmetic corrosion performance of the auto-parts. In the last years, with respect to auto-parts cosmetic corrosion, vehicle manufacturers have had to develop their own study methodologies due to progressive customer awareness and demands on automotive cosmetics. Some of them resulted in the development of standards such as ISO9227, for salt spray corrosion. Other examples are: Renault ECC1 D172028, Volvo VICT VCS1027, 149, Volskwagen PV1210, General Motors GM9540P, and Daimler Chrysler KWT-DC [34]. It must be noticed that within their test methodologies, each manufacturer implements proprietary strategies to emulate variables intervening in cosmetic corrosion such as those related to environmental pollutants, temperature, relative humidity, and test duration or cyclic exposure patterns to simulate different time periods of natural exposure. Other standards implemented by the automotive industry, in this case to study changes in plastic auto-parts are: ASTM D1435-13 (standard practice to study the exterior wear of plastics), ISO 877.2-2009 (methodology to study sunlight exposure in plastics), ASTM G7 (methodology to perform environmental exposure tests to nonmetallic materials), ASTM G24 (methodology to emulate glass filtered sunlight exposition), ISO 877.2-2009 (sunlight exposure methodology in plastics), ASTM G7 (methodology to perform environmental exposure to nonmetallic materials), ASTM G24 (methodology to perform sunlight exposure through glass), ASTM G113 (methodology to study the durability of nonmetallic materials to natural or artificial environmental exposure), ASTM G141 (guide to consider variability of factors involved in nonmetallic material exposure tests), ASTM G147 (methodologies for the conditioning and handling of nonmetallic materials during natural of artificial environmental exposure tests). On the other hand, plastic auto-parts have been subjected to quality tests similar to those performed in metallic auto-parts. Particularly, with respect to synthetic (plastic) upholstery auto-parts [35]. Automotive industry has been raising production quality standards since its beginnings. That has begun to

be coupled with demands from a new generation of customers requiring more than mechanical reliability and performance in automotive industry, opening the doors to different high impact market factors such as quality and cosmetic corrosion properties of plastic auto-parts used in contemporary mass produced vehicles.

2.2 Acousto-Optics Related Work

To our current awareness, there is no literature on the application of acousto-optic imaging to the problem of plastic auto-parts cosmetic corrosion. However, is not far-fetched to consider that the technology is appropriate to study the subject since it has found application, among others, in signal processing [5, 6], image processing [7, 8], and analytical chemistry [9]. Hyperspectral acousto-optic imaging has also found application in ecology/botany [20], and cultural heritage monitoring and preservation [15]. There are also AOTF-based spectroscopy technology proposals such as [14, 16]. Generally speaking, acousto-optic filtering based technologies are the fundamentals of technologies applicable in different fields where its ample informational gathering possibilities from objects of study are required, such as fluorescence multidimensional spectrometry, and multi-wavelength thermal lens spectrometry [10]. Therefore, is not unreasonable it could prove to be instrumental with respect to the problem at hand.

3 Materials and Methods

3.1 Image Acquisition System

Figure 1, top presents the experimental setup of the image acquisition system employed, while Fig. 1, bottom presents a simplified schematics of its functioning principle. Light coming from the studied object is concentrated through a magnification lens as a confocal optic element before being introduced to a tellurium dioxide (TeO_2) crystal which will act as an acousto-optic tunable filter (AOTF). Before that, a sound wave has to be propagated across it, in order to change its refractive index in a controllable manner. That's achieved by transducer and absorber coupled to the crystal to produce, guide, and absorb the sound wave propagating through it. The characteristics of that sound wave, which as said determine the refractive index disposition of the crystal, are controlled in turn by an RF generator followed by an RF amplifier. The RF signal produced by the generator is programmed and controlled by a computer interfaced to it. When being excited to a specific frequency via the transducer, the crystal will diffract light at an specific wavelength Bragg regime diffraction, producing $+1$, 0, and -1 diffraction order hyperspectral images [13, 14].

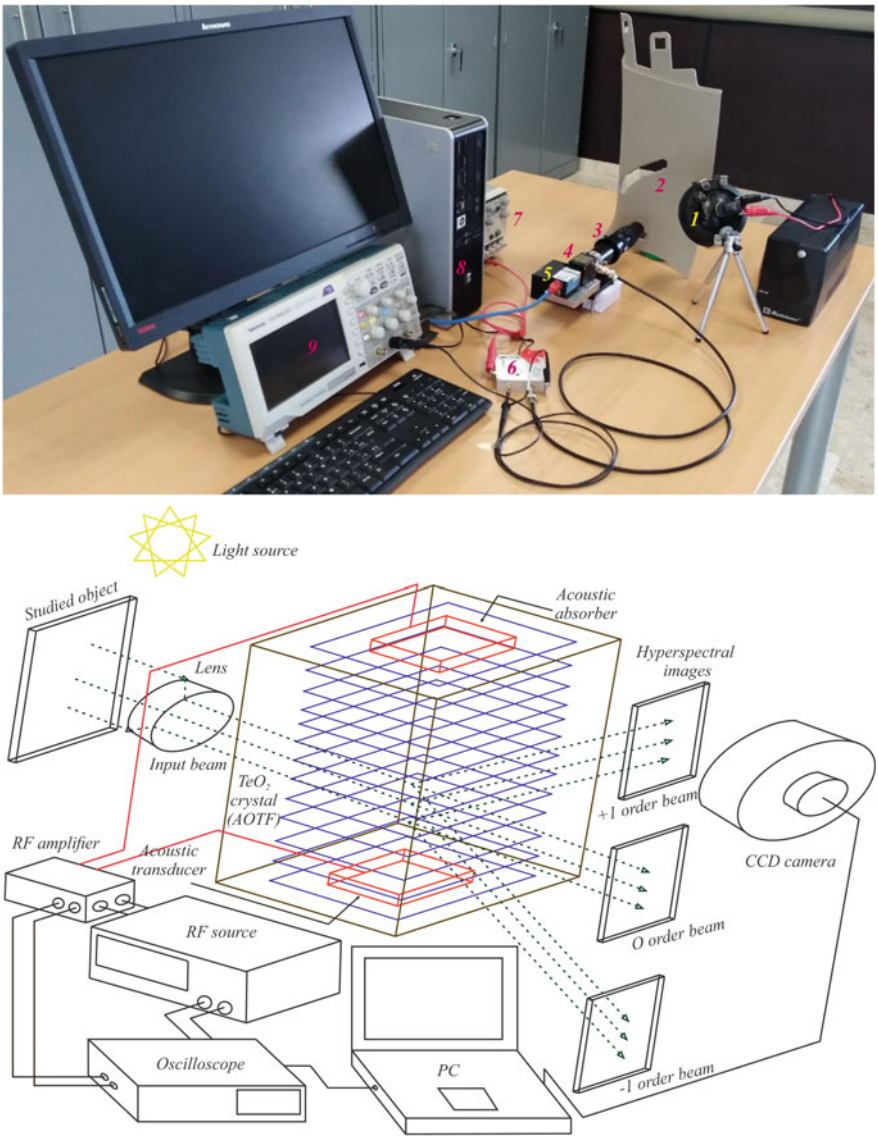

Fig. 1 Top: Experimental setup of the AOTF image acquisition system used. Components: light source (1), plastic auto-part (2), confocal optical element (3), TeO_2 crystal acoustic enclosure - AOTF- (4), CCD camera (5), RF amplifier (6), RF generator (7), computer (8), oscilloscope (9). Bottom: functioning principle simplified schematics of the AOTF-based image acquisition system employed. Light from the object gets selected in narrow wavelength bandwidths by the TeO_2 crystal while its refraction index changes according to the acoustic wave propagating through it. The control of the former is done via the computer interfaced RF generator signal sent over the transducer

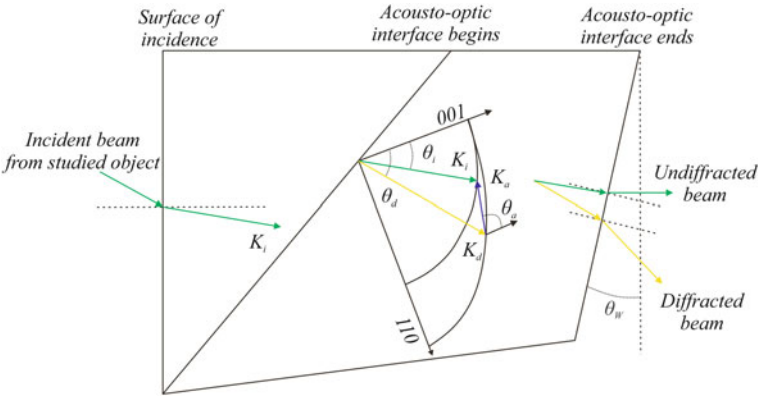

Fig. 2 Schematics of the light propagation in the acousto-optic tunable filter image acquisition system

As described in those references, the sound wave traveling through the crystal modulates its refraction index $\boldsymbol{n}$ with an spatial period equal to the sound wavelength:

$$\Lambda = \frac{u_s}{f} \tag{1}$$

where Λ, u_s, and f are the sound wave spatial period (wavelength), phase velocity, and frequency, respectively. This occurs due to the Bragg selectivity condition, which states that the diffracted light wavelength by the crystal obeys the equation:

$$\lambda = \frac{2nusin(\theta_i)}{f} \tag{2}$$

u, θ_i, and n are the sound wave's group velocity, light's angle of incidence with respect to the crystal optical axis, and integer order maximum, respectively. Momentum conservation implies that (see Fig. 2):

$$\mathbf{K}_i \pm \mathbf{K}_a = \mathbf{K}_d \tag{3}$$

where i, a, and d stand for incident, acoustic, and diffracted, respectively. θ refers to angles, and $\mathbf{K}$ refers to wave vectors. The magnitudes of those wave vectors are:

$$K_i = \frac{2\pi n_i}{\lambda_0},\ K_d = \frac{2\pi n_d}{\lambda_0},\ K_a = \frac{2\pi}{\Lambda} \tag{4}$$

λ_0 is the vacuum optical wavelength. Refraction indexes n_i and n_d can be obtained as follows:

$$n_i = n_o \tag{5}$$

Table 1 Summary of the characteristics of the AOTF image acquisition system components employed

Component	Manufacturer/Reference	Main characteristics
Light source	PLT/1X5W	12 V−5 W−33 *Lumens*
Plastic auto-part	N. A.	N. A.
Confocal optical element	TOKINA/KCM-Z	Zoom: $0.8 - 4.0\times$ Focal distance: ~ 96 mm
Enclosed AOTF	N. A./TeO_2 crystal	Range: 350–800 nm Resolution: ~ 1 nm
CCD camera	DFK/23G274 GigE	Len 2/3 Mount C
RF amplifier	Isomet/503C-3	Range: $80 - 130$ MHz Gain: ~ 36 dB
RF generator	TTi/TGR 1040	Range: $10 - 10^3$ MHz Min. Increment: 1 KHz Output amplitude: $10^{-4} - 500$ mV Output impedance: 50 Ω
Computer	HP/HP-8200 SFF-20122	Intel Core I5–8gb Memory
Oscilloscope	Instek/GDS-2072A	Range: 1 ns/div – 100 s/div

$$n_d = \left[\frac{cos^2(\theta_d)}{n_o^2} + \frac{sin^2(\theta_d)}{n_e^2} \right]^{-1/2} \tag{6}$$

n_o and n_e are the ordinary and extraordinary refraction indexes in the direction perpendicular to the crystal optical axis. Images of the +1 diffraction order will then be acquired by a CCD camera, and passed to the computer for processing. Table 1 presents a summary of the AOTF image acquisition system's main characteristics by component.

3.2 Dataset

Several experimental runs were conducted on two different plastic auto-parts under the same lighting and RF signal patterns sent into the acoustic transducer in order to drive the AOTF. For each experimental run, a different area of the auto-part was targeted by the system. That produced data acquisition under the same conditions in terms of the spectral sweep performed in all the experiments conducted. Therefore, a total of six datasets under the same conditions were obtained. In terms of lighting, during the experimental runs the laboratory was kept only with the illumination produced by the chosen light source. The RF signal generator was programmed

in order to generate frequencies directly related to wavelengths between 400 and 700 nm. The power of the signal applied directly to the acousto-optic tunable filter was of 2 W. The system was set up to acquire one spectral image per second. Thus, a full sweep over the visible spectrum was acquired in 100 s.

4 Methodology to Characterize Plastic Auto-Parts

We propose a straightforward methodology to characterize plastic auto-parts via our AOTF image acquisition system, based on the informational characteristics present in the topology of the reflectance versus wavelength curve of the plastic auto-part, obtained experimentally. The system provides us with an equally spaced spectral sweep of 100 data points over the visible range (400–700 nm). We can attempt to visualize the reflectance versus wavelength curve by means of another geometrical space whose topology allow us to both store and infer relevant information on the plastic auto-part in terms of color. Therefore, in our case data from the AOTF acquiring system comes as 100 ordered couples of wavelength versus reflectance coordinates. That is, $(\lambda_i; R_i)$: $i = 1, 2, 3, \ldots, 100$. We can use the first one as an angular coordinate via the transformation:

$$\theta_i = (\lambda_i - 400) \times (\pi/150) \tag{7}$$

That way, the spectral range of the obtained data is mapped into an angular space of $0 \leq \theta \leq 2\pi\ Rad$. As for the second one, we can use it as a radial coordinate normalized to its maximum dataset value. That is: $r_i = R_i/Max(R_i)$. We can propose also another coordinate (z_i) with a parameter closely related to color in this context, the area under the curve of reflectance versus wavelength, that is, $z_i = \int_\lambda R(\lambda)d\lambda$. Considering our datasets, it is preferable to perform this last calculation numerically (trapezoidal numerical integration was used on the non-transformed ordered couples), because it is a more direct approach than obtaining a suitable interpolation curve and then integrating it. The physical interpretation of this last coordinate for normalized reflectance would then be the fraction of electromagnetic energy reflected by the plastic auto-part along the entire visible spectrum (400–700 nm).

The new representation will then be equivalent to a discrete scalar field on cylindrical coordinates defined in such a way that its plot drawn at $z = 0$ represents the entire topological information of the reflectance versus wavelength curve of an specific plastic auto-part, which can be taken as a pattern and compared to others. On the other hand, its surface plot height ($z \neq 0$) will represent, as said, the fraction of electromagnetic energy reflected by the plastic auto-part having that specific topological (R vs. λ) signature over the entire visible spectrum. That is, $z_i = \mathcal{C}(\theta_i, r_i)$: with $z_i = \int_\lambda R(\lambda)d\lambda$. $\mathcal{C}$ stands for an hypothetical plastic auto-part "color signature" function, usable for characterization.

Figures 3, 4 and 5 show what we found for the studied auto-parts in terms of this proposed color signature representation. Each auto-part studied has a definite

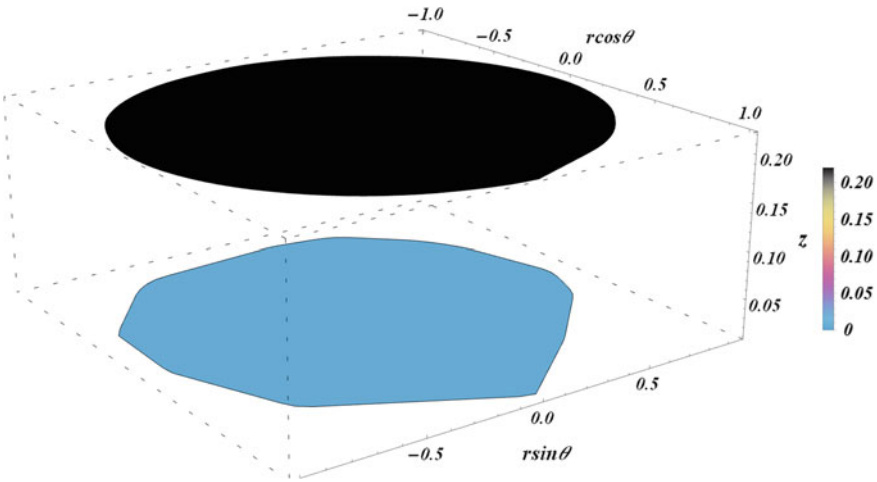

Fig. 3 Comparison of the discrete color signature functions obtained for the gray and black auto-parts used. Different colors were used to depict the ordered triplets $z_i = C(\theta_i,\ r_i)$ for each auto-part, just for visualization purposes. This image emphasizes on the differences between both signatures in terms of the (closed polygonal) shapes of their r versus θ curves, i. e., on the contour differences of those curves if their ordered couples $(\theta_i,\ r_i)$ were depicted on their respective $z = \int_{\lambda} R(\lambda)d\lambda$ planes. The color bar on the right, besides being the height of each contour, represents the fraction of the electromagnetic energy reflected by the auto-part along the entire visible spectrum sampled (400–700 nm). This means that the one depicted in blue is the black auto-part

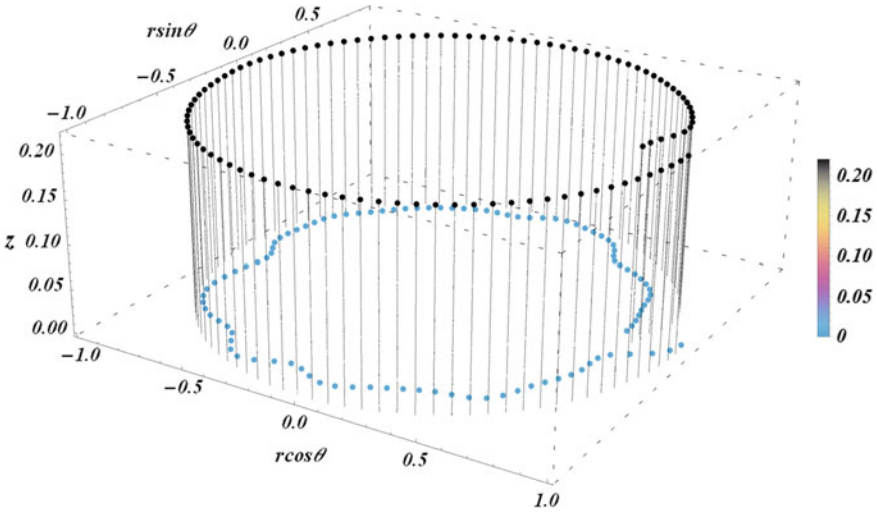

Fig. 4 Visual comparison of the discrete color signature functions obtained for the gray and black auto-parts used. Dark-gray and blue dots belong to the gray and black auto-parts, respectively

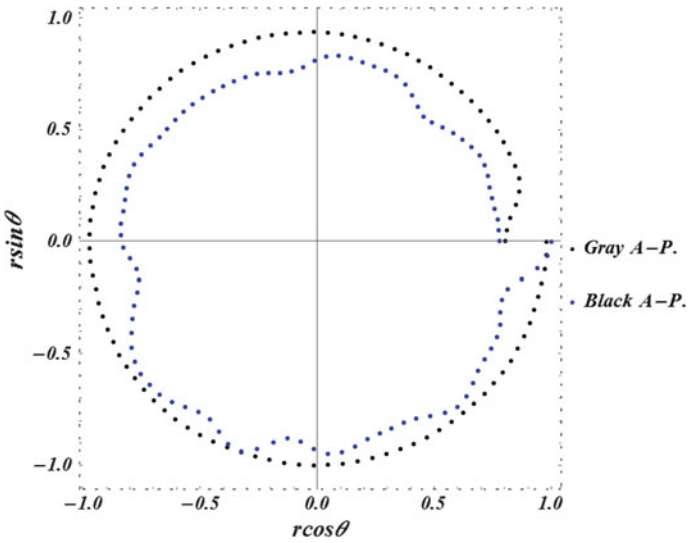

Fig. 5 2D visual comparison of the discrete color signature functions obtained for the gray and black auto-parts used without the third coordinate ($z = \int_{\lambda} R(\lambda)d\lambda$). These discrete plots represent the topological re-mapping of their respective R versus λ curves (i. e., their color signatures)

functional and geometrical representation in terms of its current color at the time of the experiments (see Fig. 5). The data gathered via the AOTF-based system provides enough information of the auto-part's R versus λ curve topology to propose a definite color signature, as described in the precedent paragraphs. That's possible due to the spectral range and resolution of the experimental sampling provided by these devices in comparison to others. Each color signature can be expressed as a distinctive color function with enough information to study its potential changes related to plastic auto-part cosmetic corrosion.

5 Experimental Results

Figures 6 and 7 present a comparison between experimental results for light reflectance on two auto-parts, black and gray in visual color, with datasets provided by a colorimeter setup operated by Centro Nacional de Metrología (CENAM, México's authority in industry-related standards and measurements), and our AOTF setup as described in Sect. 3.1. As appreciated on those figures, the data acquired by means of the AOTF system has good correspondence with CENAM's data and provides ten times more spectral information on a given auto-part. Differences in the curves for the low reflectance black auto-part can be attributed to two main factors. First, the quality of the light source used, which in the case of CENAM's data corresponds to a commercial grade colorimeter light source, introducing less noise to

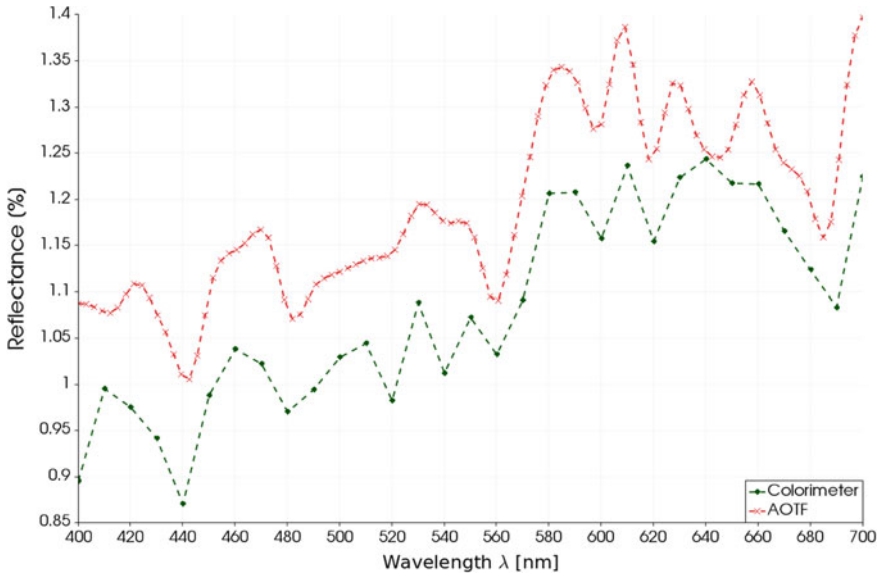

Fig. 6 Reflectance comparative for a new plastic auto-part in black color. Colorimeter and AOTF setup sample the wavelength range in 30 parts (green diamonds) and 100 parts (red crosses) respectively

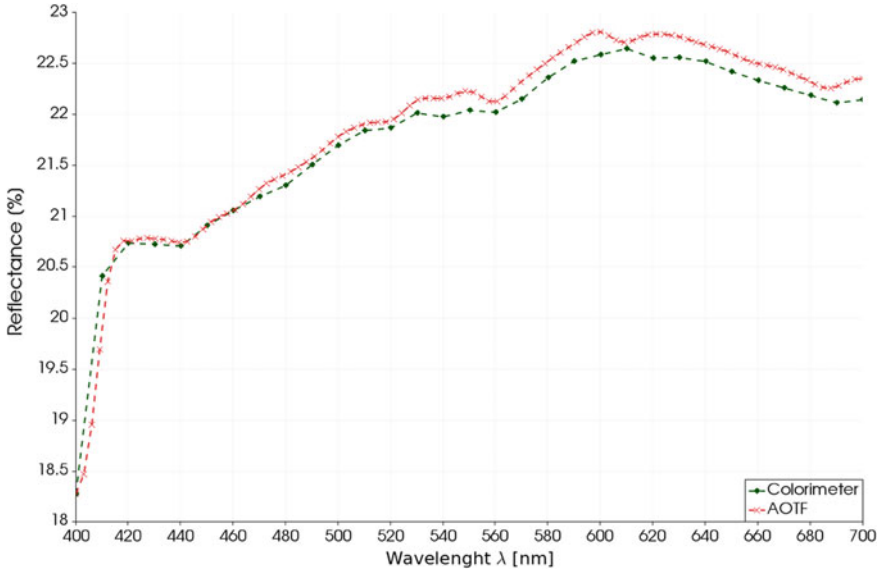

Fig. 7 Reflectance comparative for a new plastic auto-part in gray color. Colorimeter and AOTF setup sample the wavelength range in 30 parts (green diamonds) and 100 parts (red crosses), respectively

the experiments than our light source. And second, the fact that our system worked close to the limits of our CCD camera sensitivity, having this way more room to unwanted noise due to that as cause well. Nevertheless, the data clearly shows the capacity of AOTF-based systems to complement the spectral information of plastic auto-parts gathered by other means. This gives rationale to the use of these systems in the context of color study in general, and, in particular, color study related to plastic auto-part cosmetic degradation.

6 Conclusion

An AOTF-based image acquiring system was setup in order to gather hyperspectral data on plastic auto-parts. Discrete reflectance versus wavelength data on the auto-parts employed was compared to analogue data from a commercial grade colorimeter used by México's Institutional authority on measurements and standards (CENAM); showing good correspondence and complementary informational capacity on the full wide visible spectrum experimentally accessed by the AOTF system. The AOTF acquired data was then analyzed in order to propose a straightforward color signature definition of the auto-parts based on the specific topological information of their R versus λ curves coupled to their overall reflectance over the full sampled visible spectrum. A couple of examples were shown in detail. All this gives rationale to the applicability of acousto-optic dispersion data gathering into plastic auto-part color characterization.

Acknowledgements The authors would like to thank the support of this work by grant PN3967-2016 from *Consejo Nacional de Ciencia y Tecnología* (CONACYT), México, *Sistema Nacional de Investigadores* (SNI) program.

References

1. World Health Organization. Global status report on road safety 2013. Supporting a decade of action, Accessed in 1 December 2015
2. INE with data from INEGI & IHS MARKIT (2018)
3. M. Melgosa et al., Measuring color differences in automotive samples with lightness flop: a test of the AUDI2000 color-difference formula. Opt. Express **22**(3), 3458–3467 (2014)
4. O. Gómez et al., Visual and instrumental assessments of color differences in automotive coatings. Color Res. Appl. **41**(4), 384–391 (2016)
5. N.J. Berg, J.N. Lee, Acousto-optic signal processing: theory and implementation, in *New York, Marcel Dekker, Inc. Optical Engineering*. vol. 2 (1983), 496 pp. No individual items are abstracted in this volume
6. W.T. Rhodes, Acousto-optic signal processing: convolution and correlation. Proc. IEEE **69**(1), 65–79 (1981)
7. N. Gat, Imaging spectroscopy using tunable filters: a review, in *Wavelet Applications VII. International Society for Optics and Photonics*, vol. 4056 (2000), pp. 50–65

8. L.J. Denes, M.S. Gottlieb, B. Kaminsky, Acousto-optic tunable filters in imaging applications. Opt. Eng. **37**(4), 1262–1267 (1998)
9. L. Bei et al., Acousto-optic tunable filters: fundamentals and applications as applied to chemical analysis techniques. Prog. Quantum Electron. **28**(2), 67–87 (2004)
10. C.D. Tran, Principles and analytical applications of acousto-optic tunable filters, an overview. Talanta **45**(2), 237–248 (1997)
11. V.B. Voloshinov, V.Y. Molchanov, J.C. Mosquera, Spectral and polarization analysis of optical images by means of acousto-optics. Opt. Laser Technol. **28**(2), 119–127 (1996)
12. A. Korpel, Acousto-optics - a review of fundamentals. Proc. IEEE **69**(1), 48–53 (1981)
13. I.C. Chang, Tunable acousto-optic filters: an overview. Opt. Eng. **16**(5), 455–460 (1977)
14. H. Zhao et al., Field imaging system for hyperspectral data, 3D structural data and panchromatic image data measurement based on acousto-optic tunable filter. Opt. Express **26**(13), 17717–17730 (2018)
15. L. Granero-Montagud, et al., SYDDARTA: new methodology for digitization of deterioration estimation in paintings, in *Proceedings of SPIE*, vol. 8790 (2013), p. 879011
16. R. Abdlaty, et al., High throughput AOTF hyperspectral imager for randomly polarized light, in *Photonics*, vol. 5, no. 1, p. 3. Multidisciplinary Digital Publishing Institute (2018)
17. B. Zagajewski et al., Intraspecific differences in spectral reflectance curves as indicators of reduced vitality in high-arctic plants. Remote Sens. **9**(12), 1289 (2017)
18. F. Zhao et al., Simulated impact of sensor field of view and distance on field measurements of bidirectional reflectance factors for row crops. Remote Sens. Environ. **156**, 129–142 (2015)
19. J.L. Widlowski et al., The fourth phase of the radiative transfer model intercomparison (RAMI) exercise: actual canopy scenarios and conformity testing. Remote Sens. Environ. **169**, 418–437 (2015)
20. J. Liang, et al., 3D plant modelling via hyperspectral imaging, in *Proceedings of the IEEE International Conference on Computer Vision Workshops* (2013)
21. S. Liang et al., A long-term Global LAnd Surface Satellite (GLASS) data-set for environmental studies. Int. J. Digit. Earth **6**(sup1), 5–33 (2013)
22. S. Heist et al., 5D hyperspectral imaging: fast and accurate measurement of surface shape and spectral characteristics using structured light. Opt. Express **26**(18), 23366–23379 (2018)
23. W. Feng et al., 3D compressive spectral integral imaging. Opt. Express **24**(22), 24859–24871 (2016)
24. M. Kim et al., 3D imaging spectroscopy for measuring hyperspectral patterns on solid objects. ACM Trans. Graph. **31**(4), 38 (2012)
25. Z. Cherfi et al., Case study: color control in the automotive industry. Qual. Eng. **15**(1), 161–170 (2002)
26. M.K. Chao, B.P. Hake, Colorimetry applications in the automotive industry, in *Electro-Optical Instrumentation for Industrial Applications. International Society for Optics and Photonics* vol. 411 (1983), pp. 47–49
27. B. Claudé et al., Consequences of photoageing on the durability of plastic glasses for automotive applications. Polym. Test. **20**(7), 771–778 (2001)
28. T.M. Kruse, O.S. Woo, L.J. Broadbelt, Detailed mechanistic modeling of polymer degradation: application to polystyrene. Chem. Eng. Sci. **56**(3), 971–979 (2001)
29. M. Day, et al., Thermal degradation of automotive plastics: a possible recycling opportunity, in *Polymer Durability: Degradation, Stabilization, and Lifetime Prediction* (1993), pp. 47–57
30. G. Luckeneder et al., Corrosion mechanisms and cosmetic corrosion aspects of zincaluminium-magnesium and zinc-chromium alloy coated steel strip. BHM Berg-und Hüttenmännische Monatshefte **157**(3), 121–125 (2012)
31. N. LeBozec, D. Thierry, Influence of climatic factors in cyclic accelerated corrosion test towards the development of a reliable and repeatable accelerated corrosion test for the automotive industry. Mater. Corros. **61**(10), 845–851 (2010)
32. T. Prosek et al., Corrosion performance of Zn-Al-Mg coatings in open and confined zones in conditions simulating automotive applications. Mater. Corros. **61**(5), 412–420 (2010)

33. Y. Liu et al., Precipitation in an AA6111 aluminium alloy and cosmetic corrosion. Acta Mater. **55**(1), 353–360 (2007)
34. N. LeBozec, N. Blandin, D. Thierry, Accelerated corrosion tests in the automotive industry: a comparison of the performance towards cosmetic corrosion. Mater. Corros. **59**(11), 889–894 (2008)
35. B. Milligan, The degradation of automotive upholstery fabrics by light and heat. Color. Technol. **16**(1), 1–7 (1986)

Using Deep Learning to Estimate User Impressions of Designs for 3D Fabrication

Koichi Taguchi, Manabu Hashimoto, Kensuke Tobitani and Noriko Nagata

Abstract This paper proposes a method for applying three typical human impressions directly into product designs to fabricate products using 3D printers. The method automatically estimates human impressions of the three-dimensional shape of an item in terms of three representative sensibilities: "hard–soft," "flashy–sober," and "stable–volatile." This technique can be used for new 3D fabrication processes that reflect the designer's intentions directly into the shapes of products. To estimate the impressions of the shape of an object, we need to draw strong correlations between impressions, which are psychological factors, and the aspects of the shape of the object, which are physical factors. The method uses deep learning effectively to address this issue. The object being evaluated is first converted to a set of images by photographing it from 20 surrounding directions. This image set is used as input data for deep learning with parameters of human impressions of the object as supervisory signals. In experiments, we used original dataset of three-dimensional objects of a car with assigned impressions that had been quantified using the semantic differential (SD) method. The correlation coefficients between impressions estimated using this method and the supervisory signals for all the datasets were about 0.70 for "hard–soft," about 0.61 for "flashy–sober," and about 0.67 for "stable–unstable."

K. Taguchi (✉) · M. Hashimoto
Chukyo University, 101-2 Yagoto Honmachi, Showa-ku, Nagoya-shi 466-8666, Aichi, Japan
e-mail: taguchi@isl.sist.chukyo-u.ac.jp

M. Hashimoto
e-mail: mana@isl.sist.chukyo-u.ac.jp

K. Tobitani · N. Nagata
Kwansei Gakuin University, 2-1 Gakuen, Sanda-shi 669-1337, Hyogo, Japan
e-mail: tobitani@kwansei.ac.jp

N. Nagata
e-mail: nagata@kwansei.ac.jp

A. Martínez-García et al. (eds.), *Progress in Optomechatronic Technologies*,
Springer Proceedings in Physics 233, https://doi.org/10.1007/978-981-32-9632-9_8

1 Introduction

Various kinds of three-dimensional printers have been developed, and their cost has decreased. Thus, we can now use them not only in factories but also at home. Furthermore, a useful database of three-dimensional models has been prepared, and everyone can utilize it via the Internet. "Personal fabrication (production using three-dimensional printers by individuals)" will likely change the traditional way of manufacturing by mass production at factories. Enabling "personal fabrication" will require skillful modeling techniques using CAD systems to make the desired three-dimensional objects. However, not everyone has such skills. Therefore, we propose a method for using impression factors to provide support in modeling complex three-dimensional objects. To design a shape of models based on impressions, we need to associate the impressions and shape of three-dimensional models. As such, we propose a method for estimating human impressions of an object to be used in supporting such modeling technologies like an expert of CAD.

Normally, we would consider that impressions of an object would be determined holistically based on shape, color, and material, but for this research, we have assumed that the shape as a dominant factor in determining the impressions of objects based on a method from Tobitani et al. [1]. We also defined three types of impressions of objects as particularly important: "hard–soft," "flashy–sober," and "stable–unstable."

Taguchi et al. [2] calculated the relationship between features and impressions using multiple regression analysis. However, it can be used only for the "hard–soft" impression factor because the features have been optimized for a specific impression. Designing which features and classifiers to optimize for various impressions is difficult. In this research, we propose a method to estimate impressions of "hard–soft," "flashy–sober," and "stable–unstable" automatically using a deep neural network (DNN) for only the shape of a three-dimensional model. Two types of convolutional network (CNN) are used currently in the field of object classification. One type is multi-view architectures, while the other is volumetric architectures. Qi et al. [3] analyzed the challenges of object classification on three-dimensional data using these two types of CNNs. As a result, the multi-view CNN architectures were proven to be more accurate than volumetric in object recognition. In addition, a person can only recognize an object from a certain viewpoint, one at a time. Therefore, we use a multi-view CNN architecture to estimate impression factors in this method.

The remainder of this paper is organized as follows. The quantification of impression factors to the objects is described in Sect. 2. The proposed method to estimate the impression factors is presented in Sect. 3. Experimental results and analysis are provided in Sect. 4. Finally, the conclusion and discussion are given in Sect. 5.

Table 1 Various bipolar adjectives (impression factors)

Bipolar adjectives (impression factors)	
ordered–chaotic	connected–disconnected
stable–unstable	dynamic–static
active–passive	healthy–unhealthy
excitable–calm	relaxed–tense
soft–hard	smooth–rough
distinct–vague	weak–strong
blunt–sharp	intense–mild
delicate–rugged	cheerful–cheerless
flashy–sober	heavy–light

2 Quantification of Impression Factors

The relationship between impression factors and three-dimensional shape needs to be clarified in order to enable intuitive manipulation of three-dimensional shapes using an impression. Tobitani et al. [1] defined the rating scale for three-dimensional shapes using the semantic differential method to quantify sensitive bipolar adjectives (impression factors). The average values of 10 people were calculated in the SD method for every 18 bipolar adjectives. The 18 bipolar adjectives for this experiment are shown in Table 1.

In this experiment, conditions such as background, materials, lighting, and so on were kept constant, and the range of impression coefficients was −3.0 to 3.0. We analyzed using major factor analysis (PFA) and Varimax rotation. According to the literature, the impression coefficients of the three-dimensional shape can be expressed by three bipolar shapes: "hard-soft," "flashy-saw," and "stable-unstable." The experimental dataset was abstract objects manufactured by a professional designer. When generating these three-dimensional shapes, the bipolar adjectives mentioned above were presented as guidelines for shape design. Therefore, we focused on these most relevant impression factors for the three-dimensional shapes.

3 Impression Estimation Method

The flow of our method is shown in Fig. 1.

Our method uses a deep learning convolutional network with multi-viewpoint images to estimate human impressions of three-dimensional object. This method includes both the learning and estimation modules. The method is assumed to have supervised learning, so the three-dimensional models and ground-truth (impression factors) need to be made to correspond. In the learning module, we used the semantic differential (SD) method [4] to estimate values for the impressions of each object, and we used these values as supervisory signals. Incidentally, they are based on the

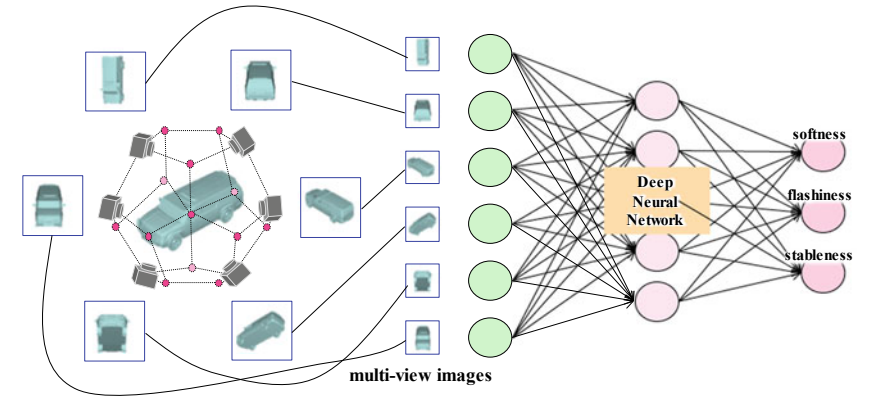

Fig. 1 Flow of our method for estimating impression factors

contents of Sect. 2. The input data for the network were the multiple images taken across viewpoints. Figure 2 shows an example of virtual viewpoints set around a three-dimensional object.

The multi-view images represent three-dimensional shapes using multiple views of three-dimensional objects that were generated by rendering. The virtual viewpoints of plurality were installed around the objects. In this study, the input data consisted of a set of images of the objects taken from 20 directions spaced equally around them. Therefore, the input data were grayscale images taken from 20 viewpoints. Here, an area in which a three-dimensional model did not exist was defined as the background and supplemented with a numerical value. The network consisting of impression estimations was achieved using this image set as the input for deep learning and the training to minimize the difference between the estimated results and the supervisory signals. However, in our method, there is a scale invariance due to transformation of

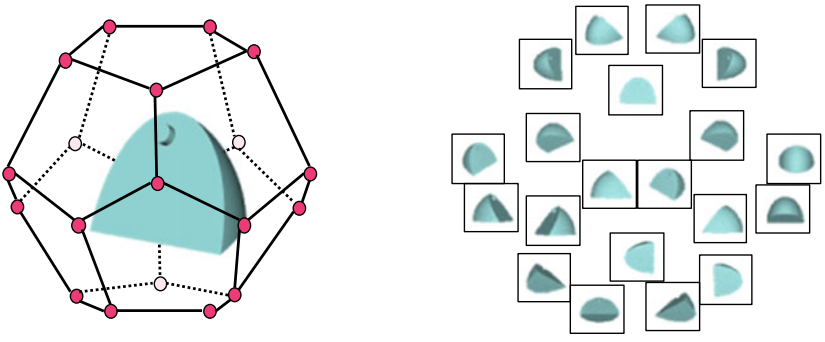

Fig. 2 Virtual viewpoints set around a three-dimensional object and the rendered images

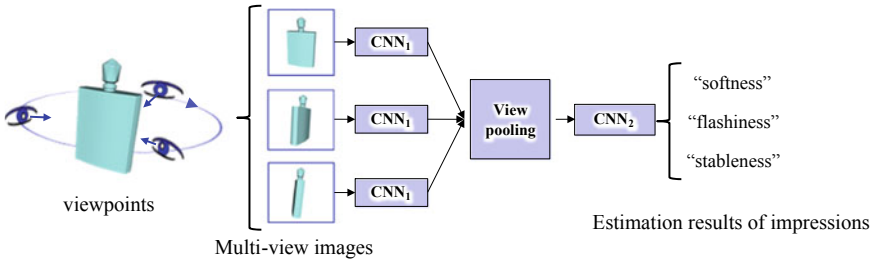

Fig. 3 Constitution of the network

three-dimensional objects to multi-view images. Therefore, we unified the size of the three-dimensional object presented to the subject when quantifying the impression of a person with respect to a three-dimensional object by SD method [4]. The network is shown in Fig. 3.

Our method consists of two stages: the first stage is with five convolutional layers and three pooling layers and the second stage is with a view-pooling layer, which integrated the multi-viewpoint image, and three fully connected layers. The error function used was softmax, and the optimization method used was Adam [5].

4 Experimental Results of Impression Estimations

In our experiments, we used the SD method [3] to associate supervisory signals with three-dimensional objects. For the objects, we used ModelNet40 [6] in specific classes: a car, vase, and chair. Each three-dimensional object was evaluated by 20–40 people, and the −3 to 3 was used for the supervisory signals. In the experiments, the proposed method was evaluated using correlation coefficients. The experimental datasets were evaluated using 20 three-dimensional objects randomly. Figure 4 shows two distributions of relationships between the estimated results and the supervisory signals. The blue dots represent the results of the previous method, and the red dots

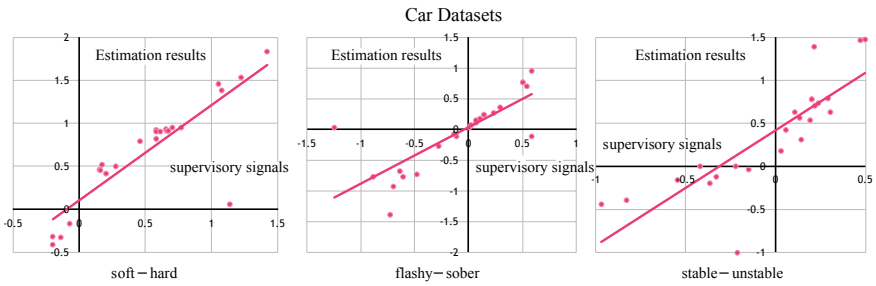

Fig. 4 Relationships between the estimated results and supervisory signals

Table 2 Correlation coefficients between estimation results and supervisory signals

Datasets	Correlation coefficients for impressions		
	Hard-soft	Sober-flashy	Unstable-stable
Car	0.70	0.61	0.67

represent the results of our new method. Also, Table 2 shows the estimation results and correlation coefficients of the supervisory signals.

The supervisory signal in Fig. 4 is an average value evaluated by 20–40 people. The correlation coefficients between impressions estimated using this method and the supervisory signals for all the datasets were about 0.70 for "hard–soft," about 0.61 for "flashy–sober," and about 0.67 for "stable–unstable." As a result, the proposed method confirmed a strong correlation with each impression. When we analyzed three-dimensional objects with large difference between estimate results and supervisory signals, the variation in supervisory signals for the three-dimensional object was large.

5 Conclusion

We proposed a method for automatically estimating three typical human impression factors, "hard–soft," "flashy–sober," and "stable–unstable," which were obtained from objects by analyzing the shapes of three-dimensional models. The results of the experiment show that the correlation coefficients between the impressions estimated using this method and the supervisory signals for the original datasets of car used were about 0.70 for "hard–soft," about 0.61 for "flashy–sober," and 0.67 for "stable–unstable."

In future work, we will clarify the impression structure of people and estimate using the RGB image, because our method cannot consider the texture and material.

Acknowledgments This research was partially supported by the Center of Innovation Program from the Japan Science and Technology Agency, JST.

References

1. K. Tobitani, S. Akizuki, K. Katahira, M. Hashimoto, N. Nagata, A comparison study on 3D features in terms of effective representation for impression of shape, in *The 2nd International Conference on Digital Fabrication*, No. 22 (2016)
2. K. Taguchi, K. Sasaki, M. Hashimoto, K. Tobitani, N. Nagata, A proposal of 3D local feature for estimating human's impression factor to shape of object, in *International Workshop on Advanced Image Technology* (2017)
3. C.R. Qi, H. Su, M. Niesner, A. Dai, M. Yan, L.J. Guibas, Volumetric and multi-view CNNs for object classification on 3D data, in *IEEE Conference on Computer Vision and Pattern Recognition* (2016)

4. C.E. Osgood, G.J. Suci, P.H. Tannenbaum, *The Measurement of Meaning* (University of Illinois Press, Oxford, England, 1957)
5. D.P. Kingma, Adam: a method for stochastic optimization, in *International Conference on Learning Representations* (2015)
6. Z. Wu, S. Song, A. Khosla, F. Yu, L. Zhang, X. Tang, J. Xiao, 3D ShapeNets: a deep representation for volumetric shapes, in IEEE *Conference on Computer Vision and Pattern Recognition* (2016), pp. 1912–1920

Mr. Koichi Taguchi received his B.E. degree from Chukyo University, Aichi, Japan, in 2017. He is now a graduate student of the university and is very interested in technologies about object recognition and its application to sensitivity information processing. He is a member of the Japanese societies of IPSJ Japan and JSPE.

Manabu Hashimoto received his B.E. and M.E. degrees from Osaka University, Osaka, Japan, in 1985 and 1987. He joined the Mitsubishi Electric Corporation in 1987, and he has been engaged in research on robot vision, image recognition, pattern recognition, and human sensing in the Manufacturing Development Laboratory, Industrial Electronics and Systems Development Laboratory, and the Advanced Technology R&D Center of the company. He received his Ph.D. degree from Osaka University in research on 3-D object recognition in 2000. Since 2008, he has been a professor of Chukyo University, and he is the Dean of the School of Engineering. He received the Technical Innovation Award in 1998 from the Robotics Society of Japan, the Excellent Academic Award in 2012 from the Symposium on Sensing via Image Information, and the Best Paper Award of IWAIT2017 and IWAIT2018. He is a member of the IEEE and Japanese societies of IEICE, IPSJ, IEEJ, and RSJ, among others.

Kensuke Tobitani received his doctoral degree in engineering from Gifu University, Japan, in 2009. He is currently a lecturer at Kwansei Gakuin University. His research interests include computer vision, computer graphics, and Kansei information processing.

Noriko Nagata received her BS degree in mathematics from Kyoto University in 1983 and her Ph.D. degree in systems engineering from Osaka University in 1996. She was a researcher at the Industrial Electronics and Systems Laboratory of Mitsubishi Electric Corporation from 1983 to 2003. She joined Kwansei Gakuin University in 2003 as an associate professor. She is currently a professor in the Department of Human System Interaction and a director of the Research Center for Kansei Value Creation. In 2009, she was a visiting scholar at Purdue University. Her research interests include Kansei (affective) information processing, computer graphics, and multimedia systems. She is a member of the IEEE and ACM.

Classification of Electromagnetic Spectrum in the Visible Range Using Machine Learning

Gonzalo Vargas, Jose A. González and Mauricio Ortiz

Abstract Spectrophotometers are instruments that measure parameters of samples as a function of the wavelength and work with a source of broad spectrum light a diffractive element and a detector. Those instruments are widely used in chemistry, physics and medicine labs, among others. The design of a spectrophotometer in the visible range of the electromagnetic spectrum is presented in this work and consists of a white LED, a holographic grating and a Samsung camera as a detector; the spectrum generated by placing a liquid sample in the spectrophotometer is analyzed by three different artificial intelligence algorithms: artificial neural networks (ANNs), convolutional neural networks (CNNs), and support vector machines (SVMs). These types of algorithms are part of the machine learning techniques that are used to solve classification and regression problems, for example, facial and speech recognition, efficient searching engines and medical diagnostic, among others. In this manuscript, these algorithms were implemented to determinate which one is the best to classify the samples, considering the accuracy and execution time.

1 Introduction

UV-Vis spectrophotometer uses UV radiation from 80 to 400 nm and visible light from 400 to 800 nm to determine some properties of samples, such as absorbance, transmittance and reflectance, among others. For instance, the spectrum of the substance can be obtained by scattering, using a diffractive element, usually, a holo-

G. Vargas (✉) · J. A. González
Laboratorio de Inteligencia Artificial y Supercomputo, Instituto de Física y Matemáticas, Universidad Michoacana de San Nicolás de Hidalgo, Morelia, Mexico
e-mail: gvargas@ifm.umich.mx

J. A. González
e-mail: gonzalez@ifm.umich.mx

M. Ortiz
Facultad de Ciencias Físico-Matemáticas, Universidad Michoacana de San Nicolás de Hidalgo, Morelia, Mexico
e-mail: mortiz@yahoo.com

A. Martínez-García et al. (eds.), *Progress in Optomechatronic Technologies*,
Springer Proceedings in Physics 233, https://doi.org/10.1007/978-981-32-9632-9_9

graphic diffraction grating and then the Beer–Lambert equation [1] can be used to determine the concentration of the sample by its absorbance. Instead of this approach, we study the relationship between the spectra and the concentration of the sample using machine learning methods.

Conventional computing is characterized by developing a mathematical formation of the problem, obtaining an algorithm to implement a solution, coding the algorithm for a specific problem, and finally executing that code. As it has been observed, this process is very successful in solving and simulating complex mathematical models and to perform repetitive, fast and well-defined tasks. Machine learning is part of artificial intelligence that focuses on developing techniques that allow computers to "learn" [2]; this learning process occurs through programs capable of generalizing behaviors from information provided in the form of examples. Therefore, it is an induction process of knowledge. There are different algorithms within machine learning such as decision trees, genetic algorithms, artificial neural networks, convolutional neural networks, support vector machines, among others. Computations based on machine learning are characterized by being massively parallel, adaptive, highly interconnected, and tolerant to noise. In general, neural networks and support vector machines have been used in applications in the area of € image processing and computational vision [3], specifically in pattern recognition analysis. In this manuscript, we implement artificial and convolutional neural networks and support vector machines in order to determine which of these is the best algorithm to classify the concentration of the samples with the best accuracy and with the minimum execution time.

2 Experimental Method

Standard spectrophotometers focus the polychromatic light of the source in a monochromator. The monochromator has, as the main components an input slot, an element to scatter light in its composition by wavelengths, and an output slot which allows the user to select the desired wavelength. That monochromatic light goes through the sample and reaches the detector. Photometric measurements are made based on the relationship between the intensity of the light reaching the detector when the sample is interposed and when it is not. Based on the basic design of a spectrophotometer, an optical array is shown in Fig. 1. It was designed to obtain the spectrum of some samples, described below, which consist of an LED extracted from a Philips model 92900II237, a holographic grating of 930 lines/mm located at 58° with respect to the LED (this angle was selected by the characteristics of the grid [4]), and a Samsung camera of 14 MP.

The substances to be analyzed are water with green vegetable dyes at 1.78%, blue at 2%, and red at 2% of the McCormick brand. For these samples, we dilute the original dyes in water, with a relation of 1.25 mL of dye per 500 mL of water. After that, the variation in concentration was the following; the highest concentration is only the diluted dye with a total volume of 3000 μL, the next sample is constructed

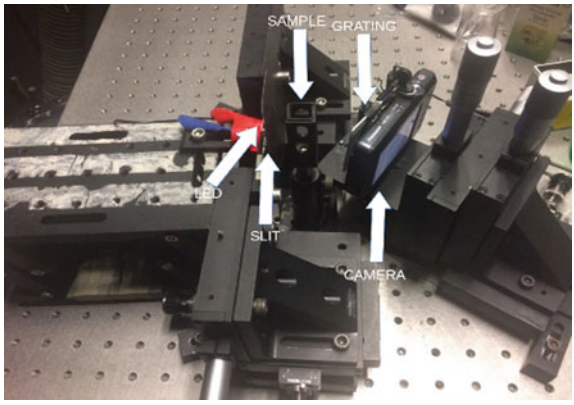

Fig. 1 Shows the experimental arrangement to obtain electromagnetic spectrum

removing 20 μL of the vegetable dye and replacing it with the same amount of water. For every 10 samples, the amount of dye replaced was 50 μL instead of 20 μL. Fifty samples were produced per color obtaining a total of 150 samples with different concentrations. For future references, the highest concentration of dye will be called sample number 50 while the lowest concentration will be called number 1. One of the spectrums obtained with this arrangement is shown in Fig. 2.

The next step is to quantify if the variations in the samples are perceptible for a calibrated instrument. For this reason, all the samples were analyzed with the Perkin-Elmer λ-35 spectrophotometer of the optics laboratory to study the behavior of the transmittance. Some ratios of the transmittance with respect to wavelength obtained by the spectrophotometer are shown in Fig. 3.

Once the image information was obtained and analyzed by a calibrated instrument, the classification of the samples was carried out in relation to their color and concentration with three different classification algorithms which use machine learning (ML) techniques: artificial neural networks (ANN), convolutional neural networks

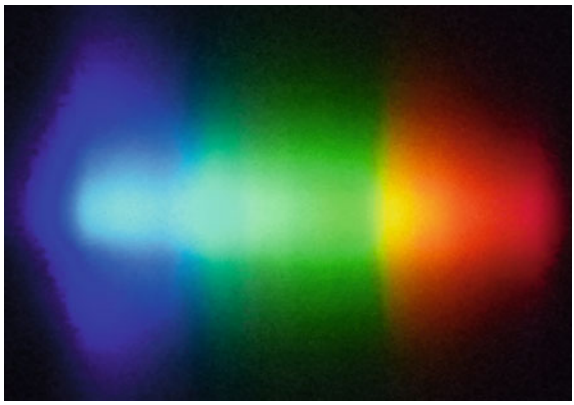

Fig. 2 Shows one of the one hundred and fifty samples obtained with the arrangement shown in Fig. 1

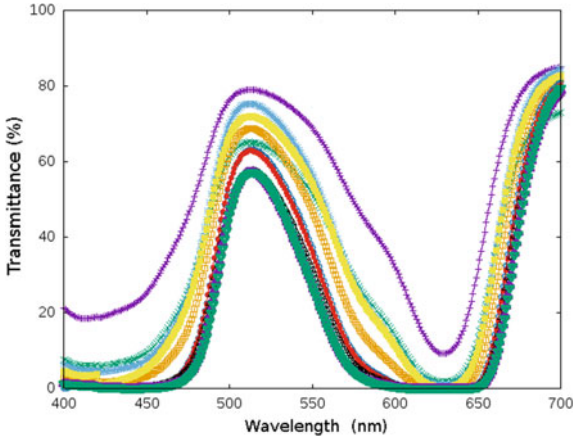

Fig. 3 Ratio between the transmittance versus wavelength obtained with the Perkin-Elmer l-35 spectrophotometer

(CNN), and support vector machines (SVM). These algorithms are described in the next section.

3 Classification Methods

ML algorithms use computational methods to "learn" directly from databases without requiring a certain equation as a model, this learning process is known as training [2]. The adaptability of the algorithms improves as the number of samples for training increases. These models can be used to solve regression or classification problems [2]; in this work we will talk about ML methods to solve classification problems; A classification problem consists of associating an input to a category (from two or more categories), which contains elements that have similar characteristics; these categories are called classes.

The artificial and convolutional neural networks were programmed in the Google platform called TensorFlow [5] while the algorithm for vector support machines was developed using LIBSVM library [6].

3.1 Artificial Neural Networks

The design of artificial neural networks is based on the behavior of biological neural networks. An ANN can be defined as a nonlinear function that converts an input into a given output. The exact form of the transformation is governed by a set of parameters called weights whose value can be determined based on a set of examples. The process of determining the values for the parameters is often called learning, and it can be a

computationally intense task [7]. However, once the weights are set, the data can be processed quickly by the network.

An ANN consists of layers of neurons fully connected to each other to assign the inputs with predetermined outputs; the intermediate layers of neurons are called hidden layers. The network is trained by iterative modifications on the weights [7] that interlace the layers in order to map the inputs to a correct output. A basic model of an ANN is shown in Fig. 4.

In this work, the input data will be arranged such as the one shown in Fig. 5. To obtain this arrangement, it is necessary to know that the images that were obtained are in RGB format; this means that each image consists of three channels, (one for each color, red, green, and blue). These channels, that can also be thought of as matrices, were averaged to obtain a grayscale image. After this, the resulting image was reduced in width by a total of 300 pixels to finally average it in its height; the result is shown in Fig. 5.

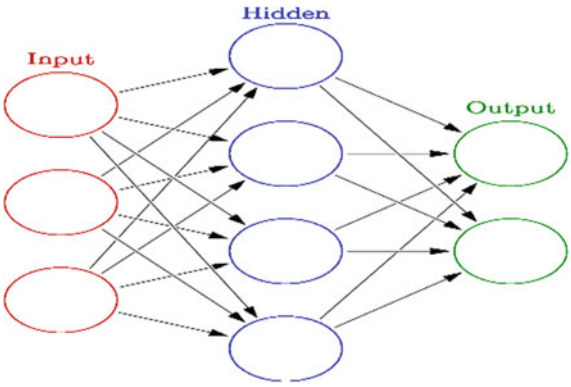

Fig. 4 Basic structure of a simple ANN

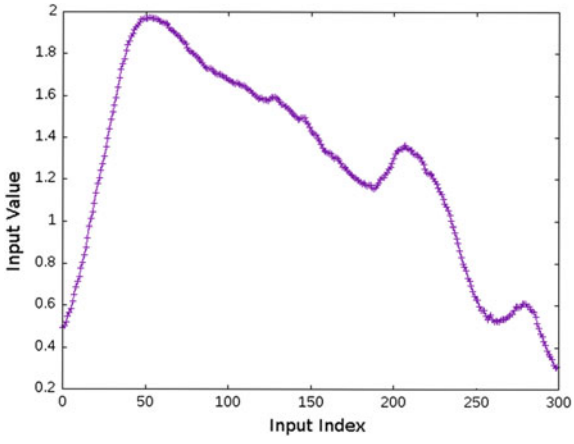

Fig. 5 Input data for the artificial neural network

The network has the purpose to classify the images by their color and concentration. With this in mind, three ANNs were built: the first to perform the classification by color and the other two to classify by the concentration. Therefore, in the first ANN, the output will be obtained by three neurons representing the three different colors. For the concentration, two ANNs were constructed and trained to quantify the capacity of the algorithms to recognize two variations in the concentration; the first one will try to identify variations of 50 mL and the second variations of 20 mL in the concentration. With this in mind, the first ANN has five neurons in the output layer, representing the variations of 50 mL for every 10 samples, whereas the second ANN has 10 neurons in the output layer.

Once the inputs and outputs of the network are obtained, we need to figure out the rest of the network configuration, i.e., how many hidden layers and how many neurons per hidden layer will be implemented. For this, we use the cross-validation method [8]. There are several free parameters to perform the implementation of networks, so our approach consists of leaving the number of hidden layers fixed to three and varyingthe number of hidden neurons. Table 1 shows the configurations of the network and Fig. 6a shows the cross-validation results for the first classification in the

Table 1 Relationship between the network configuration and the result obtained during the cross-validation

Color	First layer	Second layer	Third layer
Purple	100	100	100
Green	250	100	100
Sky Blue	250	250	100
Orange	250	250	250
Yellow	500	250	250
Dark Blue	500	500	250
Red	500	500	500

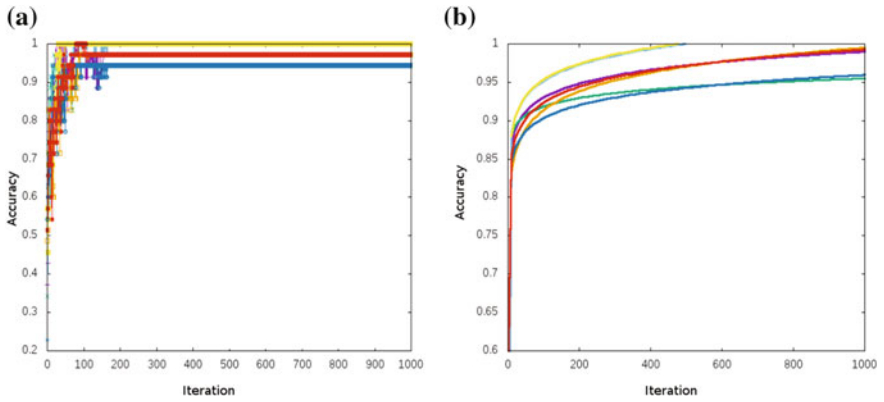

Fig. 6 **a** Results of the cross-validation for an ANN. **b** Fits of the curves presented in (**a**) by logarithm functions

concentration for the blue color. The same process is carried out for the classification by color and for the other classifications in the colors by concentration. Finally, in order to determine which one is the best configuration, we use a logarithmic fit as the one shown in Fig. 6b.

3.2 Convolutional Neural Networks

CNNs work like the ANNs, by dividing their computational processes by layers. While the ANNs process the information using hidden layers, the CNNs perform the input propagation by three different layers: the first one, known as the convolution layer, the second one called the pooling layer, and the last one is known as the fully connected layer [9].

It is known that CNNs have great efficiency when processing a big quantity of information contained in the input data, for instance, they have better results during image classification problems. However, the images of the spectra obtained in our case (see Fig. 2), have dimensions of 980 by 860 pixels; therefore, analyzing this information would require a very large number of operations for each processing layer. To avoid this problem, the images were reduced to a size of 28 by 28 pixels as shown in Fig. 7, it shows that the structure of the image is not affected.

The classification that is intended to be done with the CNNs is the same as with the ANNs, so the outputs that represent the classes are the same, that is, three output neurons for the classification by color, five for the first classification by concentration and 10 for the second classification. As we did for the ANNs, we have chosen the best configuration for CNN using cross-validation. For instance, how many layers of convolution and pooling are required? Or which is the size and the number of filters in the convolution layer? We decide to maintain two layers of convolutions and two

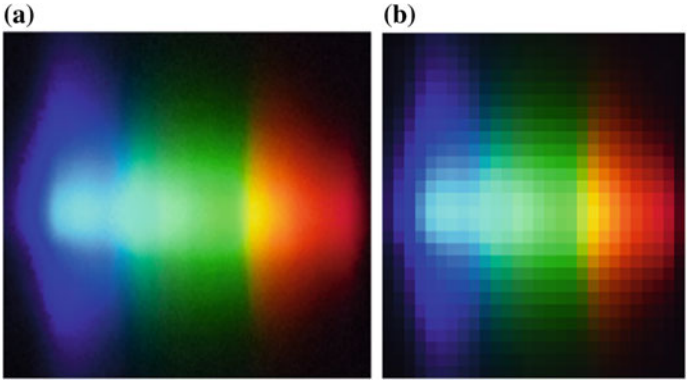

Fig. 7 Reduction of the images for the CNN input, **a** original size image (980 by 869 pixels) and **b** the down-sampled image (28 by 28 pixels)

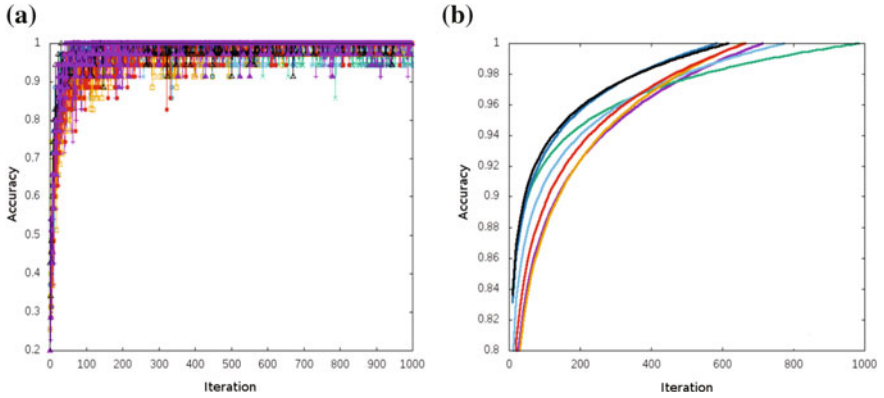

Fig. 8 **a** Result of the cross-validation for a CNN and **b** the adjustment of the curves using a logarithm fit

Table 2 Relationship between the convolutional layer configuration and the colors shown in Fig. 8

Color	Filter size	Number of filters in the first layer	Number of filters in the second layer
Purple	3×3	24	58
Green	5×5	24	58
Sky Blue	7×7	24	58
Orange	3×3	32	64
Yellow	5×5	32	64
Dark Blue	7×7	32	64
Red	3×3	40	70
Black	5×5	40	70
Mousse	7×7	40	70

layers of pooling while the quantity and size of the filters are determined with the cross-validation. The results on the first classification in the concentration for the blue color are shown in Fig. 8. Table 2 shows the dependence on the results and the configuration of the CNN using the colors presented in Fig. 8. The same procedure was carried out for the other classifications.

3.3 Support Vector Machines

The last classification algorithm we will use is the support vector machines (SVMs) which aim to solve a classification problem as shown in Fig. 9. The way the SVMs classify a 2D linear separable problem is by selecting a straight line that separates

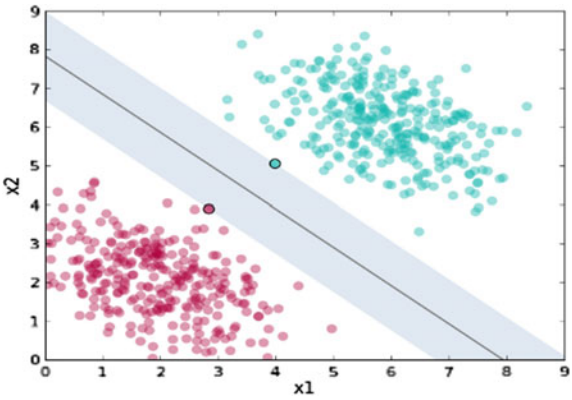

Fig. 9 Example of how a class plane can be selected with an SVM

the elements into two classes: green and red. To determine which is the best line that separates the data, the criterion of maximum distance between the line and the points is used. In general, this leads to a problem of quadratic optimization [10].

When the problems are complicated and are not linearly separable, SVMs work in a larger dimensional space, projecting the data using nonlinear functions in such a way, that the problem can be solved in a linear way in the new space. In those cases, the straight lines are hyperplanes and the dimensionality of the space is increased using nonlinear functions. In order to solve the quadratic optimization problem of the hyperplane, it is only necessary to define the norm in the final space, this is known as kernel. The most used kernel is the radial base function kernel (RBF) whose expression is

$$\mathbf{K}(\mathbf{x}, \mathbf{z}) = \exp\left(-\gamma \|\mathbf{x} - \mathbf{z}\|\text{^}2\right)$$

where **x** and **z** are points in the original space. This kernel is used in the classification of our images.

The inputs and outputs used in this case will be the same as the ones used for the CNNs, taking advantage that these type of algorithms support a large number of elements in the input data. As before, it is necessary to determine which parameters are ideal for the SVM. The parameters to be determined are the constant g of the RBF kernel and a constant in the optimization of the hyperplane named C. Again, the method used to determine these parameters is cross-validation. The results for the first classification on the concentration for the blue color are shown in Fig. 10. Each color represents an accuracy corresponding to a combination of values of g and C. The same procedure was carried out for the other classifications.

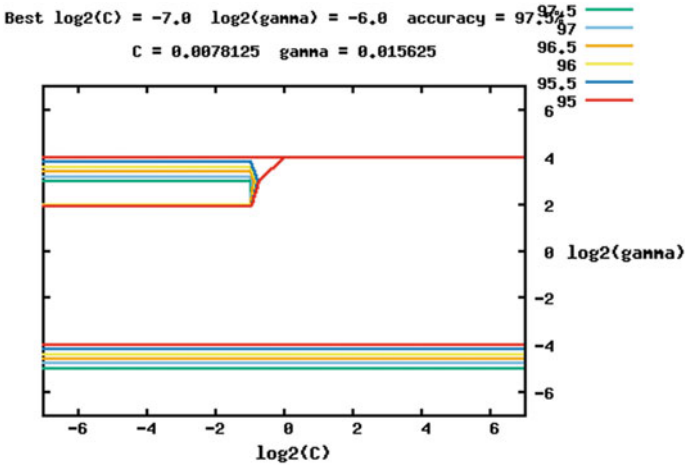

Fig. 10 Cross-validation to select the best values of g and C for the SVM

4 Results and Conclusions

Once the cross-validation was done to determine the optimal configurations for all the classification algorithms, the next step was to carry out the training. The best configurations for the algorithms are shown in Table 3. Finally, the results of the accuracy achieved with each algorithm for the different classifications are shown in Table 4. The accuracy achieved by the neural networks was estimated considering the logarithm fit, as shown in Figs. 6 and 8.

In order to decide which method is better, instead of using classification accuracy, we consider the computational time used during the cross-validation or during the training. With that criterion, the SVM takes advantage due to the shorter time required in both processes. Another important advantage of using SVMs is that when they are

Table 3 Optimal configuration for each algorithm in the classifications made

Classification	ANN	CNN	SVM
Colors	100 per layer	Size 7 × 7—24—58	$\gamma = 0.25$ $C = 0.25$
F.C.[a] Blue Color	250 per layer	Size 5 × 5—40—70	$\gamma = 0.015625$ $C = 0.0078125$
F.C. Red Color	250 per layer	Size 7 × 7—24—58	$\gamma = 1.0$ $C = 0.0625$
F.C. Green Color	250—250—50	Size 3 × 3—40—70	$\gamma = 0.015625$ $C = 0.0078125$
S.C.[b] Blue Color	100 per layer	Size 7 × 7—40—70	$\gamma = 0.0625$ $C = 0.0078125$
S.C. Red Color	250—250—50	Size 7 × 7—24—58	$\gamma = 0.0625$ $C = 0.0078125$
S.C. Green Color	250—250—50	Size 3 × 3—40—70	$\gamma = 0.0078125$ $C = 8.0$

[a]First Classification by Concentration
[b]Second Classification by Concentration

Table 4 Accuracy achieved with each algorithm for the different classifications

Classification	ANN (%)	CNN (%)	SVM (%)
Colors	100	100	100
F.C.[a] Blue Color	100	100	100
F.C. Red Color	80	100	100
F.C. Green Color	100	70	90
S.C.[b] Blue Color	50	80	80
S.C. Red Color	90	100	80
S.C. Green Color	70	60	70

[a]First Classification by Concentration
[b]Second Classification by Concentration

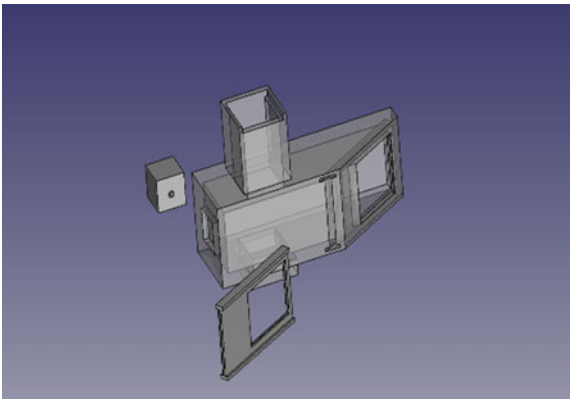

Fig. 11 Design of the device created to obtain images of electromagnetic spectrums more efficiently

implemented with the LIBSVM library executables, the algorithms can be applied not only to python but also to Java or MatLab. Under these criteria, the SVM was chosen as the best option to deal with this problem.

In the literature, an analysis for the determination of the concentration of a substance using artificial intelligence has not been carried out to date. For this reason, a device was constructed, shown in Fig. 11, which will allow obtaining electromagnetic spectra in a faster and more efficient way. A greater number of samples will help improve the algorithms for classification by increasing the number of elements with which the training and prediction process will be carried out.

It is important to mention that the minimum efficiency required by the industries to buy equipment at a global level is approximately 98%, efficiency that was almost obtained for all the colors in the first classification by concentration. By being able to obtain spectra quickly and efficiently, using the designed device, a greater variation in the concentration orders could also be made to take the algorithms to the limit and determined in which variation of concentration we obtain the best results for each algorithm. On the other hand, a combination of algorithms for classification could also be the solution to reach the minimum efficiency required to market our

spectrophotometer design. Based on the results shown, there is no doubt that the algorithms developed in conjunction with a device will be sufficient to help determine the concentration of a particular substance in the future.

Acknowledgements This research is partially supported by grant CIC-UMSNH-4.23. The authors also thank ABACUS Laboratorio de Matemticas Aplicadas y C´omputo de Alto Rendimiento del CINVESTAV-IPN, grant CONACT-EDOMEX-2011-C01-165873, for providing computer resources.

References

1. J. Luis Sánchez-Milln et al., Espectroscopía Raman: Herramienta rápida y no invasiva para determinar carotenoides en inflorescencias de Tagetes erecta L. Agrociencia **41**(8) (2007)
2. C.M. Bishop, *Pattern Recognition and Machine Learning* (Inc. Secaucus, NJ, USA, 2006)
3. R.J. Schalkoff, *Artificial Neural Networks*, vol. 1 (McGraw-Hill, New York, 1997)
4. E. Loewen, C. Palmer, *Diffraction Grating Handbook* (Newport Corporation, 2005)
5. M. Abadi et al., *TensorFlow: large-scale machine learning on heterogeneous systems*. Software available from https://www.tensorflow.org (2015)
6. C.-C. Chang, LIBSVM: a library for support vector machines. ACM Trans. Intell. Syst. Technol. **2**(3), 1–27 (2011). Article no. 27. http://www.csie.ntu.edu.tw/cjlin/libsvm2
7. D. Michie, D.J. Spiegelhalter, C.C. Taylor (eds.), *Machine Learning, Neural and Statistical Classification* (Ellis Horwood, 1994)
8. A. Krogh, J. Vedelsby, Neural network ensembles, cross validation, and active learning, in *Advances in Neural Information Processing Systems* (1995)
9. Y. LeCun, Y. Bengio, Convolutional networks for images, speech, and time series, in *The Handbook of Brain Theory and Neural Networks*, vol. 3361, no. 10 (1995)
10. S. Abe, *Support Vector Machines for Pattern Classification* (Springer, London, 2010)

Piezo-Actuated Adaptive Prisms for Optical Scanning

Florian Lemke, Pascal M. Weber, Ulrike Wallrabe and Matthias C. Wapler

Abstract We present two different piezo-actuated adaptive prisms with apertures ≥8 mm based on a tiltable glass window on top of an optical fluid. In the first prism, we realized a simple monoaxial scanner based on a lever principle. In our second design, we extended the scanning to two axes using three individually controllable piezo cantilevers. We were able to prove the concept for continuously adjustable variable prisms and achieved a tilt angle up to ±3.7° with a response time of 36 ms.

1 Introduction

While novel microscopes use focal power adaptive lenses for focusing and aberration correction along the z-axis [1, 2], scanning perpendicular to the beam path requires one-dimensional (1D) or 2D scanners [3]. These scanners normally work with tilting mirrors, leading to a complex beam path and a bulky setup. Furthermore, most of the scanners operate in resonance, which enables high scanning rates and enhanced deflection angles, but does not allow for a continuous measurement at a static position. Existing transmissive prism concepts, based on liquid crystals [4] or electrowetting [5], provide only monoaxial scanning or a noncontinuous scanning in steps for two dimensions.

For continuous actuation, to enable static measurements and to reduce the beam path complexity using a transmissive instead of a reflective scanner, we developed and characterized two different adaptive prisms. The basic concept is based on a tiltable rigid glass substrate that is located on top of a flexible chamber filled with an optical fluid and is actuated using piezo bimorph bending beams (Fig. 1). The two different configurations (Fig. 2) provide mono- or biaxial scanning ability and will have different scanning speeds and scanning angles.

F. Lemke · P. M. Weber · U. Wallrabe (✉) · M. C. Wapler
Department of Microsystems Engineering – IMTEK, Laboratory for Microactuators, University of Freiburg, Georges-Koehler-Allee 102, 79110 Freiburg, Germany
e-mail: wallrabe@imtek.uni-freiburg.de

A. Martínez-García et al. (eds.), *Progress in Optomechatronic Technologies*,
Springer Proceedings in Physics 233, https://doi.org/10.1007/978-981-32-9632-9_10

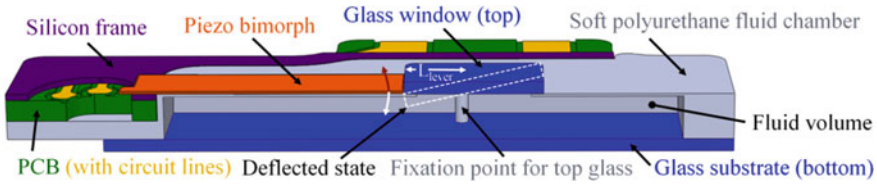

Fig. 1 Cross section of design 1 (monoaxial) shows the working principle of both prisms: a piezo bimorph deflects the glass window, what leads to a tilt. An incident light beam refracts according to Snell's law, when the chamber contains a fluid ($n \neq 1$)

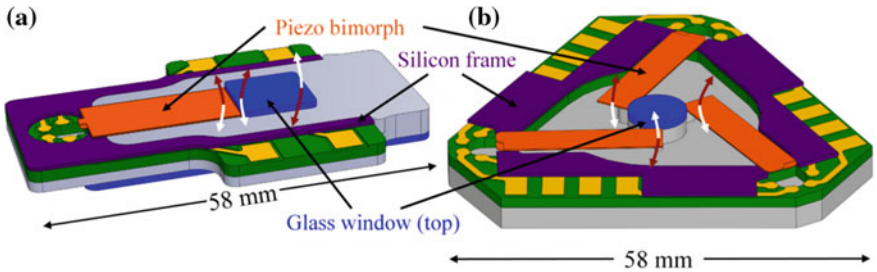

Fig. 2 **a** Monoaxial prism and **b** biaxial prism including the direction of positive/negative bending movement (*red/white arrows*) for tilt in one example direction

2 Design

The first design is a monoaxial prism with a lever actuation principle (Figs. 1 and 2a) that we actuate using a piezo bimorph actuator with length $L_{\text{piezo}} = 21$ mm and a rather large width $W_{\text{piezo}} = 10$ mm. For a given piezo thickness $t_{\text{piezo}} = 120\ \mu$m, a piezoelectric coefficient $d_{31,}$ and an applied symmetric voltage V, we can approximate the deflection D at the tip of the beam (neglecting forces) and the corresponding tilt angle α:

$$D \approx \frac{L_{\text{piezo}}^2 d_{31} V}{t_{\text{piezo}}^2}, \alpha \approx \arcsin\left(\frac{D}{L_{\text{lever}}}\right). \tag{1}$$

The lever in combination with the high force of a rather wide beam leads to a high deflection angle, with the drawback is that it provides only monoaxial scanning. We choose $L_{\text{lever}} = 4.5$ mm for our prototype with a glass window of 11 mm, but this can be changed to adjust the maximum deflection angle.

Our second design (Fig. 2b) uses three piezo bimorph beams with $L_{\text{piezo}} = 21$ mm and $W_{\text{piezo}} = 5$ mm, enabling biaxial scanning. The beams tilt at three points along the circumference of a circular glass window (diameter $d = 9$ mm) using elastic hinges that are integrated into the fluid chamber. The top glass now tilts approximately

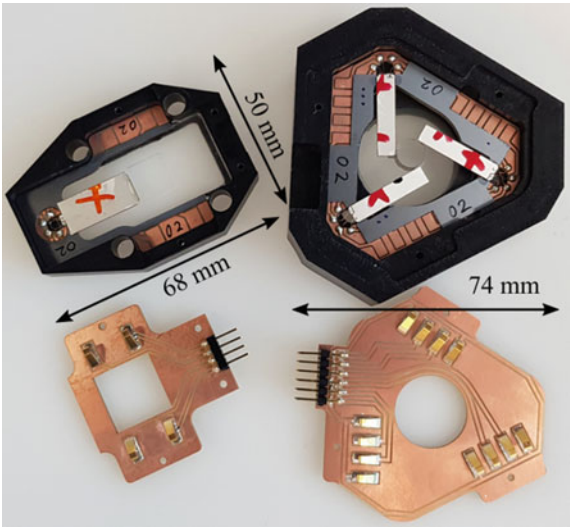

Fig. 3 Prototypes of the monoaxial prism (*left*) and the biaxial prism (*right*) with their holders and electric circuit boards

around the center point, reducing the mass of the displaced fluid and setting L_{lever} essentially to half of the aperture.

3 Fabrication

We first detach piezo sheets from sound buzzers (Ekulit) with an exceptionally high $d_{31} = 487$ pm/V [6] and laser structure them. After that, we glue these to bimorph bending beams, using hard polyurethane (shore hardness 80D). Then, we glue these parts to the silicon frame and to the molded fluid chamber made from soft polyurethane (shore hardness 50 A). Subsequently, we close the chamber with a glass substrate from the bottom and we add the upper glass window. Finally, we inject the optical fluid (paraffin oil, $n = 1.48$) into the chamber using syringes. Figure 3 shows the working prototypes in their custom-made holder that provides electrical contacts as well.

4 Measurement and Evaluation

We measure the deflection of the top glass by scanning with a confocal distance sensor to obtain the tilt and actuation speed. To determine the maximum deflection angle, we use a quasi-static sinusoidal actuation to avoid the creeping effects of the piezo. For both prisms, we apply voltages with a phase delay of 180° to the upper and lower piezo to bend the beams, limited between $V_{\text{min}} = -50$ V and $V_{\text{max}} =$

150 V to avoid depolarization and electrical breakdown. For the measurements, we aligned our devices according to Fig. 4, so that the monoaxial prism bends along the x-axis. The biaxial prism bends along the x-axis for the actuation of beam 3. Actuating beams 1 and 2 tilt the glass in the direction of 120° or 240° in respect to the x-axis, respectively.

The measurement results in Fig. 5 show that the lever prism tilts as expected only along the x-axis, with an approximately linear voltage dependence and a total tilt angle of 7.4°.

We actuated the biaxial prism by bending the piezo beams upwards (upper piezo: 150 V/lower piezo: −50 V) and downwards (−50 V/150 V) in all possible combinations. In Fig. 6, we show the deflection angle for a linear voltage sweep from one of the abovementioned states to the opposite in a polar plot. The dashed lines show the inverse actuation of two beams (one up/one down, and vice versa), while the third beam is inactive (0 V/0 V). The solid lines show actuation of all three beams (two up/one down, and vice versa) at the same time. The voltage-dependent curves look similar to Fig. 5, and the actuation of one single beam gave less deflection and is not shown for this reason. In comparison to Fig. 5, we see only a small hysteresis in Fig. 6. This indicates that even if the tilt angle shows hysteresis, the direction of the tilt is nearly free of hysteresis.

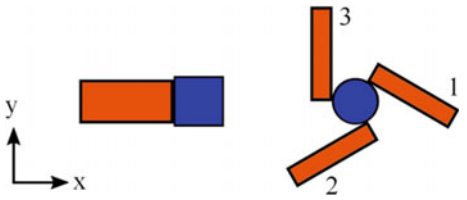

Fig. 4 Alignment of the monoaxial and biaxial prisms with beam numbers for the measurement (top view)

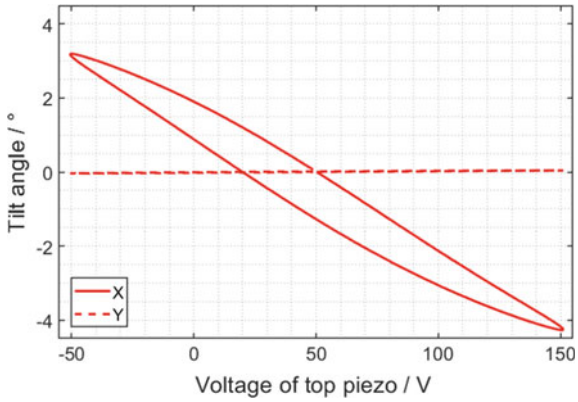

Fig. 5 Tilt angle of the monoaxial prism as a function of the applied voltage

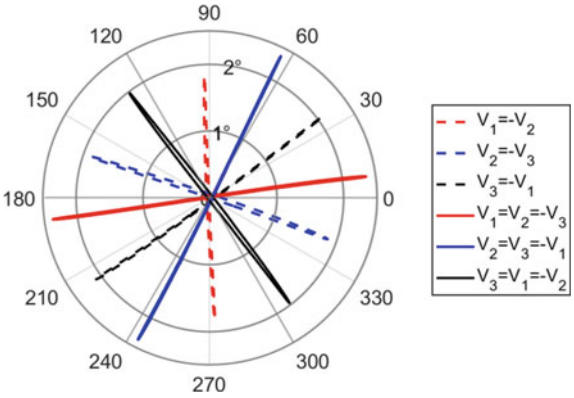

Fig. 6 Tilt angles for possible combinations of two (*dashed*) or three (*solid*) simultaneously actuated beams from one maximal deflection to the opposite maximal deflection: The numbers indicate the active beams with their starting condition for the voltage of the top piezo

Then, we postulated a voltage trajectory that outlines the working range by successively approaching all maximal deflection points. First, we bent deflected beams 1 and 2 in positive direction and beam 3 in negative direction (Fig. 7, *point* 1). Then, we bent beam 2 in negative direction (*point* 3) passing the neutral state of beam 2 (*point* 2). Subsequently, beam 3 and then beam 1 are bent to their opposite direction as well (*points* 4–7). Completing the cycle back to the starting point (points 8–12), we operated the prism in its maximum tilt angle range. The results in Fig. 7 show

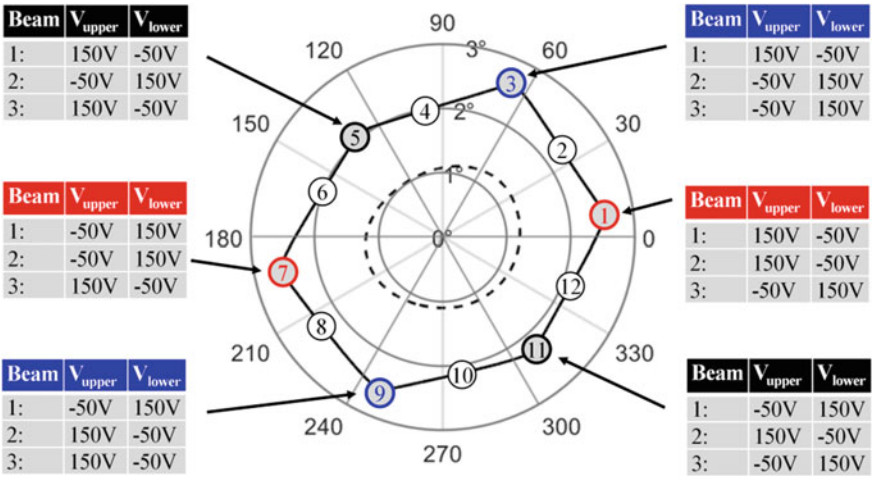

Fig. 7 Tilt angle and direction for a voltage trajectory outlining the operating region of the biaxial prism (*solid line*, maximal deflection points for three beams with applied voltages in *gray* and for two active/one neutral beam in *white*) and circular voltage trajectory (*dashed line*)

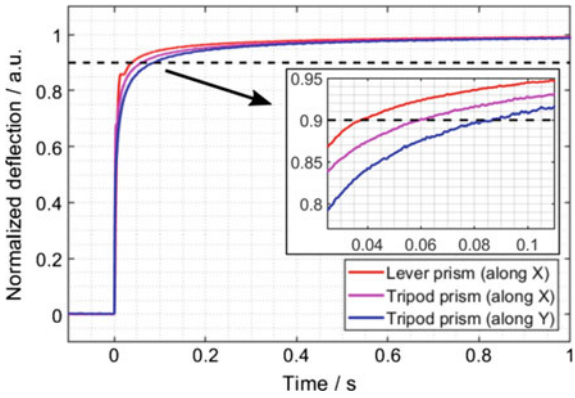

Fig. 8 Normalized deflection for a voltage step from minimal to maximal deflection (step applied at time $t = 0$ s)

that the minimum working range is 2.0° in the direction between the beams and the maximum range is 2.6° along the tilt directions of the beams. The small increase in the maximum deflection angles in Fig. 7 compared to Fig. 6 is caused by hysteresis and creep effects.

There appears a small misalignment of the axes by 8.8° and beam 2 achieves 16.2% less displacement than the other beams. The dashed line shows a circular rotation that results from applying a sinusoidal voltage with phase shifts of 120° to the different beams. In Fig. 8, we find that the response time from 0 to 90% of the maximum deflection is 36 ms for the monoaxial prism and for the biaxial prism 59 ms for a tilt along the x-axis actuating beams 1, 2 and 3 and 82 ms along the y-axis actuating beams 1 and 2. The drop times are similar.

5 Conclusion and Outlook

We successfully demonstrated the proof of concept for two continuously adjustable adaptive prisms with one- and two-dimensional scanning ability with apertures of 11 and 9 mm, respectively. We found that the monoaxial prism achieved the highest scanning angle of 7.4° and gave the shortest response time of 36 ms. By adjusting the critical dimensions of the different designs, for example, the lever length L_{lever} or the width of the fixation point to lower counteracting forces, we can improve both prisms toward higher tilt angles or speed in the future.

Acknowledgments This work was supported by the German Research Foundation (DFG) grants WA 1657/6-1 and the BrainLinks-BrainTools Cluster of Excellence (DFG grants EXC 1086).

References

1. M.C. Wapler et al., A compact, large-aperture tunable lens with adaptive spherical correction, in *International Symposium on Optomechatronic Technologies* (Seattle, WA, 2014), pp. 130–133
2. K. Philipp et al., Axial scanning and spherical aberration correction in confocal microscopy employing an adaptive lens, in *Optics, Photonics, and Digital Technologies for Imaging Applications* (2018), pp. 10679–10685
3. A.J. Nichols et al., Video-rate scanning confocal microscopy and microendoscopy. J. Vis. Exp. **56**, e3252 (2011)
4. G.D. Love et al., Liquid-crystal prisms for tip-tilt adaptive optics. Opt. Lett. **19**, 1170–1172 (1994)
5. D. Kopp et al., Tubular optofluidics as a versatile optical toolbox, in *19th International Conference on Solid-State Sensors, Actuators and Microsystems (TRANSDUCERS)* (Kaohsiung, 2017), pp. 866–869
6. B.P. Bruno et al., Properties of piezoceramic materials in high electric field actuator applications, arXiv:1804.00192 [physics.app-ph]

6D Object Pose Estimation for Robot Programming by Demonstration

Mohammad Ghahramani, Aleksandar Vakanski and Farrokh Janabi-Sharifi

Abstract Estimating the position and orientation (pose) of objects in images is a crucial step toward successful robot programming by demonstration using visual task learning. Currently, a number of algorithms exist for detecting and tracking objects in images, including conventional image processing methods and the state-of-the-art methods based on deep learning architectures. However, the problem of accurate estimation of 6D poses of objects in a sequence of video frames still poses challenges. In this paper, we present a novel deep learning method for pose estimation based on data augmentation and nonlinear regression. For training purposes, thousands of images associated with views of different poses of an object are generated based on a known CAD model of the object geometry. The trained deep neural network is employed for accurate and real-time estimation of the orientation of the object. The object position coordinates in the demonstrations are obtained from the depth information of the scene captured by a Microsoft Kinect v2.0 sensor. The resulting 6-dimensional poses are estimated at each time frame and are employed for learning robotic tasks at a trajectory level of abstraction. Robot inverse kinematics is applied to generate a program for robotic task execution. The proposed method is validated for transferring new skills to a robot in a painting application.

1 Introduction and Literature Review

One of the most important mechanisms by which we acquire new skills is through visually observing teachers (or parents, peers) while they perform the skill [1]. The robot programming by demonstration (PbD) paradigm is motivated by this learning

M. Ghahramani (✉) · F. Janabi-Sharifi
Ryerson University, Eric Palin Hall, 87 Gerrard Street East, Toronto, ON M5B 2K3, Canada
e-mail: mgh@ryerson.ca

F. Janabi-Sharifi
e-mail: fsharifi@ryerson.ca

A. Vakanski
University of Idaho, 1776 Science Center Drive, Idaho Falls, ID 83402, USA
e-mail: vakanski@uidaho.edu

A. Martínez-García et al. (eds.), *Progress in Optomechatronic Technologies*,
Springer Proceedings in Physics 233, https://doi.org/10.1007/978-981-32-9632-9_11

approach among humans and refers to transferring the required skill information from a human teacher to a robot by demonstrating skills examples [2–5]. The skill learning process in robot PbD encompasses several steps, and it typically involves sensory perception of teacher's demonstrations, representation of recorded actions into a suitable form for analysis, mathematical modeling of the demonstrations, planning and generalization, generation of a robot program, and reproduction of the skill by the robot learned [5, 6]. Each of these steps introduces various challenges and contributes to the overall complexity of the development of robot PbD systems that can learn generic tasks by observation.

The phase of perception of human demonstrations encompasses detecting, tracking, and estimating the position and orientation of relevant objects for accomplishing the required task goals. Object detection and tracking have been investigated in many works in the published literature, and subsequently, numerous approaches have been proposed to address these problems based both on conventional [7] and deep network architectures [8, 9]. The recent progress in deep artificial neural networks has led to the development of robust models for detection and tracking of objects in images and videos; in general, this subfield of machine learning has achieved enormous success in other related image processing tasks, such as image classification, segmentation, filtering, synthesis, etc.

The problem of 6-dimensional (i.e., 6D) poses estimation of objects in images represents a more challenging aspect of the phase of perception of demonstrations in robot PbD. To tackle this problem, numerous research works employed sensory systems to directly measure the pose of objects from a set of sensors (e.g., optical, inertial, and electromagnetic) attached to the object of interest or to the demonstrator's body [10–12]. However, such approaches suffer from the use of intrusive markers and/or wires, which affect the natural movements of the human teacher during the task demonstration. Conventional image processing algorithms have also been employed for pose estimation with artificial markers or labels attached to preselected locations on the object of interest [13]. Similarly, a body of work employed concepts from computer vision for pose estimation, e.g., homography transformation [14]; however, most of these approaches require prior knowledge of the object geometry and related dimensional information. Other studies employed deep network architectures for pose estimation, where a database of training images is created by manually annotating the data, i.e., the images captured from a particular view of the object are labeled with the known pose information [15]. These approaches impose constraints on the total range of object orientations because the generated database of the object images should contain many classes of orientations in order to cover various poses of the object.

The presented article introduces a general framework for object pose estimation in RGB-D images. It employs a Microsoft Kinect v2.0 sensor for capturing the demonstrations of a human teacher in the context of robot PbD. The approach uses a data augmentation technique to create a dataset of images of an object of interest that is manipulated by the demonstrator for achieving the task goals. A deep neural network model for pose estimation is designed, and it is trained on the set of images, where the output of the network is the orientation of the object in each image. The

position of the object is obtained from the point cloud range information provided by the Kinect sensor. More specifically, an image tracking algorithm is used to extract the object's position coordinates in the RGB plane of the stream of Kinect images, and the corresponding points in the depth plane are utilized for the coordinates of the object in the 3D space.

The pose estimation method is integrated into a robotic system for object painting. The painting task is repeated multiple times by a human demonstrator in front of the vision sensor. The pose estimation of the painting gun at each time step is aggregated into a set of object trajectories. A trajectory learning approach based on a Gaussian mixture model is employed for modeling the set of demonstrated trajectories, and subsequently, a Gaussian mixture regression is applied for generating a generalized task trajectory [3]. And finally, during the task execution, the robot learner manipulates the painting gun along the sequence of 6D poses of the generalized trajectory in order to paint the object.

2 Proposed Method

The proposed method is incorporated into an alpha version prototype of a system for robot PbD via visual learning [16]. The system prototype is currently being validated for learning various industrial and service robotic tasks. An overview of the steps for skill transfer to a robot for a painting task is presented in Fig. 1. A human demonstrator uses a painting spray gun to paint an object, and the aim is that the robotic system be made to learn the required trajectory of the spray gun and reproduce the painting task. The information flow is depicted in Fig. 1a. The first step pertains to a demonstration of the task by the human teacher, where the demonstrator performs the task multiple times in front of the robot learner (Fig. 1b). For the perception of the demonstrated task examples, a Kinect camera is employed, and it can be seen

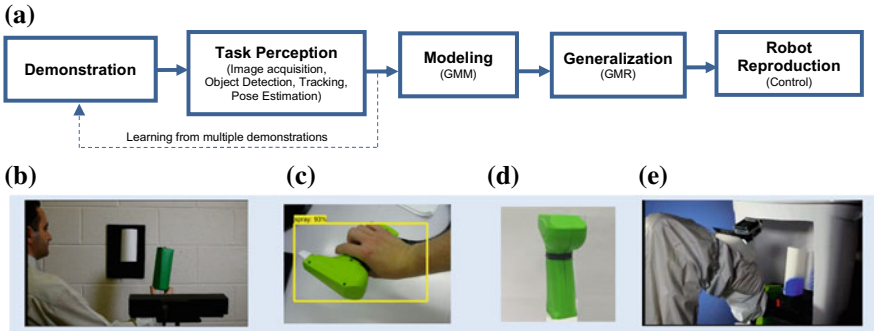

Fig. 1 **a** Overview of the steps in the proposed robot PbD method. **b** Demonstration of the painting task in front of a Kinect sensor. **c** Detection of the object of interest in an image. **d** Example of a synthetic image for pose estimation. **e** Reproduction of the painting task by the robot

in the lower portion in Fig. 1b. Next, image processing algorithms are applied for detection and tracking of the object of interest in the sequences of acquired images by the Kinect sensor. An image frame with the object of interest (i.e., the painting spray gun) detected is shown in Fig. 1c. Afterwards, a pose estimation method is implemented on the stream of RGB-D images, in order to extract the trajectory of the spray gun for each demonstration (Fig. 1d). The next step involves modeling of the multiple trajectories of the spray gun. For this purpose, a Gaussian mixture model is used to encode the density of the set of trajectories into a parametric probabilistic model. A generalized trajectory of the task is generated by employing a Gaussian mixture regression. Finally, the generalized trajectory is transferred to the robot for the reproduction of the task. The painting spray gun is grasped by the robot's gripper, and the robot is controlled to guide the spray gun along the generalized trajectory to paint the object. The robot execution is illustrated in Fig. 1e.

2.1 Pose Estimation

The focus of this study is on the step of pose estimation of the object of interest in robot PbD. The proposed approach for pose estimation entails creating a dataset of synthetic images of the object of interest and designing a deep artificial neural network for calculating the orientation of the object in RGB-D images.

2.1.1 Dataset

To generate a dataset of images of the object of interest, first, we used Autodesk ReCap® [17] to create a 3D CAD model of the object. This software was selected due to the ability to produce an accurate model of the object geometry by just providing several photos of the object captured from different viewpoints on a simple background. Another reason for selecting Autodesk Recap is because it offers a free academic license. The obtained model of the painting spray gun is displayed in Fig. 2a. Afterwards, we employed the MATLAB Java Robot library to control Autodesk 3D MAX® [18] (free academic license) to synthesize a large number of images of the CAD model of the object taken from various angles. The database consists of over 10,000 views of the object corresponding to variations of the Euler angles (yaw, pitch, and roll) values in increments of five degrees. The graphical environment of Autodesk 3D MAX and a set of synthetically generated images corresponding to different Euler angles are depicted in Fig. 2b, c. The resulting dataset of images is further augmented by generating images at various scales of the resolution of the original images as well as by introducing artificial illumination variations to the original images.

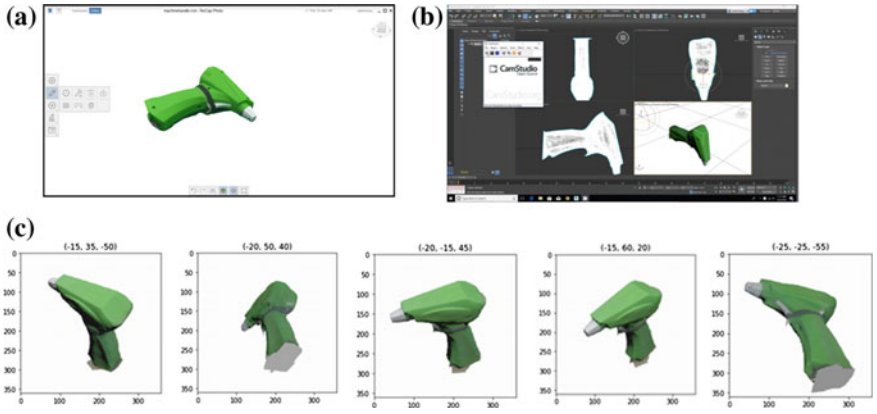

Fig. 2 **a** A screenshot of the resulting model of the painting spray gun obtained in Autodesk ReCap. **b** A screenshot of the object model and different viewing angles in Autodesk 3D MAX. **c** Examples of the resulting images from Autodesk 3D MAX, where the viewing orientation of the object expressed in yaw, pitch, and roll angles is indicated above each image

2.1.2 Network Architecture

We employed a pre-trained VGG16 neural network model [19] and performed transfer learning to calculate the orientation of the object. VGG16 was originally designed for image classification, and it consists of a stack of 13 convolutional and five pooling layers, followed by three fully connected layers, and a softmax classification layer. The size of the convolutional filters in most of the layers is 3×3 pixels with a stride of 1, whereas several layers use convolutional filters of size 1×1. The pooling layers perform a max-pool operation on 2×2 pixel size windows with a stride of 2. The fully connected layers have 4096 hidden units. ReLU activation functions are used for all layers in the network. The network was trained on the Image Net dataset for classification of images with 1,000 different classes.

For the transfer learning on the created dataset of images of the painting spray gun, we used the base model of the VGG16 network consisting of the convolutional and pooling layers. A top model then is added that replaces the last three fully connected layers of the VGG16 network. More specifically, one fully connected layer with 1024 hidden units is added, with ReLU activation functions, and a dropout of 0.25. Finally, another fully connected layer with 3 units is added. The outputs of the last layer do not include an activation function since they directly correspond to the three Euler angles: yaw, pitch, and roll.

To train the network parameters, pairs of images and Euler angles of the object orientation are employed as inputs to the network. The parameters in the layers of the base model are set to remain constant (i.e., they are "frozen"), and only the parameters of the newly added top model are trained on our dataset. The network is trained to match the provided images and the respective object orientation by iteratively reducing the mean squared error between the predicted and the true values of the

Euler angles. The size of the input images is 360 × 360 pixels. Adam optimizer is utilized for training with a batch size of 20 images.

During testing, new images that are not presented during the training phase are forward propagated through the network to calculate the Euler angles. Figure 3 presents the performance of the network for estimating the yaw, pitch, and roll angles of 1,000 randomly selected images of the painting gun. The horizontal axes in the figures correspond to the testing set of 1,000 images and the vertical axes present the values of the angles in degrees. The blue dots in the figure denote the ground truth values of the object orientation angles that were inputted into the Autodesk 3D Max software for the image generation. The black stars are the predicted values of the Euler angles by the neural network. In most cases, the model was able to accurately estimate the value of the orientation angles. For the pitch and yaw angles, the predicted values match very closely the true values of the angles. The overall accuracy for the yaw angle is slightly smaller than that of the pitch and roll angles; we believe that it is due to the geometry of the object, which provides a lesser number of discriminative attributes when seen from different views around the yaw angle. The average root-mean-squared deviation between the true and predicted values of the yaw, pitch, and roll angles is 11°, 2°, and 7°, respectively.

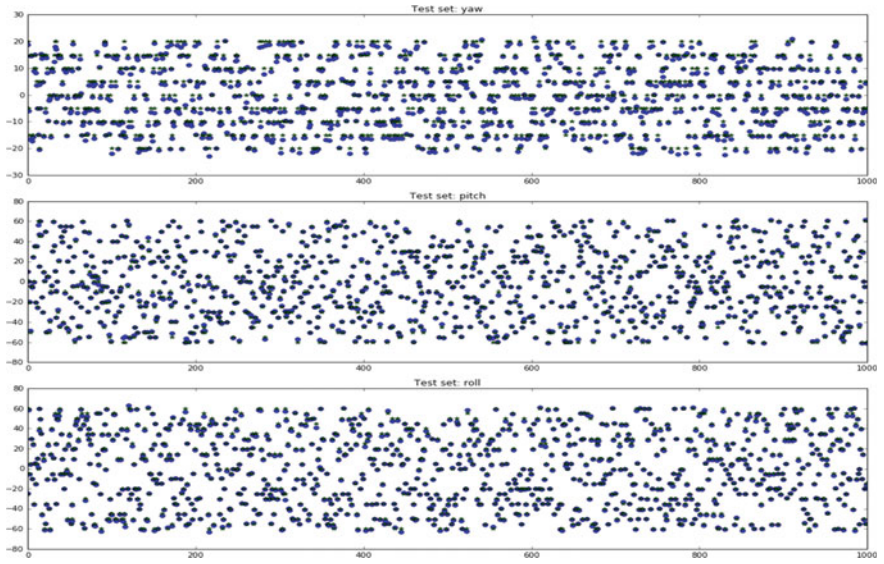

Fig. 3 From top to bottom, values of the yaw, pitch, and roll angles for a test set of 1,000 random image samples. The blue dots denote the true values of the orientation angles, while the black star marks denote the predicted values of the orientation angles by the neural network

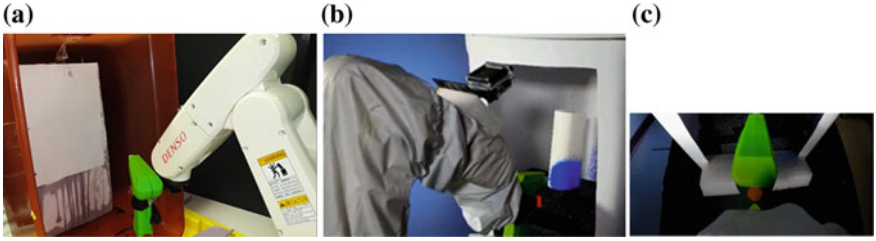

Fig. 4 **a** The used robot and the painting gun. **b** Reproduction of the painting task by the robot. **c** A view of the painting gun from a camera mounted on the upper arm of the robot

2.2 Task Learning and Robotic Reproduction

The position coordinates of the spray gun are obtained directly from the depth streams of the Kinect sensor. The combination of the 3D positions from the depth image and the 3D orientations from the neural network for each time step of the acquired videos produces 6D time series data of the object trajectory. The trajectories from multiple demonstrations are first encoded with a Gaussian mixture model. Next, a Gaussian mixture regression is applied to the probabilistic model of the demonstrated examples to generate a generalized trajectory of the painting task.

The generalized trajectory is transferred to a six-degrees-of-freedom desktop Denso robot for the reproduction of the painting task. The robot and the spray gun are depicted in Fig. 4a. An inverse kinematics algorithm is implemented for calculating the time series of the robot joint angles for following the generalized trajectory. Before the actual task execution, we covered the robot with a protective layer, to prevent damage from the paint spray. A photo from the robot executing the painting task is shown in Fig. 4b (the video is available at the link in [16]). A view of the painting task from a camera mounted on the upper arm of the robot is displayed in Fig. 4c. QuaRC toolbox for open architecture control is used for control of the robot during the task execution [20].

3 Summary

An approach for pose estimation of an object in images acquired with an RGB-D vision sensor is presented. The proposed method employs a deep convolutional neural network for calculating the orientation of the object. A large set of images of the object corresponding to different poses are synthetically generated, and the dataset is used for training the network parameters. The position of the object is extracted from the collected depth information by employing an image processing algorithm. The object poses for a sequence of RGB-D images are employed for trajectory learning in robot programming by demonstration. The method is validated on a task of painting an object. A set of teacher demonstrations are observed by a

robotic learning system and are used for inferring the trajectory of a painting gun tool, and subsequently, for the reproduction of the painting task by the robot.

Acknowledgements This work was supported by NSERC Innovation to Idea (I2I) grant (I2I PJ 486866-15). We would like to thank Miss. Kaiqi Cheng for validating the experiments. Authors received a high-end Graphical Processing Unit (GPU), Titan XP from NVIDIA which was used for this research.

References

1. G. Biggs, B. MacDonald, A survey of robot programming systems, in *Proceedings of the Australasian Conference on Robotics and Automation*, Brisbane, Australia (2003), pp. 1–10
2. S. Schaal, A. Ijspeert, A. Billard, Computational approaches to motor learning by imitation. Philos. Trans. R. Soc. Lond. Biol. Sci. **358**(1431), 537–547 (2003)
3. S. Calinon, *Robot Programming by Demonstration: A Probabilistic Approach* (EPFL/CRC Press, Boca Raton, USA, 2009)
4. A.G. Billard, S. Calinon, R. Dillmann, Learning from humans, in *Handbook of Robotics,* ed. by B. Siciliano, O. Khatib (Springer, New York, USA, 2016), pp. 1995–2014
5. B. Argall, S. Chernova, M. Veloso, B. Browning, A survey of learning from demonstration. Robot. Auton. Syst. **57**(5), 469–483 (2009)
6. A. Vakanski, F. Janabi-Sharifi, *Robot Learning from Visual Observation* (Wiley, 2017)
7. X. Jia, H. Lu, M. Yang, Visual tracking via adaptive structural local sparse appearance model, in *IEEE Conference on Computer Vision and Pattern Recognition,* Providence, USA (2012), pp. 1822–1829
8. D. Li, W. Chen, Object tracking with convolutional neural networks and kernelized correlation filters, in *Chinese Control and Decision Conference*, Chongqing, China (2017), pp. 1039–1044
9. J. Redmon, S. Divvala, R. Girshick, A. Farhadi, You only look once: unified, real-time object detection, in *IEEE Conference on Computer Vision and Pattern Recognition*, Las Vegas, USA (2016), pp. 779–788
10. R. Dillmann, Teaching and learning of robot tasks via observation of human performance. Robot. Auton. Syst. **47**(2–3), 109–116 (2004)
11. D. Martinez, D. Kragic, Modeling and recognition of actions through motor primitives, in *Proceedings of the IEEE International Conference Robotics and Automation*, Pasadena, USA (2008), pp. 1704–1709
12. A. Vakanski, I. Mantegh, A. Irish, F. Janabi-Sharifi, Trajectory learning for robot programming by demonstration using hidden Markov model and dynamic time warping. IEEE Trans. Syst. Man Cybern. Part B **41**(4), 1039–1052 (2012)
13. A. Vakanski, F. Janabi-Sharifi, I. Mantegh, An image-based trajectory planning approach for robust robot programming by demonstration. Robot. Auton. Syst. **98**, 241–257 (2017)
14. O. Faugeras, *Three-Dimensional Computer Vision: A Geometric Viewpoint* (MIT Press, Cambridge, USA, 1993)
15. P. Wohlhart, V. Lepetit, Learning descriptors for object recognition and 3D pose estimation, in *IEEE Conference on Computer Vision and Pattern Recognition*, Boston, USA (2015), pp. 3109–3118
16. Demos available at https://youtu.be/G09J57jMzmg
17. Autodesk ReCap (2018). Available at https://www.autodesk.com/products/recap/overview

18. Autodesk 3D Max (2018). Available at https://www.autodesk.com/products/3ds-max/overview
19. S. Karen, A. Zisserman, Very deep convolutional networks for large-scale image recognition, arXiv:1409.1556 (2014)
20. Quarc Real-time Control Software (2018). Available at https://www.quanser.com/products/quarc-real-time-control-software/

Visual Memory Construction for Autonomous Humanoid Robot Navigation

A. López-Martínez, F. J. Cuevas and J. V. Sosa-Balderas

Abstract A visual memory (VM) is a topological map that represents an environment as a direct graph of key images. Thus, visual information acquired from cameras onboard the robot are the only data to construct the map. This work presents the construction of a VM suited for the humanoid robot navigation framework. Additionally, a genetic algorithm that estimates the epipolar geometry is proposed to tackle the problem of image matching used within the VM construction process. Experimental results using a humanoid robot dataset are presented to validate the efficacy of our approach. Further, the solution for image matching based on the proposed genetic algorithm was compared with RANSAC.

1 Introduction

The strategies to improve the navigation capabilities of humanoid robots result in great interest in robotics. Thus, great efforts have been made to propose an efficient navigation framework for autonomous humanoid robots. These frameworks include different tasks such as mapping the environment, localizing the robot within the map, and planning path strategies for navigation. This work tackles specifically the problem of mapping the navigation environment.

Maps of environments for robot navigation can be classified into three categories: Metric representations, topological representations, and hybrid representations that include both metric and topological information. Topological maps, contrary to metric maps, relieve the computational burden of extracting and storing metric and 3D information. Furthermore, for wheeled robots, a topological map encodes sufficient

A. López-Martínez (✉) · F. J. Cuevas · J. V. Sosa-Balderas
Optical Metrology, Centro de Investigaciones en Óptica A. C., 37150 León, Mexico
e-mail: alan.lopez@cio.mx

F. J. Cuevas
e-mail: fjcuevas@cio.mx

J. V. Sosa-Balderas
e-mail: vicentesosa@cio.mx

A. Martínez-García et al. (eds.), *Progress in Optomechatronic Technologies*,
Springer Proceedings in Physics 233, https://doi.org/10.1007/978-981-32-9632-9_12

information, since reconstructing the robot's path or having 3D information is not necessary within a vision-based navigation framework [1–5].

Given the advantages of topological maps, the aim of this work is to propose the construction of a topological representation of the environment that uses only 2D information provided by a camera onboard a humanoid robot. This topological map, called visual memory (VM), was first proposed for wheeled robots [6, 7]. A VM is a collection of images ordered in a direct graph. The motivation behind the VM paradigm is to imitate the human behavior when navigating in an unknown environment for the first time. Humans memorize the key images first time when an environment is explored, in order to later use these references as landmarks for a future navigation task within the same environment [6].

As stated earlier, the VM strategy has been mainly exploited for navigation of wheeled mobile robots. Unfortunately, less effort has been made to construct a VM for humanoid robot navigation. A particular problem related to this type of robots involves images with blur effects, due to the inherent dynamic balance and the undesired sway motion introduced by bipedal motion. In the following subsections, we discuss the elements of the VM.

2 Visual Memory Navigation Framework

The proposed approach tackles the task of constructing an accurate and efficient representation for the navigation environment. An efficient representation is the one that enables a complete navigation framework; that is it permits a fast and easy localization, and allows a simple, yet robust path planning. Our proposed VM attains these goals by representing an environment with a direct graph which considers the environment topology. Within the map, the nodes of the VM are the key images that encode 2D data, and that represent relevant positions in the environment. The edges, on the other hand, describe the relationships between nodes.

The proposed VM can be used within a vision-based navigation framework for humanoid robots, regarding both robot localization and path planning. To localize the robot within the VM, the data provided by the VM is enough to qualitatively solve the robot localization given the current image from the robot's camera. The robot is localized when the "more similar" key image (in the VM) to the current image is found; this is an image retrieval task. For instance, a proposed appearance-based localization method finds the most similar key image with respect to the current image in terms of common visual information using the bag-of-visual-words (BoVW) approach [8].

To plan a path, a desired key image associated to the desired robot location is set as a target. Then, the visual path planner returns the sequence of key images to reach the desired location. Finally, to navigate, different approaches can be used. For instance, the work in [9] uses visual servoing to control a Nao humanoid robot. Further, in the case of dynamic environments, the proposed VM can be used with

an adequate navigation framework that deals with changes in the VM that were not initially present [10].

Having briefly described how our VM can be used within a vision-based navigation framework, we now describe the construction of our proposed VM.

3 Construction of the Visual Memory

The whole framework for the VM construction as proposed in this work is shown in Fig. 1. First, the robot is operated manually to capture a training video of the environment. Then, an off-line process consisting of different steps is carried out: (i) Frame extraction. From the training video, a set $V = \{I_1, I_2, \ldots, I_n\}$ containing all frames is obtained. (ii) Key image selection. From the set V, a smaller set $V_k = \{I_{k1}, I_{k2}, \ldots, I_{km}\}$ that contains only key images is obtained. (iii) Graph construction. The last step involves grouping key images (nodes) that share a common location, like a corridor or a room. We make this step manually to finally construct the VM. These steps are now described in detail.

Frame extraction is the first off-line process. The aim of this step is to extract the whole set of frames within the training video. It is noted that, since the training video is acquired manually, the quality of the VM depends on the expertise of the user. The better the training video (i.e. the more the environment is explored), the better is the VM. In other words, the number of key images in the VM is directly linked to the human-guided path complexity.

The aim of the second step, the key image selection step, is to extract key images. First, to tackle the problem of images with high motion blur due to humanoid movements, we remove the images for which the variance of the Laplacian of Gaussian (LoG) is below a threshold, commonly $\sigma^2(\text{LoG}) = 10$ [11]. This also allows us to discard images with low textures. Once low-quality images have been filtered out, the remaining images are processed in order to select key images.

Two conditions must be optimized for key image selection: (1) The overlap between key images I_{k1} and I_{k1+1} must be maximum; and (2) the number of frames between key images I_{k1} and I_{k1+1} must be maximum. Additionally, two hypotheses

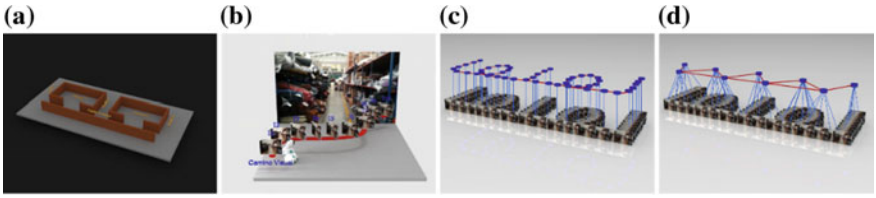

Fig. 1 Visual memory construction. **a** Environment to map. **b** The robot is operated manually to obtain the set of training images. **c** A reduced number of key images are selected from this set. **d** Finally, the key images are grouped together to form a connected graph, that is the visual memory

must be considered for key image selection: (1) Two key images I_{k1} and I_{k1+1} must contain a set P_i of matched key-points. The cardinality of the set must be enough to compute a vision-based control law for navigation. Also, for control purposes, the authorized motions during the learning stage are assumed to be limited to those of a humanoid robot. Hence, Hypothesis 2 is respected: There must be a possible path between the position of capture of image I_{k1} to the image I_{k1+1}.

As already stated, a VM is a graph where the nodes encode key images obtained during a learning phase. The weight of an edge, on the other hand, represents the cost of traveling from a node to one of the adjacent nodes. In [9, 10], the authors set the weight of an edge to be in terms of the number of matched interest points and the amount of rotation between neighboring key images. Thus, the more matches there are between nodes, or key images, the lower the cost will be. Also, the more rotation there are between nodes, or key images, the greater the cost will be. In [6, 7], on the other hand, the weights of the edges are unitary, and the cost of a path between nodes is given by the number of key images in the route. In these works, an edge connection between two nodes exists if a minimum number of point correspondences is achieved to relate neighbouring nodes.

We use the epipolar geometry to satisfy the conditions for key image selection, and to describe the relationships between nodes; that is to find the weights of the edges. To this end, we propose a genetic algorithm (GA) that validates the image matching.

3.1 Image Matching

The image matching process consists of three main operations: (1) features detection, (2) features description, and (3) optimal matching. In our approach, for the first and second step of the matching process, we used the SURF detector and descriptor, since its complexity is $O(\log(N))$ and is invariant to scale, rotation, and illumination. Then, we match the descriptors by computing the Euclidean distance between them. After that, we authenticate the matches with the epipolar constraint using a GA that estimates the essential matrix E.

The epipolar geometry describes the relation that exists between two images viewing the same scene. These two images could have been obtained by moving a camera at two different locations and taking pictures from two viewpoints, or by using two cameras, each of them taking a different picture of the scene. Let there be a set of N good matched points between the images a and b. The 2D image positions of these points are denoted in homogeneous coordinates as $\boldsymbol{P}^a = \left(x_{i^a}, \mathrm{y}_{i^a}, 1\right)^T$ in the a image, and $\boldsymbol{P}^b = \left(x_{i^b}, \mathrm{y}_{i^b} 1\right)^T$ in the b image. These positions are related by the epipolar geometry as follows:

$$\boldsymbol{P}^{b^T} F \boldsymbol{P}^a = 0, \tag{1}$$

where the F matrix is also known as the fundamental matrix and can be computed with a set of good matches using the eight-point algorithm as described in [12].

The essential matrix E is the specialization of the fundamental matrix to the case of normalized image coordinates.

$$E = K^T F K, \tag{2}$$

where K is the calibration matrix. The E matrix has fewer degrees of freedom and additional properties, compared to the F matrix. When the position in the world of the cameras is known, it may be verified that E can be computed by:

$$E = [\boldsymbol{t}]R. \tag{3}$$

Equation (3) codifies the position of the camera, where R is the rotation matrix and $\boldsymbol{t}$ is the translation vector of a given camera pose. A geometric constraint between images allows the process of points matching to be robust. We propose a GA to estimate E, and in consequence estimate the overlap of two consecutive images. Also, since the rotation between frames can be obtained from the epipolar geometry, we use this information to set the weights of the nodes as in [9, 10].

3.1.1 Stereo Matching Using the Essential Matrix Estimated with a Genetic Algorithm

To encode the chromosomes, each individual is represented by a fixed length of binary string as: $chromosome = \left[\Phi, \theta, \psi, t_x, t_y\right]$, where each variable is allowed within a specific range: $\Phi, \theta, \psi \in [0, 2\pi]$, and $t_x, t_y \in [-5, 5]$. Thus, each chromosome encodes an E matrix using Eq. (3). The production of new chromosomes from old ones is achieved through the application of the genetic operators: selection, crossover, and mutation. An iterated application of genetic operators is repeated to reach the final solution to the problem.

The selection operator aims to choose a set of individuals from a population at a given time. This operator selects those individuals with the best fitness value and puts them in the mating pool. The crossover operator exchanges genes from a pair of chromosomes and creates a new offspring. To compute the operator, a random pair of individuals from the mating pool is chosen; also, a crossover point is chosen. All the data of the first parent before the crossover point is copied to the offspring, and then the rest of the data of the second parent after the crossover point is copied to the offspring. After the crossover operation is performed, the mutation operator is executed. Mutation changes randomly the new offspring. For binary encoding we can switch a few randomly chosen bits from 1 to 0 or from 0 to 1.

The parameters for the GA are as follows: Population size, 100; crossover rate, 0.95; mutation rate, 0.01; elite size, 15. A Boltzmann fitness scale was used to control pressure selection. To score solutions, a fitness function is proposed as follows. We first extract the epipolar lines from the E matrix encoded by the chromosome. Then, the fitness value is the sum of points that deviate less than a predefined threshold ($T = 1$ pixels) from its corresponding epipolar line.

4 Experiments and Results

The proposed approach was evaluated using the *CIMAT-NAO-A* dataset, which has been used in related works [8, 11]. The dataset is publicly available in http://personal.cimat.mx:8181/~hmbecerra/CimatDatasets.zip, and contains 399 different images with blur effects and low textures. Figure 2 shows sample images from the dataset, and the key images selected by our algorithm. The image matching solution based on a GA was compared with a heuristic method call Random Sample Consensus (RANSAC). Both methods were compared with the odometry of the robot, and the results demonstrate that the GA obtains a lower error than the RANSAC method, as shown in Table 1. To compute the error, we represent the solution (camera pose) found by each method with the Rodrigues formula.

Fig. 2 Topological map for the dataset *CIMAT-NAO-A*. **a** Sample images from the dataset. **b** Training sequence; key images are highlighted in blue

Table 1 Comparison between GA and RANSAC approaches (mean values)

	GA	RANSAC
Rotation error (degrees)	1.18	1.34
Angle error between vectors (degrees)	0.24	0.28
Validated matched points	875	821

5 Conclusions

In this work, an environment representation was presented using only visual information. Further, a GA was proposed to tackle the problem of image matching. The results obtained with a humanoid walk dataset show that the proposed approach efficiently describes the environment. Consequently, an adequate VM is constructed. Our proposed VM allows humanoid localization and path following entirely based on 2D information by taking advantage of geometric constraints that can provide the estimated translation and rotation required by the controller, such as the epipolar geometry, the homography for planar and no planar scene, or the trifocal tensor.

References

1. Z. Chen, S.T. Birchfield, Qualitative vision-based mobile robot navigation, in *Proceeding of ICRA* (2006), pp. 2686–2692
2. O. Booij, Z. Terwijn, Z. Zivkovic et al., Navigation using an appearance-based topological map, in *Proceeding of ICRA* (2007), pp. 3927–3932
3. J. Ido, Y. Shimizu, Y. Matsumoto et al., Indoor navigation for a humanoid robot using a view sequence. Int. J. Robot. Res. **28**(2), 315–325 (2009)
4. A. Diosi, S. Segvic, A. Remazeilles et al., Experimental evaluation of autonomous driving based on visual memory and image-based visual servoing. IEEE Trans. Intell. Transp. Syst. **12**(3), 833–870 (2011)
5. H.M. Becerra, C. Sagues, Y. Mezouar et al., Visual navigation of wheeled mobile robots using direct feedback of a geometric constraint. Auton. Robots **37**(2), 137–156 (2014)
6. J. Courbon, Y. Mezouar, P. Martinet, Indoor navigation of a non-holonomic mobile robot using a visual memory. Auton. Robots **25**, 253–266 (2008)
7. J. Courbon, Y. Mezouar, P. Martinet, Autonomous navigation of vehicles from a visual memory using a generic camera model. IEEE Trans. Intell. Transp. Syst. **10**(3), 392–402 (2009)
8. N.G. Aldana-Murillo, J.B. Hayet, H.M. Becerra, Comparison of local descriptors for humanoid robots localization using a visual bag of words approach. Intell. Autom. Soft Co., 1–11 (2017)
9. J. Delfin, H.M. Becerra, G. Arechavaleta, Humanoid localization and navigation using a visual memory, in *International Conference on Humanoid Robots (Humanoids)* (2016), pp. 725–731
10. J. Delfin, H.M. Becerra, G. Arechavaleta, Humanoid navigation using a visual memory with obstacle avoidance. Rob. Auton. Sys. **109**, 109–124 (2018)
11. E. Ovalle, Generación de una memoria visual para la navegación autónoma de un robot humanoide (2016)
12. R.I. Hartley, A. Zisserman, *Multiple View Geometry in Computer Vision*m, 2nd edn. (Cambridge University Press, 2004)

Glucose Concentration Measurement of a Transparent Sample by Using a Gaussian Probe Beam with High Spherical Aberration

Etna Yáñez, Moisés Cywiak and S. Juan Manuel Franco

Abstract We present the results of our technique reported earlier for glucose concentration measurement of a transparent sample. The technique is based on an optical probe beam with high spherical aberration. We report that it is possible to attain better sensitivity compared to a system that uses a probe beam free of aberrations under similar conditions.

1 Introduction

Many diseases are associated to abnormal glucose concentration in blood [1, 2], so it is necessary to carry out further research to develop more accurate instruments for measurement of glucose concentration. As indicated in [2], it is difficult to attain reliable measurements, especially in the determination of hypoglycemia, in particular, for glucose concentration measurement in children and adolescents. This lack of accuracy is mainly attributed to the fact that, in general, these techniques are based on methods that offer low signal-to-noise ratios [3, 4]. To alleviate the above-mentioned limitation, in our previous report, we have presented a technique based on the diffractive properties of a transmitted Gaussian probe beam with high spherical aberration that propagates through a transparent sample under inspection. We demonstrated that aberrations contribute to increase of the sensitivity in this type of measurements [5]. The advantage of this technique is that it does not depend on the amplitude of a single weak signal as it is based on the profile of the probe beam that propagates through the sample. In addition, we showed that the system exhibits a linear response in the range of clinical interest and this linearity is maintained in spite of small system misalignments. Thus, the proposed technique is in principle immune to noise, making it highly reliable.

E. Yáñez (✉) · M. Cywiak · S. Juan Manuel Franco
Centro de Investigaciones en Óptica A.C., Loma del Bosque No. 115, León, Gto., Mexico
e-mail: etnay@cio.mx

A. Martínez-García et al. (eds.), *Progress in Optomechatronic Technologies*,
Springer Proceedings in Physics 233, https://doi.org/10.1007/978-981-32-9632-9_13

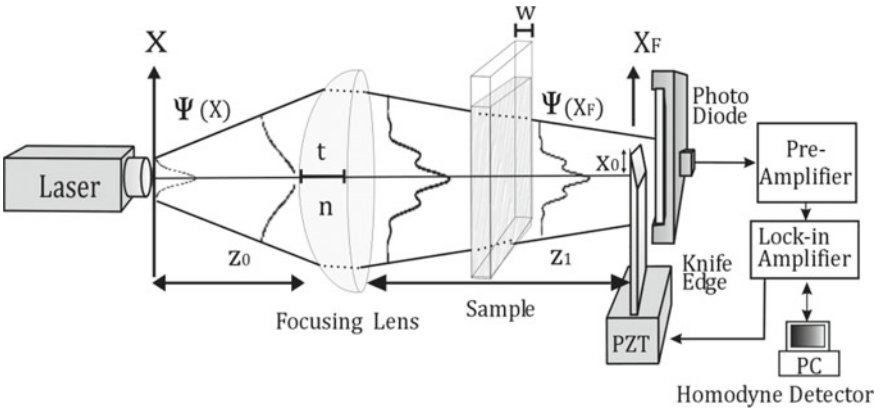

Fig. 1 The vertex of a singlet focusing lens with central thickness t is placed at a distance z_0 from the waist-plane with coordinate x of a laser Gaussian beam with amplitude distribution $\Psi(x)$. The observation plane with coordinate x_F is located at a distance z_1 from the back surface of the lens. A transparent sample with width w is placed between the lens and the observation plane. The intensity distribution $|\Psi(x_F)|^2$ is recorded by an homodyne detector (a detailed description of the method is given in [5])

2 Experimental Setup

The optical setup is depicted in Fig. 1. A Gaussian laser beam with amplitude distribution $\Psi(x)$ propagates through a single focusing lens. The Gaussian waist-plane beam is placed at a distance z_0 of the vertex of a focusing lens so that the spatial dimensions of the beam are large enough to illuminate a large area of the focusing lens and at the same time avoid visible truncation of the beam. In this way, a Gaussian probe beam with high spherical aberration is obtained at the back of the focusing lens. The aberrated beam propagates through the sample under inspection. The profile of the intensity distribution $|\Psi(x_F)|^2$ at the plane of observation is recorded by an homodyne detector placed at a distance z_1 from the back surface of the lens.

3 Results of Measurements

In Fig. 2a–d, it is depicted how at a near vicinity of the back focal plane of a focusing singlet, spherical aberrations of an illuminating commercially available He–Ne laser beam with a Gaussian intensity profile are obtained as the distance between the laser and the focusing singlet (z_0) increases.

Contrary to what would be expected intuitively, in a previous report [5], we have demonstrated that the Gaussian probe beam free of aberrations is less sensitive to glucose concentration changes as compared with the Gaussian probe beam with high spherical aberrations.

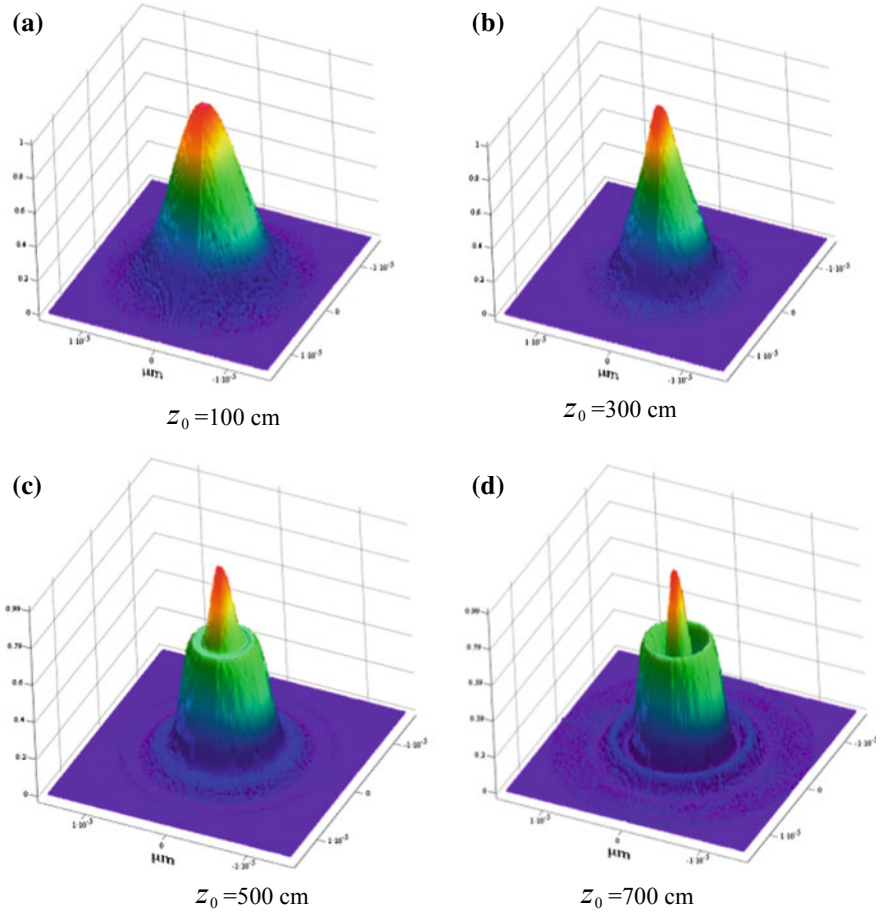

Fig. 2 **a–d** Increase of spherical aberrations at a vicinity of the back focal plane of a focusing singlet, illuminated by a commercially available laser beam with a Gaussian intensity profile as a function of (z_0)

The proposed technique is based on measuring the vertical height of the primary side-lobes of the normalized aberrated intensity profiles at the plane of detection as a function of glucose concentration. Figure 3a–b depicts how the primary side-lobes heights of the aberrated intensity profiles increase as a function of the index of refraction of the sample. We remark that this increase is linear. In turn, in a small region of interest, where the instrument is calibrated, the index of refraction of the sample is also a linear function of glucose concentration.

Figure 4 depicts experimental normalized aberrated intensity profiles at the plane of detection. The system was calibrated for three glucose concentrations $C_A = 0$ mg/dl, $C_2 = 200$ mg/dl and $C_4 = 400$ mg/dl. As the system exhibits a linear response in left and right primary side-lobes, a simple rule of three can be applied on

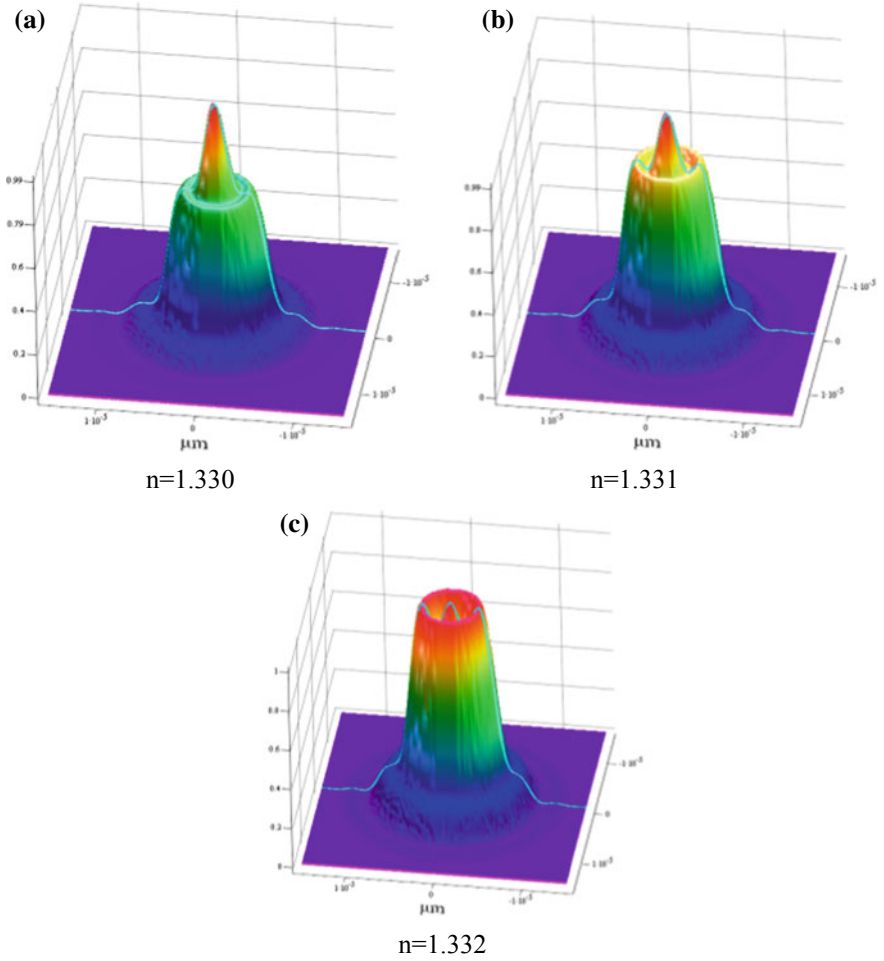

Fig. 3 **a–c** Increments of the heights of the primary side-lobes of the detected probe beam as the index of refraction increases in the sample under inspection. $z_0 = 500$ cm, $\Delta n = 0.001$ which corresponds to approximately changes of 500 mg/dl between samples (the concentration changes are exaggerated for visualization purposes)

either side to determine in a simple manner an unknown concentration. It is only necessary to perform two known glucose calibrated measurements before determining with high accuracy the concentration of an unknown sample.

We want to emphasize that due to the linear response of the system, the results of the proposed technique are simple to use in clinics, hospitals and clinical laboratories.

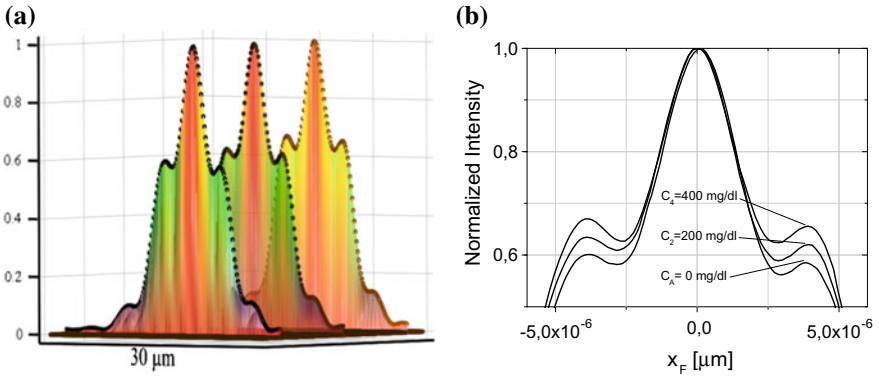

Fig. 4 **a** Normalized experimental intensity profiles for three different sample concentrations $C_A = 0$ mg/dl, $C_2 = 200$ mg/dl and $C_4 = 400$ mg/dl. **b** Corresponds to a zoom of (**a**)

4 Conclusions

We demonstrated analytically and experimentally that a Gaussian probe beam with high spherical aberration is more sensitive than a Gaussian probe beam free of aberrations for glucose concentration measurements. We demonstrated experimentally that the system has a linear response in a range of interest with high repeatability and stability, making this system feasible for glucose concentration measurements of transparent liquid media. As the system exhibits a linear response, an additional advantage is that the system is still reliable even over slight misalignments.

References

1. A. Norhammar, Å. Tenerz, G. Nilsson, A. Hamsten, S. Efendíc, L. Rydén, K. Malmberg, Glucose metabolism in patients with acute myocardial infarction and no previous diagnosis of diabetes mellitus: a prospective study. The Lancet **359**(9324), 2140–2144 (2002)
2. D.C. Klonoff, The need for separate performance goals for glucose sensors in the hypoglycemic, normoglycemic, and hyperglycemic ranges. Diabetes Care **27**(3), 834–836 (2004)
3. R.J. McNichols, G.L. Coté, Optical glucose sensing in biological fluids: an overview. J. Biomed. Opt. **5**(1), 5–16 (2000)
4. C.F. So, K.S. Choi, T.K. Wong, J.W. Chung, Recent advances in noninvasive glucose monitoring. Med. Devices (Auckland, NZ) **5**, 45 (2012)
5. E. Yáñez, M. Cywiak, S.J.M. Franco, Gaussian probe beam with high spherical aberration for glucose concentration measurement. Appl. Opt. **57**(15), 4153–4157 (2018)

Satellite Image Processing for Retrieving Historical Solar Irradiance Data Within the Mexican Territory

Juan M. Callejas-Cornejo, Manuel I. Peña-Cruz and Luis M. Valentín-Coronado

Abstract Solar resource assessment is a key subject for the viability and implementation of solar power plants. Solar sensors measure irradiance locally, but high cost of these specialized sensors makes their implementation through all the Mexican territory difficult. Satellite images provide a valuable tool for the determination of solar irradiance through image processing. In this work, an algorithm for the estimation of global solar irradiance based on determining the cloud index through pixel analysis is implemented for the central region of Mexico.

1 Introduction

Solar radiation that reaches the top of the atmosphere and reaches the surface of the earth depends on different variables, that is, the factor of atmospheric transmission, available albedo and atmospheric pollution. Solar sensors (radiometers) measure components from the solar radiation reaching the earth. Direct solar irradiance (DNI) is the component that comes directly from the sun without any deviation from the atmosphere (pyrheliometers). Diffuse solar irradiance (DHI) is what reaches the earth's surface due to the deviation or scattering of direct solar rays from the sun; commonly, caused by clouds, gases and particles in the atmosphere (shadowed pyranometers). Both components comprise the global solar irradiance (GHI) and can be measured by pyranometers sensors. However, these sensors measure solar irradiance locally, and its implementation through all the Mexican territory has been a difficult task historically due to cost and maintenance [1]. Owing to this, satellite imaging provides a valuable tool for the analysis of cloud behavior and solar irradiance assessment [2]; by replacing traditional radiometers with pixel information

J. M. Callejas-Cornejo
PICYT—Centro de Investigaciones en Optica A. C., Unidad Aguascalientes, Prol. Constitución 607, Fracc. Reserva Loma Bonita, C.P. 20200 Aguascalientes, Ags, Mexico

M. I. Peña-Cruz (✉) · L. M. Valentín-Coronado
CONACYT—Centro de Investigaciones en Optica A. C., Unidad Aguascalientes, Prol. Constitución 607, Fracc. Reserva Loma Bonita, C.P. 20200 Aguascalientes, Ags, Mexico
e-mail: mipec@cio.mx

A. Martínez-García et al. (eds.), *Progress in Optomechatronic Technologies*,
Springer Proceedings in Physics 233, https://doi.org/10.1007/978-981-32-9632-9_14

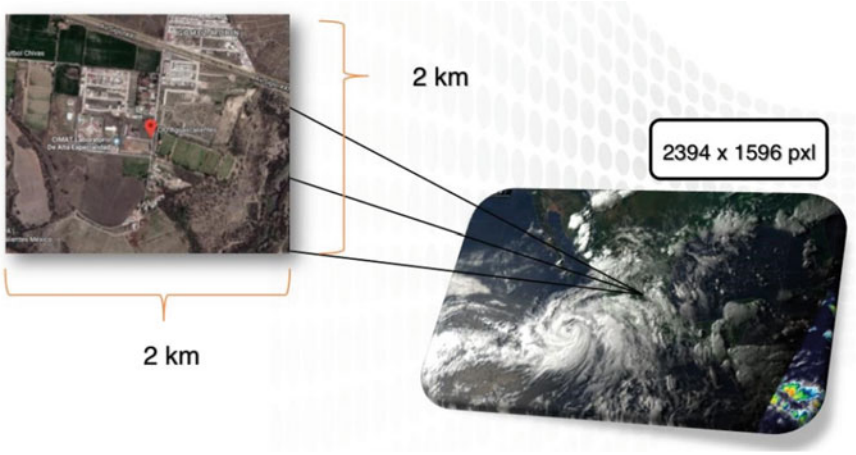

Fig. 1 Satellite image and pixel area equivalence of the zone of interest. Aguascalientes, Ags., Mexico [3]

from the satellite camera, a significant improvement can be achieved by providing higher resolution maps for the Mexican territory, thus making solar technology more cost competitive (see Fig. 1). In this work, only GHI will be addressed for central region of Mexico.

2 Methodology

GOES is a satellite sent to the exosphere by the US National Weather Service (NWS) program in 2016. The objective of the satellite is to provide information flows in the form of images for weather forecast, storm tracking and meteorological research [3].

Taking advantage of the geostationary satellite capabilities, careful analysis of the information provided by the camera is required. Pixel information contains intensity values in the RGB channels. This has to be related accordingly depending on whether there is cloudiness present in the region of interest. Water vapor affects directly the solar irradiance passing through the atmosphere, so greater accumulation of water vapor (clouds) in the atmosphere reduces the irradiance reaching the ground sensor. This can also be observed in the pixel intensity level of the image in the region of interest. The value of each pixel depends on its brightness, intensity, noise and color/gray level that the cloud is scattering back to the camera [4]. By this relationship, an irradiance measurement can be inferred from (1)–(5):

$$GHI_{SAT-TIME} = GHI_{SAT} - (GHI_{SAT} \times CF_{TIME}) \tag{1}$$

$GHI_{SAT-TIME}$ is the global horizontal irradiance calculated by the model (Wm^{-2}).

$$GHI_{SAT} = K_{tm_{(R\_G\_B)}} * GHC_{sky} * \left(0.0001 * K_{tm_{(R\_G\_B)}} * GHC_{sky} + 0.9\right) \quad (2)$$

$$GHC_{sky} = \left[cg_1 \times I_o \times \cos(z) \times e^{-cg2 \times am \times \left[fh1 + fh2 \times (T_1 - 1)\right]}\right] \times e^{0.01 \times am^{1.8}} \quad (3)$$

GHC_{sky} is the global horizontal irradiance from clear sky (Wm^{-2}), (cg_1 and cg_2) are the experimental parameters according to [5], (I_o) is the extraterrestrial solar radiation, (z) is the solar zenith angle, (am) are the coordinates mass of air, (fh_1 and fh_2) are the experimental parameters according to [5] and (T_1) is the Linke turbidity coefficient.

The $K_{tm_{(R\_G\_B)}}$ values of a particular RGB can be defined as:

$$K_{tm_{(R\_G\_B)}} = \left[2.36 * Ci^5_{(R_{G_B})\cdot}\right] - \left[6.2 * Ci^4_{(R_{G_B})\cdot}\right] + \left[6.22 * Ci^3_{(R_{G_B})\cdot}\right] - \left[2.63 * Ci^2_{(R_{G_B})\cdot}\right] - \left[0.58 * Ci_{(R_{G_B})}\right] + 1 \quad (4)$$

with

$$Ci_{(R_{G_B})} = \frac{\alpha - \alpha_{\min}}{\alpha_{\max} - \alpha_{\min}} \quad (5)$$

where Ci corresponds to cloud index and α is the pixel channel intensity of the camera for a particular region of interest.

CF_{TIME} corresponds to a correction time factor that is applied to the pixel irradiance values due to the albedo scattering reaching the satellite camera from early to late hours of the day (see Table 1).

An algorithm developed by the CIO is connected via remote communication with UNAM's National Laboratory of Earth Observation (LANOT by its Spanish acronym) [3]. Images are provided by the satellite at a 15-min interval and stored in the CIO's database. The region of interest of Aguascalientes city (coordinates:

Table 1 Correction factor (CF_{TIME}) related to time

Time	CF
08:00:00 a.m.	0.36
09:00:00 a.m.	0.33
10:00:00 a.m.	0.20
11:00:00 a.m.	n/a
12:00:00 p.m.	n/a
01:00:00 p.m.	n/a
02:00:00 p.m.	n/a
03:00:00 p.m.	n/a
04:00:00 p.m.	−0.15
05:00:00 p.m.	−0.51
06:00:00 p.m.	−0.75

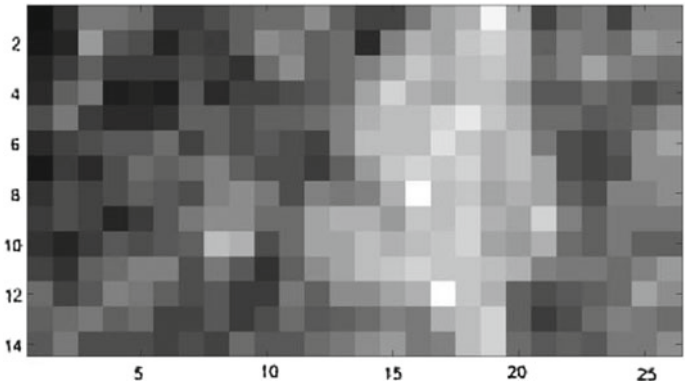

Fig. 2 Pixel zone of interest (approximately 1456 km^2), corresponding to Aguascalientes city, Ags., Mexico (coordinates: 21°50′40.4″N—102°20′34.8″W)

21°50′40.4″N—102°20′34.8″W) is identified (see Fig. 2) and processing of GHI using (1)–(5) is carried out. Data are compared with a scientific-grade solarimetric station (GHI SOLYS) located at the same region of interest.

3 Results

The results presented here are based on selecting different cases of cloudiness for the selected region (21°50′40.4″N—102°20′34.8″W) in order to test the algorithm in different scenarios.

3.1 Scenario I: Sunny Day

The results presented here are based on June 4, 2018 in Aguascalientes City, for a sunny day scenario.

From Fig. 3, green circles represent the output response of global horizontal irradiance from total clear sky calculated analytically; this means a zero cloudiness day. Blue line represents the irradiance output response from the solarimetric station and red line represents the output response of the global horizontal irradiance calculated by the model according to the applied digital image processing.

A very good agreement is found between the irradiance values obtained by the $GHI_{SAT-TIME}$ and the solarimetric station data. Maximum differences of irradiance can be noticed at 11:00 a.m. and minimum differences can be noticed at 8:00 a.m. according to Table 2.

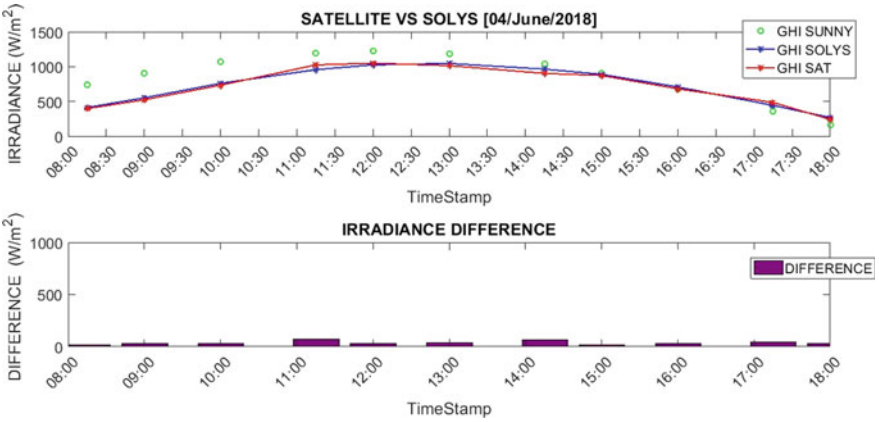

Fig. 3 $GHI_{SAT-TIME}$ versus GHI SOLYS: comparison between solar irradiance numerical model versus data from the solarimetric station on a sunny day

Table 2 $GHI_{SAT-TIME}$ versus GHI SOLYS and its difference throughout a sunny day in Wm^{-2}

Time	GHI SAT	GHI SOLYS	Difference
08:00:00 a.m.	396.48	412.80	16.32
09:00:00 a.m.	523.37	551.90	28.53
10:00:00 a.m.	733.23	760.10	26.87
11:00:00 a.m.	1025.4	956.00	69.36
12:00:00 p.m.	1050.7	1026.00	24.71
01:00:00 p.m	1014	1046.00	31.99
02:00:00 p.m.	902.34	964.00	61.66
03:00:00 p.m.	872.4	889.00	16.60
04:00:00 p.m.	680.58	707.40	26.82
05:00:00 p.m.	485.82	442.20	43.62
06:00:00 p.m.	240.27	267.90	27.63

The difference in irradiance for each particular hour of the sunny day scenario is observed in Table 2.

3.2 Scenario II: Partly Sunny Day

The results presented here are based on May 4, 2018 in Aguascalientes City, for a partly sunny day scenario.

Figure 4 shows that the behavior of the model presents a good trend, although there are some hours that the calculated irradiances differ slightly from the measured

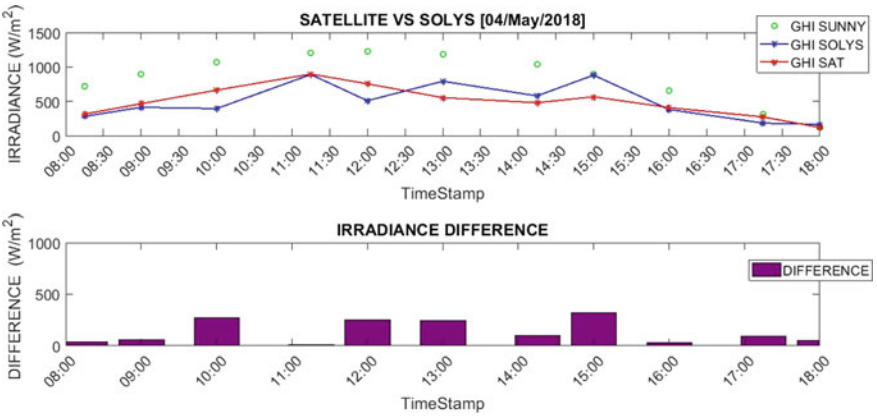

Fig. 4 $GHI_{SAT-TIME}$ versus GHI SOLYS: comparison between solar irradiance numerical model versus data from the solarimetric station on a partly sunny day

Table 3 $GHI_{SAT-TIME}$ versus GHI SOLYS and its difference throughout a partly sunny day in Wm^{-2}

Time	GHI SAT	GHI SOLYS	Difference
08:00:00 a.m.	315.72	281.50	34.22
09:00:00 a.m.	465.6	413.30	52.30
10:00:00 a.m.	662.95	394.40	268.55
11:00:00 a.m.	896.82	890.00	6.82
12:00:00 p.m.	754.48	509.50	244.98
01:00:00 p.m.	551.61	792.30	240.69
02:00:00 p.m.	478	579.50	101.50
03:00:00 p.m.	566.25	881.00	314.75
04:00:00 p.m.	408.76	381.20	27.56
05:00:00 p.m.	272.97	183.30	89.67
06:00:00 p.m.	119.69	165.30	45.61

data. Maximum difference value is observed at 3:00 p.m. while minimum value is observed at 11:00 a.m.

The difference in irradiance for each particular hour of the partly sunny day scenario is observed in Table 3.

3.3 Scenario III: Cloudy Day

The results presented here are based on May 13, 2018 in Aguascalientes City, for a cloudy day scenario.

Figure 5 shows that on a cloudy day the behavior of the model presents a good

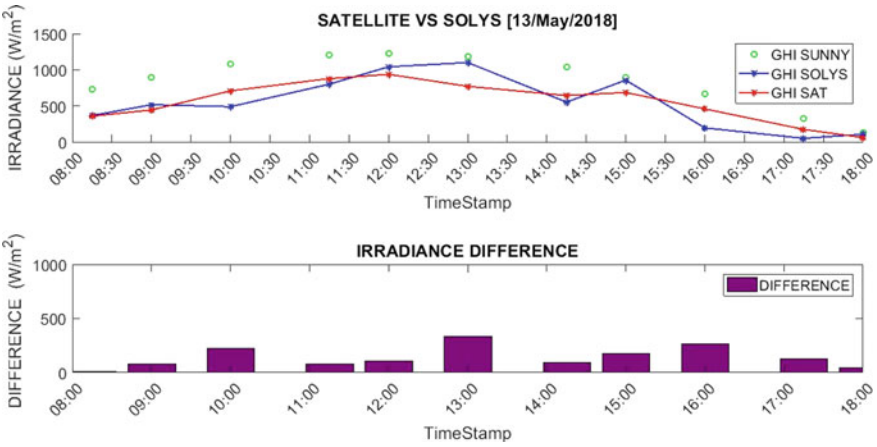

Fig. 5 $GHI_{SAT-TIME}$ versus GHI SOLYS: comparison between solar irradiance numerical model versus data from the solarimetric station on a cloudy day

trend, but maximum error margins are slightly higher than previous cases. In particular, 1:00 p.m. shows the biggest irradiance difference throughout the day, with a value of 330 Wm^{-2}, while the minimum difference occurs at 8:00 with 9 Wm^{-2}.

The irradiance difference for each particular hour of the cloudy day scenario is observed in Table 4.

Table 4 $GHI_{SAT-TIME}$ versus GHI SOLYS and its difference throughout a partly cloudy day in Wm^{-2}

Time	GHI SAT	GHI SOLYS	Difference
08:00:00 a.m.	357.63	366.90	9.27
09:00:00 a.m.	443.35	516.30	72.95
10:00:00 a.m.	708.28	489.30	218.98
11:00:00 a.m.	878.26	801.00	77.26
12:00:00 p.m.	937.03	1042.00	104.97
01:00:00 p.m.	770.68	1101.00	330.32
02:00:00 p.m.	643.87	552.00	91.87
03:00:00 p.m.	685.7	857.00	171.30
04:00:00 p.m.	458.03	194.90	263.13
05:00:00 p.m.	172.71	50.65	122.06
06:00:00 p.m.	61.061	106.40	45.34

3.4 Scenario III: Full Cloudy Day

The results presented here are based on May 16, 2018 in Aguascalientes City, for a full cloudy day scenario (Fig. 6).

It can be noticed that similar trend behavior as in previous cases is observed, and that the overall performance has a good agreement with the measured data, but there are some particular hours where the model irradiance differs significantly from the solarimetric station. In particular, mid-day presents the highest disagreements values.

The irradiance difference for each particular hour of full cloudy day scenario is observed in Table 5.

Table 6 presents the average error for particular weather scenarios. It can be

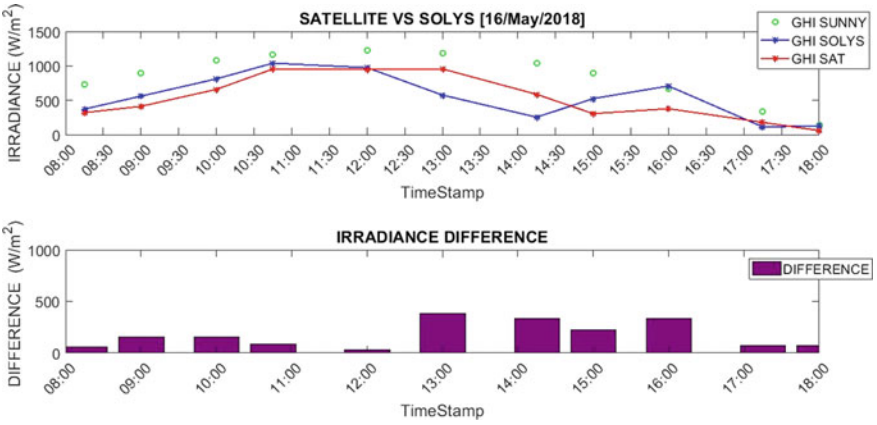

Fig. 6 $GHI_{SAT-TIME}$ versus GHI SOLYS: comparison between solar irradiance numerical model versus data from the solarimetric station on a full cloudy day

Table 5 $GHI_{SAT-TIME}$ versus GHI SOLYS and its difference throughout a full cloudy day in Wm^{-2}

Time	GHI SAT	GHI SOLYS	Difference
08:00:00 a.m.	320.03	372.10	52.07
09:00:00 a.m.	411.79	560.50	148.71
10:00:00 a.m.	658.92	811.00	152.08
11:00:00 a.m.	954.85	1040.00	85.15
12:00:00 p.m.	947.22	975.00	27.78
01:00:00 p.m.	956.45	576.00	380.45
02:00:00 p.m.	585.69	254.10	331.59
03:00:00 p.m.	303.94	524.50	220.56
04:00:00 p.m.	376.58	708.20	331.62
05:00:00 p.m.	178.36	113.70	64.66
06:00:00 p.m.	58.515	126.60	68.09

Table 6 Daily average $GHI_{SAT-TIME}$ versus GHI SOLYS error: weather scenarios (percentage)

Weather	Average error (%)
Sunny day	5
Partly cloudy day	28
Cloudy day	51
Completely day	42

seen that the algorithm behaves with good concordance for sunny days and partially cloudy days. Nevertheless, there is still much room to improve when heavy amount of clouds are present in the atmosphere.

Considering that the uncertainty from specialized sensors varies from around 5 to 10%, expressed in terms of irradiance which range from 50 to 100 Wm^{-2} typically, the developed tool presents good behavior overall. However, a more exhaustive analysis needs to be carried out in order to determine why such differences are present when heavy cloudiness appears at mid-day hours.

4 Conclusions

The developed tool is capable of generating historical solar irradiance values for the Mexican territory by processing pixel information and correlating it with the cloudiness factor with good agreement when compared to a scientific-grade solarimetric station. The model behaves with outstanding agreement when sunny or partly sunny days are present. However, when heavy clouds are present, the model tends to overestimate the solar irradiance for mid-day hours (1:00 p.m.–4:00 p.m.) in particular. This phenomenon has to be studied more thoroughly, as the dynamic range of the satellite camera might not be able to identify cloud pixel intensity values correctly and new adjusting parameters need to be proposed.

Although the algorithms presented here has room to improve, this implementation might become a valuable tool for generating historical solar irradiance maps for the Mexican territory and providing certainty for the solar power industry, paving the way to a more reliable solar national technology.

References

1. M. Valdés-Barrón, D. Riveros-Rosas, C. Arancibia-Bulnes, R. Bonifaz, The solar resource assessment in Mexico: state of the art. Energy Procedia. **57**, 1299–1308 (2014). https://doi.org/10.1016/j.egypro.2014.10.120
2. D. Riveros-Rosas, C. Arancibia-Bulnes, R. Bonifaz, M.A. Medina, R. Peon, M. Valdes, Analysis of a solarimetric database for Mexico and comparison with the CSR model. Renew. Energy **75**, 21–29 (2015). https://doi.org/10.1016/j.renene.2014.09.013
3. http://www.lanot.unam.mx

4. L. Diabaté, G. Moussu, L. Wald, Description of an operational tool for determining global solar radiation at ground using geostationary satellite images. Sol. Energy **42**(3), 201–207 (1989). Elsevier
5. R. Perez, Time specific irradiances derived from geostationary satellite images. J. Sol. Energy Eng. **124**(1) (2002). https://doi.org/10.1115/1.1435667

Toward the Development of a Low-Cost High-Precision Instrumented Mini-Solar Sensor

Arturo Díaz Ponce, Ruben Garrido, Manuel I. Peña-Cruz, Luis V. Coronado, Iván Salgado Transito, Fernando Martell and Samantha A. Cajero Roodriguez

Abstract In this work the development of a low-cost solar sensor capable of locating the position of the sun through photosensors is presented. In addition, the sensor is integrated with the instrumentation to provide the data for a solar position algorithm. As preliminary results, we present the methodology followed for the development of the sensor, as well as the theoretical characterization carried out through the Tonatiuh software.

1 Introduction

A good solar tracker for concentrating solar power (CSP) systems is a key element for achieving maximum efficiency. In practice, there are two ways of locating the position of the sun with respect to an observer on earth: (i) solar location in open

A. Díaz Ponce (✉) · M. I. Peña-Cruz · L. V. Coronado · I. Salgado Transito · F. Martell · S. A. Cajero Roodriguez
CONACYT—Centro de Investigaciones en Óptica, A. C., Unidad Aguascalientes, Prol. Constitución 607, 10 Fracc. Reserva Loma Bonita, 20200 Aguascalientes, Mexico
e-mail: adiaz@cio.mx

M. I. Peña-Cruz
e-mail: mipec@cio.mx

L. V. Coronado
e-mail: luismvc@cio.mx

I. Salgado Transito
e-mail: isalgadotr@cio.mx

F. Martell
e-mail: fmartell@cio.mx

S. A. Cajero Roodriguez
e-mail: sam.cajero019@gmail.com

R. Garrido
CINVESTAV-IPN, Departamento de Control Automático, Av. IPN 2508 San Pedro Zacatenco, 07360 Mexico City, Mexico
e-mail: garrido@ctrl.cinvestav.mx

A. Martínez-García et al. (eds.), *Progress in Optomechatronic Technologies*, Springer Proceedings in Physics 233, https://doi.org/10.1007/978-981-32-9632-9_15

loop and (ii) solar location in closed loop. In the first case, the estimation of the position is made through the solar coordinates that require some input parameters, such as the observer's geographical position, date, time, altitude and orientation, among others. Open-loop solar tracking systems have the advantage of not being affected by cloudiness. However, it is essential to provide these systems with the necessary instrumentation to obtain the input parameters in real time. On the other hand, closed-loop solar systems use photosensors, and although these systems are more complex, they achieve a high solar tracking precision. Therefore, they are used when accuracy is paramount, for instance in CSP systems. It is also worth mentioning that in recent years, hybrid solar tracking systems have been proposed. In these systems, an algorithm based on the solar coordinates provides rough tracking, and a closed-loop tracking photodiode-based sensor allows for fine tracking. One of the most precise commercial solar sensors is the MASS SENSOR from Solar MEMS Technologies, which measures direct solar radiation (DNI) and provides the sun-ray angle for close-loop control, while the azimuth and elevation for open-loop control. Besides, this sensor has a low power consumption of about 34 mA. Furthermore, the MASS SENSOR has a magnetometer to guide the tracking system to the magnetic south or north and an accelerometer to measure the inclination of the tracking system structure with respect to a horizontal reference frame. The above features make this sensor useful in open-loop and hybrid solar tracking. Nevertheless, its price is high (€1250, VAT not included) and it is not advisable for developing low-cost CSP systems.

On the other hand, a large number of solar sensors have been reported in previous works [1] and each one has different characteristics depending on its application. In this paper we present the development of a solar sensor integrated by a quadrant of photodiodes, an accelerometer, a magnetometer, an altimeter, a barometer and a temperature sensor, which provide the necessary data to carry out open-loop and hybrid tracking without using external instrumentation.

2 Methodology

The development of the proposed sensor is divided into two parts. The first part consists of using a commercial quadrant of photodiodes QP5.8-6 TO (5.8 mm^2 quadrant PIN detector), shown in the inset of Fig. 1, for determining the apparent position of the sun. The QP5.8-6 TO produces a current proportional to the incoming sun radiation. It consists of four separate P on N silicon photosensitive surfaces. This device is chosen because of their high sensitivity, small gap and low dark current. To detect only direct radiation from the sun, the QP5.8-6 TO is covered by a plastic cap with a 1 mm hole, as shown in Fig. 1. Every photodiode F_i of the detector, where $i = 1$–4 is the photodiode number, produces a current I_{Fi} proportional to the incident radiation, which is subsequently converted into a voltage V_{Fi} by a transimpedance quad ampli-

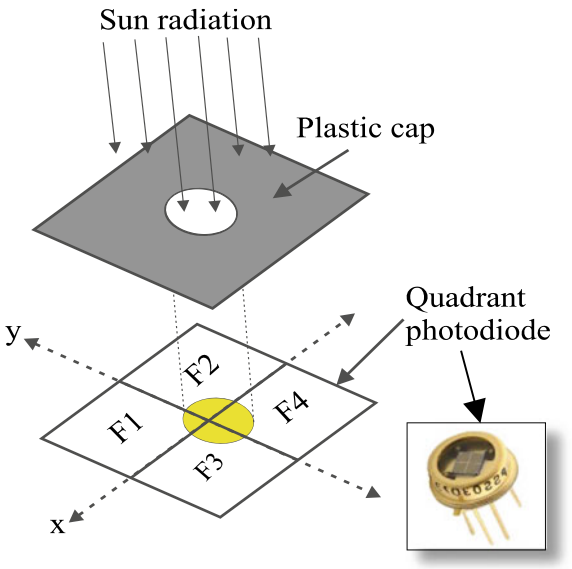

Fig. 1 Four quadrant photodetector QP5.8-6 TO

fier SLG88104 [2]. With the photodiode configuration, shown in Fig. 1 and (1) and (2), the ideal position occurs when the tracking system places the sensor perpendicular to the sun's rays; then the following equalities hold $V_{F1} = V_{F2} = V_{F3} = V_{F4}$; that is $x = 0$ and $y = 0$. On the contrary, when the sensor is not perpendicular to the sun, a voltage difference between the photodiodes is generated, which is detected by a controller driving the tracking system until the solar sensor is placed at its ideal position.

$$x = \frac{(V_{F1} + V_{F3}) - (V_{F2} + V_{F4})}{V_{F1} + V_{F2} + V_{F3} + V_{F4}} \tag{1}$$

$$y = \frac{(V_{F1} + V_{F2}) - (V_{F3} + V_{F4})}{V_{F1} + V_{F2} + V_{F3} + V_{F4}} \tag{2}$$

The second part of the mini-solar sensor consists of a microcontroller (μC) PIC18f2550 that processes the signals from all the elements that are part of the sensor (see Fig. 2): a single chip MPU-9250 with a built-in three-axis gyro, a three-axis accelerometer and a thermometer, whose characteristics are shown in Table 1, a BMP280 barometric pressure sensor and a QMC5883 L module that indicates the direction of the magnetic north with the objective of referencing the tracking structure. The experimental prototype, including the instrumentation of the designed sensor, is shown in Fig. 3. The communication between the microcontroller and the module is done through the communication protocol I^2C.

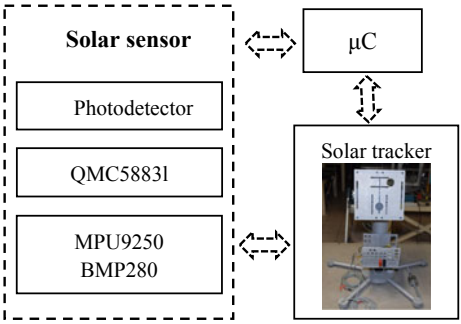

Fig. 2 General configuration of the solar sensor with the tracking system

Table 1 Characteristics of the MPU9250 + BMP280 sensors

Power supply	3–5 V
Gyroscopes range	±250, ±500, ±1000, ±2000°/s
Acceleration range	±2, ±4, ±8, ±16 g
Field range	±4800 uT
Pressure range	300–1100 hPa

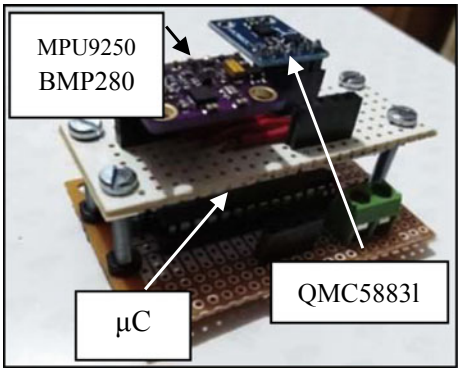

Fig. 3 Experimental prototype including the instrumentation

Using the data provided by the elements of the proposed sensor, a solar tracking algorithm described in [3] is implemented in a µC in order to perform a hybrid solar tracking without the use of other external sensors. It is worth mentioning that the cost of the proposed sensor is less than 130USD, which is a lot cheaper than the cost of high-precision commercial solar sensors [4]. Figure 4 shows the proposed design.

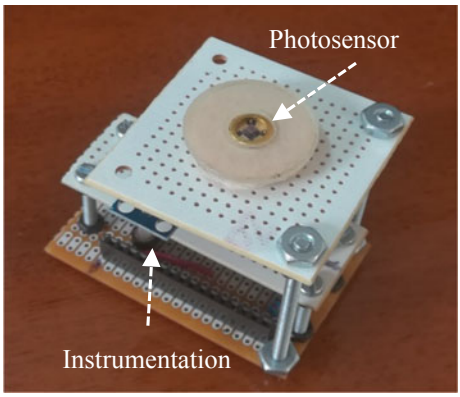

Fig. 4 Design of the proposed sensor

3 Results

Until now we have developed the first solar sensor prototype. The theoretical characterization of the sensor is carried out using the Tonatiuh ray tracing software. Figure 5 shows the optical analysis of the solar sensor in a perpendicular position with respect to the sun's rays; that is, when the conditions $x = 0$ and $y = 0$ are fulfilled (see Fig. 6). On the other hand, Fig. 7 shows the analysis of maximum field of view (FOV) of the proposed sensor. As a result of the analysis, we found that it is possible to locate the position of the sun at an angle maximum deviation between the normal of the sensor and the sun's rays of 30°; that is, FOV = 30° (see Fig. 8). It is important to mention that a wide opening angle decreases the accuracy of the sensor. Thus, it is initially necessary to pre-orient the solar sensor until the sun radiation falls within the sensor opening angle. The pre-orientation will be carried out through a solar position algorithm running on the microprocessor.

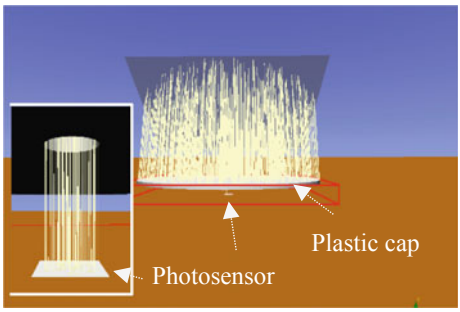

Fig. 5 Simulation of the ideal position of the solar sensor

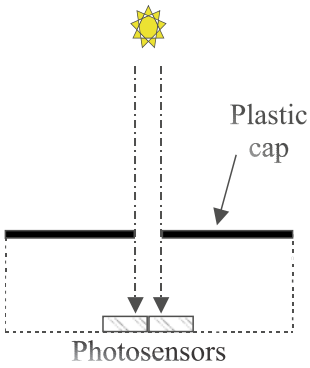

Fig. 6 Ideal position of the solar sensor: $x = 0$ and $y = 0$

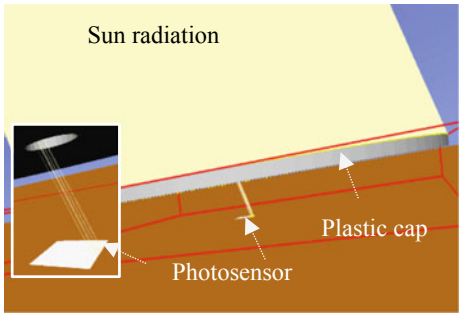

Fig. 7 Field of view of the designed sensor

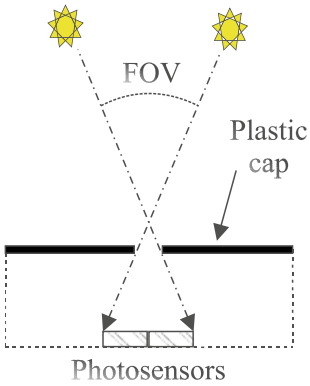

Fig. 8 Maximum FOV reached by the sensor

4 Conclusion

In this work we have presented the preliminary results obtained in the development of a low-cost solar sensor. The sensor provides two voltage signals, both proportional to the angle between the normal of the sensor plane and the sun's rays. These signals drive a tracking system whose objective is to position the sensor perpendicular to the

sun. Furthermore, the proposed measurement unit also includes an accelerometer, a magnetometer, an altimeter, a barometer and a temperature sensor that feed the necessary data to carry out hybrid tracking without using external instrumentation. The implementation of the solar tracking algorithm in the microprocessor is still under development.

We believe that this sensor will improve the performance of hybrid tracking systems, reaching the level of precision required in high solar concentration systems at a low cost.

Acknowledgments The authors would like to thank the support of Juan Margarito Sarabia Torres.

References

1. L. Salgado-Conrado, A review on sun position sensors used in solar applications. Renew. Sustain. Energy Rev. (2017)
2. SILEGO *SLG88103/4* (2017)
3. C. Cornwall, A. Horiuchi, C. Lehman, *NOAA Solar Calculator* (Department of Commerce, USA, 2015), p. 27
4. Solar-Technologies, *Sun Sensor ISS-DX: Technical Specifications.* Tecnoincubadora Marie Curie, Leonardo da Vinci 18, C.P. 41092, Seville, Spain

Semi-automatic Platform for Fabry–Perot Microcavities Construction

Carmen E. Domínguez-Flores, Josué I. Basulto, Daniel López-Cortés and David Monzón-Hernández

Abstract A semi-automatic and reconfigurable mechatronic stage was designed and implemented to control precisely the fiber cleaving in the process of manufacturing Fabry–Perot (FP) microcavities. FP interferometers with a cavity length as small as 5 μm were used with the system. The theoretical reflectance of the fiber cavities was studied by the interference phenomenon pattern simulation. Then, a comparison technique between the experimental and simulated spectra was performed for the length calculation of the FP cavities fabricated. The optical fiber structures presented can be used to develop sensor in many fields, ranging from the industrial to sensing applications.

1 Introduction

Fiber-optic interferometers have intrinsic and important advantages for sensing applications, including high resolution, good electromagnetic interference immunity, and fast response, among others. These interesting properties had attracted the study of many different configurations for diverse applications. The simplest structure is the fiber-optic Fabry–Perot interferometer (FFPI), which is attractive for its well-known high sensitivity and its impact on sensing in harsh environment [1]. The FFPI sensors have been intensively used since the early 1980s for the detection of physical parameters, such as temperature, strain, gas phase concentrations, and refractive index [2]. The most common fabrication process of the FFPIs consists of three steps: wet chemical etching, fusion splicing, and cleave. The FFPI structure is simple, in contrast to fiber Mach–Zehnder and Michelson interferometers where the use of couplers can potentially obscure the sensor operation and data analysis [3]. In works reported earlier, it has been found that the size and shape of the cavity plays an important role on the performance of these interferometers [4], making crucial the cleaving technique. In this work, a cleaving system using a semi-automatic platform for the construction of micrometric FFPI is proposed and implemented. Several FFPIs with a cavity

C. E. Domínguez-Flores (✉) · J. I. Basulto · D. López-Cortés · D. Monzón-Hernández
Centro de Investigaciones en Óptica A. C., Loma del Bosque 115, 37150 León, GTO, Mexico
e-mail: carmendmz@cio.mx

A. Martínez-García et al. (eds.), *Progress in Optomechatronic Technologies*,
Springer Proceedings in Physics 233, https://doi.org/10.1007/978-981-32-9632-9_16

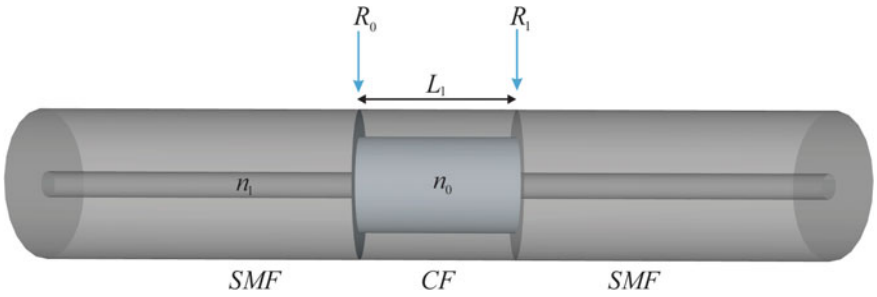

Fig. 1 Basic scheme of a FFPI, consisting of a capillary fiber spliced between two SMFs

length ranging from 5 to 300 μm were fabricated in order to characterize the system performance; the length of each structure was calculated through the interference phenomenon simulation [5].

2 Fundamentals of the Fiber-Optic Fabry–Perot Interferometers (FFPI)

A conventional FFPI sensor consists of a fiber section with special structure (cavity) sandwiched between two semi-reflecting surfaces, with reflectivity R_0 and R_1, respectively. The cavity acts as the device-sensing element and the sensitivity depends on its length; it has been shown that as the length is reduced, the sensitivity is incremented. In a sensor, the sensitivity is one of the most important factors to consider; in this circumstance, it is very important to have special attention to this parameter and fabricate the samples in a systematic way.

A typical optical fiber structure is shown in Fig. 1, which is constructed with a segment of capillary fiber (CF) spliced between two SMFs acting as a reflecting surfaces and each one with reflectivity R_0 and R_1. The reflectivity of this kind of FFPI structure is described by the (1), where φ is the initial phase and n_0 is the index refraction of the air.

$$R = R_0 + (1 - R_0)^2 R_1 + 2(1 - R_0)\sqrt{R_0 R_1}\cos(2kn_0 L_1 + \varphi) \tag{1}$$

In this work, the FFPIs fabricated were based on this kind of structure.

3 Platform Design and Fabrication

In order to construct a FFPI with a specific cavity length, some variables should be kept in mind; the most important are the optical fiber alignment, the cleaving process, and the splice. As the splice depends only on some parameter that can be adjusted

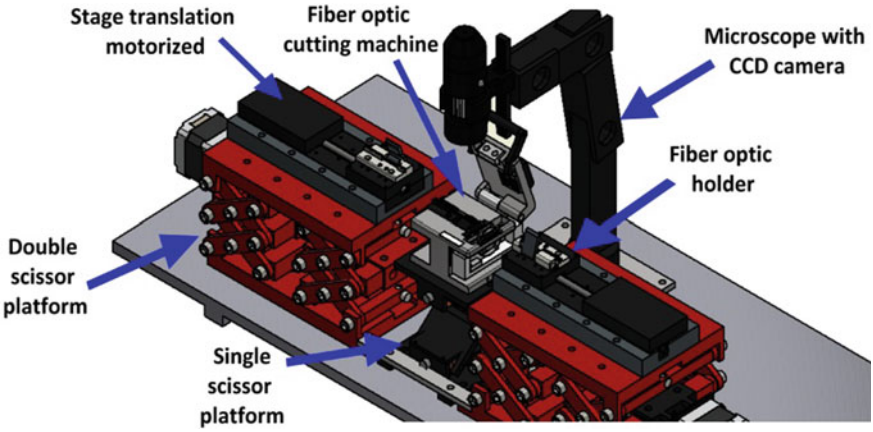

Fig. 2 Scheme of the semi-automatic platform designed and constructed

in the splicer machine, the other variables should be addressed in a different way. With this purpose, a cleaving system was designed and implemented. In Fig. 2, a representation of the portable platform manufactured is shown; this includes two double-scissor platforms to align the two bases heights for the motorized translation stages, two fiber-optic holders in order to maintain the alignment and the position of the fiber, and finally a scissor platform to adjust the cleaver position. It is worth to mention that all the mechanical components were designed and constructed in the center facilities.

A fiber cleaver FC-6, Sumitomo Electric was adapted for cleaving. Two compact motorized translation stages, MTS50-Z8E and THORLABS, with minimal increment movement of 0.05 μm were used to control the fiber movement; first, to align the splice with the blade, and second, to set the desired length of the cavity with precision. An Edmund Optics microscope and a charge-coupled device (CCD) with a resolution of 640 $\times$ 480 pixels were installed for inspection and monitoring of the fiber cleaving process. With this robust system, it is possible to increment the repeatability in the manufacture process of the FFPIs, because several variables that affect in a direct way the device performance can be discarded. To complement the system, a user-friendly computer interface using the specialized software LabVIEW was designed, in order to inspect and control the quality of the samples during the fabrication. In Fig. 3 the interface is presented, and on the screen, an image of the splice (SMF-CP) aligned with the blade (vertical shaded line) is shown. The integration of the whole system permits the easy and simple production of FFPIs serially and with a significant reduction of the error.

4 Fabrication and Characterization of Fabry–Perot Cavities

Once the platform was completely assembled and all the components tested, the first step was to establish the real capabilities of the platform by finding the smallest cavity able to be fabricated. For this reason, several samples were fabricated with the following procedure: first, using a previously tested program with optimal parameters, a SMF was spliced to a CF in the fusion machine; subsequently, the fibers were placed in the platform, where the splice was aligned to the blade of the cleaver (see Fig. 3) with the help of the motorized translation stages, and from there, the splice was moved and cleaved at the wanted length; finally, the cavity was closed splicing another SMF on the other side of the CF segment.

In order to investigate the cavity length, their experimental reflectance was obtained using an interrogator Si255 of Micron Optics, with a wide range from 1460 to 1620 nm, a coupler, and a photodetector. Then using (1), a spectrum simulation was performed, sweeping the length until it was fitted with the experimental. The results for three different cavities are shown in Fig. 4, resulting in lengths of: (a) 7.22 μm, (b) 5.401 μm, and (c) 7.0755 μm, respectively. With this technique, the cavity lengths were calculated by means of comparing their experimental and simulated spectra.

The calculated lengths of the smallest cavities fabricated are shown in Table 1. The results demonstrate that it is possible to build small FP cavities serially with a standard deviation in the cavity length L_1 of 0.97 μm.

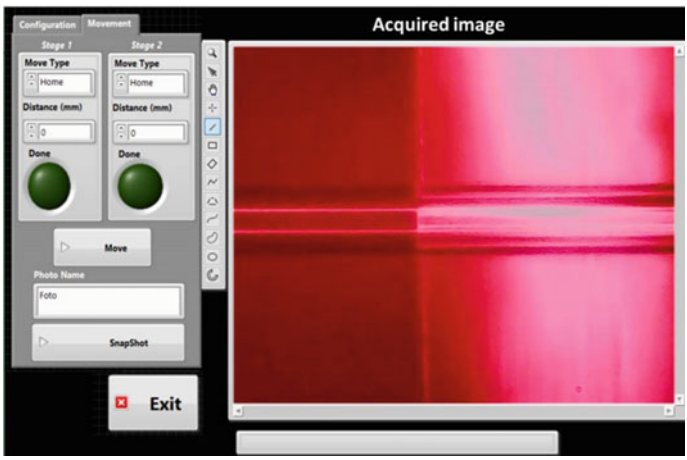

Fig. 3 Screen of the computer interface, where a splice aligned with the blade of the cleaver is displayed

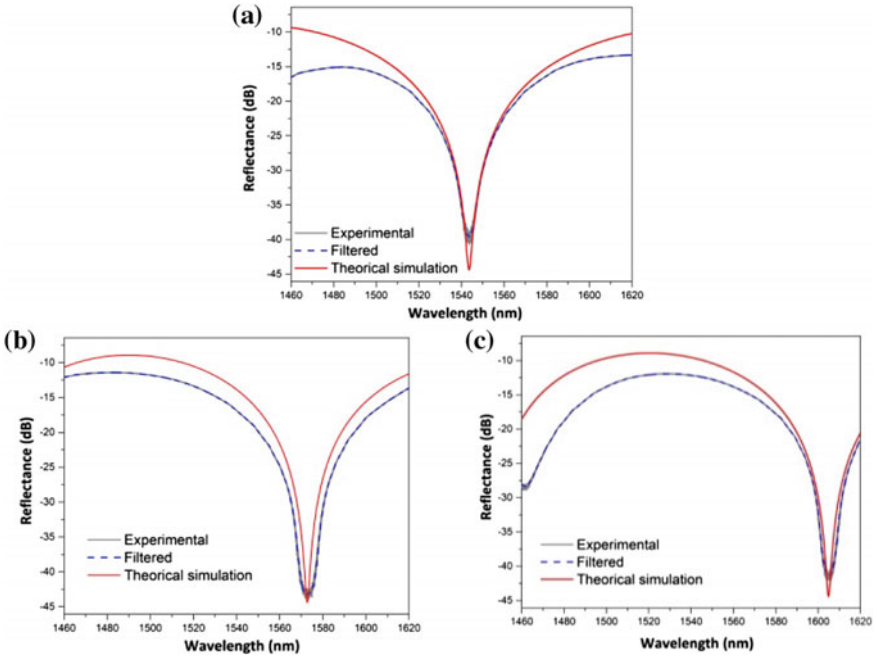

Fig. 4 Comparison of the measured reflectance with its theoretical approximation, for three different cavities

Table 1 Calculated lengths of the cavities FP constructed

No.	L_1 (μm)
1	4.9
2	5.0
3	5.1
4	5.1
5	5.4
6	5.4
7	6.4
8	6.4
9	7.0
10	7.2
11	7.3
12	7.4
Standard deviation	0.9
Mean	6.6

5 Conclusion

A semi-automatic platform was designed and built to manufacture FP cavities in a simple and repeatable way. FFPIs were fabricated and the experimental spectra were compared with the simulated spectra calculated from the interference model. It was shown that it is possible to build FP cavities up to 4.92 μm. The final cavity length was estimated comparing the simulated and experimental spectra. This platform allowed us to fabricate FFPI with potential applications to develop high-sensitivity strain sensors and other physical variables.

References

1. T. Yoshino, T. Ose, K. Kurosawa, K. Itoh, Fiber-optic Fabry-Perot interferometer and its sensor applications. IEEE Trans. Microw. Theory Tech. **30**, 1612–1621 (1982). https://doi.org/10.1109/TMTT.1982.1131298
2. D.-W. Duan, Y. Rao, Y.-S. Hou, T. Zhu, Microbubble based fiber-optic Fabry-Perot interferometer formed by fusion splicing single-mode fibers for strain measurement. Appl. Opt. **51**, 1033 (2012). https://doi.org/10.1364/AO.51.001033
3. L.H. Chen, C.C. Chan, R. Menon, P. Balamurali, W.C. Wong, X.M. Ang, P.B. Hu, M. Shaillender, B. Neu, P. Zu, Z.Q. Tou, C.L. Poh, K.C. Leong, Fabry-Perot fiber-optic immunosensor based on suspended layer-by-layer (chitosan/polystyrene sulfonate) membrane. Sens. Actuators, B Chem. **188**, 185–192 (2013). https://doi.org/10.1016/j.snb.2013.06.093
4. F.C. Favero, L. Araujo, G. Bouwmans, V. Finazzi, J. Villatoro, V. Pruneri, Spheroidal Fabry-Perot microcavities in optical fibers for high-sensitivity sensing. Opt. Express **20**, 7112 (2012). https://doi.org/10.1364/OE.20.007112
5. C. Domínguez, Diseño, fabricación y caracterización de inferferómetros Fabry-Perot de fibra óptica extrínsecos y su aplicación en sistemas de sensado de variables físicas, Thesis of Master Degree (Centro de Investigaciones en Óptica A. C. León, Guanajuato, México, 2018)

Adaptive 3D Object Pose Estimation Through Particle Swarm Optimization

Akbar Assa and Farrokh Janabi-Sharifi

Abstract Estimating the 3D pose of objects is an important problem in vision-based robotics. Kalman filters are commonly used as efficient solutions to this problem. However, the performance of these filters deteriorates when system's noise statistics are not known a priori. This work proposes an adaptive scheme based on particle swarm optimization (PSO) to adjust the measurement noise covariance of the filter. The experimental results confirm the effectiveness of the proposed adaptive solution for Kalman-based pose estimation with uncertain noise statistics.

1 Introduction

Acquiring the pose of observed objects is a crucial requirement in many vision-based robotic and computer vision applications, such as visual servoing [1] and augmented reality [2]. Numerous methods were proposed in the literature to accurately estimate the pose of the objects exploiting the features extracted from images (see, for instance, [3–5]). However, most of these methods approximate the relative pose of the objects without considering the measurement noise, induced by the camera and the image processing algorithms. In contrast, Kalman filters provide accurate estimations despite the uncertainties of the visual measurements and therefore have gained popularity in computer vision and robotic applications.

While Kalman-based pose estimation algorithms perform well under known noise statistics, their performance diminishes in the absence of such knowledge. Traditionally, adaptive methods such as multiple model-based schemes [6] and innovation-based methods [7] are used to simultaneously adjust the noise parameters of the filter using the observed measurements. However, the former methods combine the estimations of multiple filters each tuned with a set of parameters without adjusting the

A. Assa (✉)
University of Toronto, Toronto, Canada
e-mail: akbar.assa@utoronto.ca

F. Janabi-Sharifi
Ryerson University, Toronto, Canada
e-mail: fsharifi@ryerson.ca

A. Martínez-García et al. (eds.), *Progress in Optomechatronic Technologies*,
Springer Proceedings in Physics 233, https://doi.org/10.1007/978-981-32-9632-9_17

noise parameters, while the latter schemes estimate the noise parameters from the innovation sequence, assuming the system to be linear. In another group of works, optimization-based methods, in particular PSO [8], were used to estimate the noise parameters. These works were focused on adaptation of the process noise, assuming the measurement noise to be known. However, the measurement noise covariance is the most important parameter of the filter and its estimation is usually non-trivial.

This work proposes an adaptive extended Kalman filter (AEKF) for camera pose estimation. The PSO algorithm is adopted to estimate the measurement noise covariance. The PSO method that is used allows multiple samples of the noise covariance to evolve toward the correct value for the measurement noise covariance. The closeness of the particles to the true value is measured exploiting the measurement likelihood function. The experimental results confirm the effectiveness of the proposed AEKF method for object pose estimation in a robotic application.

2 Pose Estimation and Extended Kalman Filter

To estimate the pose of the object of interest with respect to the camera, the camera images are processed to extract the image features. If the relative position and orientation of the object are parameterized by $L^c_{o,k} = \begin{bmatrix} x^c_{o,k} & y^c_{o,k} & z^c_{o,k} \end{bmatrix}$ and $\Phi^c_{o,k} = \begin{bmatrix} \varphi^c_{o,k} & \theta^c_{o,k} & \psi^c_{o,k} \end{bmatrix}$, where the latter is the minimum representation of the orientation in terms of Euler angles, the image features may be represented as follows, assuming point image features and the pin-hole model for the camera,

$$\begin{bmatrix} u_j & v_j \end{bmatrix}^T = f \begin{bmatrix} \frac{\Gamma^c_o(1)L^o_j + x^c_o}{\Gamma^c_o(3)L^o_j + z^c_o} & \frac{\Gamma^c_o(2)L^o_j + y^c_o}{\Gamma^c_o(3)L^o_j + z^c_o} \end{bmatrix}^T, \tag{1}$$

where $\begin{bmatrix} u_j & v_j \end{bmatrix}$ is the image coordinate of jth feature point, $\Gamma^c_o(i)$ is the ith row of the rotation matrix between the object and camera coordinate frames, L^o_j is the 3D position of the jth feature in object frame, and f is the camera focal length. Using the extracted image coordinates as system measurements, a Kalman filter may be used to estimate the relative pose of the object. For that purpose, the state of the system is selected as a vector of pose parameters and their time derivatives,

$$X^c_{o,k} = \begin{bmatrix} L^c_{o,k} & \Phi^c_{o,k} & \dot{L}^c_{o,k} & \dot{\Phi}^c_{o,k} \end{bmatrix}, \tag{2}$$

The state and its error covariance are initialized through prior knowledge of the initial pose of the object as follows:

$$X^c_{o,0} = X^c_o(0), \tag{3}$$

$$P_0 = P(0), \tag{4}$$

where P_k is the error covariance of the state at time step k. Then, at each time step, first the state and its error covariance are predicted using the dynamics of the system,

$$X^c_{o,k|k-1} = FX^c_{o,k-1}, \tag{5}$$

$$P_{k|k-1} = FP_{k-1}F^T + Q_k, \tag{6}$$

where F is the state transition matrix and Q_k is the process noise covariance. The state and its error covariance are then updated using the acquired image measurement through the camera image at time step k,

$$K_k = P_{k|k-1}H_k^T(H_kP_{k|k-1}H_k^T + R_k)^{-1}, \tag{7}$$

$$X^c_{o,k} = X^c_{o,k|k-1} + K_k\big(Y_k - h(X^c_{o,k|k-1})\big), \tag{8}$$

$$P_k = (I - K_kH_k)P_{k|k-1}(I - K_kH_k)^T + K_kR_kK_k^T, \tag{9}$$

where $h(X^c_{o,k|k-1})$ is the measurement function, H_k is the derivative of the measurement function with respect to state prediction, R_k is the measurement noise covariance, Y_k is the vector of image features, I is the identity matrix, and K_k is the Kalman gain. In order to correctly estimate the object pose, the process and measurement noise covariance matrices (i.e., Q_k and R_k) should be known. However, if these values are not available, they should be estimated using the system measurements. In this work, the adaptation of the measurement noise covariance exploiting the PSO approach is suggested, which is explained in the sequel.

3 Particle Swarm Optimization

Particle swarm optimization offers an interesting solution toward finding a proper value for the measurement noise covariance. In PSO, multiple samples (particles) are initialized first, and then are evolved through a constant velocity approach (i.e., each particle is updated through integration of its velocity). The velocity of each particle is updated iteratively as follows:

$$v^m_{i+1} = av^m_i + b_1r_1(p - \rho^m_i) + b_2r_2(g - \rho^m_i). \tag{10}$$

where ρ^m_i is the position of particle m at iteration i, p is the best particle position in this iteration, g is the global best particle position, a, b_1, b_2, r_1, and r_2 are model parameters. The particle positions are then updated through integration as follows:

$$\rho^m_{i+1} = \rho^m_i + v^m_i. \tag{11}$$

Each particle represents the diagonal parameters of the measurement noise (i.e., $R_k^m = diag(x_k^m)$). The fitness of each particle is measured through its measurement likelihood, that is,

$$\begin{aligned} \text{FIT} &= P(Y_K | R_k^m, X_{o,k|k-1}^c) \\ &= \frac{\exp\left(-\frac{1}{2}\left(Y_k - h(X_{o,k|k-1}^c)\right)^T (H_k P_{k|k-1} H_k^T + R_k^m)^{-1}\left(Y_k - h(X_{o,k|k-1}^c)\right)\right)}{\left|(2\pi (H_k P_{k|k-1} H_k^T + R_k^m))\right|} \end{aligned} \tag{12}$$

At each iteration, the best particle position (p) and global best particle position (g) are found through the FIT function and then the particles velocities and positions are updated. The updating continues till satisfactory FIT value for the global particle position is obtained.

4 Experimental Results

The proposed AEKF is used on data collected from a robotic cell, where a robot-mounted camera is maneuvered around an object with four circular features. The centers of these features are extracted using a blob detector and used as measurements of the filter. The robot and camera are both calibrated. The parameters of the filter are initially set as follows:

$$F = \begin{bmatrix} I_6 & 0.016 I_6 \\ 0_6 & I_6 \end{bmatrix}, Q_k = diag\{0, 0, 0, 0, 0, 0, 25, 1, 1, 36, 36, 36\}, R_k = 10^{-6} I_8,$$

$$X_o^c(0) = \begin{bmatrix} 0.01 & 0.02 & 0.20 & 0 & -0.02 & 0.03 \end{bmatrix}^T, P(0) = 10 I_{12},$$

where I_n is the $n \times n$ identity matrix. The parameters of the PSO adaptation scheme are selected as follows: $a = 0.7$, $r_1 b_1 = 0.06$, and $r_2 b_2 = 0.06$.

In the experiment, the pose of the object is estimated using the proposed AEKF and the estimation results are compared with that of the system without the adaptation mechanism. The estimation error of each algorithm is measured as the absolute difference between the estimated pose value and the ground truth, which is obtained using an optical tracker. The pose estimation error is depicted in Fig. 1. As it can be seen, the proposed adaptive method could adjust the value of the measurement noise covariance correctly to enhance the accuracy of the estimations, while the non-adaptive filter cannot provide accurate result due to lack of knowledge about the measurement noise covariance.

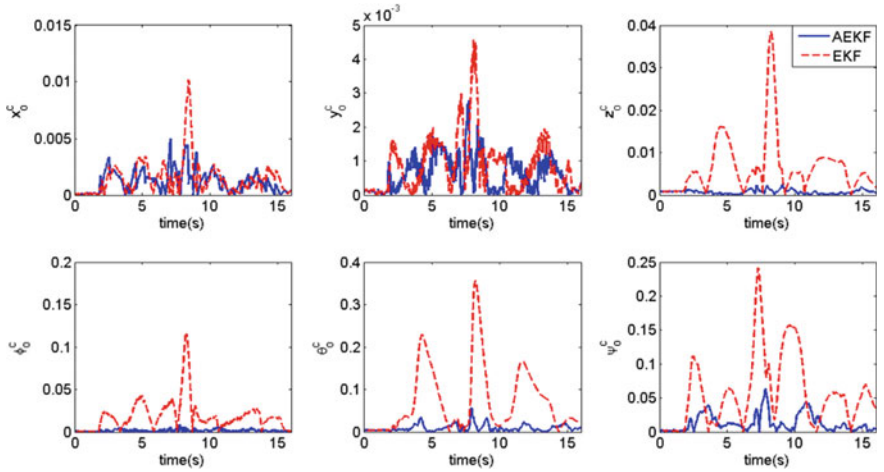

Fig. 1 Pose estimation errors using the proposed AEKF as compared to non-adaptive EKF

5 Conclusion

An AEKF was proposed in this work for accurate pose estimation. In the proposed scheme, the measurement noise covariance was updated using the PSO algorithm, which resulted in satisfactory results in the experiment. In the future works, the adaptation scheme will be extended to encompass a more general form of the measurement noise as well as other filter parameters.

References

1. K. Fathian, J. Jin, S.G. Wee, D.H. Lee, Y.G. Kim, N.R. Gans, Camera relative pose estimation for visual servoing using quaternions, Robot. Auton. Syst. (2018)
2. E. Marchand, H. Uchiyama, F. Spindler, Pose estimation for augmented reality: a hands-on survey. IEEE Trans. Vis. Comput. Graph. **22**(12), 2633–2651 (2016)
3. A. Assa, F. Janabi-Sharifi, Virtual visual servoing for multicamera pose estimation. IEEE/ASME Trans. Mechatron. **20**(2), 789–798 (2015)
4. A. Tejani, R. Kouskouridas, A. Doumanoglou, D. Tang, T.K. Kim, Latent-class Hough forests for 6 DoF object pose estimation. IEEE Trans. Pattern Anal. Mach. Intell. **40**(1), 119–132 (2018)
5. T.N. Tan, G.D. Sullivan, K.D. Baker, Linear algorithms for object pose estimation, in *BMVC92* (Springer, London, 1992), pp. 600–609
6. P.D. Hanlon, P.S. Maybeck, Multiple-model adaptive estimation using a residual correlation Kalman filter bank. IEEE Trans. Aerosp. Electron. Syst. **36**(2), 393–406 (2000)
7. A.H. Mohamed, K.P. Schwarz, Adaptive Kalman filtering for INS/GPS. J. Geod. **73**(4), 193–203 (1999)
8. D.J. Jwo, S.C. Chang, Particle swarm optimization for GPS navigation Kalman filter adaptation. Aircr. Eng. Aerosp. Technol. **81**(4), 343–352 (2009)

Suppression of Kelly Sidebands and Compression of Soliton Spectrum Using a Polarization Imbalance Nonlinear Loop Mirror

Mahrokh Avazpour, Georgina Beltrán Pérez and Evgeny Kuzin

Abstract Cleaning and compressing soliton spectrum is an important part of the all-optical processing systems. In the present work, we report the suppression of Kelly sideband as well as compressing the soliton spectrum through a polarization-imbalanced nonlinear loop mirror (NOLM). The polarization-imbalanced NOLM has zero transmission at low power signals, which can make it a valuable mechanism for cleaning of soliton by elimination of noise and Kelly sidebands which are always present at the output of fiber soliton lasers. Polarization imbalance in the NOLM can be produced by inserting the quarter wave retarder (QWR) in the loop. Rotation of the angle of the QWR allows adjustment of the characteristics of the NOLM that can be used to choose the features that are most adequate to clean solitons with different pulse duration. As an input source, we used a mode-locked fiber ring laser with 0.6 ps duration and 1550 nm central wavelength. The results show more than 95% suppression of Kelly sidebands and two times compression of bandwidth. The maximum transmission of NOLM was 20%. Cleanup of soliton spectrum is possible using a NOLM as intensity filter without dependence of wavelength.

1 Introduction

In the passive mode-locked fiber laser, the spectrum of solitons is typically accompanied by dispersive waves that can produce spectral sidebands, which are explained well in [1–3]. Sidebands, which are called Kelly sidebands, are because of a constructive interference between the soliton and dispersive waves that happen at frequencies when phase difference is 2π [4]. The suppression of sidebands is required for many applications, such as optical sensors and processing [5], optical communication, optical switching [6–8] and wavelength de-multiplexing [9]. The nonlinear optical loop

M. Avazpour (✉) · G. Beltrán Pérez
Facultad de Ciencias Físico Matemáticas, Benemérita Universidad Autónoma de Puebla, Ciudad Universitaria, Avenida San Claudio y 18 Sur, Colonia San Manuel, C.P. 72570 Puebla, Mexico
e-mail: Mahrokh.avazpour@gmail.com

E. Kuzin
INAOE, Enrique Erro 1, Tonantzintla, C.P. 72840 Puebla, Mexico

A. Martínez-García et al. (eds.), *Progress in Optomechatronic Technologies*,
Springer Proceedings in Physics 233, https://doi.org/10.1007/978-981-32-9632-9_18

mirror (NOLM), which was first announced by Doran and Wood [10], found to be a good technique for cleaning of Kelly sidebands [11]. Indeed, this simple system consists of a coupler with fiber output ports. To operate the NOLM, providing nonlinear phase shift between clockwise (CW) and counter-clockwise (CCW) propagation through the loop is necessary. This condition can be obtained by adjusting the asymmetrical coupler to have imbalance of power between CW and CCW signal beams in the loop [12]. Using a different fiber to make dispersion asymmetry inside the loop also proved to be efficient [13, 14]. Residual birefringence, which is unavoidable with the standard fiber, strongly affects the NOLM operation. In the high transmission at low input power and low transmission at high input power, or in other words, when there is inversion of transmission, the birefringence can appear [12]. Highly twisted fiber is suggested to eliminate the birefringence in the loop that keeps the system simple and reduces the device cost [15, 16]. Polarization asymmetry inside loop is another measurement technique to operate the NOLM. Using quarter wave retarder (QWR) inside the loop close to the coupler output is suggested for changing the polarization from circular to linear for making the polarization imbalance inside the loop [17]. In this case, the input of the NOLM has circular polarization, and one of the counter-propagating beams in the loop has a circular polarization but the other once passed through the QWR has a linear polarization [18]. In fact, nonlinear phase shift of the linear polarization is 1.5 times bigger than the circular polarized light [19]. Even with the symmetrical coupler the counter-propagating beams can produce the phase difference with power-dependent. The angle of QWR, which can be adjusted between 0 and 0.5, is the cause of low power transmission. The easy change in the angle of QWR for low power transmission makes this kind of NOLM useful for some applications, like in all-optical regenerative systems [20], among others. Considerably, the options of adjustment for switch power which provides the NOLM with polarization asymmetry are less investigated. One option is the use of linear polarization input light, where the rotation of linear polarization of input light permits the modification of nonlinear transmission [21]. Though, by changing the retardation of the birefringence elements can have one way to adjust nonlinear characteristic [22].

In the present work, we experimentally investigated the elimination of Kelly sidebands with adjustment of the nonlinear properties of the NOLM by the use of QWR in the loop. The solitons with 0.6 ρs duration were used as the input source. They were generated by a fiber optical ring laser. The result shows that applying 1.7 mW of input average power is sufficient to get very good suppression of sidebands at different wavelengths. On the other hand, for 0.9 mW of input average power more than two times compressing of spectrum was observed at the output of NOLM, and only the 5% of Kelly sidebands remained.

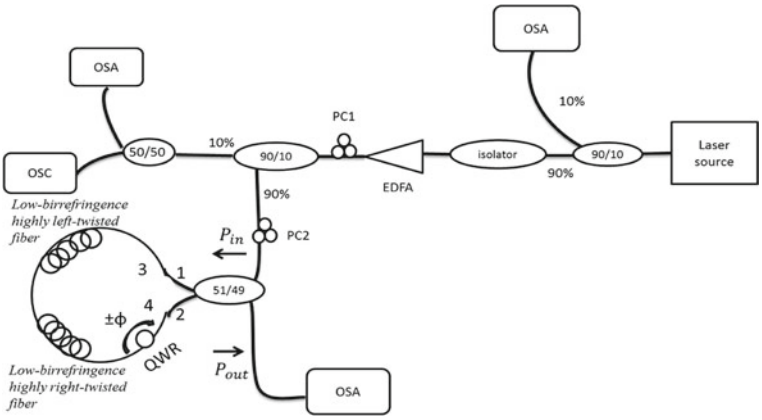

Fig. 1 Experimental setup

2 Experimental Setup

The experimental setup used for suppression of sidebands and compression of the spectrum is shown in Fig. 1. As input pulse we used solitons with 0.6 ps duration and 1550 nm central wavelength generated by a mode-locked fiber ring laser. The pulses are amplified by an EDFA. The pulses from the output of amplifier are passed through an isolator to avoid the reflection of light back to the laser source. Then, the light went toward the polarization controller (PC1) to adjust circular polarization. The pulses are divided by a 90:10 coupler, where a 10% port is used to monitor the polarization and power and a 90% port is connected to the NOLM through the PC2 to obtain circular polarization at the input of the NOLM. The NOLM consists of a nearly symmetrical coupler (49:51). Two 50 m pieces of highly right and left-twisted optical fiber SMF-28 at the rate of 7 turns/m used with the aim of elimination of azimuth rotation, followed by conserving the polarization in the loop and making the NOLM wavelength independent [20, 23]. The quarter wave retarder (QWR) is asymmetrically located in the loop to break up the symmetry of the loop and attain different nonlinear phase shifts for counter-propagating pulses. Because the pulses which are propagated in the CW direction have circular polarization while the pulses that are propagated in the CCW direction after passing the QWR have linear polarization. This is the result of differential phase shift for counter-propagating pulses. The spectrum was measured at input and output of the NOLM using optical spectrum analyzer.

3 Results

Figure 2a shows the spectrum at the input of NOLM when amplification of the EDFA

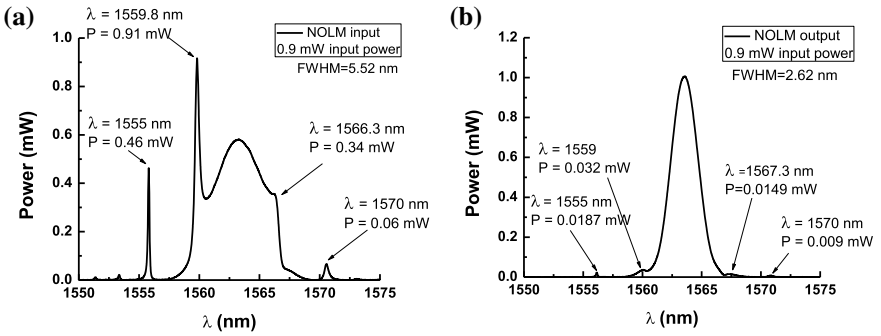

Fig. 2 **a** Input spectrum of NOLM with power of 0.9 mW and FWHM = 5.5 nm, **b** output spectrum of NOLM with power of 0.9 mW and FWHM = 2.62 nm

was set to have the average input power of 0.9 mW. The FWHM of the spectrum is 5.5 nm centered at 1563.3 nm. In the figure we can see several Kelly sidebands. The maximum Kelly sidebands appeared at 1559.8 nm with the power around 9E−4 W. At another side of the spectrum there is symmetrical sideband at 1566.3 nm with power of 3.6E−4 W. The others are at 1555 and 1570 nm, with powers of 4.6E−4 and 6.3E−5 W, respectively. Figure 2b indicates the spectrum at the output of NOLM. The spectrum centered at 1563.4 nm and has the bandwidth of 2.62 nm, which means that there is two times spectrum compression. For the 1559.8, 1566.3 and 1555 nm Kelly bands, we observed more than 50 times suppression of power as compared with the maxima of soliton spectra. In this case the transmission of NOLM is 1.5%.

Figure 3a shows the input spectrum of NOLM when the EDFA is set to have the average power of 1.7 mW. Some change in the spectrum is observed. The FWHM decreases to 4.23 nm. Figure 3b shows the spectrum at the output of the NOLM with FWHM of 1.9 nm. The spectrum shows two well-visible sidebands at 1560.5 and 1566.1 nm. However, we can see that the wavelengths of these sidebands do not coincide with wavelengths of the Kelly sidebands at the NOLM input. We suppose

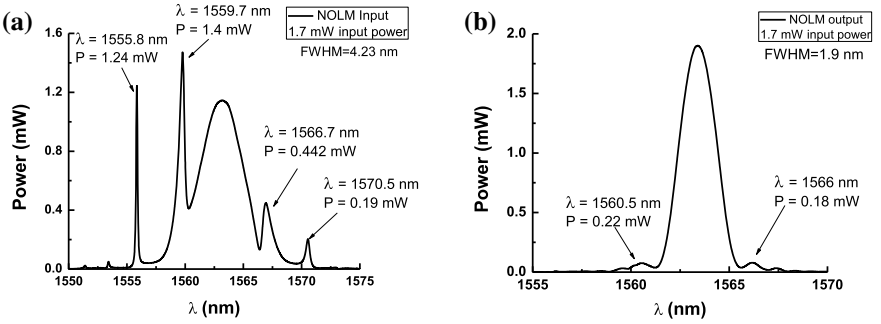

Fig. 3 **a** Input spectrum of NOLM with power of 1.7 mW and FWHM = 4.23 nm, **b** output spectrum of NOLM with power of 1.7 mW and FWHM = 1.9 nm

that these maxima appear because of the process of spectrum compression in the NOLM loop. At the wavelengths corresponding to the Kelly sidebands, the output spectra do not show any maxima. We may conclude that the suppression of sidebands is more than 100 times. Sidebands of 1555 and 1570 nm are below the OSA noise. The transmission of NOLM in this case is 20%.

4 Conclusion

In summary, an experimental study of the use of the polarization-imbalanced NOLM to clean and compress solitons was presented. At the average input power of 0.9 and 1.7 mW, we observed the compression of the spectrum more than two times. The strong sidebands present at the input were suppressed by more than 30 times for 0.9 mW input power and more than 100 times for 1.7 mW of input average power.

References

1. N. Pandit, D.U. Noske, S.M.J. Kelly, J.R. Taylor, Characteristic instability of fibre loop soliton lasers. Electron. Lett. **28**(5), 455–457 (1992)
2. N.J. Smith, K.J. Blow, I. Andonovic, Sideband generation through perturbations to the average soliton model. J. Light. Technol. **10**(10), 1329–1333 (1992)
3. M.L. Dennis, I.N. Duling, Experimental study of sideband generation in femtosecond fiber lasers. IEEE J. Quantum Electron. **30**(6), 1469–1477 (1994)
4. R. Weill, A. Bekker, V. Smulakovsky, B. Fischer, O. Gat, Spectral sidebands and multipulse formation in passively mode-locked lasers. Phys. Rev. A **83**(4), 43831 (2011)
5. S. Boscolo, S.K. Turitsyn, K.J. Blow, Nonlinear loop mirror-based all-optical signal processing in fiber-optic communications. Opt. Fiber Technol. **14**(4), 299–316 (2008)
6. J.D. Moores, K. Bergman, H.A. Haus, E.P. Ippen, Optical switching using fiber ring reflectors. JOSA B **8**(3), 594–601 (1991)
7. O. Pottiez, E.A. Kuzin, B. Ibarra-Escamilla, J.T. Camas-Anzueto, F. Gutierrez-Zainos, Experimental demonstration of NOLM switching based on nonlinear polarisation rotation. Electron. Lett. **40**(14), 892–894 (2004)
8. W. Cao, P.K.A. Wai, Comparison of fiber-based Sagnac interferometers for self-switching of optical pulses. Opt. Commun. **245**(1–6), 177–186 (2005)
9. H. Sotobayashi, C. Sawaguchi, Y. Koyamada, W. Chujo, Ultrafast walk-off-free nonlinear optical loop mirror by a simplified configuration for 320-Gbit/s time-division multiplexing signal demultiplexing. Opt. Lett. **27**(17), 1555–1557 (2002)
10. N.J. Doran, D. Wood, Nonlinear-optical loop mirror. Opt. Lett. **13**(1), 56–58 (1988)
11. M.D. Pelusi, Y. Matsui, A. Suzuki, Pedestal suppression from compressed femtosecond pulses using a nonlinear fiber loop mirror. IEEE J. Quantum Electron. **35**(6), 867–874 (1999)
12. N. Finlayson, B.K. Nayar, N.J. Doran, Switch inversion and polarization sensitivity of the nonlinear-optical loop mirror. Opt. Lett. **17**(2), 112–114 (1992)
13. N. Nishizawa, K. Takahashi, Y. Ozeki, K. Itoh, Wideband spectral compression of wavelength-tunable ultrashort soliton pulse using comb-profile fiber. Opt. Express **18**(11), 11700–11706 (2010)
14. L. Sha, W. Jian-Ping, K. Zhe, Y. Chong-Xiu, Optimizational 6-bit all-optical quantization with soliton self-frequency shift and pre-chirp spectral compression techniques based on photonic crystal fiber. Chin. Phys. B **24**(8), 84212 (2015)

15. B. Ibarra-Escamilla et al., Fiber optical loop mirror with a symmetrical coupler and a quarter-wave retarder plate in the loop. Opt. Commun. **242**(1–3), 191–197 (2004)
16. E.A. Kuzin, N. Korneev, J.W. Haus, B. Ibarra-Escamilla, Theory of nonlinear loop mirrors with twisted low-birefringence fiber. JOSA B **18**(7), 919–925 (2001)
17. B. Ibarra-Escamilla et al., Experimental investigation of the nonlinear optical loop mirror with twisted fiber and birefringence bias. Opt. Express **13**(26), 10760–10767 (2005)
18. L.A. Rodriguez-Morales et al., Experimental investigation of polarization-imbalanced nonlinear loop mirror with double-sense twisted fiber as a filter to clean up solitons. J. Opt. **20**(1), 15502 (2017)
19. G. Agrawal, *Applications of Nonlinear Fiber Optics* (Academic Press, 2001)
20. M. Sorokina, Design of multilevel amplitude regenerative system. Opt. Lett. **39**(8), 2499–2502 (2014)
21. O. Pottiez, E.A. Kuzin, B. Ibarra-Escamilla, J.T. Camas-Anzueto, F. Gutiérrez-Zainos, Easily tunable nonlinear optical loop mirror based on polarization asymmetry. Opt. Express **12**(16), 3878–3887 (2004)
22. I. Armas-Rivera et al., Experimental study of the polarization asymmetrical NOLM with adjustable switch power. Opt. Commun. **350**, 165–169 (2015)
23. O. Pottiez, E.A. Kuzin, B. Ibarra-Escamilla, F. Mendez-Martinez, Theoretical investigation of the NOLM with highly twisted fibre and a $\lambda/4$ birefringence bias. Opt. Commun. **254**(1), 152–167 (2005)

A Nonlinear Adaptive Model-Predictive Approach for Visual Servoing of Unmanned Aerial Vehicles

Sina Sajjadi, Mehran Mehrandezh and Farrokh Janabi-Sharifi

Abstract Aerial vehicles, due to the nature of their operations, are subject to many uncertainties. In particular, their positioning control problem is aggravated in GPS-denied environments. As a result, vision-based control (or visual servoing) solutions are sought to address their navigation control issue. In this work, visual servoing is formulated as a nonlinear optimization problem in the image plane. The proposed approach is based on a class of nonlinear model-predictive control that takes constraints into consideration. A 2-DOF model helicopter is considered for initial formulations and verification of the approach. The considered model helicopter has a coupled nonlinear pitch/yaw dynamics. It is also capable of a pitch over (i.e., hover at a non-zero pitch angle) around its pivotal axis of rotation due to the offset between the center of mass (CoM) of its fuselage and the rotation axis. This further makes the linearized model (calculated around any pitch angle). A linear parameter varying (LPV) system for an adaptive control is formulated under a model-predictive visual servoing framework. In this paper, a design guideline is provided under a model-predictive visual servoing paradigm that considers field of view (FOV) constraints, the constraint on the pitch angle, and also the maximum voltages that can be applied to independently controlled pitch/yaw motors. The control space is parameterized via Laguerre basis network functions that make the optimization scheme computationally less expensive, thus suitable for real-time applications.

1 Introduction

Improving the control performance of UAVs has been an on-trend research topic due to the dramatic growth of applications of UAVs in recent years. In 2005, a sliding mode controller via linear quadratic regulator for a two degrees-of-freedom (or 2-DOF) model helicopter was designed, where a linear quadratic regulator (LQR) was

S. Sajjadi · M. Mehrandezh (✉)
Faculty of Engineering and Applied Science, University of Regina, Regina, Canada
e-mail: Mehran.Mehrandezh@uregina.ca

F. Janabi-Sharifi
Department of Mechanical and Industrial Engineering, Ryerson University, Toronto, Canada

A. Martínez-García et al. (eds.), *Progress in Optomechatronic Technologies*,
Springer Proceedings in Physics 233, https://doi.org/10.1007/978-981-32-9632-9_19

used to control pitch and yaw motions of the helicopter and sliding mode controller was used to guarantee robustness over uncertainties [1]. It was claimed that the proposed approach provides robustness against external disturbances. In another work [2], a feedback-linearization control law was applied to the longitudinal subsystem of a laboratory helicopter in two steps. First, it was used for the nonlinear actuator and then for the entire system to compensate gravity. A switching control law between exact and approximate input–output linearization was presented and tested on the experimental setup. In [3], a fast model-predictive controller was developed for a miniature remote-controlled coaxial helicopter. The nonlinear dynamic behavior of the helicopter was identified and approximated by a linear time varying (LTV) model. The results demonstrated the superiority of MPC approach over a proportional integral differential (PID) controller in trajectory tracking. Also, a nonlinear general model-predictive controller (GPC) was applied to a 2-DOF model helicopter in [4] and the results were compared with the linear GPC controller. It was shown that the nonlinear GPC algorithm would work for a wider operating range and the guarantee of stability was also investigated.

During recent decade, vision-based UAV control has gained attention due to its wide range of applications, such as autoflight in GPS-denied environments, autonomous landing, and search and rescue. In [5], an adaptive image-based visual servoing controller for a rotary-wing UAV was designed in which the controller regulates the relative position and yaw of the vehicle to a planar target consisting of multiple points. Exponential stability of the error dynamics of the proposed algorithm was proved, and the controller performance was demonstrated through experiments. The problem of using computer vision as a feedback sensor to control the landing of a dynamic UAV with a geometric algorithm for estimating the camera angular and linear velocity was addressed in [6]. In the same work, a nonlinear controller was proposed based on differential flatness for a UAV dynamic model. Through simulations, it was shown that the vision-based controller results in stable landing maneuvers for large noise levels. A vision-based servoing technique for a 2-DOF model helicopter equipped with a camera was presented in [7]. The proposed tracking control algorithm consisted of two steps: the image processing algorithm, which uses a linearized image Jacobian to relate the optical flow from a single video camera to motion commands for correcting the error; and the joint-level position-based LQR controller, which tracks the incremental set points and servo the pixel-level error to zero. Test results proved that the designed controller is able to servo the image of the ball to the center of the image frame regardless of its initial position. In the next step, the performance of the controller was also optimized by introducing an error clamping gain.

In this paper, a two-step adaptive MPC algorithm for visual servoing of a 2-DOF model helicopter is proposed, which can perform visual servoing tasks optimally under a model-predictive control paradigm. The proposed control algorithm can consider field of view (FOV) constraints, the constraint on the pitch angle, and also the maximum voltages that can be applied to independently controlled pitch/yaw motors. In the first step, an MPC calculates the desired pitch and yaw velocities to minimize the error between the center of the image and projection of target point

in camera, within a prediction horizon. The calculated pitch/yaw velocities are integrated and fed into the second MPC as the desired trajectory. The second MPC computes the manipulated variables subject to nonlinear helicopter dynamics, in an effort to optimally track the desired pitch/yaw trajectories. A good performance in the servoing/tracking task can be achieved even for large initial error between current and target image. The proposed control method has been simulated for two cases, namely (1) servoing toward a stationary target, and (2) tracking a mobile target. By using Laguerre basis network functions for parameterizing control domain, the computational cost of optimizations in MPC is reduced significantly, leading to the possibility of using the proposed control method in real time.

This paper is organized as follows: Sect. 2 revolves around problem formulation and description of the proposed MPC servoing algorithm. The results of the simulations can be found in Sect. 3. Conclusions and future works are provided in Sect. 4.

2 Problem Definition

An adaptive model-predictive visual servoing in the presence of task, sensor, and control-space constraints is designed and developed. The control algorithm is implemented, via simulation, on a 2-DOF model helicopter from Quanser [1]. Problem formulation for the system dynamics assumes a front-looking perspective camera being mounted on the 2-DOF model helicopter. A pinhole projection model, without any lens distortion, is assumed. Figure 1 shows a picture of the 2-DOF model helicopter. As can be seen from Fig. 1, the helicopter can turn around a pivot point (aka, axis of rotation) via two axes, namely yaw (or pan motion) and pitch (tilt motion). The CoM of the helicopter is located in front of the rotation axis; therefore, a constant pitch torque would be required to compensate for gravitation forces. This additional pitch torque can make the 2-DOF model helicopter hover at any pitch angle.

This model helicopter was chosen as a test bench due to its coupled and nonlinear pitch/yaw dynamics. Furthermore, the linearization of the dynamic model around any pitch angle would lead to a linear parameter varying (LPV) system, whose state interaction matrix will have time/state-dependent elements. A local adaptive model-predictive visual servoing is formulated to account for time/state-dependent parameters in system's dynamics via successive linearization that outperforms a global nonlinear optimization in terms of time complexity and convergence. Furthermore, a Laguerre network function is used for parameterizing the control space under an infinite-horizon control framework. Reducing the size of the control space via proposed parameterization makes it suitable for real-time applications, without compromising the stability.

Fig. 1 The 2-DOF model helicopter, [8]

Performance of the proposed visual servoing strategy is depicted via simulations with the case study of tracking/servoing a ball. The center point of the ball in the image is taken as the only image feature to track or servo to. The distance between the camera and the ball can be estimated from the size of the ball in the image.

2.1 Problem Formulation

The governing dynamics equations for model helicopter are derived by using the Lagrange method [7].

$$\left(J_{eq,p} + m_{heli}l_{cm}^2\right)\ddot{\theta}K_{pp}V_{m,p} + K_{py}V_{m,y}m_{heli}gl_{cm}cos\theta - B_p\dot{\theta} - m_{heli}l_{cm}^2\sin\theta\cos\theta\dot{\varphi}^2 \tag{1a}$$

$$\left(J_{eq,y} + m_{heli}l_{cm}^2cos^2\theta\right)\ddot{\varphi} = K_{yp}V_{m,p} + K_{yy}V_{m,y} - B_y\dot{\varphi} + 2m_{heli}l_{cm}^2\sin\theta\cos\theta\dot{\varphi}\dot{\theta} \tag{1b}$$

Equations (1a, 1b) can be presented in a compact form as:

$$\tau = M(q)\ddot{q} + C(q,\dot{q})\dot{q} + g(q) \tag{2}$$

where M denotes the inertial terms, C denotes the Coriolis and centrifugal acceleration terms, g denotes the gravitation terms, and τ denotes the force/torque terms. The

state vector of the model helicopter consists of pitch angle, θ, and the yaw angle, φ, q = [θ, ϕ]. The control space consists of the input voltages applied to the independently controlled pitch and yaw motors, $V_{m,p}$ and $V_{m,y}$. Owing to gyroscopic effects, the pitch and yaw motions will be coupled. The dynamics of the system and constraints on motion control inputs denoted by o can be presented in a compact form as follows:

$$\begin{gathered} \dot{x} = f(x(t), u(t)) \\ o_l \ll o(x(t), u(t)) \leq o_u \\ x(0) = x_0 \end{gathered} \tag{3}$$

Equations (1a, 1b) are written with the assumption that the aerodynamic effects on the fuselage are negligible due to its slow rotational motion. The variables in (1a, 1b) are described in Table 1.

The objective is to: (1) servo toward a stationary target, and (2) track a mobile target, by using images taken from the object by the front-looking camera. The object of interest is assumed to have a ball shape. The center point of the ball is used as the only image feature for tracking. The optical flow associated with this proposed image feature, $\dot{s}$ is related to the rate of change in pitch and yaw motions, $\dot{q}$ via image Jacobian, L_s, and helicopter Jacobian J_r as in (4) [2]:

$$\begin{gathered} \dot{s} = L_s(s) J_r(q) \dot{q} \\ h_l \ll h(s(t), x(t)) \ll h_u \\ s = [u, v]^T, q = [\theta, \varphi]^T, \end{gathered} \tag{4}$$

Table 1 Description of variables found in (1a, 1b)

Variable	Description
m_{heli}	Total moving mass of the helicopter
l_{cm}	Distance from pitch axis of the center-of-mass along the body
g	Earth gravitational acceleration coefficient
θ	Pitch angle
ϕ	Yaw angle
$J_{eq,p}$	Total moment of inertia about pitch pivot
$J_{eq,y}$	Total moment of inertia about yaw pivot
K_{pp}	Thrust torque constant acting on pitch axis from pitch motor
K_{py}	Thrust torque constant acting on pitch axis from yaw motor
K_{yp}	Thrust torque constant acting on yaw axis from pitch motor
K_{yy}	Thrust torque constant acting on yaw axis from yaw motor
$V_{m,p}$	Voltage applied to pitch motor
$V_{m,y}$	Voltage applied to yaw motor
B_p	Viscous rotary friction acting about pitch axis
B_y	Viscous rotary friction acting about yaw axis

where image and helicopter Jacobian can be defined as:

$$L_s = \begin{bmatrix} \frac{-1}{z} 0 \frac{u}{z} uv - (1+u^2)v \\ 0 \frac{-1}{Z} \frac{v}{Z} (1+v^2) - uv - u \end{bmatrix} \tag{5}$$

$$J_r = \begin{bmatrix} -l\sin\varphi\cos\theta & -l\cos\varphi\sin\theta \\ l\cos\varphi\cos\theta & -l\sin\varphi\sin\theta \\ 0 & 2l\cos\theta \\ 0 & \sin\varphi \\ 0 & -\cos\theta \\ 1 & 0 \end{bmatrix} \tag{6}$$

l, φ, θ represent the distance of the camera to pivot point of helicopter, pitch, and yaw angle, respectively.

2.2 Proposed MPC Algorithm

The design objective of MPC is to compute a trajectory of future manipulated variables to optimize the predicted behavior of system output. The optimization is performed within a limited time window known as prediction horizon [9]. The control objective is to bring the point feature, associated with the center point of the ball (i.e., the candidate image moment representing the ball), to the center point of the image while minimizing the motion and also the energy consumption based on a quadratic performance index. A control-space parameterization is also carried out to conduct the optimization over an infinite horizon in real time by using an exponentially decaying basis function based on orthonormal *Laguerre* functions. This basis function fulfills the following recursive identity:

$$\dot{L}(t) = M_\rho L(t), \forall t \in [0, \infty) \tag{6}$$

$$\mathrm{u(t)} \ominus (\mathrm{I}_2 \otimes \mathrm{L(t)})^{\mathrm{T}} \eta \tag{7}$$

$$\eta = [c_1 c_2 \ldots c_N]$$

where N is the number of Laguerre functions used for expansion and η is the set of coefficients used for linearly adding Laguerre functions, to be calculated via optimization. To perform visual-servoing task optimally by considering the constraints of the image (FOV), applied voltage to the motors, and mechanical limitations of the helicopter, a two-step successive linearization-based adaptive MPC algorithm is proposed.

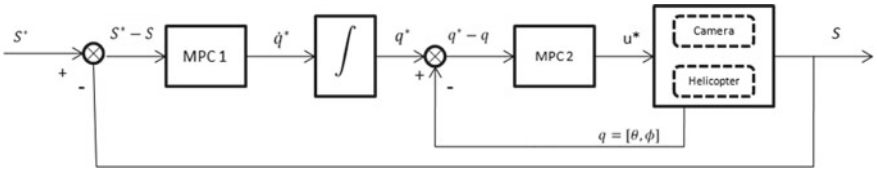

Fig. 2 Architecture of the proposed two-tier model-predictive control algorithm

As shown in Fig. 2, first, MPC1 computes desired velocity trajectory subject to dynamics of the vision system (3), which is being successively linearized in the proximity of operation point. Constraints in MPC1 include FOV constraints to guarantee that the control algorithm will keep the target point in image plan $h(s(t), x(t))$ and constraints on pitch/yaw accelerations, $(\ddot{q})$.

$$\begin{gathered} \underset{\eta(t)}{min} \left\{ \int_0^{\infty} \left((s^*(t) - s(t))^T Q_1 (s^*(t) - s(t)) + \eta(t)^T R_1 \eta(t) \right) dt \right\} \\ \dot{q}(t) \ominus \left(I_2 \otimes \dot{L}(t) \right)^T \eta(t), \; and \; \dot{L}(t) = M_\rho L(t), \forall t \in [0, \infty) \\ s(0) = s_0, \; and \; \eta(0) = \eta_0 \\ h_{min} \ll h(s(t), x(t)) \ll h_{max} \\ \ddot{q}_{min} \ll \ddot{q} \ll \ddot{q}_{max} \end{gathered} \tag{8}$$

Integration of the computed pitch/yaw velocities generates desired pitch/yaw trajectory for MPC2 (q^*), where the dynamics of the helicopter is exploited to compute optimal voltages to be applied to the pitch/yaw motors. Performance index optimization is performed by considering mechanical limitations and constraints on the voltages applied to the pitch/yaw motors of the helicopter.

$$\begin{gathered} \underset{\eta(t)}{min} \left\{ \int_0^{\infty} \left((q^*(t) - q(t))^T Q_2 (q^*(t) - q(t)) + \eta(t)^T R_2 \eta(t) \right) dt \right\} \\ u(t) \ominus \left(I_2 \otimes \dot{L}(t) \right)^T \eta(t), \; and \; \dot{L}(t) = M_\rho L(t), \forall t \in [0, \infty) \\ q(0) = q_0, \; and \; \eta(0) = \eta_0 \\ q_{min} \ll q(s(t), x(t)) \ll q_{max} \\ u_{min} \ll u \ll u_{max} \end{gathered} \tag{9}$$

It is noteworthy that this parameterization will guarantee an asymptotic stability via successive linearization of the nonlinear system [10].

3 Simulation and Results

Simulation results of the proposed two-tier adaptive MPC for visual servoing are presented in this section. In order to test the validity and performance of the proposed controller, two cases were tested under different scenarios as representative simulation results. In case #1, the target is initially located in the 3D space, at a known distance from the optical axis of the camera. In this case, we also assume that the target remains stationary (i.e., static target). The goal is to servo the camera toward the target, bringing it onto the camera's optical axis (i.e., putting the image of the ball right in the center of the image) while minimizing an objective function, subjected to the sensor's task constraints. The projected image trajectories for four different scenarios corresponding to four different initial positions of the target are shown in Fig. 3. As demonstrated, regardless of the initial position and despite large initial error between current and target image, the proposed control algorithm can servo the feature point to its target position.

Figure 4 depicts the simulation results for servoing a stationary target, where the target feature point is initially projected on the image at: $s_0 = [152, 230]$ pixels. Figure 4a shows the variation of the pixel coordinates associated with the target object versus time. Figure 4b illustrates the desired and real pitch/yaw trajectories. Figure 4c depicts the output of MPC1, which is the desired pitch/yaw velocities for the helicopter ($\dot{q}^*$), without violating its permissible acceleration limits. Computed angular accelerations by MPC1 are presented in Fig. 4d, e. It can be seen that computed acceleration trajectories do not violate the pre-defined limits. Finally, voltages applied to motors of the helicopter along with their maximum permissible values are shown in Fig. 4f, g.

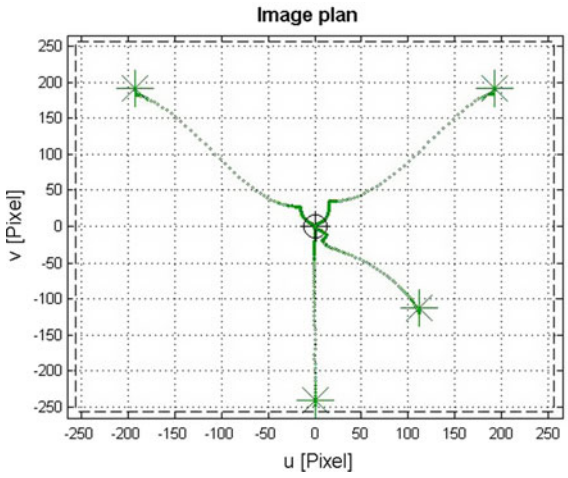

Fig. 3 Image-plane trajectories of a stationary target located at four different initial positions

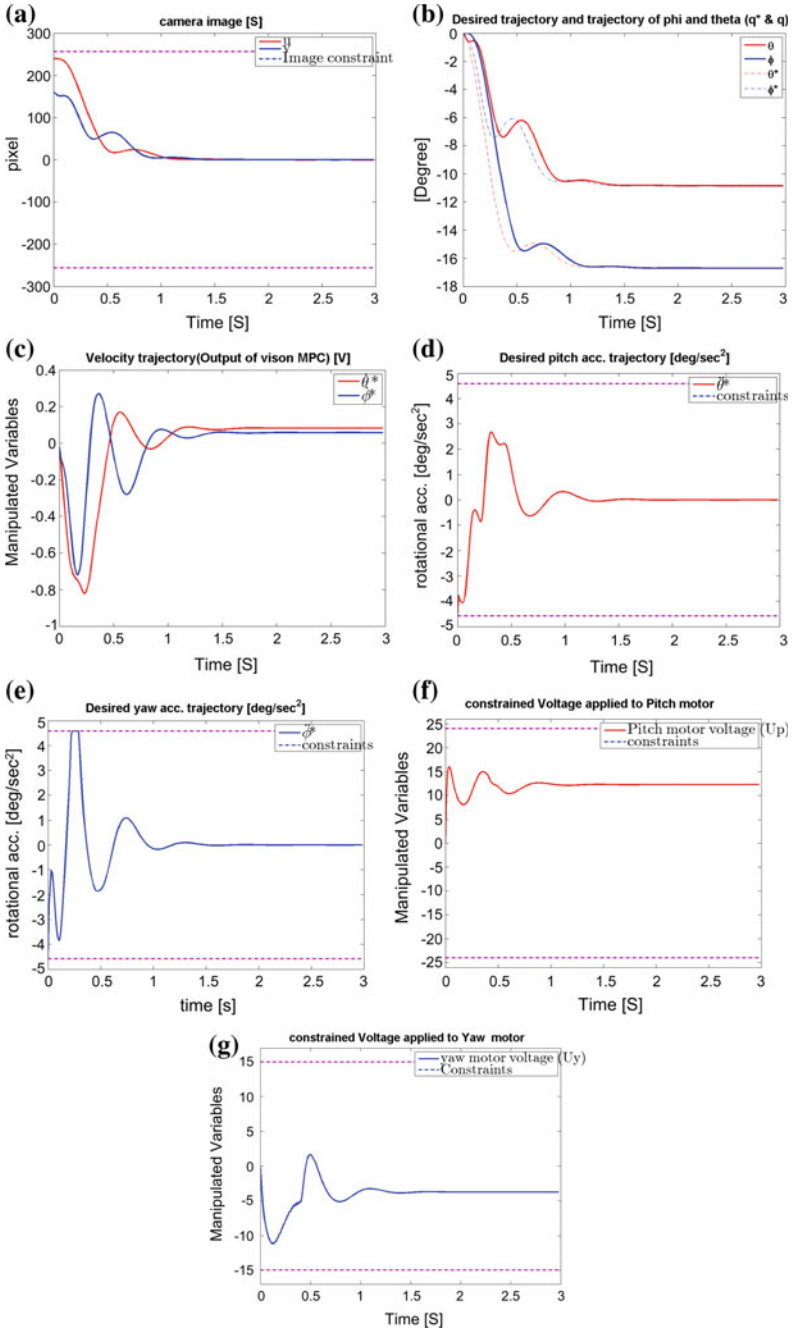

Fig. 4 Servoing toward a stationary target

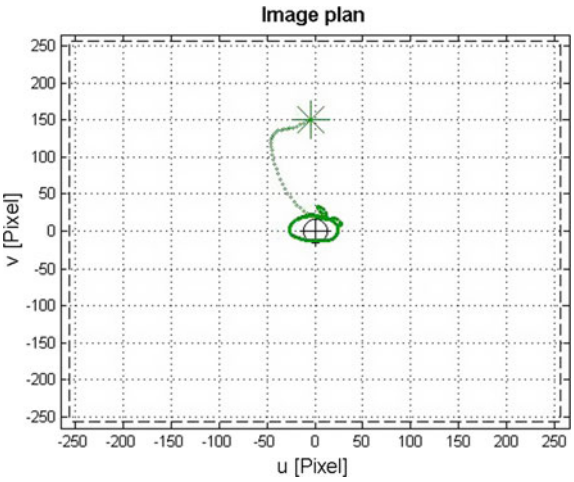

Fig. 5 Image-plane trajectory of the target's feature point (Z = 5 m, r = 0.75 m, f = 0.4 Hz)

In case #2, the target object is considered to be moving on a planar circle at a distance of 5 m from the camera and perpendicular to its optical axis. The objective is to track this moving target and to keep it on the optical axis of the camera all the time. Figure 5 shows the image-plane trajectory of the target's feature point.

Figure 6a–g shows the simulation results.

4 Conclusion and Future Work

A model predictive visual servoing strategy was formulated as a nonlinear optimization problem in the image plane. Sensor, task, and control constraints were taken into consideration. The performance of the proposed controller was evaluated via simulations using a 2-DOF model helicopter equipped with a front-looking camera. Two case scenarios were investigated, namely (1) servoing the model helicopter toward a stationary target, and (2) tracking a mobile target. The model helicopter has a nonlinear dynamics. Therefore, an adaptive model-predictive control strategy via successive linearization was proposed. The linearized model of the system also yields a linear parameter varying (LPV) system due to the gravitational torque around the model helicopter's axis of rotation. To make the servoing in real time, the control space was parameterized using Laguerre basis functions. In the proposed two-tier control strategy, first the desired pitch/yaw velocities of the helicopter for servoing/tracking a target were calculated, considering the acceleration and image constraints. These desired velocities were then integrated to produce the desired trajectories that were then tracked by the second MPC while considering motion and control constraints. In the future, we will implement the proposed algorithm on

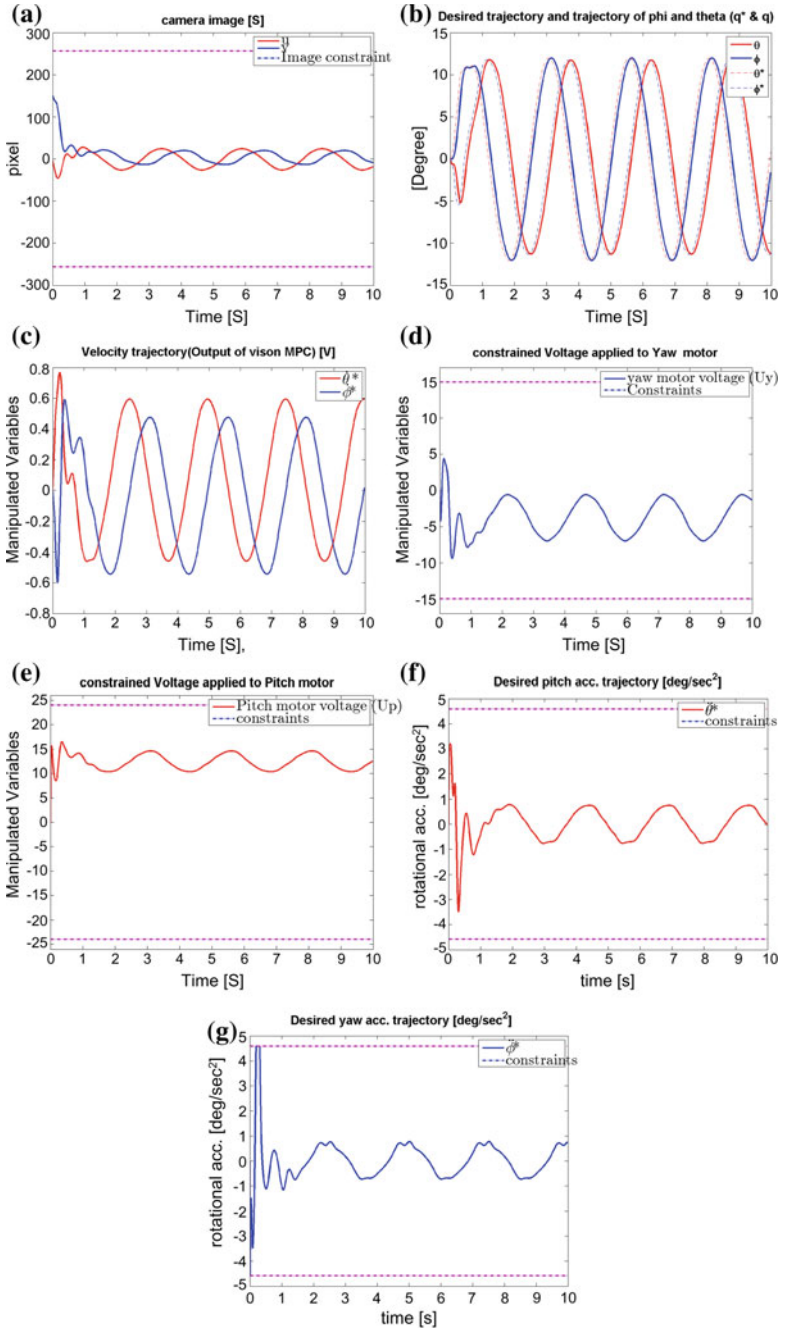

Fig. 6 Results of tracking a mobile target moving on a circle. **a** Image-plane trajectories, **b** pitch/yaw trajectories, **c** desired pitch/yaw velocities computed by MPC1, **d**, **e** voltages provided to the pitch/yaw motors versus time, **f**, **g** pitch/yaw accelerations and their limits. The target is moving on a circle perpendicular to the camera's optical axis (Z = 5 m, r = 0.75 m, f = 0.4 Hz)

the real system. Furthermore, we will investigate about making the control strategy robust against uncertainties in the dynamic model of the helicopter due to external disturbances such as wind.

References

1. G.-R. Yu, H.-T. Liu, Sliding mode control of a two-degree-of-freedom helicopter via linear quadratic regulator, in *2005 IEEE International Conference on Systems, Man and Cybernetics*
2. M. Lopez-Martinez, J. Diaz, M. Ortega, F. Rubio, Control of a laboratory helicopter using switched 2-step feedback linearization, in *Proceedings of the 2004 American Control Conference* (2004)
3. K. Kunz, S.M. Huck, T.H. Summers, Fast model predictive control of miniature helicopters, in *2013 European Control Conference (ECC)* (2013)
4. A. Dutka, A. Ordys, M. Grimble, Non-linear predictive control of 2 DOF helicopter model, in *42nd IEEE International Conference on Decision and Control (IEEE Cat. No. 03CH37475)*
5. H. Xie, G. Fink, A.F. Lynch, M. Jagersand, Adaptive visual servoing of UAVs using a virtual camera. IEEE Trans. Aerosp. Electron. Syst. **52**(5), 2529–2538 (2016)
6. O. Shakernia, Y. Ma, T.J. Koo, S. Sastry, Landing an unmanned air vehicle: vision based motion estimation and nonlinear control. Asian J. Control **1**(3), 128–145 (2008)
7. M. Alizadeh, C. Ratanasawanya, M. Mehrandezh, R. Paranjape, Optimal error-clamping design for position-based visual servoing of a 2-DOF model helicopter, in *Volume 3: 2011 ASME/IEEE International Conference on Mechatronic and Embedded Systems and Applications, Parts A and B* (2011)
8. www.quanser.com (last viewed on 6 August 2018)
9. S. Qin, T.A. Badgwell, A survey of industrial model predictive control technology. Control Eng. Pract. **11**(7), 733–764 (2003)
10. M. Muehlebach, C. Sferrazza, R. Dandrea, Implementation of a parametrized infinite-horizon model predictive control scheme with stability guarantees, in *2017 IEEE International Conference on Robotics and Automation (ICRA)* (2017)

Construction and Characterization of a Laser Doppler Velocimeter Printed in 3D

H. Méndez-Dzul, M. Pérez-Cortés, M. Ortíz-Gutiérrez, M. de Coss-Maritza, J. Lugo-Jiménez and C. Vinajera

Abstract This work shows the development of a mechanical design for mounting optical systems and this is built in a 3D printer for its implementation as a laser velocimeter and some of its applications.

1 Introduction

An optical system [1] is a set of mechanical and optical elements [2] placed in an aligned and systematized form, their objective is to make a measurement that is recorded through a natural or artificial sensor. The interest of this work was to realize through a 3D printer the construction of a mechanical system, and implement an optical system adjusted to our possibilities, as well as adjust a Hamamatsu avalanche sensor. A small experiment was carried out to show the functioning of our system built with an adaptation with some mechanical elements.

H. Méndez-Dzul
Instituto Nacional de Astrofísica, Óptica y Electrónica, Luis Enrrique Erro #1, 72000 Tonantzintla, Puebla, Mexico
e-mail: og.heck.5500@gmail.com

M. Pérez-Cortés (✉) · M. de Coss-Maritza · J. Lugo-Jiménez · C. Vinajera
Universidad Autónoma de Yucatán, Av. Industrias no Contaminantes s/n, 97200 Mérida, Yucatán, Mexico
e-mail: mperez.cortes@correo.uady.mx

M. de Coss-Maritza
e-mail: dcgomez@correo.uady.mx

J. Lugo-Jiménez
e-mail: jorge.lugo@correo.uady.mx

C. Vinajera
e-mail: vreyna@correo.uady.mx

M. Ortíz-Gutiérrez
Facultad de Ciencias Físico Matemáticas, Universidad Michoacana de San Nicolás de Hidalgo, Morelia, Michoacán, Mexico
e-mail: mortizg@yahoo.com

A. Martínez-García et al. (eds.), *Progress in Optomechatronic Technologies*,
Springer Proceedings in Physics 233, https://doi.org/10.1007/978-981-32-9632-9_20

To characterize the flow profile, there are currently multiple tools available, among which are the computational techniques that allow the calculation of the fields related to the fluid, and the optical techniques, which have the advantage of being non-invasive. Particularly the laser velocimeter, and their variations [3], which allow the direct measurement of the velocity of a fluid in a very small volume are accepted. In recent decades, these devices have been used and suitable for multiple applications like the flow inside tissue and others [4–8].

Donald [6] measured the instantaneous velocity of tracer particles suspended in a flow, without alterations. Their work expanded the dynamic range, versatility and non-interference of the measurement systems, so laser-Doppler anemometry has been widely used in applications such as wind tunnel velocity measurement, low speed rotation and combustion fluxes at high speed with high temperature; other applications are in remote sounding of the atmospheric wind speed and the vortex of the airplanes.

We utilized a Fredriksson et al. work [7, 8] that presented a method for estimating the measurement depth and volume in laser Doppler flowmetry (LDF). The method is based on Monte Carlo simulations of light propagation in tissue and a non-invasive method to estimate the blood perfusion in the microcirculation.

We present in this work the measurement of a pair of experiments for the characterization of the optical 3D-PLA system, these experiments consisted in measuring the speed of a chopper, and the water velocity of a small source system.

2 Design of the Laser Velocimeter

Our system is composed as follows: A laser light source of a wavelength is used to obtain an interference volume, which will act as a measurement point. There are various arrangements for this purpose to guarantee the interference conditions, the first step must be divided. Subsequently the beams will be collimated, and intersection will be seen obtain the measurement volume. The optical signal will be transformed into voltage signals by means of a sensor, to be digitized and processed to finally obtain the velocity profile.

There are multiple arrangements to obtain a speed measurement system using light sources. In this work, a laser velocimeter is designed by Doppler effect, due to its operation and implementation. In first instance, when adding 2 coherent light sources, and of the same polarization, interference occurs. When performing the calculation on the fringes that are presented using 2 wavelength plane waves λ, and at a relative angle θ, we get the following expression:

$$d = \frac{\lambda}{2\sin(\theta/2)} \tag{1}$$

If a particle flow occurs perpendicular to the interference fringes, and at a velocity v, pulses of light are presented at a frequency:

$$f = \frac{1}{t} = \frac{v}{d} = \frac{2v\sin(\theta/2)}{\lambda} \tag{2}$$

The Equation (2) has a relationship between the parameters of our system: the wavelength of the beam used, the frequency of pulses emitted, the angle between the beams and the measurable limit speed. We can make the first selection of parameters where the maximum limit for the frequency should be around 5 MHz. Similarly, λ must be such that it presents few losses when interacting with the environment. From this, we have two main frequencies: red and infrared, approximately 650 and 800 nm.

To guarantee the crossing of the beams, as well as to maximize the energy in the measurement volume, it is most convenient to use a converging lens. In this work a laser anemometer is designed based on Figs. 1 and 2. When adding 2 coherent spatial and temporal light sources of the same polarization interference occurs. The optical system is designed for a lens with a diameter of 5 cm and a focal length of 20 cm. With the above considerations, the maximum measurable speed turns out to be about 13 m/s for a wavelength of 650 nm and 16 m/s for a wavelength of 800 nm.

To produce interference, light from the same source will be used. For this, we will use a 50–50 beam splitter. It is equally necessary to concentrate the largest amount of scattered light, so an eyepiece is needed for the sensor. Likewise, two parallel beams

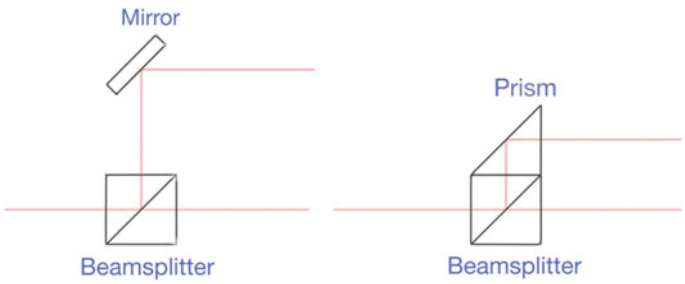

Fig. 1 Scheme for the generation of interference in the laser speedometer

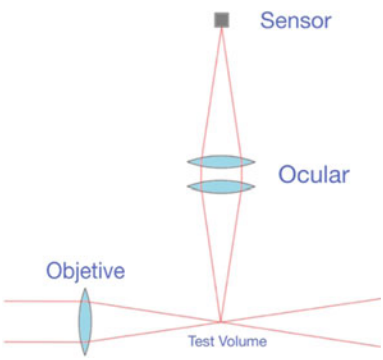

Fig. 2 General scheme of the laser velocimeter

are necessary, so it is possible to use first surface mirrors, or a prism. The choice between one and the other depends especially on the quality of the components, as will be analyzed later. With the above, we have a basic design for the system, Fig. 2. The system generates a test volume where the interference system is located, the particles that pass through this volume will emit a pulse of light that will be sent to the Hamamatzu brand sensor.

The mechanical parts were designed in a CAD software where the printing was done using a Dremel 20 3D printer. A 640 nm laser diode was adhered to the optical system. The parasitic light was controlled by a matt black paint coating. We proceeded to use a chopper and measure the speed of the system to verify the correct functioning of the system, electronic and optical. Figure 3 shows the design of the constructed optical device.

To evaluate the prototype, the water flow velocity inside a cylindrical duct was measured. Considering a laminar flow, it is found:

$$vc = \frac{8Q}{D^2\pi} \tag{3}$$

as well as

$$vc = 2vp, \tag{4}$$

where vc is the velocity in the axis of the pipe, vp is the average speed, and Q is the volumetric flow. The experimental arrangement consisted of a water reservoir, a cylindrical pipe with windows, and a reservoir, controlling the volumetric flow through a valve. The flow was measured by a graduated cylinder and the filling time. The sensor signals were obtained from a Tektronix TDS1001B oscilloscope, and analyzed by FFT.

The fluid behaves like a sheet when it goes at different speeds for a fluid, it depends on the speed at which the particles advance according to the number of Reynols [9].

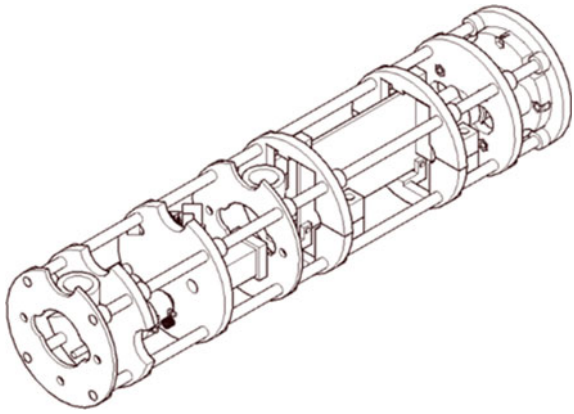

Fig. 3 LVD system designed to be printed in 3D

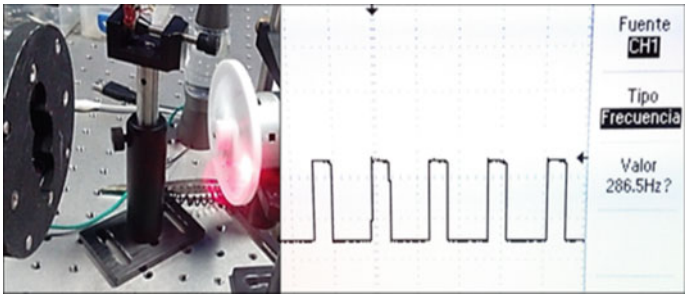

Fig. 4 Evaluation of the operation of the optical system laser velocimeter

The calibration of the system is in accordance with this situation, based on the laminar flow and the next experiments.

3 Results

Two experiments were carried out described below:

First Experiment:

The operation of the system was evaluated by comparing the system signal and the rotation speed of a chopper. Figure 4, the left part shows the installation of the experiment, the right side shows the signal in square pulses that the laser velocimeter system measures, here we can identify the amplitude of the signal in time as well as its frequency corresponding to the chopper speed.

Second Experiment:

In the second experiment, low speeds were used (1). To estimate flows and velocities, the following procedure was carried out: by means of the valve, the flow rate was limited (Fig. 5), and the filling time of a beaker was measured. Multiple samples were taken, to obtain an average time of the speed to be measured.

The velocimeter response signal Fig. 6a was captured and processed to obtain the power spectrum, where the power spectrum is shown in Fig. 6b, which indicates the maximums related to the velocity inside the tube. The result correspoding to these signals is shown in Table 1, the measured speed of our system was 0.681 cm/s.

4 Conclusions

Through the construction of this prototype, and its evaluation in the previous experiments, the utility was demonstrated in applications where it is necessary to measure

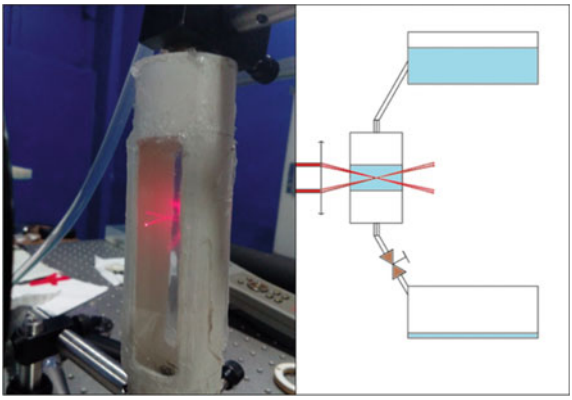

Fig. 5 Graphic description of the experiment for the flow of water in a pipeline

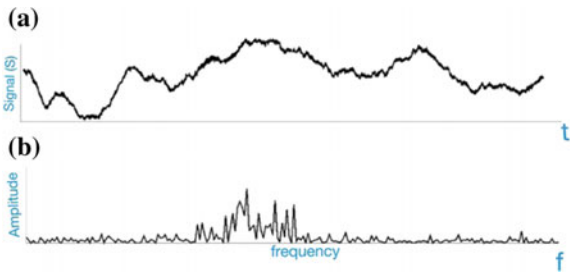

Fig. 6 **a** Graph of the signal measured in time. **b** Its power spectrum

Table 1 The calculation to determine particle velocity by equations (1) and (2)

Frecnenda leida (hz)	v_c (cm/seg)	$\bar{v}$ (cm/seg)	Q (cm^3/seg)	$t_{llenado}$ (seg)
4332	0.641	0.320	2.26	441
4639	0.686	0.343	2.42	412
4528	0.670	0.335	2.36	422
4684	0.693	0.346	2.44	408
4803	0.711	0.355	2.51	397
4711	0.697	0.348	2.46	405
4851	0.718	0.359	2.53	394
4538	0.672	0.336	2.37	421
4376	0.648	0.324	2.29	436

the speed in a non-invasive way. It is planned to continue with the research of the system, as well as to make improvements in the proposed design.

1. Improvement of the optical system: perform the design and construction of an objective system with variable focal distance, and present corrections of the spherical aberration, to be able to make measurements in positions further away from the anemometer.

2. Perform fiber optic application, to decrease the physical size of the system.
3. Improvement of the light source: implement a spatial filtering on the source, as well as the lens of collimation and concentration.
4. Improvements on the data acquisition system: design and implement a system that performs the analog-digital conversion, dimensioned to a specific band. Implement wireless communication from the acquisition system to the processing system.
5. Improvements on the software: make the program through the Python language and implement it on Android.

We intend to patent our system. By rules of intellectual property in Mexico, after making a publication with the details of the development of the system would pass to the public domain, so we would lose the rights.

References

1. E. Hecht, *Optics*, vol. 1, 4th edn. (Addison Wesley Publishing Company, 2001)
2. N. Menn, *Practical Optics*, 1st edn. (Elsevier, 2004)
3. H.-E. Albrecht, M. Borys, N. Damaschke, C. Tropea, *Laser Doppler and Phase Doppler Measurement Techniques*, vol. 43 (Cryogenics, 2003)
4. Y.A. Cengel, *Mecánica de Fluidos*, vol. 1 (McGraw-Hill, 2006)
5. J. Coupland, Laser Doppler and pulsed laser velocimetry in fluid mechanics. Photo-mechanics **412**, 373–412 (2000)
6. O. Donald, *Elements of Modern Optical Design*, 1st edn. (Wiley, Atlanta, 1985); F. Durst, A. Melling, J.H. Whitelaw, C.P. Wang, Principles and practice of laser-doppler anemometry. J. Appl. Mech. (1977)
7. I. Fredriksson, C. Fors, J. Johansson, Laser doppler flowmetry—a theoretical framework. Measurement 1–22 (2007)
8. I. Fredriksson, M. Larsson, T. Strömberg, Measurement depth and volume in laser Doppler flowmetry. Microvasc. Res. **78**(1), 4–13 (2009)
9. Y. Cengel, J. Cimbala, *Mecanica de Fluidos Fundamentos y Aplicaciones* (McGraw Hill, Primera Ed., 2010)

Modeling and Control of a Two-Axis Solar Tracking System

Yves J. Pérez D., Ruben Garrido and Arturo Díaz Ponce

Abstract The present work focuses on the analysis of a two-axis pedestal-type solar tracking system controlled by a Proportional-Integral-Derivative (PID) control law plus feedforward applied to the motors that drive the tracking system. The implementation of a solar positioning algorithm is performed to calculate the trajectories of the solar tracking system to track the movement of the sun. These trajectories are applied as desired trajectories to the PID control loops controlling the motors. Results of real-time experiments are presented, and the energy consumption of the motors is analyzed.

1 Introduction

Currently, different types of technological devices are available to facilitate the way of life of humans; most of them require electrical energy for its operation. Knowing that the electric demand is very high, the world faces a lack of fossil fuels in the future, so the use of alternative energy sources must increase considerably. It should be noted that the way in which the natural energy resources have been exploited has had negative consequences on the environment, which is why it is necessary to continue innovating in the field of renewable energies to improve their efficiency and production. One of the main sources of renewable energy is the sun, which produces energy in its inner core in a process called nuclear fusion. This energy is radiated to

Y. J. Pérez D. (✉) · R. Garrido
Departamento de Control Automático, CINVESTAV-IPN, Av. IPN 2508, San Pedro Zacatenco, México City, Mexico
e-mail: yperez@ctrl.cinvestav.mx

R. Garrido
e-mail: garrido@ctrl.cinvestav.mx

A. Díaz Ponce
CONACYT—Centro de Investigaciones En Óptica, A.C Unidad Aguascalientes—Prol. Constitución 607, Fracc. Reserva Loma Bonita, Aguascalientes, 20200 Aguascalientes, Mexico
e-mail: adiaz@cio.mx

A. Martínez-García et al. (eds.), *Progress in Optomechatronic Technologies*,
Springer Proceedings in Physics 233, https://doi.org/10.1007/978-981-32-9632-9_21

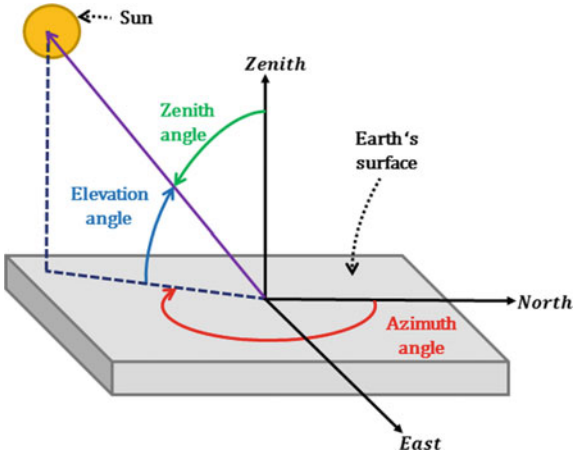

Fig. 1 Solar angles

space and is known as solar energy. One fact to note is that the sun radiates more energy in one day than the total energy consumed on earth over a year [1].

A solar tracking system takes advantage of the largest amount of solar energy by maintaining a photovoltaic cell surface as perpendicular as possible with respect to the sun radiation. Therefore, the optimal energy generation by the cell is reached by tracking the apparent sun movement. Tracking improves photovoltaic cell energy production under clear sky conditions by 35–40% with respect to static cells [2, 3].

The two most common topologies employed in solar tracking are one-axis and two-axis systems. The former is employed to follow the sun from East to West [4, 5], whereas the latter tracks the sun movement in almost any direction thus taking full advantage of the solar radiation [6, 7]. To compute the sun position relative to any point on the surface of the Earth, two angles are enough, i.e., the elevation and azimuth angles, or the zenith and the azimuth angles. These angles are shown in Fig. 1 and vary throughout the day, and they also depend on the geographic coordinates of the place and the day of the year [8].

2 Methodology

The trajectories aimed to track the sun are computed through the Matlab/Simulink® software using the solar positioning algorithm described in [9], on March 15, 2018, in the interval between 6:00 a.m. and 7:00 p.m., with a step of 1 s between each calculation of the position. Location is the CINVESTAV-Unidad Zacatenco. The time zone is UTC-6. The coordinates are as follows: longitude −99.13047°, latitude 19.50991°, and altitude 2224 m. An annual average temperature of 16.6°C and atmospheric pressure of 781 mBar are assumed. The use of third and fifth-order polynomials are proposed to smooth out the beginning of the trajectories and for restoring the ini-

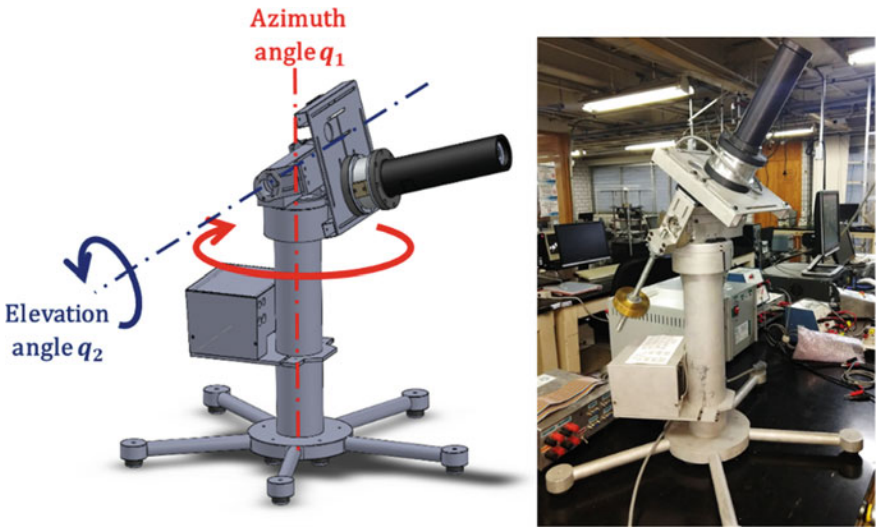

Fig. 2 Two-axis solar tracking system

tial conditions of the tracker. The generated trajectories feed a trajectory generation block to estimate their first and second time derivatives.

A two-axis solar tracker composed of revolute joints is shown in Fig. 2. Its dynamic model is obtained through the Euler–Lagrange formalism [10] shown in (1). The solar tracker joints correspond to the azimuth and elevation angles and they are taken as the generalized coordinates $q = \left[q_1, q_2\right]^T$ of this mechanical system.

$$D(q)\ddot{q} + C(q, \dot{q})\dot{q} + G(q) = \tau \tag{1}$$

which has the next alternative writing, where I_{xi}, I_{yi} and I_{zi} are the principal moments of inertia of each link, r_2 is the distance between the axis of rotation and the mass center of the second link, m_2 is the mass of the second link, τ_i are the torques applied on each joint.

$$\begin{bmatrix} I_{y1} + I_{x2}\sin^2(q_2) + I_{y2}\cos^2(q_2) + m_2 r_2^2 \cos^2(q_2) & 0 \\ 0 & m_2 r_2^2 + I_{z2} \end{bmatrix} \begin{bmatrix} \ddot{q}_1 \\ \ddot{q}_2 \end{bmatrix} + \begin{bmatrix} -\frac{1}{2}(m_2 r_2^2 - I_{x2} + I_{y2})\sin(2q_2)\dot{q}_2 & -\frac{1}{2}(m_2 r_2^2 - I_{x2} + I_{y2})\sin(2q_2)\dot{q}_1 \\ \frac{1}{2}(m_2 r_2^2 - I_{x2} + I_{y2})\sin(2q_2)\dot{q}_1 & 0 \end{bmatrix} \begin{bmatrix} \dot{q}_1 \\ \dot{q}_2 \end{bmatrix} + \begin{bmatrix} 0 \\ g m_2 r_2 \cos(q_2) \end{bmatrix} = \begin{bmatrix} \tau_1 \\ \tau_2 \end{bmatrix}$$

Two brushed direct current motors (DC motors) endowed with reduction gearboxes are used to produce the torque at the joints of the solar tracking system. We consider the next mechanical model of a DC motor

$$J_m\ddot{\theta}_m + B_m\dot{\theta}_m = \tau_e - \tau_m + h_m \tag{2}$$

The term J_m corresponding to the inertias of the motor and its gearbox, B_m is the gearmotor viscous friction coefficient, τ_e is the electromagnetic torque produced by the motor, τ_m is the load torque action on the motor due to the dynamics of the solar tracker mechanism, and h_m are disturbances in the motor produced by parasitic voltages produced by the power amplifier, mechanical static friction, or unmodeled torques. The use of a power amplifier in current mode for driving the DC motor produces the proportional relationship $\tau_e = ku$ where k is a constant and u is the control signal.

Consider the relationships $\theta_m = Rq$ and $\tau = R\tau_m + h_l$ where R is the gearbox reduction ratio and h_l are the external mechanical disturbances at the joints of the solar tracker mechanism such as wind loads. If the gearbox is rigid, then it allows merging models (1) and (2) to obtain the dynamic model of the solar tracker considering the DC gearmotors,

$$J_m\ddot{\theta}_m + B_m\dot{\theta}_m = ku - R^{-1}[D(q)\ddot{q} + C(q,\dot{q})\dot{q} + G(q) - h_l] + h_m$$

Replacing $q = R^{-1}\theta_m$ yields

$$\begin{aligned} J_m\ddot{\theta}_m + B_m\dot{\theta}_m = {} & ku - R^{-1}D(q)R^{-1}\ddot{\theta}_m - R^{-1}C(q,\dot{q})R^{-1}\dot{\theta}_m - R^{-1}G(q) \\ & + R^{-1}h_l + h_m \end{aligned}$$

For $k = 1, 2$ the equations of motion of the solar tracker can be written as

$$\begin{aligned} J_{mk}\ddot{\theta}_{mk} + B_{mk}\dot{\theta}_{mk} = {} & k_k u_k - \sum_{j=1}^{n} d_{jk}(q)\frac{\ddot{\theta}_{mk}}{R_j}\frac{1}{R_k} - \sum_{i,j=1}^{n} C_{ijk}(q)\frac{\dot{\theta}_{mi}}{R_i}\frac{\dot{\theta}_{mj}}{R_j}\frac{1}{R_k} \\ & - \frac{g_k(q)}{R_k} + \frac{h_{lk}}{R_k} + h_{mk} \end{aligned}$$

If R_jR_k and $R_iR_jR_k \forall i, j, k$ are much greater than 1, then the next terms are very small and can be neglected

$$-\sum_{j=1}^{n} d_{jk}(q)\ddot{\theta}_{mk}\frac{1}{R_jR_k} - \sum_{i,j=1}^{n} c_{ijk}(q)\frac{\dot{\theta}_{mi}}{R_i}\frac{\dot{\theta}_{mj}}{R_j}\frac{1}{R_k} \approx 0$$

So we can write the next simplified models as

$$J_{mk}\ddot{\theta}_{mk} + B_{mk}\dot{\theta}_{mk} = k_k u_k - \frac{g_k(q)}{R_k} + \frac{h_{lk}}{R_k} + h_{mk}$$

Therefore, in terms of the generalized coordinates q, the simplified models for each DC gearmotor are

$$\ddot{q}_k + a_k \dot{q}_k = b_k u_k + d_k; \quad k = 1, 2 \tag{3}$$

where $a_k = \frac{B_{mk}}{J_{mk}}$, $b_k = \frac{k_k}{J_{mk} R_k}$, $d_k = \frac{h_{mk}}{R_k J_{mk}} + \frac{h_{lk}}{R_k^2 J_{mk}} - \frac{g_k(q)}{R_k^2 J_{mk}}$.

A PID plus feedforward control is proposed for controlling each DC gearmotor. Define the tracking error $e_k = r_k - q_k$ where r_k is the trajectory generated by the solar positioning algorithm.

The proposed control law is

$$u_k = \frac{1}{b_k}[a_k \dot{r}_k + \ddot{r}_k] + \frac{1}{b_k}\left[K_{pk} e_k + K_{dk} \dot{e}_k + k_{ik} \int_0^t e_k(\tau) d\tau\right]$$

where

$$u_{pk} = \frac{1}{b_k}[a_k \dot{r}_k + \ddot{r}_k]$$

is the feedforward part and

$$u_{rk} = \frac{1}{b_k}\left[K_{pk} e_k + K_{dk} \dot{e}_k + K_{ik} \int_0^t e_k(\tau) d\tau\right]$$

is the feedback part. The constants K_{pk}, K_{ik}, and K_{dk} are the Proportional-Integral-Derivative gains. The control scheme is shown in Fig. 3.

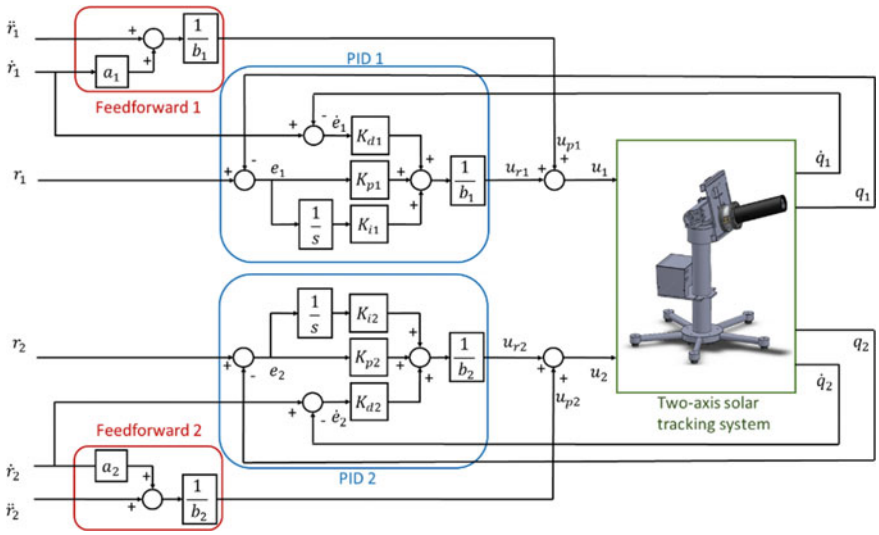

Fig. 3 PID + feedforward controller applied to each servomotor

Replacing the control law $u_k = \frac{1}{b_k}[a_k \dot{r}_k + \ddot{r}_k] + u_{rk}$ into (3) and defining the state variable $X_k = \left[e_k, \dot{e}_k, \int_0^t e_k(\tau)d\tau\right]^T$ allow writing the model in state space for each servomotor in closed loop as shown in (4)

$$\dot{X}_k = \underbrace{\begin{bmatrix} 0 & 1 & 0 \\ 0 & -a_k & 0 \\ 1 & 0 & 0 \end{bmatrix}}_{A_k} X_k + \underbrace{\begin{bmatrix} 0 \\ -b_k \\ 0 \end{bmatrix}}_{B_k} u_{rk} + \underbrace{\begin{bmatrix} 0 \\ -1 \\ 0 \end{bmatrix}}_{F_k} d_k \tag{4}$$

An LQR optimal control is proposed to tune the gains of the PID controller. The closed-loop system associated with each DC gearmotor in state space without disturbances is represented as

$$\dot{X}_k = \underbrace{\begin{bmatrix} 0 & 1 & 0 \\ 0 & -a_k & 0 \\ 1 & 0 & 0 \end{bmatrix}}_{A_k} X_k + \underbrace{\begin{bmatrix} 0 \\ -b_k \\ 0 \end{bmatrix}}_{B_k} u_{rk}, \quad \text{with} \quad X_k = \left[e_k, \dot{e}_k, \int_0^t e_k(\tau)d\tau\right]^T$$

Solution of the next algebraic Riccati equation in (5) allows computing the optimal gains for the PID control [11], where Q_{1k} is a weighting matrix associated with the state variables, Q_{2k} is a weighting parameter associated with the control signal, and S_k is the solution of the Riccati equation.

$$\begin{aligned} &Q_{1k} + A_k^T S_k + S_k A_k - S_k B_k Q_{2k}^{-1} B_k^T S_k = 0 \\ &Q_{1k} \geq 0, \quad Q_{2k} > 0; \text{unknown matrix:} \quad S_k > 0 \end{aligned} \tag{5}$$

The optimal control law by state feedback is

$$u_{rk} = -L_k X_k \quad \text{where} \quad L_K = Q_{2k}^{-1} B_k^T S_k$$

Therefore, the optimal gains for the PID control are computed as

$$\left[K_{pk}, K_{dk}, K_{ik}\right]^T = -b_k Q_{2k}^{-1} B_k^T S_k$$

The undisturbed system with state feedback is defined as

$$\dot{X}_k = A_k X_k + B_k u_{rk} = X_k - B_k L_k X_k = \underbrace{[A_k - B_k L_k]}_{A_{clk}} X_k$$

which corresponds to the next linear system in closed loop.

$$\dot{X}_k = A_{clk} X_k$$

When the linear quadratic regulator is used, it is ensured that the closed-loop system is stable, so A_{clk} is Hurwitz; therefore $\forall Q_{clk} > 0, \exists P_k = P_k^T > 0$ such that

$$A_{clk}^T P_k + P_k A_{clk} = -Q_{clk}$$

The stability in the sense of Lyapunov will be analyzed for the following closed-loop system considering the perturbation d_k

$$\dot{X}_k = A_{clk} X_k + F_k d_k$$

Assume that d_k is bounded, that is $|d_k| \leq D_k < \infty$ and consider the following Lyapunov function candidate

$$V_k = X_k^T P_k X_k$$

Its time derivative is

$$\begin{aligned}
\dot{V}_k &= \dot{X}_k^T P_k X_k + X_k^T P_k \dot{X}_k \\
&= (X_k^T A_{clk}^T + F_k^T d_k) P_k X_k + X_k^T P_k (A_{clk} X_k + F_k d_k) \\
&= X_k^T \underbrace{[A_{clk}^T P_k + P_k A_{clk}]}_{-Q_{clk}} X_k + 2 F_k^T P_k X_k d_k \\
&= -X_k^T Q_{clk} X_k + 2 F_k^T P_k X_k d_k
\end{aligned}$$

which is upper bounded as follows:

$$\dot{V}_k \leq -\lambda_{\min}(Q_{clk}) \|X_k\|^2 + 2\|F_k\| \|X_k\| \lambda_{\max}(P_k) D_k$$

Since $F_k = [0, -1, 0]^T \quad \Rightarrow ||F_k|| = \sqrt{(-1)^2} = 1$ then

$$\dot{V}_k \leq -\lambda_{\min}(Q_{clk}) ||X_k|| \left[||X_k|| - 2 \frac{\lambda_{\max}(P_k)}{\lambda_{\min}(Q_{clk})} D_k \right]$$

Therefore

$$\dot{V}_k < 0 \quad \text{if} \quad ||X_k|| > \frac{\lambda_{\max}(P_k)}{\lambda_{\min}(Q_{clk})} 2 D_k = R_{ck}$$

Let the set $B_{Rk} = \{||X_k(t)|| \leq R_{ck}\}$ inside of the disk of radius R_{ck}. Then, $\dot{V}$ is negative outside of B_{Rk}, so solutions that start outside B_{Rk} will enter this set in a finite time T and remain in the set for all future time. Therefore, the solutions to $X_k(t)$ are uniformly ultimately bounded (UUB).

3 Experimental Results

The experimental setup is described next. Two Harmonic Drive servomotors model RH-14D6002-E100AL drive the solar tracker axes. Each servomotor has the experimental setup shown in Fig. 4. The servomotor has a gearbox reduction of 50:1 and is endowed with an incremental encoder with 1000 pulses/rev with two channels coupled to the motor shaft, therefore the resolution is 200000 pulses/rev at the output of the gearbox shaft. A Sensoray data acquisition card model 626, which has 16-bit analog–digital converters, 14-bit digital-to-analog converters, and is able to read optical encoders. A Copley Controls power amplifier model 432 working in current mode. It has current and voltage monitoring signal outputs. A first isolation box with two channels for the current and voltage monitoring. These signals are filtered by analog RC filters. A second isolation box has one channel for the control signal. Programming of the control algorithms is performed through a PC Intel Core 2 quad computer and the Matlab/Simulink software and the real-time environment Quarc by Quanser Consulting.

The energy consumption is monitored by measuring the current $i(t)$ and the voltage $v(t)$ applied to each DC gearmotor; the instantaneous power $P(t)$ is computed according to (6). The energy consumption W_{fi} is obtained by integrating with respect to time the power $P_{fi}(t)$ (see (7)). The Integral of the Square Error (ISE) is used

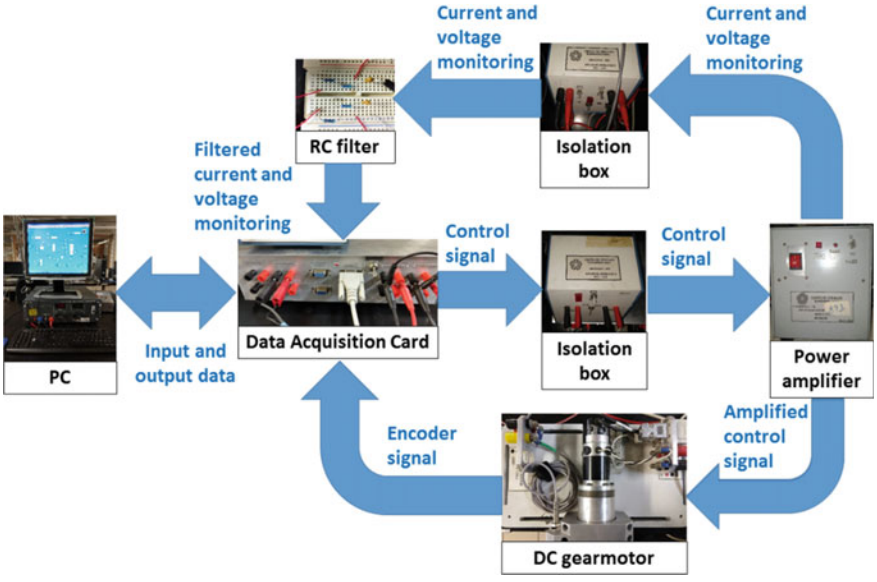

Fig. 4 Experimental setup

as a performance criterion and is defined in (8). The signals v_{fi}, i_{fi}, e_{fi} are the filtered voltage, filtered current, and filtered tracking error in this order for each DC gearmotor

$$P_{fi}(t) = v_{fi}(t) i_{fi}(t) \tag{6}$$

$$W_{fi}(t) = \int_0^t P_{fi}(\tau) d\tau \tag{7}$$

$$\text{ISE}_\text{i} = \int_0^t (100 e_{fi}(\tau))^2 d\tau \tag{8}$$

The estimated parameters are $a = a_1 = a_2 = 10.2250$ and $b = b_1 = b_2 = 1275.8$, determined by the Least Squares Method. The same parameters for both gearmotors are used $Q_1 = Q_{1k}$ and $Q_2 = Q_{2k}$. The experimental results are shown in Table 1 using the weighting matrix $Q_1 = \text{diag}\big[\, 500 \;\; 1 \;\; 600 \,\big]$. Note that different values of the PID gains are obtained by changing the value of the weight parameter Q_2. If the value of Q_2 increases, so does the ISE criterion but the energy consumption W_{fi} decreases.

Figure 5 shows the trajectory tracking results where r_1 is the desired trajectory of the azimuth axis and q_1 the actual trajectory, while r_2 is the desired trajectory of the elevation axis and q_2 the actual trajectory. The time evolution is compressed by a factor of 1000 to be able to perform the experiments of a full day in a time of 86.4 s. Figure 6 shows the control signals.

Table 1 Experimental results for different values of the weight parameter Q_2

Q_2	K_p	K_d	K_i	W_{f1}	W_{f2}	ISE_1	ISE_2
800	1078.01	55.312	1104.88	39.182	17.944	60.396	28.204
900	1017.43	52.608	1041.69	37.819	17.772	65.047	30.414
1000	966.17	50.311	988.23	37.548	17.686	74.269	33.312
1100	922.06	48.327	942.24	37.243	17.588	84.166	36.992
1200	883.58	46.591	902.13	36.852	17.448	95.376	40.399
1300	849.62	45.055	866.74	36.822	17.246	91.792	42.796
1400	819.36	43.681	835.21	36.603	17.242	99.539	46.84
1500	792.18	42.444	806.89	35.968	16.987	115.158	49.733
1600	767.59	41.321	781.26	35.910	16.804	119.077	52.372
1700	745.19	40.296	757.94	35.806	16.779	124.277	56.79

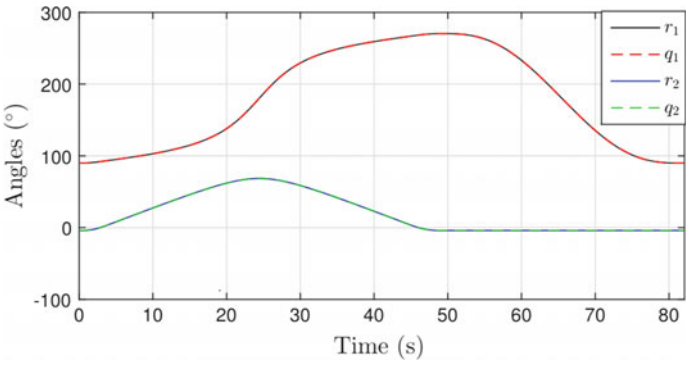

Fig. 5 Tracking with $Q_2 = 800$

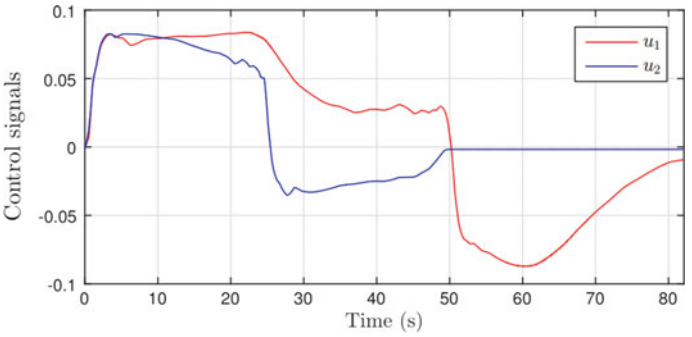

Fig. 6 Control signals with $Q_2 = 800$

4 Conclusion

The trajectories of the azimuth and elevation angles are obtained with a solar position algorithm, and it is verified that the PID plus feedforward controller makes a good trajectory tracking in both axes of these trajectories. On the other hand, the experiments suggest that the trade-off between energy consumption and tracking quality may be modulated through a single parameter, namely the weighting factor Q_2 associated with the LQR methodology. In this regard, note that improving tracking quality will raise the efficiency in energy production, which is particularly paramount in Concentrating Photovoltaics, but at the expense of more energy consumption. On the other hand, a solar tracking system must consume only a very small portion of the energy produced by itself, but it still must maintain high tracking quality. Therefore, the proposed tuning methodology allows for solving the above trade-off in a simple manner.

Acknowledgements The authors would like to thank the support of Gerardo Castro Zavala, Jesus Meza Serrano in setting up the laboratory testbed. The first author would like to thank the support given by CONACyT and CINVESTAV-IPN. This work has been supported by CONACyT Mexico under grant 222140.

References

1. C.J. Rhodes, Solar energy: principles and possibilities. Sci. Prog. **93**(1), 37–112 (2010)
2. R. Arreola Gómez, y col. Diseño, construcción y evaluación de un sistema de seguimiento solar para un panel fotovoltaico. Revista mexicana de ciencias agrícolas **6**(8), 1715–1727 (2015)
3. D.M. Mosher, R.E. Boese, R.J. Soukup, The advantages of sun tracking for planar silicon solar cells. Sol. Energy **19**, 91–97 (1977)
4. R. Garrido, A. Díaz, Cascade closed-loop control of solar trackers applied to HCPV systems. Renew. Energy **97**, 689–696 (2016)
5. J.M. Hallas, K.A. Baker, J.H. Karp, E.J. Tremblay, J.E. Ford, Two-axis solar tracking accomplished through small lateral translations. Appl. Opt. **51**(25), 6117–6124 (2012)
6. Y. Yao, Y. Hu, S. Gao, G. Yang, J. Du, A multipurpose dual-axis solar tracker with two tracking strategies. Renew. Energy **72**, 88–98 (2014)
7. B.J. Huang, F.S. Sun, Feasibility study of one axis three positions tracking solar PV with low concentration ratio reflector. Energy Convers. Manag. **48**(4), 1273–1280 (2007)
8. G.N. Tiwari, *Solar Energy: Fundamentals, Design, Modelling and Applications*. Alpha Science Int'l Ltd. (2002)
9. I. Reda, A. Andreas, Solar position algorithm for solar radiation applications. Sol. Energy **76**(5), 577–589 (2004)
10. M.W. Spong, Seth Hutchinson Mathukumalli Vidyasagar. *Robot Nodeling and Control*, vol. 3. (Wiley, New York, 2006)
11. R. Garrido, R. Miranda, Autotuning of a DC servomechanism using closed loop identification, in *IEEE Industrial Electronics, IECON 2006-32nd Annual Conference on. IEEE* (2006), pp. 258–263

Comparison of Nulling Interferometry and Rotational Shearing Interferometry for Detection of Extrasolar Planets

Beethoven Bravo-Medina, Marija Strojnik and Erick Ipus

Abstract In the last few years, the extrasolar planet detection has been an important science topic. An overwhelming number of the current detections were accomplished using indirect methods. In order to achieve direct detection of planets, a number of interferometric techniques have been proposed. Among those, some are already implemented in terrestrial observatories. The most published of these techniques is the nulling interferometry. We are working on a derivative interferometric technique, referred to as rotational shearing interferometry. We perform a comparison between these techniques and report on the status of their development.

1 Challenges of Detecting an Extrasolar Planet

The interest of the scientific community and general population about the planets outside our Solar System has been increased during the last 30 years. The main reason for this interest is the search of habitable planets [7]. The number of confirmed extrasolar planets has increased only in the latest decade, from 427 in 2011 [17] to over 3500 in 2018. The Kepler space telescope has performed the majority of these detections. This telescope has detected 4034 planet candidates [16]. The main detection techniques used in these observations are transit and radial velocity [13]. Unfortunately, these techniques are indirect techniques; they provide indirect and limited data. Therefore, a direct detection technique is necessary to validate the current observations [11].

The main challenge in the extrasolar planet detection lies in the very-large distance of the nearest stars to the Earth. This distance implies two resolution problems: the radiometric and the spatial one. The radiometric resolution is the minimum irradiance change that may be detectable by the sensor. The radiation ratio between the planet and the star is at least 10–6 in the visible region. The spatial resolution is the minimum

B. Bravo-Medina (✉) · M. Strojnik · E. Ipus
Centro de Investigaciones en Óptica A. C., Apdo Postal 1-948, 37150 León, Mexico
e-mail: beethoven@cio.mx

M. Strojnik
e-mail: mstrojnik@gmail.com

A. Martínez-García et al. (eds.), *Progress in Optomechatronic Technologies*,
Springer Proceedings in Physics 233, https://doi.org/10.1007/978-981-32-9632-9_22

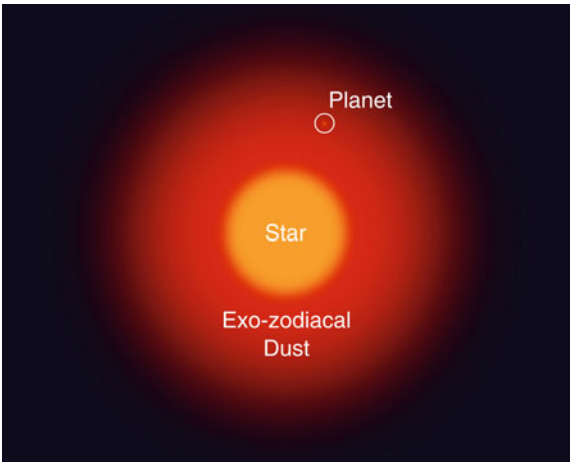

Fig. 1 Star with an exo-zodiacal cloud around it. The radiation from the exo-zodiacal dust makes the detection of a planet significantly difficult

angular separation that allows us to distinguish between two point sources. For a planet with an orbit similar to that of the Earth, that orbits a star at ten parsecs from the observatory, the angle between the planet and the star as seen from the Earth is 0.1 arc-sec.

Additionally, the stars are surrounded by the exo-zodiacal dust (see Fig. 1). This dust is located in the habitable zone of the planetary systems, meaning where the planets are likely to be located. Its presence obstructs the detection of exoplanets acting as a veil [6]. In order to decrease these resolution challenges and the effect of exo-zodiacal dust, several interferometric techniques have been proposed. The most highly developed of these techniques is the nulling interferometry [8, 9]. We are pursuing an alternate interferometric technique, the rotational shearing interferometry where we already demonstrated some initial promising results [12, 14].

In this work, we compare the nulling interferometry and the rotational shearing interferometry for exoplanet detection. In Sect. 2, we describe the operating principle of each technique. Then, we present the state of development and implementation of each technique in Sect. 3. Finally, we present the summary in Sect. 4.

2 Analysis

Due to the large distance between the star–planet system and the Earth, it is necessary to model the star and the planet as point sources. Additionally, their wave fronts may be modeled as planar. If the star is aligned with the optical axis, its wave front is perpendicular to the optical axis and the planet wave front is slightly tilted as illustrated in Fig. 2.

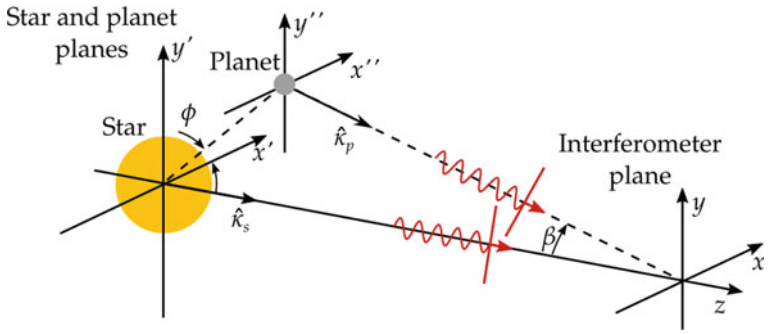

Fig. 2 Star–planet system viewed for the interferometer. The star is aligned with the interferometer optical axis. The star and planet wave fronts may be modeled as plains due to the large distance from the Earth

2.1 Nulling Interferometry

The nulling interferometry technique interferes the star wave front with itself. The star wave front through two interferometer arm may be canceled when the optical-path difference is an odd multiple of π. Due to the planet wave front tilt, its wave front propagates by a slightly different optical path and avoids the cancelation. Figure 3 illustrates the diagram of a nuller interferometer incorporating an optical-path modulator. The result of the stars self-interference is a uniform irradiance level without fringes. This irradiance level depends on the angular separation between the planet and the star, and the optical path difference (OPD) between the interferometer arms. This technique results in improvement of the radiometric resolution.

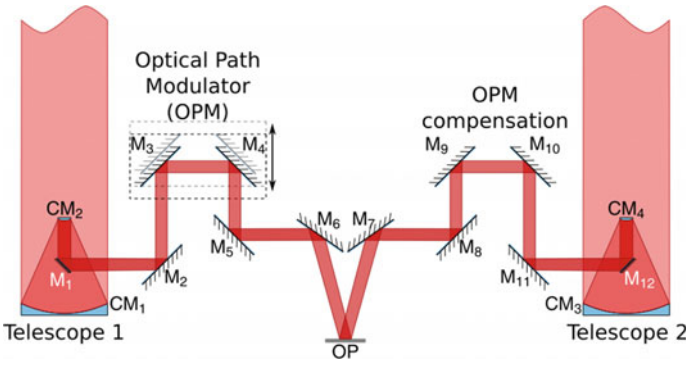

Fig. 3 The nuller interferometer (NI) interferes the star and planet wave fronts with a delayed version of them

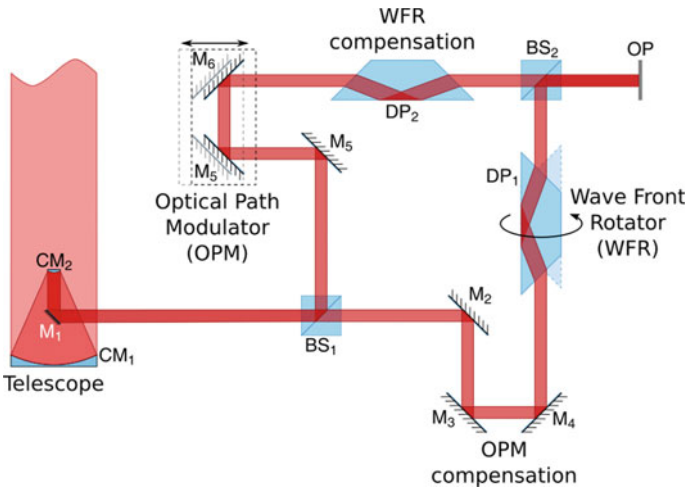

Fig. 4 The rotationally shearing interferometer (RSI) interferes the star and planet wave fronts with a rotated version of them

2.2 Rotationally Shearing Interferometry

The rotationally shearing interferometer (RSI) interferes the wave front with a rotated version of itself. Figure 4 illustrates the rotationally shearing interferometer incorporating an optical path modulator and a Dove prism as wave- front rotator. The RSI is insensitive to rotationally invariant wave fronts. When the rotationally symmetric star wave front interferes with its rotated version, the resultant interference pattern has uniform irradiance with a single fringe, characterized by a uniform field. Furthermore, the star irradiance may be canceled when the interferometer OPD has adjusted to 2. This adjustment may be performed with a wedge prism [1] or a Risley prism [2]. The planet wave front is rotationally asymmetric because it is tilted with respect to the optical axis. Therefore, the interferometric pattern generated in the RSI of the planet wave front consists of straight fringes. The fringe density and orientation depend on the shearing angle [15]. This technique allows the improvement of radiometric and spatial resolution. Finally, the RSI may be used to cancel symmetric rings of exo-zodiacal dust.

3 Implementation

Since the first proposal in 1979, several projects to implement nulling interferometry in exoplanets detection have been proposed. The most important of these projects is the Darwin/ TPF project [5]. This project contemplates a spatial nulling-interferometer, whose deployment is planned for about 2030. There are additional

subprojects that involve nulling interferometry. Two of these subprojects are the Keck Nuller Interferometer (KNI) [10] and the Large Binocular Telescope interferometer (LBTI) [3]. The initial objective of these interferometers is the characterization of the exo-zodiacal dust. The first detection of warm dust with the LBTI around the star η Crv was reported in 2015. Meanwhile, the non-nulling interferometers like the very-large-telescope interferometer report challenges in detecting the exo-zodiacal dust [4].

Meanwhile, we proposed the RSI for implementation in an observatory on the moon.

4 Summary and Future Work

Both, the nulling interferometry and the rotational shearing interferometry have been proposed and studied for the exoplanet detection. Both techniques may be used to enhance the radiometric resolution of a stellar observatory. However, only the RSI allows the enhancement of the spatial resolution. The search for direct detection of extrasolar planets is a long-term project. We continue demonstrating RSI features in laboratory experiments. Its current capabilities include the cancelation or at least attenuation of rotationally-symmetrical structures of exo-zodiacal dust.

Acknowledgements This material is based upon work partially supported by the Air Force Office of Scientific Research under award number FA9550-18-1-0454. Any opinions, finding, and conclusions or recommendations expressed in this material are those of the authors and do not necessarily reflect the views of the United States Air Force.
The author B.B.M. acknowledges the Fellowship of the Consejo Nacional de Ciencia y Tecnología (CONACYT), México, for the economic support to accomplish this research.

References

1. B. Bravo-Medina, G. Garcia-Torales, M. Strojnik, J.L. Flores, E. de la Fuente, Shearing interferometer with adjustable optical path difference for exoplanet detection, in *Infrared Remote Sensing and Instrumentation XXIV*, vol. 9973. International Society for Optics and Photonics (2016), pp. 99730W. https://doi.org/10.1117/12.2238035
2. B. Bravo-Medina, M. Strojnik, G. Garcia-Torales, H. Torres-Ortega, R. Estrada-Marmolejo, A. Beltrán-González, J.L. Flores, Error compensation in a pointing system based on Risley prisms. Appl. Opt. **56**(8), 2209–2216 (2017). https://doi.org/10.1364/AO.56.002209
3. D. Defrere, P. Hinz, A. Skemer, G. Kennedy, V. Bailey, W. Hoffmann, B. Mennesson, R. Millan-Gabet, W. Danchi, O. Absil et al., First-light LBT nulling interferometric observations: warm exozodiacal dust resolved within a few au of η crv. Astrophys. J. **799**(1), 42 (2015)
4. S. Ertel, O. Absil, J.C. Augereau, D. Defrere, B. Mennesson, Prospects for the characterization of exozodiacal dust with the vlti. Future of optical-infrared interferometry in Europe (2017), pp. 22–25
5. C. Fridlund, Darwin-the infrared space interferometry mission. ESA Bull. **103**(3), 20–25 (2000)

6. Q. Kral, A.V. Krivov, D. Defrère, R. van Lieshout, A. Bonsor, J.C. Augereau, P. Thébault, S. Ertel, J. Lebreton, O. Absil, Exozodiacal clouds: hot and warm dust around main sequence stars. Astron. Rev. **13**(2), 69–111 (2017)
7. S. Martin, A. Booth, Demonstration of exoplanet detection using an infrared telescope array. Astron. Astrophys. **520**, A96 (2010)
8. S. Martin, A. Booth, K. Liewer, N. Raouf, F. Loya, H. Tang, High performance testbed for four-beam infrared interferometric nulling and exoplanet detection. Appl. Opt. **51**(17), 3907–3921 (2012)
9. B. Mennesson, A. Léger, M. Ollivier, Direct detection and characterization of extrasolar planets: the mariotti space interferometer. Icarus **178**(2), 570–588 (2005)
10. E. Serabyn, B. Mennesson, M. Colavita, C. Koresko, M. Kuchner, The Keck interferometer nuller. Astrophys. J. **748**(1), 55 (2012)
11. M. Strojnik, B. Bravo-Medina, G. Garcia-Torales, M. Scholl, Optimal band for extra solar planet detection: sub-millimeter spectral region, in *2017 42nd International Conference on Infrared, Millimeter, and Terahertz Waves (IRMMW-THz)* (IEEE, 2017), pp. 1–2. https://doi.org/10.1109/IRMMW-THz.2017.8066946
12. M. Strojnik, Rationally shearing interferometer for extra-solar system planet detection, in *Infrared Remote Sensing and Instrumentation XXVI*, vol. 10765 (2018), pp. 10765–10765–11. https://doi.org/10.1117/12.2515618
13. M. Strojnik, B. Bravo-Medina, Extra-solar planet detection methods, in *Infrared Remote Sensing and Instrumentation XXVI*, vol. 10765. International Society for Optics and Photonics (2018), p. 107650Y
14. M. Strojnik, G. Paez, Simulated interferometric patterns generated by a nearby star–planet system and detected by a rotational shearing interferometer. JOSA A **16**(8), 2019–2024 (1999). https://doi.org/10.1117/12.2319177
15. M. Strojnik, G. Paez, R. Baltazar-Barron, Detection of planet in nearby solar system with rotational shearing interferometer: concept demonstration, in *Latin America Optics and Photonics Conference*. Optical Society of America (2014), pp. LM1A–2. https://doi.org/10.1364/LAOP.2014.LM1A.2
16. S.E. Thompson, J.L. Coughlin, K. Hoffman, F. Mullally, J.L. Christiansen, C.J. Burke, S. Bryson, N. Batalha, M.R. Haas, J. Catanzarite, et al., Planetary candidates observed by Kepler. viii. A fully automated catalog with measured completeness and reliability based on data release 25. Astrophys. J. Suppl. Ser. **235**(2), 38 (2018)
17. J.T. Wright, O. Fakhouri, G.W. Marcy, E. Han, Y. Feng, J.A. Johnson, A.W. Howard, D.A. Fischer, J.A. Valenti, J. Anderson et al., The exoplanet orbit database. Publ. Astron. Soc. Pac. **123**(902), 412 (2011)